V. 120, NO. 2
MARCH 2023

ACI MATERIALS JOURNAL

A JOURNAL OF THE AMERICAN CONCRETE INSTITUTE

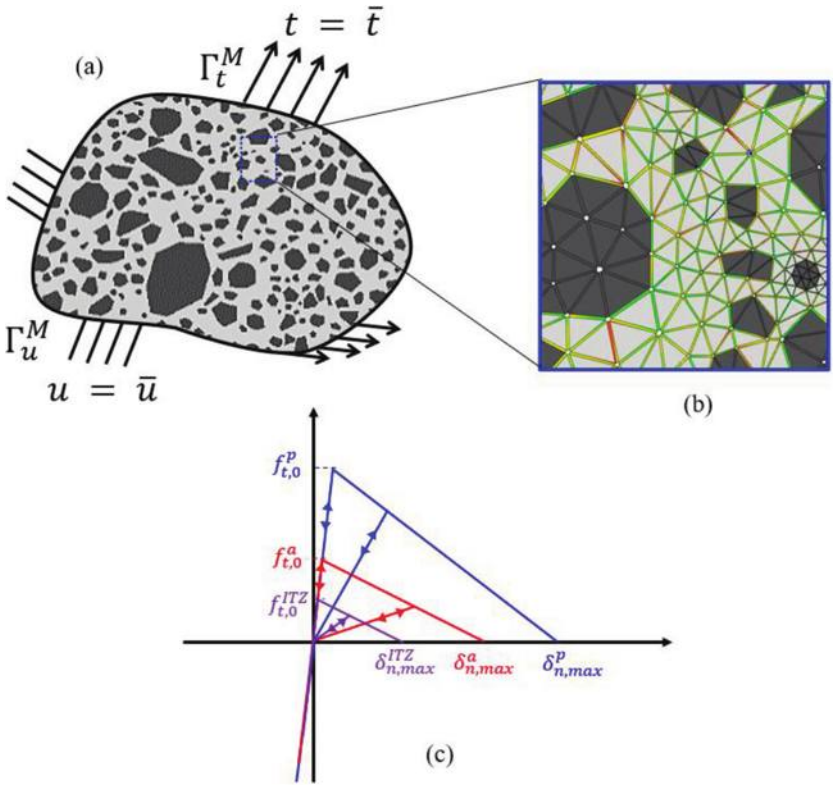

American Concrete Institute

CONTENTS

ACI Materials Journal

March 2023, V. 120, No. 2

A JOURNAL OF THE AMERICAN CONCRETE INSTITUTE
AN INTERNATIONAL TECHNICAL SOCIETY

Discussion is welcomed for all materials published in this issue and will appear ten months from this journal's date if the discussion is received within four months of the paper's print publication. Discussion of material received after specified dates will be considered individually for publication or private response. ACI Standards published in ACI Journals for public comment have discussion due dates printed with the Standard.

The *ACI Materials Journal* (ISSN 0889-325x) is published bimonthly by the American Concrete Institute. Publication office: 38800 Country Club Drive, Farmington Hills, MI 48331. Periodicals postage paid at Farmington, MI, and at additional mailing offices. Subscription rates: $192 per year, payable in advance. POSTMASTER: Send address changes to: *ACI Materials Journal*, 38800 Country Club Drive, Farmington Hills, MI 48331.

Canadian GST: R 1226213149.

Direct correspondence to 38800 Country Club Drive, Farmington Hills, MI 48331. Telephone: +1.248.848.3700.
Website: http://www.concrete.org.

PRINTED WITH SOY INK

MEETINGS

APRIL

17-19—2023 ICRI Spring Convention, Vancouver, BC, Canada, www.icri.org/event/spring-convention-2023-std

APRIL-MAY

30-3—PTI Convention, Miami, FL, https://www.post-tensioning.org/events/convention/2023convention.aspx

MAY

22-23—2023 Slag Cement School, Cape Canaveral, FL, www.slagcement.org/post/registration-opens-for-2023-slag-cement-school

MAY-JUNE

31-2—15th International Workshop on Micropiles, Vail, CO, www.ismicropiles.org/workshops.asp

JUNE

14-16—SynerCrete'23, Milos, Greece, https://synercrete.com

JULY

2-6—Eighth International Symposium on Life-Cycle Civil Engineering (IALCCE2023), Milan, Italy, https://ialcce2023.org

17-18—ACI Professors' Workshop, Online, https://www.concrete.org/events/professorsworkshop.aspx

17-20—Bridge Engineering Institute Conference 2023 (BEI-2023), Rome, Italy, www.beibridge.org

20-23—ASCC Concrete Executive Leadership Forum, Beaver Creek, CO, https://ascconline.org/Events

23-26—CICE 2023: 11th International Conference on FRP Composites in Civil Engineering, Rio de Janeiro, Brazil, https://easychair.org/cfp/CICE2023

25-26—ACI Professors' Workshop, Farmington Hills, MI, https://www.concrete.org/events/professorsworkshop.aspx

26-28—Second International Conference on Advances in Civil Infrastructure and Construction Materials (CICM 2023), Dhaka, Bangladesh, https://cicm2023.mist.ac.bd

27-29—CFACON23, San Antonio, TX, www.cfaconcretepros.org/index.php?option=com_jevents&task=icalrepeat.detail&evid=29&Itemid=1

ACI CONCRETE CONVENTION: FUTURE DATES

2023—Oct. 29-Nov. 2, Boston Convention Center & Westin Boston Waterfront, Boston, MA
2024—March 24-28, Hyatt Regency New Orleans, New Orleans, LA
2024—November 3-7, Marriott Philadelphia Downtown, Philadelphia, PA
2025—Mar. 30-Apr. 3, Sheraton Centre Toronto, Toronto, ON, Canada

For additional information, contact:
Event Services, ACI
38800 Country Club Drive
Farmington Hills, MI 48331
Telephone: +1.248.848.3795
email: conventions@concrete.org

ON FRONT COVER: 120-M30, p. 109, Fig. 2—Schematic representation of two-dimensional mesostructure of heterogeneous cementitious material: (a) under mixed-mode loading. This heterogeneous structure is composed of: (b) continuum bulk elements for paste and aggregate, and interface elements for paste, aggregate, and interfacial transition zone (ITZ), with cohesive law defined in: (c) cohesive opening model.

Contributions to *ACI Materials Journal*

The *ACI Materials Journal* is an open forum on concrete technology and papers related to this field are always welcome. All material submitted for possible publication must meet the requirements of the "American Concrete Institute Publication Policy" and "Author Guidelines and Submission Procedures." Prospective authors should request a copy of the Policy and Guidelines from ACI or visit ACI's website at **www.concrete.org** prior to submitting contributions.

Papers reporting research must include a statement indicating the significance of the research.

The Institute reserves the right to return, without review, contributions not meeting the requirements of the Publication Policy.

All materials conforming to the Policy requirements will be reviewed for editorial quality and technical content, and every effort will be made to put all acceptable papers into the information channel. However, potentially good papers may be returned to authors when it is not possible to publish them in a reasonable time.

Discussion

All technical material appearing in the *ACI Materials Journal* may be discussed. If the deadline indicated on the contents page is observed, discussion can appear in the designated issue. Discussion should be complete and ready for publication, including finished, reproducible illustrations. Discussion must be confined to the scope of the paper and meet the ACI Publication Policy.

Follow the style of the current issue. Be brief—1800 words of double spaced, typewritten copy, including illustrations and tables, is maximum. Count illustrations and tables as 300 words each and submit them on individual sheets. As an approximation, 1 page of text is about 300 words. Submit one original typescript on 8-1/2 x 11 plain white paper, use 1 in. margins, and include two good quality copies of the entire discussion. References should be complete. Do not repeat references cited in original paper; cite them by original number. Closures responding to a single discussion should not exceed 1800-word equivalents in length, and to multiple discussions, approximately one half of the combined lengths of all discussions. Closures are published together with the discussions.

Discuss the paper, not some new or outside work on the same subject. Use references wherever possible instead of repeating available information.

Discussion offered for publication should offer some benefit to the general reader. Discussion which does not meet this requirement will be returned or referred to the author for private reply.

Send manuscripts to:
http://mc.manuscriptcentral.com/aci

Send discussions to:
Journals.manuscripts@concrete.org

ACI MATERIALS JOURNAL TECHNICAL PAPER

Title No. 120-M21

Design of Ambient-Cured Alkali-Activated Reactive Powder Concrete Using Taguchi Method

by Nabeel A. Farhan, M. Neaz Sheikh, and Muhammad N. S. Hadi

In this paper, the Taguchi method was used to identify the optimum mixture proportions of alkali-activated reactive powder concrete (AARPC) by considering the most influential parameters. Five main parameters, including binder content, alkaline activator-binder ratio (Al-binder), binder-fine aggregate ratio, sodium silicate to sodium hydroxide ratio (Na_2SiO_3-NaOH), and sodium hydroxide (NaOH) concentration, were considered in the mixture design. A total of 18 trial batches were designed according to the L18 array obtained from the Taguchi method. The results showed that the highest average compressive strength was 110.9 MPa (16.08 ksi) and the lowest average compressive strength was 50.6 MPa (7.34 ksi). The test results of the 18 trial batches were then evaluated by the analysis of variance (ANOVA) method to determine the optimum level of each parameter. It was found that specimens with a binder content of 700 kg/m^3 (0.025 lb/in.^{3}), Al-binder ratio of 0.3, binder-fine aggregate ratio of 0.8, Na_2SiO_3-NaOH ratio of 2, and NaOH concentration of 14 M produced the highest 28-day compressive strength (116.77 MPa [16.94 ksi]) at the ambient curing conditions.

Keywords: alkaline activator; compressive strength; Taguchi method; ultra-high-strength concrete.

INTRODUCTION

Concrete is the most widely used construction material in the world. Ordinary portland cement (OPC) is the primary material used in the production of concrete.[1] However, the production of cement contributes approximately 5 to 7% of the total carbon dioxide (CO_2) emissions into the atmosphere.[1,2] It has been reported that the production of cement in Australia releases 36 billion tonnes of CO_2 into the atmosphere.[3] The production of OPC is the second largest source of CO_2 emissions worldwide, releasing approximately 0.8 tonnes of CO_2 for the manufacturing of 1 tonne of OPC.[4-7]

The use of alternative binders such as industrial by-products can be an attractive solution for the reduction of the adverse environmental impact associated with the production of OPC. Studies into green concrete as an alternative to OPC concrete started a few decades ago.[1,4,5] Green concrete is a form of eco-friendly concrete, which is manufactured using waste or residual materials from different industries and requires less energy for production. Alkali-activated concrete (AAC) and geopolymer concrete (GC) do not contain any cement, and hence they are considered green concrete. AAC and GC have recently gained popularity as construction materials.[8] It should be noted that there have been disagreements among the research community regarding the definition of AAC and GC.[7] In general, AAC is a calcium-rich raw material activated with high-alkaline solutions. After the dissolution of the precursors, a binder paste with hydraulic potential is built, leading to the simultaneous formation of calcium-silicate-hydrate (C-S-H) gels. GC can be defined as covalently bonded noncrystalline networks in which silicate (Si) and aluminate (Al) tetrahedral frameworks are linked by shared oxygen to form a dense amorphous to semi-crystalline three-dimensional framework.[9]

AAC can be produced by mixing an alkaline solution with aluminosilicate materials such as slag cement, silica fume (SF), and fly ash (FA). The use of industrial by-products in the manufacturing of AAC and GC introduces environmental and economic benefits and resolves issues related to the disposal of large quantities of industrial wastes such as slag cement from metal production and FA from coal-fired power stations, which may otherwise be dumped as landfills with adverse environmental impacts.[10]

Slag cement is the most common choice as the main raw material for the production of AAC.[5] AAC is proven to have good mechanical properties with reduced greenhouse gas emissions. It not only reduces greenhouse gas emissions but also uses a large amount of industrial waste materials such as slag cement, SF, and FA.[11-13]

There are two main components in AAC: a source of aluminosilicate materials and an alkaline activator. The source materials of the binder used in AAC depend on the source of the aluminosilicate materials, which should be rich in aluminate (Al), silicate (Si), and calcium oxide (CaO).[14] In general, the choice of source material for the production of AAC depends on several factors, including cost, availability, and application. The most common alkaline activator used in the production of AAC is a combination of sodium silicate (Na_2SiO_3) and sodium hydroxide (NaOH) solutions.

The effects of the Na_2SiO_3-NaOH ratio on the compressive strength of AAC and GC have not been extensively investigated yet. Only a few studies have investigated the effects of the Na_2SiO_3-NaOH ratio on the compressive strength of AAC and GC.[14-18] Some of the studies[14,16,18] reported that the compressive strength of GC mixtures increased due to the increase in the Na_2SiO_3-NaOH ratio. Hadi et al.[14] reported that higher content of Na_2SiO_3 had a positive influence on the early-age strength development of alkali-activated slag

ACI Materials Journal, V. 120, No. 2, March 2023.

MS No. M-2021-129.R3, doi: 10.14359/51738489, received October 25, 2022, and reviewed under Institute publication policies.

concrete. Olivia and Nikraz[16] also observed a similar variation in the compressive strength with the Na_2SiO_3-NaOH ratio for FA-based GC. Mijarsh et al.[19] stated that the higher silica content due to a higher amount of Na_2SiO_3 in the alkaline activator enhanced the alkali-activation process and resulted in higher compressive strength of GC. On the contrary, some other studies[15,17] reported that the compressive strength of GC mixtures decreased with the increase in the Na_2SiO_3-NaOH ratio. Deb et al.[15] and Nazari et al.[17] stated that the type of aluminosilicate source material is an important factor for selecting the Na_2SiO_3-NaOH ratio to achieve a higher compressive strength of GC mixtures.

Heat curing is generally used for the production of AAC. Hence, the application of AAC is limited mostly to precast concrete members.[14] The production of AAC under ambient curing conditions will have wider applications in cast-in-place construction as well as in precast construction. Ambient curing will also reduce the energy and cost associated with the heat-curing process in the production of AAC.[14]

The main parameters that affect the production and properties of AAC include aluminosilicate sources, the ratio of the binder content to the alkaline activator, the type of activator, the combination and concentration of the activator, and the curing conditions. It would be difficult to investigate all these parameters in a single investigation. However, the influences of the parameters on the properties of AAC can be effectively examined by using an efficient method of the design of experiments, such as the Taguchi method. The Taguchi method has been widely used in other engineering applications, but the application of the Taguchi method to GC is very limited.[14,16-18] The Taguchi method is a factorial design, which uses an orthogonal array (OA) for the design of experiments to investigate a large number of variables with a small number of experiments. The use of the OA design is a more efficient method compared to traditional experimental design methods.[13] The OA reduces the number of experiments required and minimizes uncontrollable parameters.[20] The Taguchi method uses a signal-to-noise ratio (*S*/*N*) for the optimization. The *S*/*N* helps in the data analysis and the prediction of the optimum result. The main advantages of the Taguchi method are efficiency, robustness, cost-effectiveness, and ease of interpretation of the output.[16]

Reactive powder concrete (RPC) is a special type of ultra-high-performance concrete that displays high strength, high durability, and high toughness. RPC is considered a promising construction material for civil engineering applications due to its superior properties. The superior properties of RPC are obtained by using very fine sand, a low water-binder ratio (*w*/*b*), and no coarse aggregates, achieving high density and reduced porosity.[21-23]

The use of RPC in structural applications such as columns and beams increases the design efficiency by decreasing the dimensions of the concrete elements and reducing the volume of concrete used for the construction of the entire structure. RPC, however, causes adverse environmental impacts by increasing greenhouse gas emissions, mainly due to the use of a huge amount of OPC in the production of RPC. Even though AAC causes significantly lower greenhouse gas emissions than RPC, the compressive strength of AAC is significantly lower.[12-14] Hence, extensive investigative research is needed to develop an environmentally friendly ultra-high-strength concrete with superior engineering properties that can be used in structural applications. An extensive review of the literature reveals that the development of sustainable ultra-high-strength concrete has not been adequately investigated.[12-14] This study aimed to identify the optimum mixture proportions of ultra-high-strength AAC (compressive strength > 100 MPa [14.50 ksi]) at 28 days by considering the influence of different parameters using the Taguchi method. The investigation of other factors—for example, shrinkage, durability, and moisture susceptibility—is considered beyond the scope of the paper.

RESEARCH SIGNIFICANCE

The process of the production of OPC is associated with high energy consumption, causing adverse environmental impacts. Hence, the use of alternative binders to OPC such as industrial by-products is considered an attractive solution to reduce or alleviate adverse environmental impacts. In this study, a new type of sustainable ultra-high-strength concrete at ambient curing conditions has been developed. No OPC has been used in the developed ambient-cured sustainable ultra-high-strength concrete, which is named alkali-activated reactive powder concrete (AARPC). The finding of this study will be beneficial in the design of AARPC at ambient curing conditions and in ascertaining the suitability of AARPC in structural applications.

EXPERIMENTAL DETAILS

Materials

The binder used for the production of AARPC in this study was slag cement, which was supplied by the Australasian (Iron & Steel) Slag Association.[24] The bulk density of slag cement varies from 1050 to 1375 kg/m^3 (66 to 86 lb/ft^3). The chemical composition of the slag cement was determined by X-ray fluorescence (XRF) spectroscopy. The chemical composition analysis of slag cement was conducted in the School of Earth, Atmospheric and Life Sciences at the University of Wollongong, Australia, and the chemical composition of the slag cement is presented in Table 1. River sand with a maximum particle size of 600 µm was used as the fine aggregate in this study. The bulk density of the sand varied from 1520 to 1680 kg/m^3 (95 to 105 lb/ft^3) and the fineness modulus was 1.75. The alkaline activator was a combination of sodium silicate (Na_2SiO_3) and sodium hydroxide (NaOH) solutions. Grade D sodium silicate solution (Na_2SiO_3) was supplied by a company in Australia.[25] The sodium silicate solution (Na_2SiO_3) includes 29.4% silicate, 14.7% sodium oxide, and 44.1% solids (sodium salt and silicic acid). The density of the sodium silicate solution (Na_2SiO_3) was 1530 kg/m^3 (0.055 lb/in.^{3}). Caustic soda (NaOH) was dissolved in potable water to produce sodium hydroxide solution with different concentrations. The mass of NaOH pellets varied depending on the concentration of the solution. For example, for preparing the NaOH solution with a concentration of 12 mol/L, 480 g (1.06 lb) (12 pellets at 40 g [0.09 lb] = 480 g [1.06 lb]) NaOH solid was mixed with potable water, where 40 is the molecular

Table 1—Chemical compositions (mass %) of slag cement

Component	Slag cement
SiO_2	32.40
Al_2O_3	14.96
Fe_2O_3	0.83
CaO	40.70
MgO	5.99
K_2O	0.29
Na_2O	0.42
TiO_2	0.84
P_2O_5	0.38
Mn_2O_3	0.40
SO_3	2.74
LOI	NA

Note: LOI is loss on ignition; NA is not available.

weight of NaOH. A magnetic stirrer was used to mix the NaOH pellets with water. The mixture was stirred until the pellets were fully dissolved in the water. The NaOH solution was prepared 24 hours before the mixing of concrete. The Na_2SiO_3 and NaOH solutions were blended together for 30 minutes before the mixing of AARPC.

Optimal mixture design of AARPC

The Taguchi method was used to design the optimum mixture proportions for AARPC with slag cement as an aluminosilicate source at ambient-curing conditions. The influences of five main parameters—including binder content (500, 600, and 700 kg/m^3 [0.018, 0.022, and 0.025 lb/in.^{3}]), alkaline activator-binder ratio (Al-binder) (0.30, 0.35, and 0.40), binder-fine aggregate ratio (binder-fine aggregate) (0.70, 0.75, and 0.80), sodium silicate-sodium hydroxide ratio (Na_2SiO_3-NaOH) (1.5, 2, and 2.5), and sodium hydroxide (NaOH) concentration (12, 14, and 16 M)—were investigated in this study (Table 2). The Taguchi experiment was designed using Qualitek-4.[26] The main parameters and their levels were selected based on the results of preliminary experiments conducted in the structural engineering laboratory at the University of Wollongong, together with the findings of an extensive literature review.

The Taguchi method uses an OA to evaluate multiple process variables, which influence the performance characteristics while, at the same time, reducing the number of experiments required.[27] In this study, to select an appropriate OA for five parameters at three levels (Table 2), a total of 18 AARPC trial batches were prepared. The component parameters of each of the AARPC trial batches (M1 to M18) are shown in Tables 3 and 4.

The optimization process using the Taguchi method consists of the following steps[20]:

1. Determine the main parameters to be evaluated.
2. Determine the number of levels for each parameter and possible interactions between the parameters.
3. Select the appropriate OA and assign the independent parameters.

Table 2—Parameters and levels used in Taguchi experiment design

Parameters	Level 1	Level 2	Level 3
(A) Binder content, kg/m^3	500	600	700
(B) Al-binder ratio	0.30	0.35	0.40
(C) Binder-aggregate ratio	0.70	0.75	0.80
(D) Na_2SiO_3-NaOH ratio	1.5	2.0	2.5
(E) NaOH, M	12	14	16

Note: 1 kg/m^3 = 3.61 × 10^{-5} lb/in.^{3}

Table 3—AARPC trial batches based on OA for four parameters at three levels (L18 array)

Experiment series	Parameters and their levels				
	A	B	C	D	E
M1	1	1	1	1	1
M2	1	2	2	2	2
M3	1	3	3	3	3
M4	2	1	1	2	2
M5	2	2	2	3	3
M6	2	3	3	1	1
M7	3	1	2	1	3
M8	3	2	3	2	1
M9	3	3	1	3	2
M10	1	1	3	3	2
M11	1	2	1	1	3
M12	1	3	2	2	1
M13	2	1	2	3	1
M14	2	2	3	1	2
M15	2	3	1	2	3
M16	3	1	3	2	3
M17	3	2	1	3	1
M18	3	3	2	1	2
Total	36	36	36	36	36

4. Conduct the experiments based on the arrangement of the OA.
5. Calculate the *S*/*N*.
6. Analyze the experimental results using the *S*/*N* and ANOVA.
7. Select the optimal levels of each parameter.
8. Verify the optimal parameters through the confirmation experiment.

Preparation, casting, and testing of specimens

Table 5 illustrates the mixture proportions of the AARPC trial batches. The AARPC specimens were prepared by mixing the dry materials (slag cement and sand) in a pan mixer for approximately 2 minutes. Afterward, half of the alkaline activator (a combination of Na_2SiO_3 with NaOH)

was added to the dry mixture and mixed for approximately 3 minutes. The remaining amount of alkaline activator was placed into the pan mixer and mixed for approximately 10 minutes until the mixture became homogeneous.

Table 4—AARPC trial batch parameters

Experiment series	A	B	C	D	E
M1	500	0.3	0.7	1.5	12
M2	500	0.35	0.75	2	14
M3	500	0.4	0.8	2.5	16
M4	600	0.3	0.7	2	14
M5	600	0.35	0.75	2.5	16
M6	600	0.4	0.8	1.5	12
M7	700	0.3	0.75	1.5	16
M8	700	0.35	0.8	2	12
M9	700	0.4	0.7	2.5	14
M10	500	0.3	0.8	2.5	14
M11	500	0.35	0.7	1.5	16
M12	500	0.4	0.75	2	12
M13	600	0.3	0.75	2.5	12
M14	600	0.35	0.8	1.5	14
M15	600	0.4	0.7	2	16
M16	700	0.3	0.8	2	16
M17	700	0.35	0.7	2.5	12
M18	700	0.4	0.75	1.5	14

The fresh AARPC was then placed into polyvinyl chloride (PVC) molds in three layers, and no difficulties occurred during casting. All the fresh AARPC mixtures were handled, placed, compacted, and finished easily. In each layer, the AARPC mixture was vibrated using a table vibrator for approximately 10 seconds to remove any air bubbles or voids. After casting, all specimens were covered with plastic sheets to retain moisture for 24 hours. The specimens were then removed from the molds and left in ambient conditions at a temperature of 23 ± 3°C (64.4 ± 5.4°F) and relative humidity of 60 ± 10% until the day of testing. The compressive strength tests were performed at 7, 14, and 28 days in accordance with AS 1012.9-1999.[28] The compressive strengths of the ambient-cured AARPC trial batches were evaluated using cylindrical specimens of 50 mm (1.97 in.) diameter and 100 mm (3.93 in.) height, as shown in Fig. 1, using a testing machine with a capacity of 1800 kN (404.66 kip). Cylindrical specimens with 50 mm (1.97 in.) diameter and 100 mm (3.93 in.) height were used in the experimental trial batches to avoid wastage of materials, as smaller specimens were easier to prepare and handle in the laboratory. For each trial batch, three specimens were tested; the average test results are shown in Fig. 2.

RESULTS AND DISCUSSION

Compressive strength

The compressive strength of the AARPC at 28 days was used as a criterion for evaluating the 18 AARPC trial batches (M1 to M18) designed according to the Taguchi method, as shown in Table 6. This is because the specimens at the age

Table 5—Mixture proportions of AARPC trial batches

Experiment series	Binder content, kg/m^3	Al-binder	Binder-fine aggregate	Fine aggregate content, kg/m^3	Na_2SiO_3-NaOH	Na_2SiO_3	NaOH	NaOH, M
M1	500	0.30	0.70	714.3	1.5	90.0	60.0	12
M2	500	0.35	0.75	666.7	2.0	116.7	58.3	14
M3	500	0.40	0.80	625.0	2.5	142.9	57.1	16
M4	600	0.30	0.70	857.1	2.0	120.0	60.0	14
M5	600	0.35	0.75	800.0	2.5	150.0	60.0	16
M6	600	0.40	0.80	750.0	1.5	144.0	96.0	12
M7	700	0.30	0.75	933.3	1.5	126.0	84.0	16
M8	700	0.35	0.80	875.0	2.0	163.3	81.7	12
M9	700	0.40	0.70	1000.0	2.5	200.0	80.0	14
M10	500	0.30	0.80	625.0	2.5	107.1	42.9	14
M11	500	0.35	0.70	714.3	1.5	105.0	70.0	16
M12	500	0.40	0.75	666.7	2.0	133.3	66.7	12
M13	600	0.30	0.75	800.0	2.5	128.6	51.4	12
M14	600	0.35	0.80	750.0	1.5	126.0	84.0	14
M15	600	0.40	0.70	857.1	2.0	160.0	80.0	16
M16	700	0.30	0.80	875.0	2.0	140.0	70.0	16
M17	700	0.35	0.70	1000.0	2.5	175.0	70.0	12
M18	700	0.40	0.75	933.3	1.5	168.0	112.0	14

Note: 1 kg/m^3 = 3.61 × 10^{-5} lb/in.^{3}

of 28 days achieved the highest compressive strength, which provided more accurate results for evaluating the mixtures.

It was observed that all the specimens achieved approximately 45% of compressive strength at the age of 7 days and 90% of compressive strength at 14 days under ambient-curing conditions (Fig. 2), although there was a slight increase in the compressive strength at 28 days (Table 6), which confirmed their potential for the application where high early strength is required. Most of the slag cement particles were partially dissolved by the alkaline activator to form C-S-H gel by the geopolymerization reaction. The geopolymerization reaction initiates with the dissolution of Al and Si from the precursor materials in an alkaline environment.[29] Thus, high early strength of AARPC was obtained. The findings of this study agree with Farhan et al.,[12] in which it was reported that AAC developed most of the compressive strength at 14 days and there was a marginal increase in the compressive strength at 28 days.

Fig. 1—AARPC specimens for compressive strength tests.

From the experimental results, the highest average compressive strength (110.9 MPa [16.08 ksi]) of the AARPC was obtained by the M8 specimens with a binder content of 700 kg/m^3 (0.025 lb/in.^{3}), Al-binder ratio of 0.35, binder-fine aggregate ratio of 0.8, Na_2SiO_3-NaOH ratio of 2, and NaOH concentration of 12 M. The lowest average compressive strength (50.6 MPa [7.34 ksi]) of the AARPC was obtained by the M5 specimens with a binder content of 600 kg/m^3 (0.022 lb/in.^{3}), Al-binder ratio of 0.35, binder-fine aggregate ratio of 0.75, Na_2SiO_3-NaOH ratio of 2.5, and NaOH concentration of 16 M. It is noted that the Al-Binder ratio for mixtures M5 and M8 was 0.35, and the main differences were the binder content, binder-fine aggregate ratio, Na_2SiO_3-NaOH ratio, and NaOH concentration.

It is difficult to determine the optimum proportions for each considered parameter from the test results. Hence, the factorial analysis was conducted using Qualitek-4[26] to explore the influence of each parameter on the compressive strength of the AARPC. The compressive strengths of the AARPC trial batches were used in calculating the *S*/*N*. The

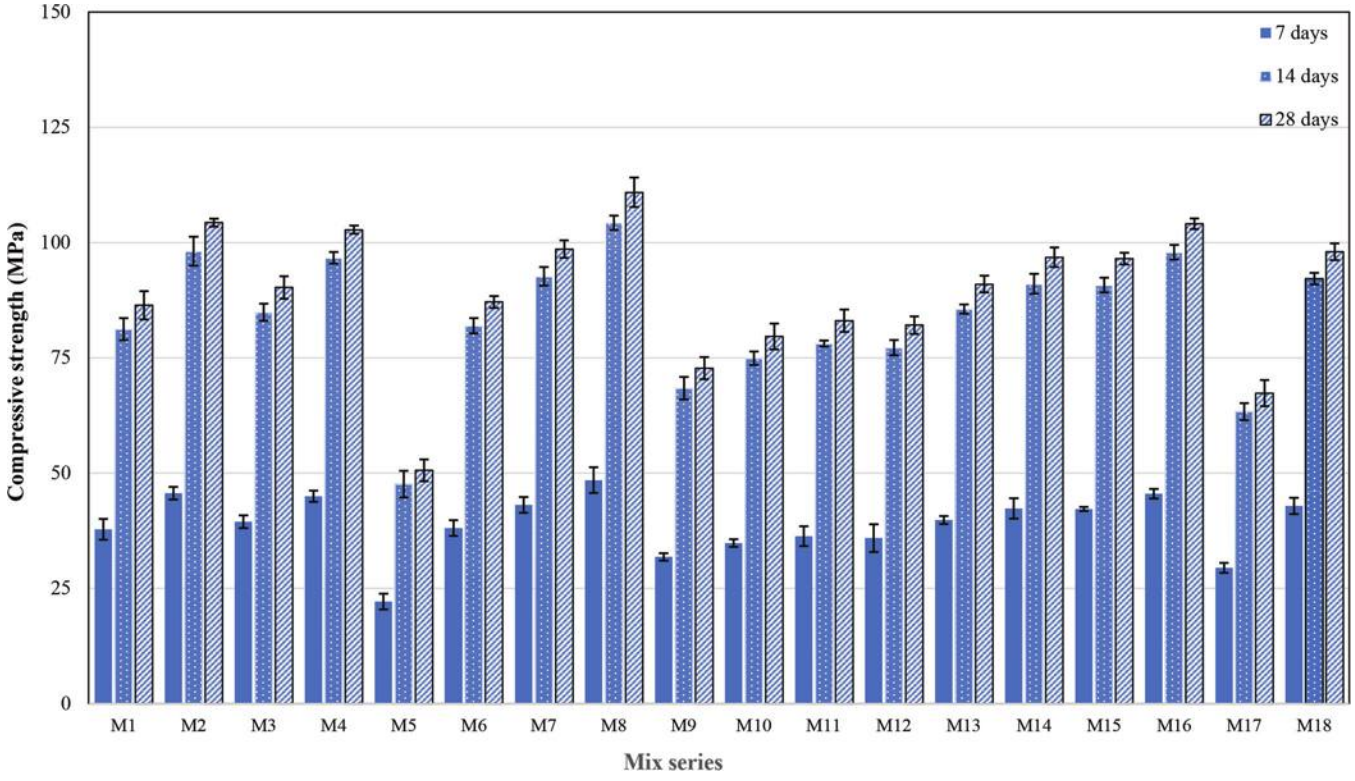

Fig. 2—Compressive strength of AARPC specimens. (Note: 1 MPa = 0.145 ksi.)

Table 6—Compressive strength of AARPC trial batches

Compressive strength, MPa, at 28 days						
Trial batch	Specimen 1	Specimen 2	Specimen 3	Average	S.D.	*S*/*N*
M1	88.2	82.6	88.4	86.4	3.06	38.7
M2	101.8	106.5	104.7	104.3	0.86	40.4
M3	94.5	89.5	86.9	90.3	2.45	39.1
M4	98.9	107.0	102.4	102.8	0.87	40.2
M5	51.8	47.9	52.1	50.6	2.35	34.1
M6	87.7	85.8	87.8	87.1	1.29	38.8
M7	102.4	97.3	96.1	98.6	1.90	39.9
M8	114.8	110.4	107.4	110.9	3.20	40.9
M9	77.3	74.4	66.6	72.8	2.41	37.2
M10	79.3	80.9	78.7	79.6	2.83	38.0
M11	86.4	83.9	78.9	83.0	2.43	38.4
M12	85.3	81.1	79.9	82.1	1.90	38.3
M13	89.2	89.5	94.3	91	1.81	39.2
M14	99.2	98.3	92.9	96.8	2.13	39.7
M15	96.5	93.9	99.1	96.5	1.28	39.7
M16	104.6	107.7	99.9	104.1	1.14	40.3
M17	69.5	63.1	69.4	67.4	2.86	36.5
M18	96.8	98.2	99.0	98.0	1.81	39.8

Note: S.D. is standard deviation; 1 MPa = 0.145 ksi.

S/*N* helps in data analysis and prediction of the optimum result. The *S*/*N* ratio was computed by using Eq. (1)

$$(S/N) = -10\log\left(\frac{1}{n}\sum\frac{1}{Y^2}\right) \quad (1)$$

where Y is the experimental result (compressive strength); and n is the number of experiments conducted for each trial batch. The *S*/*N* are computed using Eq. (1) for each of the 18 AARPC trial batches (Table 6).

The compressive strengths obtained from the AARPC trial batches were used in calculating the mean *S*/*N* for each parameter. The mean *S*/*N* of compressive strength of the AARPC trial batches at various parameters are shown in Fig. 3. The mean *S*/*N* for each parameter was determined by taking the average of the 28-day compressive strengths for the trial batches that included the considered parameter. For example, a binder content (Parameter A3) of 700 kg/m^3 was tested in six trial batches: M7, M8, M9, M16, M17, and M18 (Table 4). The *S*/*N* of the M7, M8, M9, M16, M17, and M18 trial batches were 39.9, 40.9, 37.2, 40.3, 36.5, and 39.8, respectively (Table 6). The mean *S*/*N* of binder content (Parameter A3) was equal to 39.1 ([39.9 + 40.9 + 37.2 + 40.3 + 36.5 + 39.8]/6 = 39.1), which was greater than the mean *S*/*N* for binder content of 500 kg/m^3 (Parameter A1) and binder content of 600 kg/m^3 (Parameter A2). Hence, the optimum binder content was 700 kg/m^3. It can be seen from Fig. 3(a) that the binder content of 700 kg/m^3 showed the highest mean *S*/*N* among the AARPC mixtures. The increase in the mean *S*/*N* with the highest binder content at 28 days may be due to the greater dissolution of Si, Al, and Ca species, which increased the extent of the alkali-activation process and resulted in higher compressive strength of AARPC.

The highest mean *S*/*N* was at an Al-binder ratio of 0.3, as observed in Fig. 3(b). Several studies investigated the effect of the Al-binder ratio on the compressive strength of AAC and GC.[14,30-32] The test results revealed that increasing the Al-binder ratio resulted in lower compressive strength of AAC and GC. The reason for this decrease in the compressive strength can be attributed to the excess alkaline activator, which caused an increase in the amount of water in the mixture and hindered the alkali-activation process.[14]

It can be seen from Fig. 3(c) that the mean *S*/*N* of the AARPC mixtures increased with the increase in the binder-fine aggregate ratio. The highest mean *S*/*N* was at a binder-fine aggregate of 0.8. The high calcium content in slag cement might have improved the compressive strength of the AARPC mixtures.[15] This might be because the rate of the alkali-activation process increased due to an increase in slag cement content in the AARPC mixture.[33] In addition, a higher amount of calcium in slag cement resulted in the formation of C-S-H gel, which contributed to the compressive strength development of the AARPC mixtures.[34]

Based on the data obtained in this study, the highest mean *S*/*N* for 28-day compressive strength was achieved with a Na_2SiO_3-NaOH ratio of 2, as shown in Fig. 3(d). It is considered that for AARPC with a Na_2SiO_3-NaOH ratio of 2, the availability of more Na_2SiO_3 solution compared with a lower quantity of NaOH solution along with the presence of Al, Si, and Ca species in precursor materials might have increased

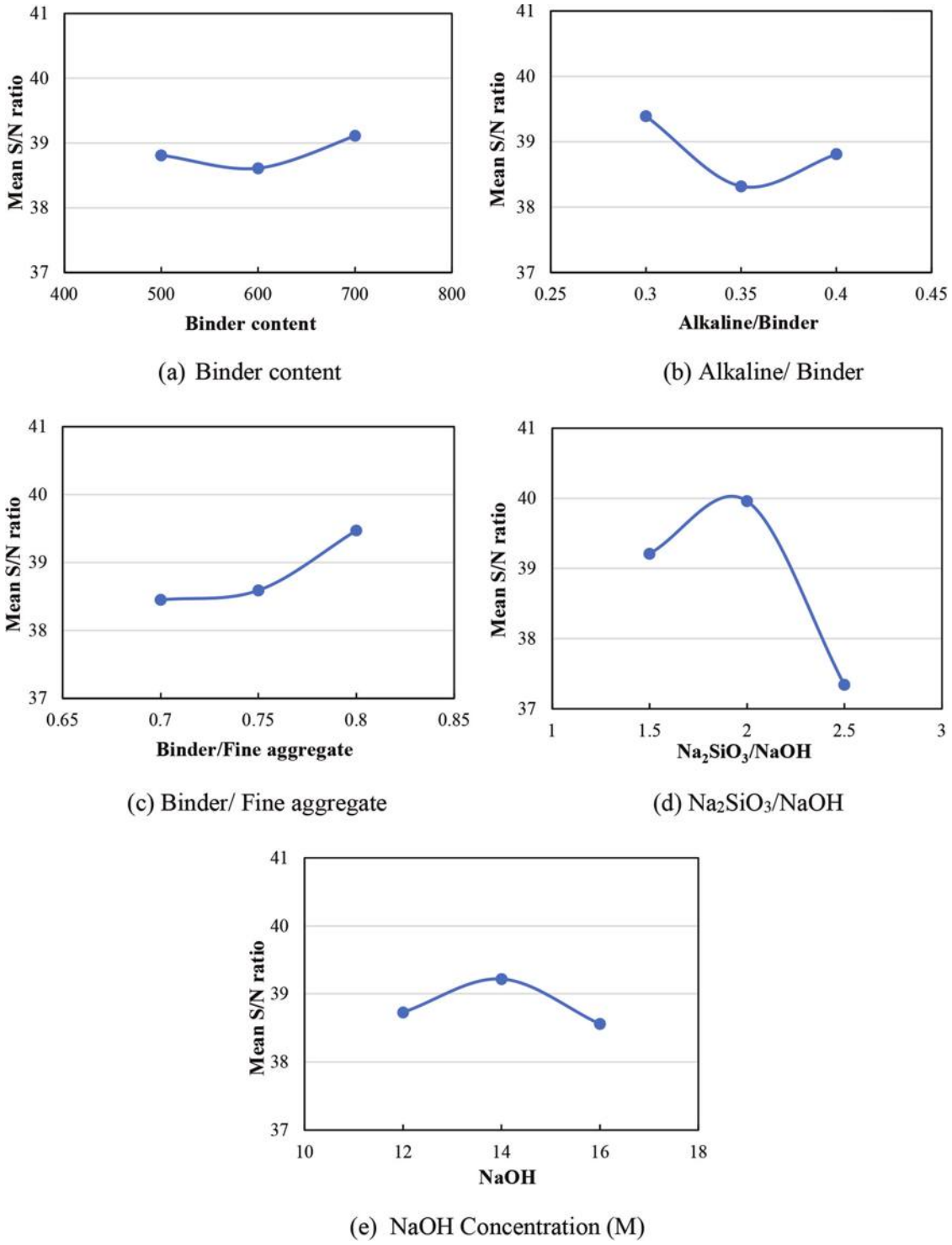

Fig. 3—Factorial diagrams of mean S/N *of 28-day compressive strength of AARPC.*

the extent of the alkali-activation process, thus resulting in higher strength development of AARPC at 28 days.

Figure 3(e) shows that the mean *S*/*N* increased with an increase in the NaOH concentration up to 14 M. However, increasing the NaOH concentration beyond 14 M led to a reduction in the mean *S*/*N*, as shown in Fig. 3(e). At a lower NaOH concentration, the lower extent of the alkali-activation process resulted in less compressive strength of AARPC mixtures. However, increasing the concentration of NaOH solution to 14 M results in the dissolution of Si, Al, and Ca species to a greater extent, thereby increasing the extent of the alkali-activation process. This results in the formation of a stable aluminosilicate network along with C-S-H gel in the mixture, which led to the higher compressive strength of the mixtures.[35] It was noted that the mean *S*/*N* decreases with an increase in the NaOH concentration with 16 M. This can be attributed to the variation in the nature and type of the molecules of the slag cement. The differences in the type of the molecules affect the extent of dissolution of the Si, Al, and CaO in the alkaline activator, as the dissolution of the

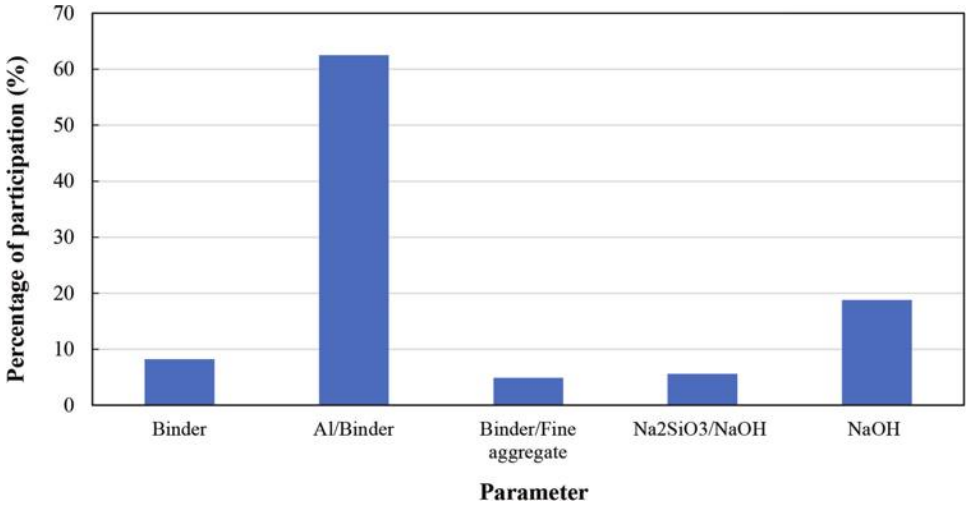

Fig. 4—Percentage of participation of considered parameters on compressive strength of AARPC.

Table 7—Percentage of participation and optimum levels of considered parameters of 28-day compressive strength

Parameter	Binder content	Al-binder	Binder-fine aggregate	Na_2SiO_3-NaOH	NaOH
Optimum level	700 kg/m^3	0.30	0.8	2	14 M

Note: 1 kg/m^3 = 3.61 × 10^{-5} lb/in.^{3}

Si is slower than the dissolution of the other components of slag cement, which results in a lower extent of the alkali-activation process.[36]

Finally, the results were evaluated by ANOVA to determine the percentage of participation of the considered parameters and the optimum level of each parameter. The percentage of participation of the considered parameters and the optimum level of each parameter are shown in Fig. 4 and Table 7. It can be seen in Fig. 4 that the Al-binder ratio is the most significant parameter that influences the AARPC, with a percentage of participation of 62.5%. The Al-binder ratio of 0.30 was found to be the optimum level. This is due to the comparatively denser microstructure of AARPC, which produces a more homogenous microstructure with fewer pores. It is noted that investigations on the microstructure of AARPC are considered beyond the scope of this study and are part of future research investigations. It can be observed that the second important parameter that influences the AARPC is the NaOH concentration, with a percentage of participation of 18.8%. The NaOH concentration of 14 M was found to be the optimum level. The third influential parameter is the binder content, with a percentage of participation of 8.2%. The binder content of 700 kg/m^3 (0.025 lb/in.^{3}) was found to be the optimum level. The binder-fine aggregate ratio and Na_2SiO_3-NaOH ratio have the lowest percentages of participation of 4.9% and 5.6%, respectively. The binder-fine aggregate ratio of 0.8 was found to be the optimum level. The NaOH-Na_2SiO_3 ratio of 2 was found to be the optimum level. It is noted that the optimal values obtained in this study are dependent on the range of values of the five main parameters used in this study.

Verification experiment

The Taguchi method has been used to identify the optimum mixture proportions of AARPC by considering the most influential parameters. To confirm the test results, an additional mixture, M19, was prepared and tested using cylindrical specimens of 100 mm (3.93 in.) diameter and 200 mm (7.87 in.) height considering the optimum levels of the parameters (binder content of 700 kg/m^3 [0.025 lb in.^{3}]), Al-binder ratio of 0.3, binder-fine aggregate ratio of 0.8, Na_2SiO_3-NaOH ratio of 2, and NaOH concentration of 14 M) presented in Table 7. The average compressive strength of M19 was 45.2, 108.2, and 116.8 MPa (6.56, 15.69, and 16.94 ksi) at 7, 14, and 28 days, respectively. The average compressive strength of M19 was greater than the average compressive strength of the 18 AARPC trial batches (M1 to M18).

CONCLUSIONS

Based on the results of this experimental investigation, the following conclusions are drawn:

1. Industrial by-products such as slag cement can be advantageously used in producing sustainable ultra-high-strength concrete (alkali-activated reactive powder concrete [AARPC]) with compressive strength higher than 100 MPa (14.50 ksi) at 28 days under ambient curing conditions.

2. The AARPC with a binder content of 700 kg/m^3 (0.025 lb/in.^{3}), Al-binder ratio of 0.3, binder-fine aggregate ratio of 0.8, Na_2SiO_3-NaOH ratio of 2, and NaOH concentration of 14 M achieved the highest 28-day compressive strength (116.8 MPa [16.94 ksi]) at ambient-curing conditions.

3. All the AARPC specimens achieved 90% of compressive strength at the age of 14 days, which confirmed their potential for applications where high early strength is required.

4. The Al-binder ratio had the most significant influence on the compressive strength of AARPC, with a percentage of participation of 62.5%. A lower Al-binder ratio (0.3) produced higher compressive strength of AARPC specimens. This is due to the comparatively denser microstructure

of AARPC, which produces a more homogenous microstructure with fewer pores.

5. The binder-fine aggregate ratio and Na_2SiO_3-NaOH ratio have the lowest significant parameter that influences the AARPC, with a percentage of participation of 4.9% and 5.6%, respectively. The binder-fine aggregate ratio of 0.8 was found to be the optimum level. The Na_2SiO_3-NaOH ratio of 2 was found to be the optimum level.

AUTHOR BIOS

Nabeel A. Farhan *is a Lecturer at the University of Fallujah, Anbar, Iraq. He received his BSc in civil engineering from the University of Anbar, Anbar, Iraq, in 2004; his MS from Universiti Sains Malaysia (USM), Penang, Malaysia, in 2012; and his PhD from the School of Civil, Mining, Environmental and Architectural Engineering at the University of Wollongong, Wollongong, NSW, Australia, in 2020. His research interests include ambient curing geopolymer concrete.*

M. Neaz Sheikh *is an Associate Professor in the School of Civil, Mining, Environmental and Architectural Engineering at the University of Wollongong. He received his BSc in civil engineering from Chittagong University of Engineering and Technology, Chittagong, Bangladesh, and his MPhil and PhD from The University of Hong Kong, Hong Kong. His research interests include earthquake engineering, concrete structures, and composite structures.*

ACI member **Muhammad N. S. Hadi** *is a Professor in the School of Civil, Mining, Environmental and Architectural Engineering at the University of Wollongong. He received his BSc and MS from the University of Baghdad, Baghdad, Iraq, in 1977 and 1980, respectively, and his PhD from the University of Leeds, Leeds, UK, in 1989. His research interests include the analysis and design of concrete structures.*

ACKNOWLEDGMENTS

The authors gratefully acknowledge the help of the technical staff of the Structural Engineering Laboratories at the University of Wollongong, Australia. The authors also gratefully acknowledge the Australasian (Iron & Steel) Slag Association, Wollongong, Australia, for providing the slag cement required for this study. The first author is grateful for the financial support received from the Iraqi government.

REFERENCES

1. Farhan, N. A.; Sheikh, M. N.; and Hadi, M. N. S., "Behaviour of Ambient Cured Steel Fibre Reinforced Geopolymer Concrete Columns under Axial and Flexural Loads," *Structures*, V. 15, Aug. 2018, pp. 184-195. doi: 10.1016/j.istruc.2018.07.001

2. McLellan, B. C.; Williams, R. P.; Lay, J.; van Riessen, A.; and Corder, G. D., "Costs and Carbon Emissions for Geopolymer Pastes in Comparison to Ordinary Portland Cement," *Journal of Cleaner Production*, V. 19, No. 9-10, June-July 2011, pp. 1080-1090. doi: 10.1016/j.jclepro.2011.02.010

3. Canadell, P., and Raupach, M., "Global Carbon Report: Emissions Will Hit New Heights in 2014," *The Conversation*, Sept. 21, 2014, http://theconversation.com/global-carbon-report-emissions-will-hit-new-heights-in-2014-31834. (last accessed March 1, 2023)

4. Farhan, N. A.; Sheikh, M. N.; and Hadi, M. N. S., "Experimental Investigation on the Effect of Corrosion on the Bond between Reinforcing Steel Bars and Fibre Reinforced Geopolymer Concrete," *Structures*, V. 14, June 2018, pp. 251-261. doi: 10.1016/j.istruc.2018.03.013

5. Farhan, N. A.; Sheikh, M. N.; and Hadi, M. N. S., "Behavior of Ambient-Cured Geopolymer Concrete Columns under Different Loads," *ACI Structural Journal*, V. 115, No. 5, Sept. 2018, pp. 1419-1429. doi: 10.14359/51702250

6. Al-Hedad, A. S. A.; Farhan, N. A.; Zhang, M.; Sheikh, M. N.; and Hadi, M. N. S., "Effect of Geogrid Reinforcement on the Drying Shrinkage and Thermal Expansion of Geopolymer Concrete," *Structural Concrete*, V. 21, No. 3, June 2020, pp. 1029-1039. doi: 10.1002/suco.201900299

7. Farhan, N. A.; Sheikh, M. N.; and Hadi, M. N. S., "Engineering Properties of Ambient Cured Alkali-Activated Fly Ash–Slag Concrete Reinforced with Different Types of Steel Fiber," *Journal of Materials in Civil Engineering*, ASCE, V. 30, No. 7, July 2018, p. 04018142. doi: 10.1061/(ASCE)MT.1943-5533.0002333

8. Ken, P. W.; Ramli, M.; and Ban, C. C., "An Overview on the Influence of Various Factors on the Properties of Geopolymer Concrete Derived from Industrial By-Products," *Construction and Building Materials*, V. 77, Feb. 2015, pp. 370-395. doi: 10.1016/j.conbuildmat.2014.12.065

9. Waldmann, D., and Thapa, V. B., "A Short Review on Alkali-Activated Binders and Geopolymer Binders," *Vielfalt im Massivbau: Festschrift zum 65. Geburtstag von Prof. Dr.-Ing. Jürgen Schnell*, M. Pahn, C. Thiele, and C. Glock, eds., Ernst & Sohn, Berlin, Germany, 2018, pp. 576-591.

10. Barcelo, L.; Kline, J.; Walenta, G.; and Gartner, E., "Cement and Carbon Emissions," *Materials and Structures*, V. 47, No. 6, June 2014, pp. 1055-1065. doi: 10.1617/s11527-013-0114-5

11. Reed, M.; Lokuge, W.; and Karunasena, W., "Fibre-Reinforced Geopolymer Concrete with Ambient Curing for In Situ Applications," *Journal of Materials Science*, V. 49, No. 12, June 2014, pp. 4297-4304. doi: 10.1007/s10853-014-8125-3

12. Farhan, N. A.; Sheikh, M. N.; and Hadi, M. N. S., "Investigation of Engineering Properties of Normal and High Strength Fly Ash Based Geopolymer and Alkali-Activated Slag Concrete Compared to Ordinary Portland Cement Concrete," *Construction and Building Materials*, V. 196, Jan. 2019, pp. 26-42. doi: 10.1016/j.conbuildmat.2018.11.083

13. Farhan, N. A.; Sheikh, M. N.; and Hadi, M. N. S., "Effect of Steel Fiber on Engineering Properties of Geopolymer Concrete," *ACI Materials Journal*, V. 117, No. 3, May 2020, pp. 29-40.

14. Hadi, M. N. S.; Farhan, N. A.; and Sheikh, M. N., "Design of Geopolymer Concrete with GGBFS at Ambient Curing Condition Using Taguchi Method," *Construction and Building Materials*, V. 140, June 2017, pp. 424-431. doi: 10.1016/j.conbuildmat.2017.02.131

15. Deb, P. S.; Nath, P.; and Sarker, P. K., "The Effects of Ground Granulated Blast-Furnace Slag Blending with Fly Ash and Activator Content on the Workability and Strength Properties of Geopolymer Concrete Cured at Ambient Temperature," *Materials & Design*, V. 62, Oct. 2014, pp. 32-39.

16. Olivia, M., and Nikraz, H., "Properties of Fly Ash Geopolymer Concrete Designed by Taguchi Method," *Materials & Design*, V. 36, Apr. 2012, pp. 191-198.

17. Nazari, A.; Khanmohammadi, H.; Amini, M.; Hajiallahyari, H.; and Rahimi, A., "Production Geopolymers by Portland Cement: Designing the Main Parameters' Effects on Compressive Strength by Taguchi Method," *Materials & Design*, V. 41, Oct. 2012, pp. 43-49. doi: 10.1016/j.matdes.2012.04.045

18. Khalaj, G.; Hassani, S. E. S.; Khezrloo, A.; and Haratifar, E., "Split Tensile Strength of OPC-Based Geopolymers: Application of DOE Method in Evaluating the Effect of Production Parameters and Their Optimum Condition," *Ceramics International*, V. 40, No. 7, Part B, Aug. 2014, pp. 10945-10952. doi: 10.1016/j.ceramint.2014.03.094

19. Mijarsh, M. J. A.; Megat Johari, M. A.; and Ahmad, Z. A., "Synthesis of Geopolymer from Large Amounts of Treated Palm Oil Fuel Ash: Application of the Taguchi Method in Investigating the Main Parameters Affecting Compressive Strength," *Construction and Building Materials*, V. 52, Feb. 2014, pp. 473-481. doi: 10.1016/j.conbuildmat.2013.11.039

20. Türkmen, İ.; Gül, R.; and Çelik, C., "A Taguchi Approach for Investigation of Some Physical Properties of Concrete Produced from Mineral Admixtures," *Building and Environment*, V. 43, No. 6, June 2008, pp. 1127-1137. doi: 10.1016/j.buildenv.2007.02.005

21. Lee, M.-G.; Wang, Y.-C.; and Chiu, C.-T., "A Preliminary Study of Reactive Powder Concrete as a New Repair Material," *Construction and Building Materials*, V. 21, No. 1, Jan. 2007, pp. 182-189. doi: 10.1016/j.conbuildmat.2005.06.024

22. Al-Tikrite, A., and Hadi, M. N. S., "Mechanical Properties of Reactive Powder Concrete Containing Industrial and Waste Steel Fibres at Different Ratios under Compression," *Construction and Building Materials*, V. 154, Nov. 2017, pp. 1024-1034. doi: 10.1016/j.conbuildmat.2017.08.024

23. Elchalakani, M.; Karrech, A.; Dong, M.; Mohamed Ali, M. S.; and Yang, B., "Experiments and Finite Element Analysis of GFRP Reinforced Geopolymer Concrete Rectangular Columns Subjected to Concentric and Eccentric Axial Loading," *Structures*, V. 14, June 2018, pp. 273-289. doi: 10.1016/j.istruc.2018.04.001

24. ASA, "Ground Granulated Blast Furnace Slag (GGBFS)," Australasian (Iron & Steel) Slag Association, Wollongong, NSW, Australia, https://www.asa-inc.org.au/products/ground-granulated-blast-furnace-slag. (last accessed March 1, 2023)

25. PQ Australia, "Sodium Silicate," PQ Australia Pty Ltd., Chipping Norton, NSW, Australia, http://www.pqcorp.com/products/. (last accessed March 10, 2023)

26. Nutek, Inc., "Qualitek-4: IBM/Compatible Software for Automatic Design and Analysis of Taguchi Experiments," Nutek, Inc., Bloomfield Hills, MI, http://nutek-us.com/wp-q4w.html. (last accessed March 10, 2023)

27. Ross, P. J., *Taguchi Techniques for Quality Engineering: Loss Function, Orthogonal Experiments, Parameter and Tolerance Design*, McGraw Hill Professional, New York, 1996.

28. AS 1012.9-1999, "Methods of Testing Concrete. Method 9: Determination of the Compressive Strength of Concrete Specimens," Standards Australia, Sydney, NSW, Australia, 1999, 10 pp.

29. Bernal, S. A., Mejíade Gutiérrez, R. M.; Pedraza, A. L.; Provis, J. L.; Rodriguez, E. D.; and Delvasto, S., "Effect of Binder Content on the Performance of Alkali-Activated Slag Concretes," *Cement and Concrete Research*, V. 41, No. 1, Jan. 2011, pp. 1-8. doi: 10.1016/j.cemconres.2010.08.017

30. Humad, A. M.; Kothari, A.; Provis, J. L.; and Cwirzen, A., "The Effect of Blast Furnace Slag/Fly Ash Ratio on Setting, Strength, and Shrinkage of Alkali-Activated Pastes and Concretes," *Frontiers in Materials*, V. 6, Feb. 2019, Article No. 9. doi: 10.3389/fmats.2019.00009

31. Farhan, N.; Sheikh, M. N.; and Hadi, M. N. S., "Design of Alkali Activated Concrete Using the Taguchi Method," *Mechanics of Structures and Materials XXIV: Proceedings of the 24th Australian Conference on the Mechanics of Structures and Materials*, H. Hao and C. Zhang, eds., Perth, WA, Australia, 2016, pp. 465-469.

32. Liu, Y.; Zhu, W.; and Yang, E.-H., "Alkali-Activated Ground Granulated Blast-Furnace Slag Incorporating Incinerator Fly Ash as a Potential Binder," *Construction and Building Materials*, V. 112, June 2016, pp. 1005-1012. doi: 10.1016/j.conbuildmat.2016.02.153

33. Puligilla, S., and Mondal, P., "Role of Slag in Microstructural Development and Hardening of Fly Ash-Slag Geopolymer," *Cement and Concrete Research*, V. 43, Jan. 2013, pp. 70-80. doi: 10.1016/j.cemconres.2012.10.004

34. Saha, S., and Rajasekaran, C., "Enhancement of the Properties of Fly Ash Based Geopolymer Paste by Incorporating Ground Granulated Blast Furnace Slag," *Construction and Building Materials*, V. 146, Aug. 2017, pp. 615-620. doi: 10.1016/j.conbuildmat.2017.04.139

35. Diaz-Loya, E. I.; Allouche, E. N.; and Vaidya, S., "Mechanical Properties of Fly-Ash-Based Geopolymer Concrete," *ACI Materials Journal*, V. 108, No. 3, May-June 2011, pp. 300-306.

36. Marjanović, N.; Komljenović, M.; Baščarević, Z.; and Nikolić, V., "Improving Reactivity of Fly Ash and Properties of Ensuing Geopolymers through Mechanical Activation," *Construction and Building Materials*, V. 57, Apr. 2014, pp. 151-162. doi: 10.1016/j.conbuildmat.2014.01.095

ACI MATERIALS JOURNAL TECHNICAL PAPER

Title No. 120-M22

Quantifying Conservativeness of Water-Soluble Chloride Testing

by Ahmed A. Ahmed and David Trejo

Proponents of water-soluble chloride testing argue that only chlorides in the pore solution contribute to corrosion and that this testing is more representative of free chlorides and therefore should be required. Proponents of acid-soluble chloride testing argue that although water-soluble testing may be more representative of free chlorides in the pore solution at early ages, bound chlorides can become unbound with time, making the water-soluble test unconservative for predicting later-age free chlorides. However, water-soluble testing likely unbinds some admixed chlorides during testing. If the number of chlorides released as part of the water-soluble test exceeds the number of chlorides released at later ages (that is, from carbonation), the water-soluble test should be sufficiently conservative. This research quantifies the release of admixed chlorides as a result of testing and carbonation. Results indicate that water-soluble testing is sufficiently conservative in most cases for assessing admixed chloride contents in various cementitious systems.

Keywords: admixed chlorides; bound chlorides; carbonation; chloride release; chloride testing; specialty cements.

INTRODUCTION

The presence of chlorides in sufficient quantities in a cementitious system can disrupt the passive layer on embedded steel reinforcement, which protects this reinforcement from corrosion. Chlorides in concrete can increase the risk of corrosion and reduce the service life of these structures. Chlorides can be present in the concrete constituent materials, intentionally added to the fresh mixture, or can be transported into the cementitious system from the surrounding environment.

Chlorides in the fresh mixture—that is, the admixed chlorides—can react during the cement hydration process, and some can become bound within the hydrated products. The binding of these chlorides can influence whether the concrete meets specifications for chloride limits and whether these chlorides can contribute to corrosion initiation of the reinforcing steel in the concrete. Bound chlorides that are physically (loosely) or chemically (tightly) bound in or on the hydrated cement products are initially unavailable for corrosion initiation and propagation. However, free chlorides—that is, chlorides that are present in the pore solution of the cementitious system—do contribute to corrosion initiation and propagation. The sum of the free and bound chlorides in the cementitious system represents the total admixed chlorides. Although the total admixed chlorides could be constant with time (assuming no external chloride exposure), the amount of free and bound chlorides could change with time and with exposure to CO_2 or sulfates. Knowing the time variant, free and bound chlorides under different exposure conditions can assist users in selecting an appropriate test that will provide a representative estimate of later-age free chlorides, which will provide a better estimate of the future risk of corrosion and service life.

The free chlorides in the pore solution of the cementitious system are quantified by the extraction of the pore solution using high pressure. Longuet et al. (1973) developed the pore extraction method, and this process has been used by many researchers to extract pore solutions from cementitious systems (Barneyback and Diamond 1981; Page and Vennesland 1983; Arya et al. 1987; Dhir et al. 1990; Haque and Kayyali 1995; Pavlík 2000; Plusquellec et al. 2017). Longuet et al. (1973) provided a method to express the pore solution from crushed cement pastes. The general process reported is to crush a cementitious sample into manageable sizes, place this crushed cementitious material into the extraction equipment, place a load on the equipment to extract the pore solution, then collect and analyze this pore solution. One drawback of this method is that it is not yet standardized and statistics and error measures are needed.

ASTM C1218/C1218M-17 is a standardized test commonly reported to be an indicator of free chlorides. This test is performed by mixing 10 g (0.35 oz.) of powdered samples with 50 ± 1 mL (1.7 ± 0.034 fl oz.) of reagent water. The sample is then boiled for 5 minutes and allowed to stand for 24 hours for chloride extraction. After filtering residues from the sample, the filtrate is mixed with 3 mL (0.1 fl oz.) of 1:1 nitric acid and 3 mL (0.1 fl oz.) of 30% hydrogen peroxide. After 2 minutes, the sample is boiled again for several seconds, then after cooling to room temperature, is tested for chlorides using manual potentiometric titration following ASTM C114 requirements. Arya et al. (1990) distinguished between the pore solution and water-soluble chlorides and reported that although pore solution chlorides are more representative of the free chlorides, some loosely bound chlorides are released during water-soluble chloride testing. Shakouri et al. (2018) reported that the pore solution results are, on average, 77% of the water-soluble results. This finding is in line with the findings of Arya et al. (1990). Therefore, results from water-soluble chloride testing are generally higher than results from pore solution

ACI Materials Journal, V. 120, No. 2, March 2023.

MS No. M-2021-178.R2, doi: 10.14359/51738499, received January 7, 2022, and reviewed under Institute publication policies.

chloride testing, and water-soluble testing likely causes the unbinding of bound chlorides and thereby overestimates the number of free chlorides.

ASTM C1152/C1152M-04 is commonly reported to be an indicator of total chlorides. Shakouri et al. (2018), Trejo et al. (2019), and Trejo and Ahmed (2019) reported that ASTM C1152/C1152M detects, on average, approximately 94%, 93%, and 95% of the total admixed chlorides in ordinary portland cementitious (OPC) systems, respectively. These results indicate that acid-soluble chloride testing slightly underestimates the total chlorides, but even so, is likely a good indicator of total chlorides.

Water-soluble testing, following ASTM C1218/C1218M, is common practice for evaluating admixed chlorides in concrete. Several ACI documents also allow acid-soluble testing (ASTM C1152/C1152M). Some of these documents note that acid-soluble chloride testing is likely more appropriate because chlorides can be released at later ages because of carbonation, and that water-soluble testing may underestimate the number of chlorides released as a result of carbonation. Very little research has been performed to assess how much of the bound admixed chlorides are released during water-soluble chloride testing. In addition, very little research has been performed to quantify the number of chlorides that are released because of carbonation. The objective of this research is to quantify these chloride releases for different cementitious systems to determine if water-soluble testing is conservative or unconservative for estimating chlorides that can be unbound at later ages because of carbonation.

Dhir et al. (1990) performed acid- and water-soluble testing to evaluate the chloride content of OPC concrete specimens containing admixed chlorides. The authors reported that the acid extraction method yielded up to 70% more chlorides than the conventional water-soluble method (water-soluble to acid-soluble test ratio is ~0.6). The authors also reported that water-soluble chlorides provided an immediate indication of corrosion risk and that acid-soluble chlorides can be used to evaluate the overall risk of corrosion of the cementitious systems when exposed to carbonation. However, if water-soluble testing extracts some of the bound chlorides as reported by Shakouri et al. (2018) and Arya et al. (1990), water-soluble chloride testing may be sufficiently conservative to evaluate "overall risks," as referred to by Dhir et al. In addition, the ACI 222 documents (ACI Committee 222 2010, 2019) report that the average content of water-soluble chlorides is approximately 75 to 80% of the acid-soluble chlorides; that is, the acid-soluble test yields 25 to 33% more chlorides than the water-soluble test. Trejo et al. (2019) reported that results from the water-soluble tests can range from 8 to 77% of the acid-soluble tests for various cementitious systems and reported that the range published in ACI 222R-01(10) was in most cases incorrect for admixed chlorides.

Knowing the amount of free and bound chlorides is important as this information can influence material acceptance and future corrosion performance. However, the amount of free and bound chlorides can change with time and knowing the free, bound, or total chlorides in new concrete provides limited information on these chlorides at later ages. The concentration change in free and bound chlorides is related to the carbonation of cementitious systems. Because bound chlorides can be released under certain exposure conditions, researchers have recommended that acid-soluble chloride testing be used to assess the overall risk of corrosion (Vesikari 2009; Geng et al. 2016). However, this would be appropriate only if nearly all bound chlorides were released upon carbonation at later ages. If only a very small number of chlorides are released upon carbonation, using acid-soluble chloride testing could significantly overestimate the later-age free chlorides and could be overly conservative. What is more important in selecting an appropriate test method is whether the results from that test method are representative of the free chlorides at later ages after carbonation. If the number of bound chlorides released from water-soluble testing exceeds the number of chlorides released as a result of carbonation, the water-soluble test would be a more appropriate test to assess free chlorides at later ages and potential risk of corrosion (that is, after carbonation). Alternatively, if the number of free chlorides after carbonation exceeds the number of bound chlorides released from water-soluble testing, the acid-soluble test may be the more appropriate test. The objective of this research is to identify the most appropriate chloride test that minimizes corrosion risk for OPC and specialty cements.

One significant variable that affects the binding of chlorides in cementitious systems is the hydration products of the cementitious system. When chlorides are included in the fresh mixture, binding of chlorides occurs during the process of forming these hydration products. Page and Vennesland (1983) reported that the hydration products of OPC bind approximately 60% of the total admixed chloride content. The authors also reported that after the addition of chlorides to the fresh mixture, these chlorides can be bound through chemical substitution or physical sorption to the OPC hydration products. Hirao et al. (2005), Florea and Brouwers (2012), and Geng et al. (2016) also reported that when chlorides are intentionally added to a fresh OPC mixture, chlorides will react with monosulfate to form Friedel's salt ($C_3A{\cdot}CaCl_2{\cdot}H_{10}$), or these chlorides can be physically adsorbed onto the outer layers of calcium-silicate-hydrate (C-S-H) gel. Friedel's salt, in turn, can physically interact with chlorides through ion exchange, dissolution, and precipitation, and because of its large surface area, can further bind chlorides. Florea and Brouwers (2012) reported that C-S-H could bind between 25 and 28% of the total admixed chlorides and monosulfate hydrate can bind up to approximately 70% of the total admixed chlorides. The authors also noted that ettringite and calcium hydroxide exhibit minimal binding capacities. However, Arya et al. (1990) reported that chlorides could react with the ettringite to produce calcium chloroaluminate.

Calcium aluminate cement (CAC) systems and calcium sulfoaluminate cement (CSA) are two common specialty cement systems. These systems exhibit different hydration products than that of OPC; therefore, the chloride binding capacities of these cements could be different from OPC systems.

The primary hydration products of CAC are CAH_{10} and small amounts of C_2AH_8 with AH_3. These products convert to C_3AH_6 with time, depending on time and temperature, where high temperatures increase this conversion rate. Limited research has been performed to assess the binding of chlorides in CAC systems. Sanjuán (1997) studied the conversion of CAC with the presence of admixed chlorides. The author reported that Friedel's salt is formed when the hexagonal-shaped CAH_{10} converts to the cubic C_3AH_6 through dissolution, and the formation of Friedel's salt could occur through the replacement of hydroxide anions in the cubic-shaped C_3AH_6 with chloride anions. Ann et al. (2010a,b) reported that low-alumina CAC systems exhibit lower chloride-binding capacities than OPC systems and attributed this lower binding to the lower level of hydration products that bind chlorides. The authors also reported that CAC is resistant to the release of bound chlorides, even at low pH levels. Later, Ann and Cho (2014) investigated the binding of chlorides in OPC and CAC systems and concluded that the binding of chlorides in CAC is lower than that of OPC.

Zhang and Glasser (2002), Winnefeld and Lothenbach (2010), and Zajac et al. (2016) reported that the main hydration products of CSA cement are ettringite ($CaO·Al_2O_3·3CaSO_4·32H_2O$) and calcium monosulfate ($3CaO·Al_2O_3·CaSO_4·12H_2O$), along with amorphous aluminium hydroxide (AH_3). Calcium monosulfate hydrate forms in the presence of lower $CaSO_4$ quantities, whereas ettringite forms in the presence of higher $CaSO_4$ quantities.

CSA systems have been reported to exhibit higher chloride-binding capacities than OPC systems. Ioannou et al. (2015) assessed concrete samples with a CSA-fly ash cement blend and reported that the binding of chlorides increased in the ettringite-rich environment. Monosulfate quantities in the CSA system are higher than that of OPC and therefore these systems can exhibit higher binding capacities. Hirao et al. (2005), Florea and Brouwers (2012), and Geng et al. (2016) all reported that calcium monosulfate, even in small quantities, exhibits high binding capacities. Therefore, the high binding capacities reported for CSA systems seem to be attributed mostly to the presence of calcium monosulfate.

This literature review indicates that CSA systems could initially bind more chlorides than OPC systems, while CAC systems likely initially bind less chlorides than OPC systems. The binding of chlorides is a critical parameter because the number of chlorides that are bound could influence whether certain concrete mixtures meet allowable chloride limits, and the number of free chlorides could influence future corrosion activity. Because the number of free chlorides could be a time-variant function (that is, it changes when carbonation occurs), accurately measuring these free and bound early- and later-age chlorides is important. If a cementitious system can bind all chlorides at early ages but all these chlorides are later released, the value of the results from early-age testing, which indicated no free chlorides, would be limited. It is well known that free chlorides are responsible for corrosion initiation and propagation. The water-soluble test method is a derived method that is believed to measure the free chlorides. However, some bound chlorides are released during testing. The conservativeness of this test for predicting later-age free chlorides and eventual risk of corrosion is unknown, especially when the number of free chlorides increases when the cementitious system is exposed to carbonation. Knowing the amount of released chlorides after exposure to carbonation can help in determining the most appropriate testing to assess the later-age free chlorides.

The carbonation of OPC systems is a chemical reaction between gaseous CO_2 and calcium-bearing phases such as $Ca(OH)_2$ and C-S-H. CO_2 gas can be transported into the cementitious system matrix and change the chemical makeup by attacking the soluble $Ca(OH)_2$ to form calcium carbonate, $CaCO_3$, and water. Geng et al. (2016) assessed the release of bound chlorides in OPC under the exposure of carbonation and reported that carbonation of OPC resulted in the release of bound chlorides due to the decomposition of Friedel's salt and C-S-H gel, leading to an increase of free chlorides.

Pérez et al. (1983), Blenkinsop et al. (1985), and Vasudevan and Trejo (2022) reported that CAC exhibits a higher rate of carbonation than OPC because of the lower pH of the CAC pore solution. It has been reported that carbonation of CAC can rapidly decrease the pore solution pH. Fernández-Carrasco et al. (2001) reported that the carbonation of CAC decreases the porosity through the formation of the $CaCO_3$ polymorphs, vaterite, and aragonite in the pores. In addition to the formation of $CaCO_3$, conversion is inhibited because the carbonation rate of hexagonal calcium aluminates, CAH_{10} and C_2AH_8, is faster than that of the cubic aluminate, C_3AH_6. Therefore, carbonation can inhibit the conversion of CAC systems by reducing the number of aluminates that can be converted. Goñi and Guerrero (2003) studied the influence of accelerated carbonation on the stability of Friedel's salt and the number of free chlorides in the pore solution of the CAC system and reported that the carbonation of Friedel's salt did not increase the free chlorides in the pore solution.

The hydration products of CSA systems have also been reported to decompose when exposed to CO_2. Mesbah et al. (2012) reported that under increasing CO_2 concentrations, calcium monosulfate hydrate can react to form calcite. Nishikawa et al. (1992) reported that when CSA is exposed to CO_2, ettringite dissolves into gypsum, calcium carbonate, and alumina gel. Robl et al. (1996) reported that calcite replaces gypsum when exposed to CO_2. Therefore, carbonation can result in the decomposition of the hydration products in CSA cementitious systems, possibly resulting in the release of bound chlorides.

Mesbah et al. (2012) reported that Friedel's salt forms from the reaction of chlorides and monosulfate in CSA cementitious systems. Suryavanshi and Swamy (1996) reported that chlorides can be disassociated from Friedel's salt upon exposure to carbonation, and this could increase free chloride levels and elevate the risk of corrosion. Canonico et al. (2012) reported that the carbonation rate of CSA could be higher than that of OPC because of the low pH of the CSA pore solution. The literature indicates that the decomposition of the hydration products of CSA because of carbonation can release bound chlorides. However, how much bound chlorides are released is not known.

A review of the literature indicates that carbonation can increase the number of free chlorides in the pore solution of OPC cementitious systems. The review also indicates that the carbonation rates of CAC and CSA systems are typically higher than OPC systems and these higher rates could influence the rate and degree of release of bound chlorides. Knowing the number of bound chlorides that are released when exposed to CO_2 is important in assessing the risk of corrosion and service life of a structure. The objective of this paper is to first determine the number of bound chlorides that are released during water-soluble and acid-soluble testing and then to compare the amount of released chlorides with the number of chlorides that are released upon carbonation. If the number of bound chlorides released due to carbonation is less than or near the number of bound chlorides released from water-soluble testing at early ages, water-soluble testing should be used for assessing allowable chloride limits. If the number of bound chlorides released as a result of carbonation is more than the number of bound chlorides released from water-soluble testing at early ages, acid-soluble testing should be used. The results from this research will be used to identify the appropriate test method (water-soluble or acid-soluble) that should be used to assess allowable chloride limits to minimize risk of corrosion.

This study contains three parts. First, the study will assess the amount of early-age free chlorides using results from pore extraction and water-soluble testing for OPC, CAC, and CSA systems and will quantify how much of the bound admixed chlorides are released because of the ASTM C1218/C1218M (water-soluble chloride test) procedure. Second, the study will quantify the number of free chlorides, using water-soluble testing, of carbonated OPC, CAC, and CSA systems. This will provide data on how much chlorides are released because of carbonation. Lastly, using the information from the first two objectives, this research will identify the test that is most representative of later-age free chlorides of carbonated cementitious systems. The authors anticipate that this research will provide information to resolve the long debate on whether water- or acid-soluble testing is more appropriate for assessing admixed chlorides in different cementitious systems.

RESEARCH SIGNIFICANCE

Debate exists as to whether admixed chlorides should be quantified with water- or acid-soluble testing. Because free chlorides in cementitious systems change with time and degree of carbonation, selecting an appropriate test method influences the risk associated with later-age corrosion. When chlorides become unbound, the risk of corrosion increases. This study quantifies the number of admixed chlorides released because of standardized water-soluble testing and as a result of carbonation exposure for various cementitious systems. These data provide information to determine if water-soluble testing is sufficiently conservative and more appropriate for assessing admixed chlorides in new concrete.

EXPERIMENTAL PROGRAM

A full factorial design was used to assess the influence of four testing parameters on chloride measurements. The four testing parameters include the type of cementitious system, the percentage of total admixed chlorides by mass of cement (Cl_{total}), the water-cement ratio (w/c), and the status of the cementitious system (uncarbonated or carbonated). The concentration of water-soluble chlorides was evaluated as the dependent variable. OPC, CAC, and CSA systems were assessed. Four levels of Cl_{added} by mass of cement (0, 0.05, 0.25, and 1%) and three levels of w/c (0.35, 0.45, and 0.55) were evaluated. Because background chlorides were present in the constituent materials, the total chloride concentration, Cl_{total}, is defined as the sum of $Cl_{background}$ and Cl_{added}. A total of 36 (three types of cementitious systems × four Cl_{added} percentages × three w/c levels) scenarios for uncarbonated and carbonated cementitious systems were assessed with five replicates for each scenario (total of 360 samples) using a modified ASTM C1218/C1218M (auto-titration was used instead of manual titration). All chloride concentration tested following ASTM standards used the equations in the standards to quantify chloride concentrations. The pore solution chlorides ($Cl_{pore\text{-}uncarb}$) obtained through extraction for each w/c and Cl_{total} level were evaluated using one sample. Note that this study assumes that the pore extraction method represents the early-age free chlorides. It should be noted that pore extraction could result in the release of some bound chlorides but as reported, chloride concentrations in free water-soluble testing are generally significantly higher than chloride concentrations from pore solution extraction.

Materials

The materials used to prepare paste mixtures in this study included an OPC, a standard-grade CAC, and a commercial CSA. The oxide compositions of the cements were determined using X-ray fluorescence (XRF) analysis and are reported by Ahmed and Trejo (2020). The manufacturers reported that the chemistry of the cements and other characteristics meet standard requirements.

Primary standard reagents, NaCl (>99.9% purity) and $AgNO_3$ (≥99.80% purity), were used to prepare chemical solutions. The same NaCl was also used as the admixed chlorides. The mixing water was Type II reagent water that met ASTM D1193 requirements. All chemical solutions were prepared with the same reagent water.

Background chloride quantities for each cementitious system and w/c are shown in Table 1. These background chlorides were determined following ASTM C1152/C1152M but using auto-titration instead of manual titration.

Specimen preparation

A total of 180 cylindrical specimens with diameters and heights of 34.3 x 52.1 mm (1.35 x 2.05 in.), respectively, were prepared. Two test samples were cut from each cast specimen. In addition to these specimens, three cube specimens with dimensions of 50.8 x 50.8 x 50.8 mm (2 x 2 x 2 in.) were prepared from each mixture to determine the chloride content and pH of the pore solution using the pore extraction test. Prior to mixing, NaCl was premixed with the mixing water at the predefined levels.

Cement pastes were prepared following the procedure prescribed by ASTM C305-14. Cement paste mixtures

were mixed in the laboratory under an ambient temperature of 22°C (73°F). To prevent bleeding of the paste mixtures, cement pastes were cast in sealed vials and rotated along their longitudinal axis at 30 rpm for 10 hours. The addition of NaCl retarded the final setting time of CAC pastes. Therefore, the CAC specimens with 0.25% and 1% admixed chloride levels were removed from the vials after 48 hours. OPC and CSA specimens were removed from the vials after 24 hours. All specimens were moist-cured at 22°C (73°F) for 28 days after casting.

At the end of the curing period, specimens were cut into two disc samples with thicknesses of 6 mm (0.24 in.) for carbonation exposure assessment. This disc thickness was selected to ensure that sufficient material was available for chloride testing and to ensure that these discs could be fully carbonated in a reasonable time. Specimens and disc samples were air-dried for 24 hours in the laboratory to remove surface moisture prior to CO_2 exposure.

Disc samples were subjected to accelerated carbonation in an environmental chamber with 20% CO_2, ±65% relative humidity (RH), and 20°C (68°F). The RH was maintained using saturated salt solution in accordance with ASTM E104-02. The remaining samples from the cut specimens were tightly sealed with plastic wrap and stored in the laboratory (~22°C [73°F]) to prevent carbonation. The carbonated and uncarbonated samples were then ground into powders passing a No. 20 (850 µm) sieve and evaluated for water-soluble chlorides.

Carbonated samples were tested for water-soluble chloride concentration after the entire depth of the disc was carbonated. The depth of carbonation was determined in accordance with CPC-18 (1988). Disc samples were split along the longitudinal axis to expose the fractured section and sprayed with phenolphthalein solution to confirm complete carbonation.

The pore solution was extracted using the pore extraction method. A cube specimen was removed from curing, sealed with plastic wrap, placed in a sealed plastic bag, and stored in a freezer to inhibit hydration until the extraction of pore solution. In this test, another cube specimen from each mixture was dried to a constant weight in a laboratory oven at 105°C (221°F) to determine the amount of evaporable water. The amount of evaporable water was then used to determine the percentage of free chlorides in the pore solution by the mass of cement. Samples were then crushed for pore solution extraction. The pH of the expressed pore solution was measured within 1 hour after extraction. The pH measurements were performed using a benchtop pH meter with a pH electrode.

Table 1—Background chlorides for different systems

Cementitious system	*w*/*c*	Background chlorides, % by mass of cement
OPC	0.35	0.007
	0.45	0.002
	0.55	0.008
CAC	0.35	0.008
	0.45	0.007
	0.55	0.006
CSA	0.35	0.056
	0.45	0.045
	0.55	0.026

RESULTS AND DISCUSSION

In this study, different cementitious systems were subjected to full carbonation. The time to complete carbonation is shown in Fig. 1. The results indicate that the rate of carbonation for the OPC system is lower than the carbonation rates for the CAC and CSA systems. The results also indicate that the rate of carbonation is influenced by the *w*/*c* and the Cl_{total} level. Interestingly, higher admixed chloride concentrations seem to reduce the rate of carbonation. Lower carbonation rates are observed at lower *w*/*c* values and higher Cl_{total} levels in all systems. This is because systems with a lower *w*/*c* have lower porosity values and increased tortuosity. In addition, it has been reported that cementitious systems with higher levels of Cl_{total} can have higher early-age strengths and lower porosities (Abrams 1924), which could reduce carbonation rates.

Results and discussion from the experimental program will be separated into early-age (pre-carbonated) and later-age (post-carbonated) analyses. A comparison of these results will then be performed to assess the applicability of the test

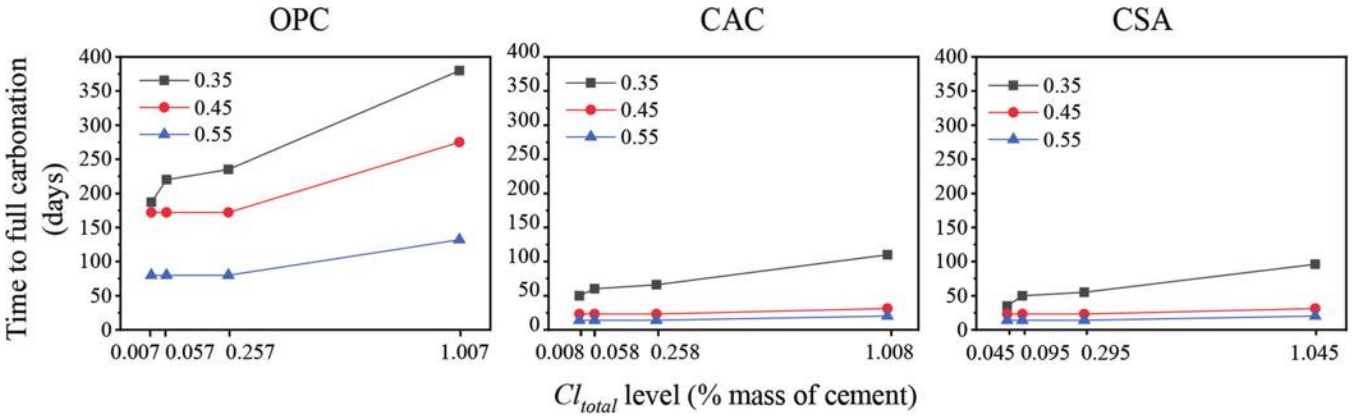

Fig. 1—Time to full carbonation as function of Cl_{total} *level and* w/c *for different cementitious systems.*

methods. Linear regression statistical analysis will be used to compare the test results (as percent by mass of cement).

Chloride testing of uncarbonated specimens

To assess the number of free chlorides in uncarbonated specimens, the chloride concentrations from the pore press method (that is, $Cl_{pore\text{-}uncarb}$) and the water-soluble test method before carbonation ($Cl_{ws\text{-}uncarb}$) are compared. Figure 2 shows the $Cl_{pore\text{-}uncarb}$ and the $Cl_{ws\text{-}uncarb}$ for the different cementitious systems as a function of the *w*/*c* and Cl_{total} levels. Here, $Cl_{pore\text{-}uncarb}$ and $Cl_{ws\text{-}uncarb}$ are represented as a percentage of the total chloride concentration (Cl_{total}), where Cl_{total} is the sum of Cl_{added} and $Cl_{background}$ in the cementitious samples. Results indicate that the percentages of $Cl_{pore\text{-}uncarb}$ and $Cl_{ws\text{-}uncarb}$ generally increase with increasing *w*/*c* and Cl_{total} levels for the OPC system. Results also indicate that the percentages of $Cl_{pore\text{-}uncarb}$ and $Cl_{ws\text{-}uncarb}$ generally decrease with an increase in *w*/*c* and Cl_{added} levels for the CAC and CSA systems. This reduction in chloride concentrations could be attributed to the increased hydration of the mixtures with higher *w*/*c* values. Results indicate that $Cl_{pore\text{-}uncarb} < Cl_{ws\text{-}uncarb}$ for all cases. A two-sample *t*-test indicates that there is a significant difference between $Cl_{pore\text{-}uncarb}$ and $Cl_{ws\text{-}uncarb}$ for OPC, CAC, and CSA. The two-sample *t*-test *p*-values at a 0.05 significance level for all systems were less than 0.0001.

The number of bound chlorides released as a result of water-soluble testing, $Cl_{released\text{-}ws\ testing}$, can be estimated as follows

$$Cl_{released\text{-}ws\ testing} = Cl_{ws\text{-}uncarb} - Cl_{pore\text{-}uncarb} \quad (1)$$

The values of $Cl_{released\text{-}ws\ testing}$ are shown in Fig. 3. The results indicate that the chloride concentrations determined

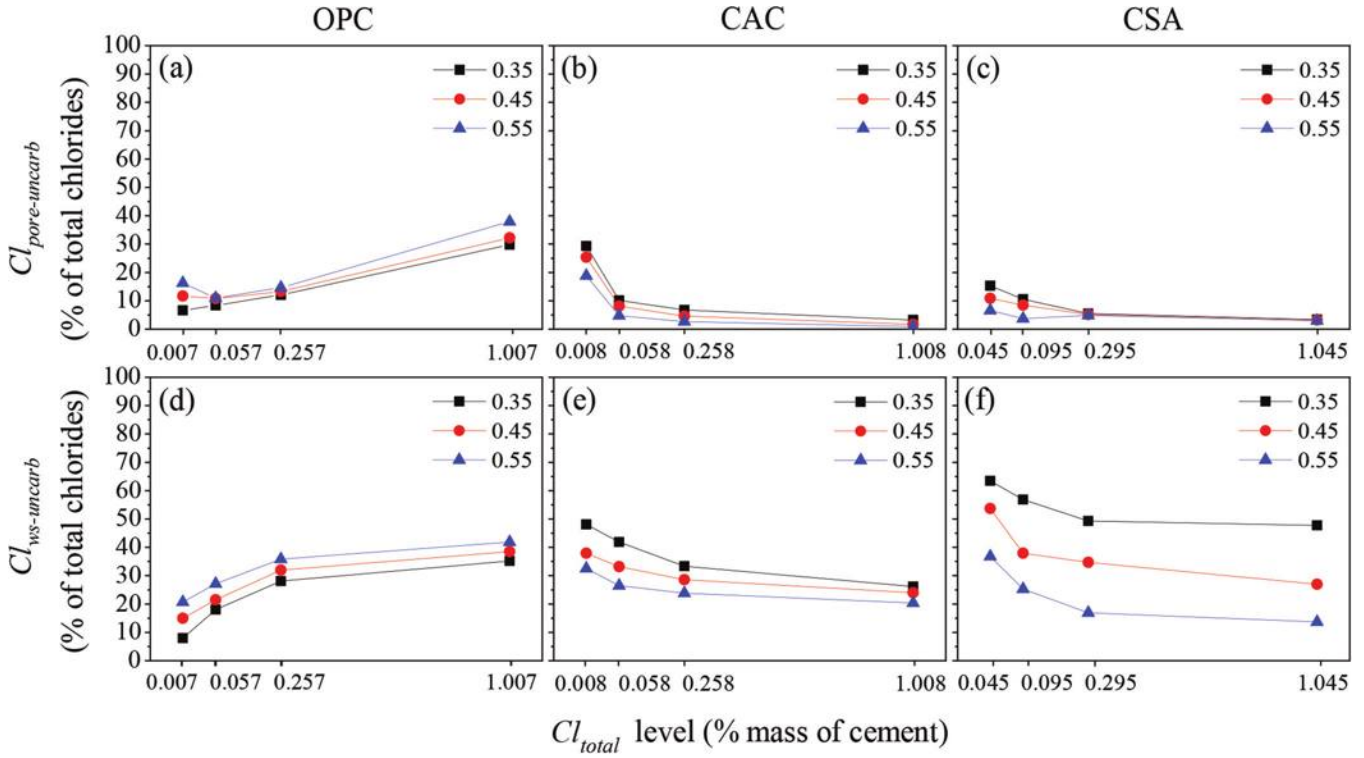

Fig. 2—Comparison of pore solution chlorides ($Cl_{pore\text{-}uncarb}$) and water-soluble chlorides ($Cl_{ws\text{-}uncarb}$) for different uncarbonated cementitious systems.

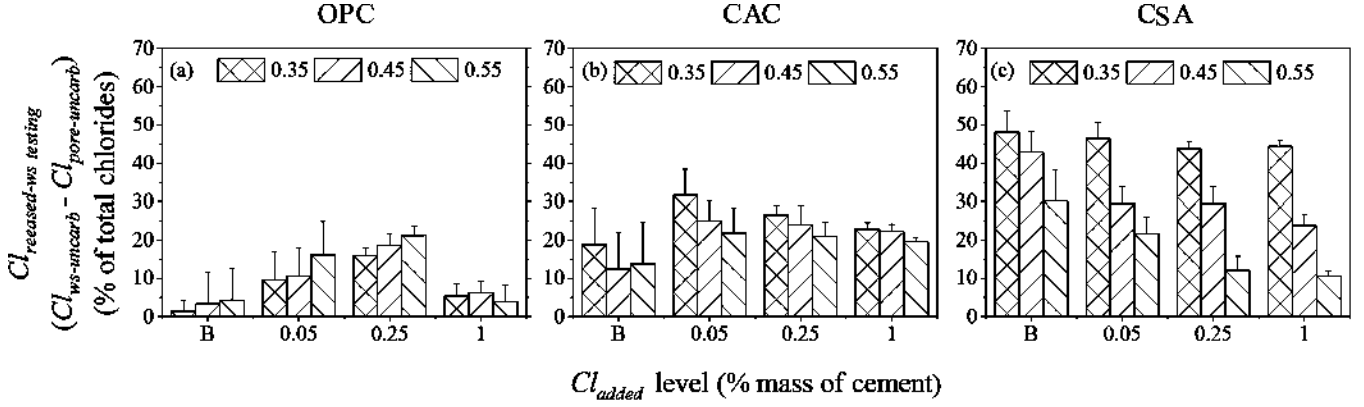

Fig. 3—Amount of bound admixed chlorides released as result of water-soluble testing.

using the water-soluble test are significantly higher than the free chloride results using the pore extraction test. For OPC systems, the water-soluble chloride test results overestimate the free chlorides as measured by pore extraction testing by up to approximately 20% of total admixed chlorides. For the CAC systems, the water-soluble test overestimates the free chlorides by up to approximately 30% of total admixed chlorides, and for CSA systems, the water-soluble chloride test overestimates the free chlorides (as measured with the pore solution extraction) by up to approximately 50%. These results indicate that the water-soluble testing regime extracts more bound chlorides in the CSA and CAC systems when compared to the OPC system. In addition, water-soluble testing overestimates the number of free chlorides, as measured by pore extraction testing, for all systems. Note that the results in Fig. 2 and 3 are shown as a percentage of the total admixed chlorides.

Regression results indicate that $Cl_{pore\text{-}uncarb}$ measurements are on average 86, 7.2, and 7.8% of $Cl_{ws\text{-}uncarb}$ measurements, with 95% upper confidence level values (95% UCL) of 92, 10, and 11% for OPC, CAC, and CSA, respectively. These results are shown in Fig. 4. Note that the regression results are reported here as a percentage by mass of cement and not as a percentage of total admixed chlorides.

To determine how much of the bound chlorides are released as a result of water-soluble testing, the β values from Fig. 4 can be used in Eq. (1) as follows

$$Cl_{released\text{-}ws\ testing} = (1-\beta_A) \times Cl_{ws\text{-}uncarb} \quad (2)$$

Using this equation, it is determined that 14, 92, and 93% of the water-soluble chlorides measured using ASTM C1218/C1218M were bound chlorides released as part of the water-soluble test procedure for the OPC, CAC, and CSA cementitious systems, respectively.

In general, results indicate that the number of admixed chlorides that are released from water-soluble chloride testing in CAC and CSA systems are significantly greater than the number of admixed chlorides that are released during water-soluble testing in OPC systems. If the number of admixed chlorides released as a result of carbonation is less than the number of chlorides released from the water-soluble testing, water-soluble testing is likely sufficiently conservative for assessing admixed chlorides in concrete. The following section presents results on the amount of bound admixed chlorides released because of carbonation.

Chloride testing of carbonated specimens

After the chloride testing of uncarbonated samples, the number of free chlorides for carbonated OPC, CAC, and CSA systems was assessed using water-soluble testing. The number of chlorides released as a result of carbonation, $Cl_{released\text{-}carb}$, can be estimated as follows

$$Cl_{released\text{-}carb} = Cl_{ws\text{-}carb} - Cl_{ws\text{-}uncarb} \quad (3)$$

where $Cl_{ws\text{-}carb}$ is the number of water-soluble chlorides for carbonated samples. This difference represents the number of chlorides released as a result of carbonation. Figure 5 shows the $Cl_{ws\text{-}uncarb}$ and $Cl_{ws\text{-}carb}$ values for the OPC, CSA, and CAC cementitious systems for different *w*/*c* and Cl_{total} levels.

Figure 5(a) shows that the percentage of $Cl_{ws\text{-}uncarb}$ for the OPC mixtures increases slightly with an increase in *w*/*c*. Analysis indicates this increase is not statistically significant. This figure also shows that the percentage of $Cl_{ws\text{-}uncarb}$ increases with increasing Cl_{total} levels. In general, at lower total chloride concentrations, the binding of these chlorides is expected to be high (in other words, the number of chlorides as measured using water-soluble testing would be expected to be low); as the total chloride concentration increases, the binding capacity of the system is reached and the percentage of binding stabilizes. Lower variability in $Cl_{ws\text{-}uncarb}$ is associated with higher Cl_{total} concentrations; this is likely a result of testing at lower concentrations. Figure 5(d) shows the $Cl_{ws\text{-}carb}$ values for the OPC samples. The $Cl_{ws\text{-}carb}$ values for the OPC samples are higher than those of the uncarbonated OPC samples, indicating that chlorides are being released due to carbonation. The water-soluble chlorides increase as the *w*/*c* level increases, which is likely a result of increased carbonation of the specimens with higher *w*/*c* values. However, at

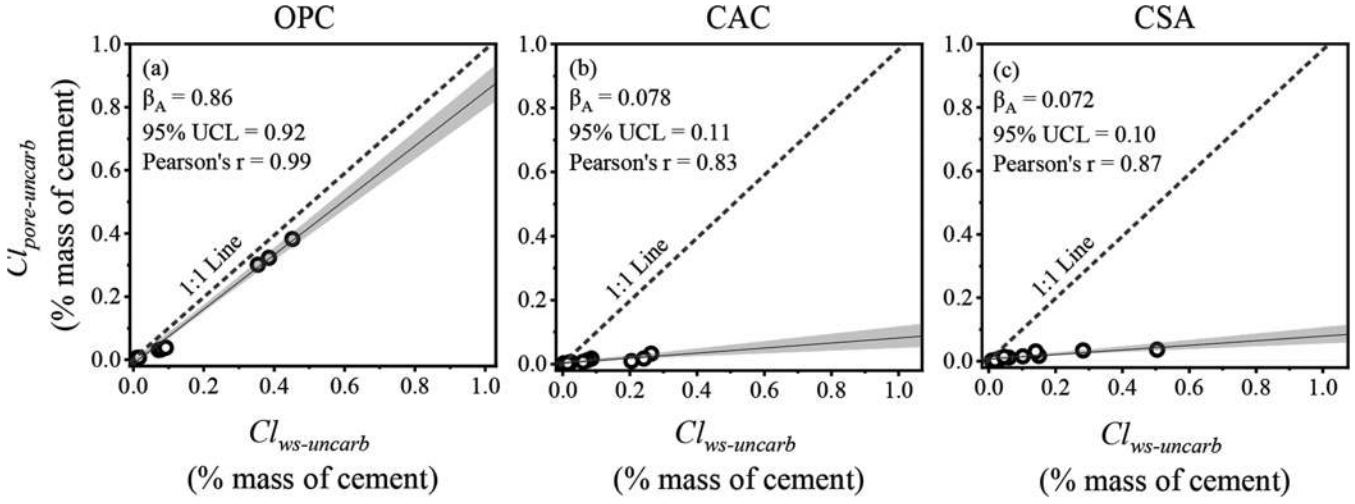

Fig. 4—Relationship between $Cl_{pore\text{-}uncarb}$ *and* $Cl_{ws\text{-}uncarb}$ *for different uncarbonated cementitious systems.*

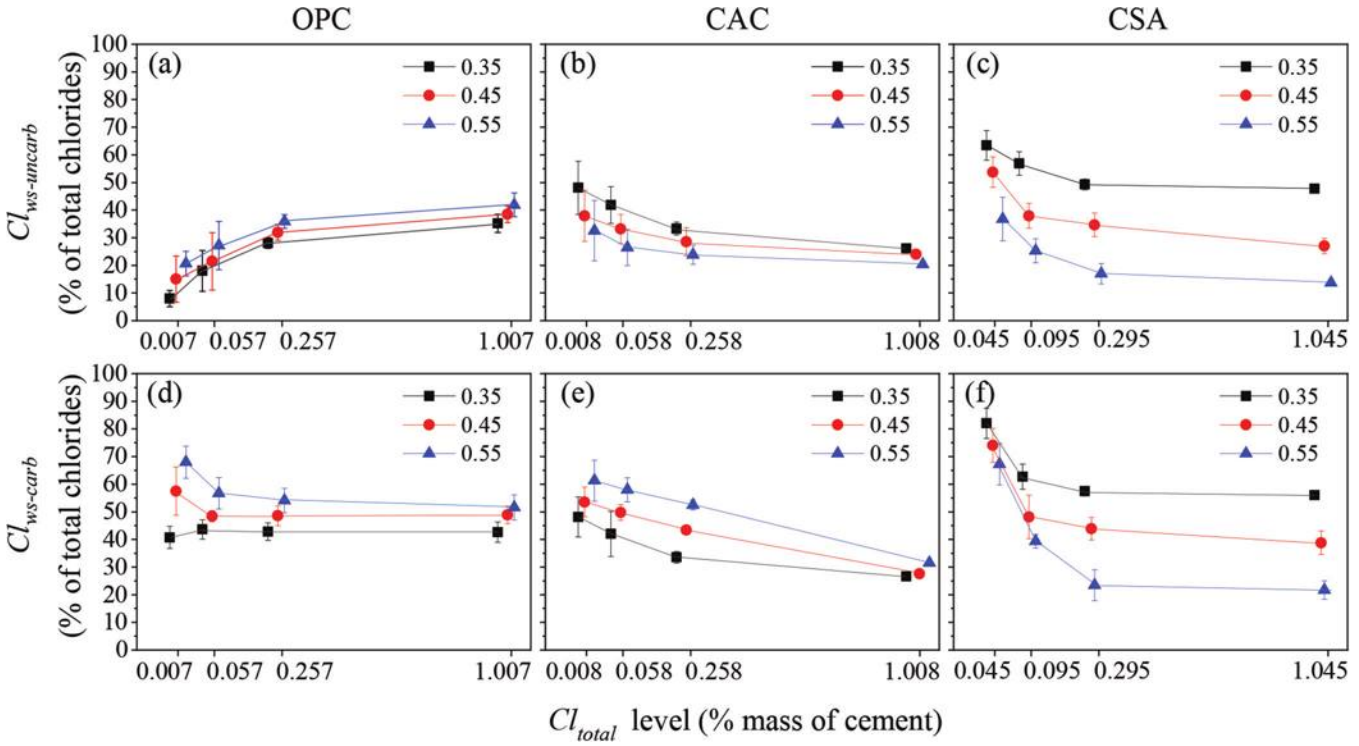

Fig. 5—Comparison of water-soluble chlorides for different uncarbonated and carbonated cementitious systems (values offset to distinguish error bars).

the higher Cl_{total} levels, the mean $Cl_{ws\text{-}carb}$ changes negligibly, indicating that above some *w*/*c* value, increased carbonation does not occur. The variability in the measured $Cl_{ws\text{-}carb}$ is generally similar for different *w*/*c* and Cl_{total} levels.

Figure 5(b) shows the $Cl_{ws\text{-}uncarb}$ values for the CAC. Higher $Cl_{ws\text{-}uncarb}$ values are observed at lower *w*/*c*, and the $Cl_{ws\text{-}uncarb}$ decreases with increasing Cl_{total} levels. The $Cl_{ws\text{-}uncarb}$ values for the CAC specimens exhibit higher variability at lower Cl_{total} levels and lower variability at higher Cl_{total} levels. Figure 5(e) shows the $Cl_{ws\text{-}carb}$ values for the CAC. The $Cl_{ws\text{-}carb}$ values do not significantly differ from the $Cl_{ws\text{-}uncarb}$ values for the CAC with a *w*/*c* of 0.35. However, the $Cl_{ws\text{-}carb}$ values for the carbonated CAC are higher than that of the uncarbonated CAC with *w*/*c* values of 0.45 and 0.55. This indicates that the *w*/*c* likely has a significant influence on the release of bound chlorides in CAC systems when exposed to CO_2 and carbonated. In general, at each Cl_{total} level, the $Cl_{ws\text{-}carb}$ is lower at lower *w*/*c* values. The variability in chloride measurements is higher at the lower Cl_{total} levels and lower at higher Cl_{total} levels.

Figure 5(c) shows the measured $Cl_{ws\text{-}uncarb}$ for the CSA specimens. The $Cl_{ws\text{-}uncarb}$ decreases with an increase in *w*/*c* and a decrease in Cl_{total} levels. The variability in $Cl_{ws\text{-}uncarb}$ measurements for the CSA samples decreases with increasing Cl_{total} levels. Figure 5(f) shows the $Cl_{ws\text{-}carb}$ for the CSA samples. The $Cl_{ws\text{-}carb}$ values are higher than that of the uncarbonated CSA samples, again indicating that chlorides are released due to carbonation. The $Cl_{ws\text{-}carb}$ percentages of the carbonated CSA samples exhibited similar trends as the $Cl_{ws\text{-}uncarb}$.

The differences in chloride measurements using the water-soluble testing methods before and after carbonation indicate that chlorides are being released because of carbonation. The difference between pre- and post-carbonated samples, $Cl_{released\text{-}carb}$, is shown in Fig. 6 for the different cementitious systems.

Figure 6(a) shows the number of bound chlorides that are released in the OPC system after carbonation. Higher percentages of bound chlorides are released at lower Cl_{total} levels, and the *w*/*c* influences the release of bound chlorides at these lower Cl_{total} levels. The mean number of chlorides released after carbonation ranges from approximately 7.5 to 47.3% of the total chlorides.

Figure 6(b) shows the concentrations of bound chlorides that are released after carbonation in the CAC system. The unbinding of chlorides due to carbonation in the CAC system increases with increasing *w*/*c* and is negligible for all Cl_{total} levels at a *w*/*c* value of 0.35. For the background, 0.05, and 0.25 Cl_{added} levels, approximately 0 to 31.4% of the total chlorides are released because of carbonation. These changes in chloride concentrations are less than the values observed for OPC systems.

Figure 6(c) shows the concentration of bound chlorides released in the CSA system because of complete carbonation. The results indicate that lower amounts of chlorides are released from the CSA system when compared with the OPC system. For the background and 0.05 Cl_{added} levels (that is, the lower Cl_{total} levels), the change in concentration of chlorides increases at higher *w*/*c* values. For most cases, the change in concentration of released chlorides decreases with increasing Cl_{total} levels. The *w*/*c* negligibly affects the release of bound chlorides at the 0.25 and 1% Cl_{added} levels (that is, higher Cl_{total} levels) for CSA systems. The mean amount of change in chlorides after carbonation ranges from

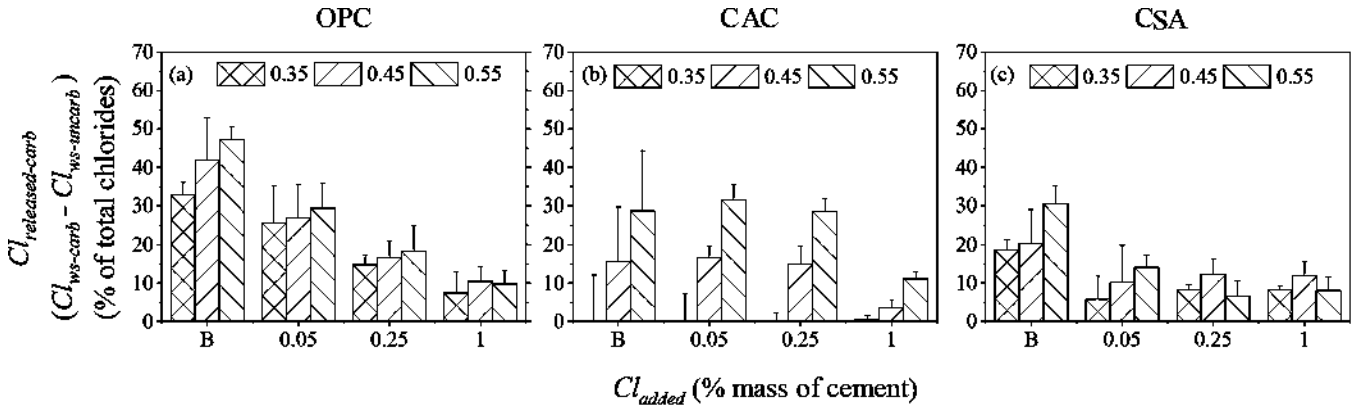

Fig. 6—Amount of bound chlorides released as result of carbonation.

approximately 5.8 to 30.4% of the total chlorides. Note that these changes in values are lower than the changes observed in the OPC system.

Linear regression can be performed to investigate the relationship between $Cl_{ws\text{-}uncarb}$ and $Cl_{ws\text{-}carb}$ for the different cementitious systems. This regression output is shown in Fig. 7 and indicates that $Cl_{ws\text{-}uncarb}$ and $Cl_{ws\text{-}carb}$ are strongly and positively correlated. This relationship is confirmed by the Pearson correlation coefficient of 0.99 for OPC and CSA, and 0.96 for CAC. $Cl_{ws\text{-}uncarb}$ provided β coefficients with 95% UCL of 0.85 and 0.88 for OPC, 0.8 and 0.96 for CAC, and 0.81 and 0.87 for CSA. Regression analysis results are reported by percent mass of cement because the published allowable chloride limits are reported using these units.

The relationship between the concentration of water-soluble chlorides before and after carbonation indicates that bound chlorides, likely tighter-bound chlorides, can be released and become unbound in the pore solution because of complete carbonation. Thus, carbonation increases the number of free chlorides in the cementitious system. In addition, *w*/*c* and Cl_{total} levels influence the measured water-soluble chloride values after carbonation. In general, Fig. 7 indicates that the $Cl_{ws\text{-}carb}$ measurements are, on average, 15, 20, and 19% higher than the $Cl_{ws\text{-}uncarb}$ results (that is, $\%\Delta CI_{ws\text{-}carb} = ((1/\beta) - 1) \times 100$) for the OPC, CAC, and CSA, respectively. This indicates that 15, 20, and 19% of the bound chlorides for the different cementitious systems can be released because of carbonation.

Selecting appropriate chloride test

As already noted, both ASTM C1218/C1218M (water-soluble chloride testing) and ASTM C1152/C1152M (acid-soluble chloride testing) are allowed to assess chloride concentrations of concrete in ACI documents. It is argued that acid-soluble chloride testing is likely the more appropriate test because chlorides can be released at later ages because of carbonation, and that water-soluble testing may underestimate the number of chlorides released as a result of carbonation. Limited research has been performed to assess how much of the bound admixed chlorides are released during water-soluble chloride testing and how much of the bound chlorides are released because of carbonation. The objective of this research is to quantify these chloride releases for different cementitious systems to determine if water-soluble testing is sufficiently conservative. ACI documents assume that water-soluble chlorides are approximately 75 to 80% of the acid-soluble chlorides. However, Trejo et al. (2019) reported that the range published in ACI 222R-01 was in most cases incorrect for admixed chlorides. Because of this, only one test should be specified in ACI documents.

This research generated data on how much of the bound admixed chlorides are released because of water-soluble testing ($Cl_{released\text{-}ws}$) and how much of the admixed chlorides are released when specimens are completely carbonated ($Cl_{ws\text{-}carb}$). The number of admixed chlorides released as part of the water-soluble testing (ASTM C1218/C1218M) was determined to be 14, 92, and 93% of the water-soluble results ($Cl_{ws\text{-}uncarb}$) for the OPC, CAC, and CSA cementitious systems, respectively. The number of admixed chlorides released because of carbonation (not testing) was determined to be 15, 20, and 19% of the water-soluble test results ($Cl_{ws\text{-}uncarb}$) for the OPC, CAC, and CSA cementitious systems, respectively.

If the amount of bound admixed chlorides that are released because of water-soluble testing extraction is greater than the amount of bound admixed chlorides released as a result of carbonation, then it could be concluded that water-soluble testing is sufficiently conservative and can account for the release of bound chlorides as a result of carbonation. Alternatively, if the ratio of these variables is greater than unity—that is, if

$$\frac{Cl_{released\text{-}ws}}{Cl_{released\text{-}carb}} > 1 \tag{4}$$

then the water-soluble test method following ASTM C1218/C1218M could be considered sufficiently conservative.

Using Eq. (1) and (3) and substituting these into Eq. (4) provides the following

$$\frac{Cl_{ws\text{-}uncarb} - Cl_{pore\text{-}uncarb}}{Cl_{ws\text{-}carb} - Cl_{ws\text{-}uncarb}} - 1 > 0 \tag{5}$$

From the chloride testing of uncarbonated samples, regression results indicate a significant relationship between $Cl_{pore\text{-}uncarb}$ and $Cl_{ws\text{-}uncarb}$ values for OPC, CAC, and CSA (p-value < 0.001). The relationship between $Cl_{pore\text{-}uncarb}$ and $Cl_{ws\text{-}uncarb}$ values for different *w*/*c* values and Cl_{total} levels can be represented by

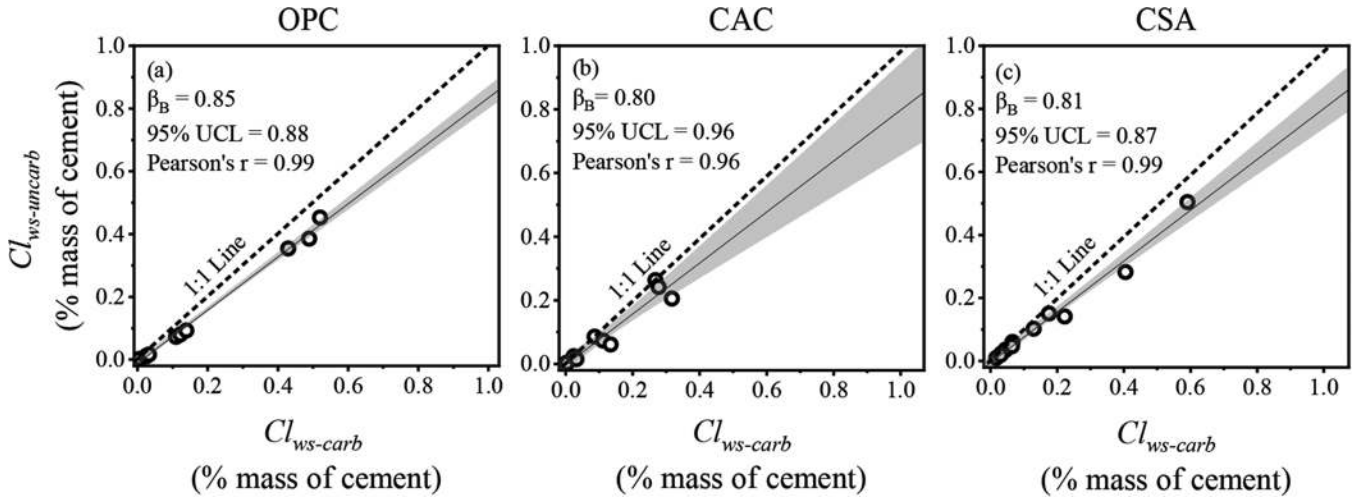

Fig. 7—Relationship between uncarbonated and carbonated water-soluble chloride results for different cementitious systems.

$$Cl_{pore\text{-}uncarb} = \beta_A \times Cl_{ws\text{-}uncarb} \quad (6)$$

From the testing of carbonated samples, regression results indicate a significant relationship between $Cl_{ws\text{-}uncarb}$ and $Cl_{ws\text{-}carb}$ values for all cementitious systems at varying *w*/*c* values and Cl_{total} levels (*p*-value < 0.001). This relationship is represented by

$$Cl_{ws\text{-}uncarb} = \beta_B \times Cl_{ws\text{-}carb} \quad (7)$$

Equation (7) can also be written as follows

$$Cl_{ws\text{-}carb} = \frac{Cl_{ws\text{-}uncarb}}{\beta_B} \quad (8)$$

Substituting Eq. (6) and (8) into Eq. (5) gives

$$\frac{Cl_{ws\text{-}uncarb} - \left(\beta_A \times Cl_{ws\text{-}uncarb}\right)}{\frac{Cl_{ws\text{-}uncarb}}{\beta_B} - Cl_{ws\text{-}uncarb}} - 1 > 0 \quad (9)$$

and simplifying Eq. (9) gives

$$\frac{\left(1-\beta_A\right)}{\left(\frac{1}{\beta_B} - 1\right)} - 1 > 0 \quad (10)$$

The left part of the equation can be referred to as a measure of the conservativeness of the water-soluble test method for assessing later-age free chlorides and will be referred to here as the conservative factor for the water-soluble test method, CF_{ws}. Table 2 shows the values of β_A, β_B, and CF_{ws}.

These results indicate that the CF_{ws} value for OPC is less than zero and would be considered unconservative for most admixed chloride levels. However, the largest difference between the chlorides released because of carbonation and testing was for the background conditions, where the release of chlorides due to carbonation only exceeded the release of chlorides due to testing for the two lower chloride concentrations. The CF_{ws} values for both CAC and CSA are significantly greater than zero and thus water-soluble testing would be considered very conservative for both systems. It should be noted that specimens in this research project were completely carbonated to pH levels less than 9, which is considered severe. Although the CF_{ws} for OPC is less than zero, the severity of the test condition in this research likely makes this value slightly negative.

SUMMARY, CONCLUSIONS, AND RECOMMENDATIONS

The study determined that water-soluble testing, following ASTM C1218/C1218M, extracts some bound chlorides. The results indicate that 14, 92, and 93% of the water-soluble chlorides are likely bound chlorides in the ordinary portland cement (OPC), calcium aluminate cement (CAC), and calcium sulfoaluminate cement (CSA) systems, respectively. This research also assessed how much chlorides are released because of complete carbonation of the cementitious systems. The results indicate that 15, 20, and 19% of the bound admixed chlorides in the OPC, CAC, and CSA systems can be released because of carbonation.

This research also assessed whether the water-soluble test is sufficiently conservative to assess later-age free chloride concentrations in OPC, CAC, and CSA systems after carbonation. The number of chlorides released because of carbonation in the OPC system was determined to be greater than the number of chlorides released as part of the ASTM water-soluble test method. This indicates that the water-soluble test may not be sufficiently conservative to estimate later-age free chlorides. However, because the samples were completely carbonated and this occurred mostly at lower admixed chloride concentrations, the water-soluble test method following ASTM C1218/C1218M can be sufficiently conservative. This indicates that water-soluble testing likely not only assesses "immediate" risks of corrosion, but also is sufficient to assess the "overall" risk of corrosion. Testing indicates that ASTM C1218/C1218M is sufficiently conservative to allow for the chlorides released due to carbonation in CAC and CSA systems; the amount of bound admixed chlorides released because of testing is significantly greater than the amount of bound admixed chlorides released because of complete carbonation.

Table 2—Values of β_A, β_B, and $CF_{ws\text{-}test}$

Cementitious system	β_A	β_B	CF_{ws}
OPC	0.86	0.85	–0.21
CAC	0.078	0.80	2.69
CSA	0.072	0.81	2.96

The findings of this research result in the following recommendations:

1. For OPC systems, there is a small risk that the amount of bound admixed chlorides released because of carbonation may exceed the amount of bound admixed chlorides released because of the ASTM water-soluble testing protocol. However, because past research has shown little correlation between the ASTM water-soluble and acid-soluble test results (Trejo et al. 2019) and the water-soluble testing accounts for chloride binding within the different systems, the authors believe the risk is relatively small and water-soluble testing following ASTM C1218/C1218M should be required in the ACI documents that specify allowable chlorides.

2. For the CAC and CSA systems assessed in this research, it is determined that ASTM C1218/C1218M is sufficiently conservative and the amount of bound admixed chlorides released as part of the ASTM test protocol significantly exceeds the amount of admixed bound chlorides released because of complete carbonation. This is an important finding as Ahmed and Trejo (2020) reported that acid-soluble testing following ASTM C1152 results in the formation of a gel-like structure in the test solution which likely binds chlorides. This binding of chlorides in the acid-soluble testing can result in an underestimation of total chlorides. In the same context, Ahmed and Vaddey (2021) reported that the concentration of acid-soluble chlorides in fully carbonated OPC, CAC, and CSA paste samples is lower than the concentration of acid-soluble chlorides in uncarbonated paste samples; this indicates some binding of acid-soluble chlorides after carbonation.

3. Three findings suggest that water-soluble testing should be the required testing for background chlorides in concrete as a result of the following: i) there is a lack of correlation between water-soluble and acid-soluble test results and binding varies significantly; ii) the challenges associated with acid-soluble testing of CAC and CSA systems; and iii) the results from this research indicate that the ASTM C1218/C1218M test procedure (water-soluble chloride testing) will in most cases be sufficiently conservative for assessing free chlorides at later ages.

Based on these findings, the authors recommend that ACI documents specify only water-soluble testing for assessing admixed chlorides. If the ASTM standard could be modified to extract slightly more of the bound admixed chlorides (for example, longer boiling time), the test standard may be sufficiently conservative for all cementitious types evaluated in this research.

AUTHOR BIOS

ACI member **Ahmed A. Ahmed** *is a Faculty Member of infrastructure materials in the Department of Civil Engineering at Mustansiriyah University, Baghdad, Iraq. He received his PhD from the School of Civil and Construction Engineering at Oregon State University, Corvallis, OR. He is a member of ACI Committees 201, Durability of Concrete; 222, Corrosion of Metals in Concrete; and 546, Repair of Concrete. His research interests include transport properties, carbonation, chloride profiling and corrosion evaluation, and durability of specialty cementitious systems.*

David Trejo, *FACI, is a Professor and Hal D. Pritchett Endowed Chair in the School of Civil and Construction Engineering at Oregon State University. He is past Chair of ACI Committee 222, Corrosion of Metals in Concrete; and a member of ACI Committees 201, Durability of Concrete, and 236, Material Science of Concrete. His research interests include the evaluation of material deterioration processes and mechanisms; service-life prediction of infrastructure systems; life-cycle modeling; and constructability, durability, and performance of infrastructure systems.*

REFERENCES

Abrams, D. A., 1924, "Calcium Chloride as an Admixture in Concrete," Structural Materials Research Laboratory, Chicago, IL, 57 pp.

ACI Committee 222, 2010, "Protection of Metals in Concrete Against Corrosion (ACI 222R-01) (Reapproved 2010)," American Concrete Institute, Farmington Hills, MI, 41 pp.

ACI Committee 222, 2019, "Guide to Protection of Reinforcing Steel in Concrete against Corrosion (ACI 222R-19)," American Concrete Institute, Farmington Hills, MI, 60 pp.

Ahmed, A. A., and Trejo, D., 2020, "Assessing Standard Tests for Admixed Chlorides in Calcium Aluminate and Calcium Sulfoaluminate Cement Systems," *ACI Materials Journal*, V. 117, No. 1, Jan., pp. 71-84. doi: 10.14359/51720290

Ahmed, A. A., and Vaddey, N. P., 2021, "Reliability of Chloride Testing Results in Cementitious Systems Containing Admixed Chlorides," *Sustainable and Resilient Infrastructure*, Apr., pp. 1-13. doi: 10.1080/23789689.2021.1917059

Ann, K. Y., and Cho, C.-G., 2014, "Corrosion Resistance of Calcium Aluminate Cement Concrete Exposed to a Chloride Environment," *Materials (Basel)*, V. 7, No. 2, pp. 887-898. doi: 10.3390/ma7020887

Ann, K. Y.; Hwang, J. P.; Kim, S. H.; and Jang, I. L., 2010a, "Effect of Calcium Aluminate Cement in Mitigating the Corrosion of Steel in Concrete," 2nd International Symposium on Service Life Design for Infrastructure, Delft, the Netherlands, pp. 699-705.

Ann, K. Y.; Kim, T. S.; Kim, J. H.; and Kim, S. H., 2010b, "The Resistance of High Alumina Cement Against Corrosion of Steel in Concrete," *Construction and Building Materials*, V. 24, No. 8, pp. 1502-1510. doi: 10.1016/j.conbuildmat.2010.01.022

Arya, C.; Buenfeld, N. R.; and Newman, J. B., 1987, "Assessment of Simple Methods of Determining the Free Chloride Ion Content of Cement Paste," *Cement and Concrete Research*, V. 17, No. 6, pp. 907-918. doi: 10.1016/0008-8846(87)90079-2

Arya, C.; Buenfeld, N. R.; and Newman, J. B., 1990, "Factors Influencing Chloride-Binding in Concrete," *Cement and Concrete Research*, V. 20, No. 2, pp. 291-300. doi: 10.1016/0008-8846(90)90083-A

ASTM C114-18, 2018, "Standard Test Methods for Chemical Analysis of Hydraulic Cement," ASTM International, West Conshohocken, PA.

ASTM C305-14, 2014, "Standard Practice for Mechanical Mixing of Hydraulic Cement Pastes and Mortars of Plastic Consistency," ASTM International, West Conshohocken, PA.

ASTM C1152/C1152M-04, 2004, "Standard Test Method for Acid-Soluble Chloride in Mortar and Concrete," ASTM International, West Conshohocken, PA.

ASTM C1218/C1218M-17, 2017, "Standard Test Method for Water-Soluble Chloride in Mortar and Concrete," ASTM International, West Conshohocken, PA.

ASTM D1193-06(2018), 2018, "Standard Specification for Reagent Water," ASTM International, West Conshohocken, PA.

ASTM E104-02, 2022, "Standard Practice for Maintaining Constant Relative Humidity by Means of Aqueous Solutions," ASTM International, West Conshohocken, PA.

Barneyback, R. S. Jr., and Diamond, S., 1981, "Expression and Analysis of Pore Fluids From Hardened Cement Pastes and Mortars," *Cement and Concrete Research*, V. 11, No. 2, pp. 279-285. doi: 10.1016/0008-8846(81)90069-7

Blenkinsop, R. D.; Currell, B. R.; Midgley, H. G.; and Parsonage, J. R., 1985, "The Carbonation of High Alumina Cement, Part I," *Cement and Concrete Research*, V. 15, No. 2, pp. 276-284. doi: 10.1016/0008-8846(85)90039-0

Canonico, F.; Buzzi, L.; and Schäffel, P., 2012, "Durability Properties of Concrete Based on Industrial Calcium Sulfoaluminate Cement," International Congress on the Durability of Concrete, Trondheim, Norway.

CPC-18, 1988, "Measurement of Hardened Concrete Carbonation Depth," *RILEM Recommendations for the Testing and Use of Constructions Materials*, RILEM, Champs-sur-Marne, France, pp. 56-58.

Dhir, R. K.; Jones, M. R.; and Ahmed, H. E. H., 1990, "Determination of Total and Soluble Chlorides in Concrete," *Cement and Concrete Research*, V. 20, No. 4, pp. 579-590. doi: 10.1016/0008-8846(90)90100-C

Fernández-Carrasco, L.; Puertas, F.; Blanco-Varela, M.; and Vázquez, T., 2001, "Carbonation of Calcium Aluminate Cement Pastes," *Materiales de Construcción*, V. 51, No. 263-264, pp. 127-136. doi: 10.3989/mc.2001.v51.i263-264.358

Florea, M. V. A., and Brouwers, H. J. H., 2012, "Chloride Binding Related to Hydration Products: Part I: Ordinary Portland Cement," *Cement and Concrete Research*, V. 42, No. 2, pp. 282-290. doi: 10.1016/j.cemconres.2011.09.016

Geng, J.; Easterbrook, D.; Liu, Q. F.; and Li, L. Y., 2016, "Effect of Carbonation on Release of Bound Chlorides in Chloride-Contaminated Concrete," *Magazine of Concrete Research*, V. 68, No. 7, pp. 353-363. doi: 10.1680/jmacr.15.00234

Goñi, S. A., and Guerrero, A., 2003, "Accelerated Carbonation of Friedel's Salt in Calcium Aluminate Cement Paste," *Cement and Concrete Research*, V. 33, No. 1, pp. 21-26. doi: 10.1016/S0008-8846(02)00910-9

Haque, M. N., and Kayyali, O. A., 1995, "Free and Water Soluble Chloride in Concrete," *Cement and Concrete Research*, V. 25, No. 3, pp. 531-542. doi: 10.1016/0008-8846(95)00042-B

Hirao, H.; Yamada, K.; Takahashi, H.; and Zibara, H., 2005, "Chloride Binding of Cement Estimated by Binding Isotherms of Hydrates," *Journal of Advanced Concrete Technology*, V. 3, No. 1, pp. 77-84. doi: 10.3151/jact.3.77

Ioannou, S.; Paine, K.; Reig, L.; and Quillin, K., 2015, "Performance Characteristics of Concrete Based on a Ternary Calcium Sulfoaluminate–Anhydrite–Fly Ash Cement," *Cement and Concrete Composites*, V. 55, pp. 196-204. doi: 10.1016/j.cemconcomp.2014.08.009

Longuet, P.; Burglen, L.; and Zelwer, A., 1973, "La Phase Liquide du Ciment Hydrate, Rev des Materiaux de Constructions et des Travaux Publics," *Ciments et Betons*, V. 676, pp. 35-41.

Mesbah, A.; Cau-dit-Coumes, C.; Renaudin, G.; Frizon, F.; and Leroux, F., 2012, "Uptake of Chloride and Carbonate Ions by Calcium Monosulfoaluminate Hydrate," *Cement and Concrete Research*, V. 42, No. 8, pp. 1157-1165. doi: 10.1016/j.cemconres.2012.05.012

Nishikawa, T.; Suzuki, K.; Ito, S.; Sato, K.; and Takebe, T., 1992, "Decomposition of Synthesized Etrringite by Carbonation," *Cement and Concrete Research*, V. 22, No. 1, pp. 6-14. doi: 10.1016/0008-8846(92)90130-N

Page, C. L., and Vennesland, Ø., 1983, "Pore Solution Composition and Chloride Binding Capacity of Silica-Fume Cement Pastes," *Materiales de Construcción*, V. 16, No. 1, pp. 19-25.

Pavlík, V., 2000, "Water Extraction of Chloride, Hydroxide and Other Ions from Hardened Cement Pastes," *Cement and Concrete Research*, V. 30, No. 6, pp. 895-906. doi: 10.1016/S0008-8846(00)00261-1

Pérez, M.; Vázquez, T.; and Trivino, F., 1983, "Study of Stabilized Phases in High Alumina Cement Mortars Part I Hydration at Elevated Temperatures Followed by Carbonation," *Cement and Concrete Research*, V. 13, No. 6, pp. 759-770. doi: 10.1016/0008-8846(83)90077-7

Plusquellec, G.; Geiker, M. R.; Lindgård, J.; Duchesne, J.; Fournier, B.; and De Weerdt, K., 2017, "Determination of the pH and the Free Alkali Metal Content in the Pore Solution of Concrete: Review and Experimental Comparison," *Cement and Concrete Research*, V. 96, pp. 13-26. doi: 10.1016/j.cemconres.2017.03.002

Robl, T. L.; Graham, U. M.; Taulbee, D. N.; and Giles, W., 1996, "The Effect of Carbonation Reactions on the Long-Term Stability of Products Made From Dry FGD Materials," Report No. CONF-960376, 211th American Chemical Society (ACS) National Meeting, New Orleans, LA.

Sanjuán, M. A., 1997, "Formation of Chloroaluminates in Calcium Aluminate Cements Cured at High Temperatures and Exposed to Chloride Solutions," *Journal of Materials Science*, V. 32, No. 23, pp. 6207-6213. doi: 10.1023/A:1018624824702

Shakouri, M.; Trejo, D.; Vaddey, N. P.; and Isgor, O. B., 2018, "Development of Empirical Models for Chloride Binding in Cementitious Systems Containing Admixed Chlorides," *Construction and Building Materials*, V. 189, Nov., pp. 157-169.

Suryavanshi, A. K., and Swamy, R. N., 1996, "Stability of Friedel's Salt in Carbonated Concrete Structural Elements," *Cement and Concrete Research*, V. 26, No. 5, pp. 729-741. doi: 10.1016/S0008-8846(96)85010-1

Trejo, D., and Ahmed, A. A., 2019, "Adopting Auto-Titration to Assess Chlorides in Concrete," *ACI Materials Journal*, V. 116, No. 3, May, pp. 43-52.

Trejo, D.; Vaddey, N. P.; and Shakouri, M., 2019, "Factors Influencing Chloride Test Results of Cementitious Systems," *ACI Materials Journal*, V. 116, No. 1, Jan., pp. 135-145. doi: 10.14359/51712240

Vasudevan, G., and Trejo, D., 2022, "Suitability of CPC-18 and Carbonation of Specialty Cementitious Systems," *ACI Materials Journal*, V. 119, No. 3, May, pp. 79-90.

Vesikari, E., 2009, "Carbonation and Chloride Penetration in Concrete With Special Objective of Service Life Modelling by the Factor Approach," VTT Technical Research Centre of Finland, Espoo, Finland.

Winnefeld, F., and Lothenbach, B., 2010, "Hydration of Calcium Sulfoaluminate Cements—Experimental Findings and Thermodynamic Modelling," *Cement and Concrete Research*, V. 40, No. 8, pp. 1239-1247. doi: 10.1016/j.cemconres.2009.08.014

Zajac, M.; Skocek, J.; Bullerjahn, F.; and Haha, M. B., 2016, "Effect of Retarders on the Early Hydration of Calcium-Sulpho-Aluminate (CSA) Type Cements," *Cement and Concrete Research*, V. 84, pp. 62-75. doi: 10.1016/j.cemconres.2016.02.014

Zhang, L., and Glasser, F. P., 2002, "Hydration of Calcium Sulfoaluminate Cement at Less Than 24 h," *Advances in Cement Research*, V. 14, No. 4, pp. 141-155. doi: 10.1680/adcr.2002.14.4.141

ACI MATERIALS JOURNAL TECHNICAL PAPER

Title No. 120-M23

Durability Aspects of Concrete Containing Nano-Titanium Dioxide

by Garima Rawat, Sumit Gandhi, and Yogesh Iyer Murthy

The current paper investigates the effects of partial cement replacement with nano-titanium dioxide (nano-TiO_2 [NT]) in varying weight proportions in concrete. In the C20/25 grade of concrete, NT was added by weight of cement with partial replacement of 0, 0.5, 1.5, 2.0, 2.5, and 3.0% using portland pozzolana cement. The physical and mechanical properties of the resulting concrete were assessed, as well as aspects of durability such as sorptivity and nondestructive tests (NDT) such as ultrasonic pulse velocity (UPV). Compared with the control mixture, the fresh concrete produced showed a drastic reduction in slump with increasing percentage of replacement, with a 54% reduction at a 3.0% replacement. Furthermore, for 1.5% NT, the compressive, flexural, and splitting tensile strengths peaked at 7, 28, 56, and 90 days, after which the values decreased. The addition of NT improved the homogeneity and integrity of the resulting concrete based on the UPV values. As the percentage of NT increased, chloride penetration decreased. From microstructural studies, it can be concluded that NT acts as a filler material and can be used as a partial replacement for cement in concrete up to 2% by weight.

Keywords: chloride penetration; durability; mechanical properties; nano-titanium dioxide (nano-TiO_2 [NT]); slump.

INTRODUCTION

The use of concrete in buildings and construction may have begun a century ago. However, as the use of concrete has increased from decade to decade, extensive and effective research has been conducted on improving concrete properties by incorporating a wide range of supplementary cementitious materials such as pozzolans and nanoparticles.[1] The addition of fine fillers has been shown to alter the initial hydration reaction, setting time, dimensional stability, and strength development of cement.[2] Owing to the growing interest in inert additives to cement, such as nano-titanium dioxide (nano-TiO_2 [NT]), a study focusing exclusively on the effects of chemically inert fillers on cement hydration is required.[3] In recent years, nanoparticles have received much attention, and their various forms have been shown to be very useful in enabling the development of stronger and more durable concrete with better mechanical properties.[4]

NT is one of the most commonly used nano-additives in cement-based materials.[3,4] Titanium dioxide is a noncombustible, odorless powder that has been widely produced and used in a variety of applications[5] because of its high chemical stability, nontoxicity, anticorrosion, electrical, and superior photocatalytic properties.[6] It exists in three stages: brookite, rutile, and anatase.[7] Although the majority of TiO_2 used to date has not been nanosized, the use of titania nanoparticles has increased significantly and is expected to surpass the use of conventional titanium dioxide in the coming years.[8] When compared to conventional TiO_2, NT has a 500% increase in the surface area.[9] It is also available in extremely pure form (99.9%).

Several researchers[5,6,10] have developed cement-based or asphalt-based concrete that incorporates TiO_2 nanoparticles to increase its durability or impart certain desirable properties. Due to its chemical stability, high catalytic activity, and low cost, the incorporation of NT into cement-based materials has garnered considerable interest.[8] However, its effects on the properties of cement-based materials are far from satisfactory.

Due to the strong binding property of cementitious materials, NT can be used in these materials without any additional processing.[8] In addition, hardened mortars/concretes have porous structures that are ideal for the adsorption of NT particles. The three most common forms of titanium dioxide are rutile, anatase, and brookite. Titanium dioxide is also referred to as self-cleaning concrete or white concrete.[11] It not only ensures the structural integrity of the structures, but also their aesthetic appearance.

According to some reports,[12,13] NT can extend the service life of cement-based materials and thus their construction, resulting in long-term economic benefits.

- Spurred by the increasing value of sustainability, there is a growing interest in TiO_2 use in construction materials to create photocatalytic coatings and materials.
- In the presence of near-ultraviolet (UV)/UV radiation ($h\upsilon$), oxygen, and water, a chain of photochemical surface reactions occur, which lead to strong oxidizing capability and which can oxidize NO_x ($NO + NO_2$), organic (volatile organic compounds [VOCs]), and inorganic compounds.
- The addition of NT provides a reduction in porosity, leading to pore structure refinement (smaller pores) while reducing clinker content.
- Strength is maintained while reducing clinker fraction; nanoparticles densify the paste structure.

Cementitious materials mixed with NT have the functions of air purification,[11] self-cleaning,[8] and disinfection,[14] which are the reasons for their wide application in the exterior

ACI Materials Journal, V. 120, No. 2, March 2023.
MS No. M-2022-067.R3, doi: 10.14359/51738490, received October 6, 2022, and reviewed under Institute publication policies.

Table 1—Physical properties of OPC (Grade 53)

Fineness, %	Le Chatelier soundness, in. (mm)	Specific gravity	Consistency, seconds (minutes)	Setting time, seconds (minutes)		Compressive strength, psi (MPa)		
				Initial setting time	Final setting time	3 days	7 days	28 days
2.0	0.29 (7.5)	3.14	1800 (30)	6000 (100)	14,400 (240)	4206.09 (29)	5511.43 (38)	8412.18 (58)

surface of buildings including hospitals, restaurants, and airports.

There are few cases of nanoparticles being incorporated into cement-based concrete. Lee[15] examined the characteristics of cement mortars containing nanoparticles to determine their super-mechanical and smart (temperature and strain-sensing) potentials. So far, however, research[7,16] has mostly focused on establishing good mechanical performance with cement replacement materials at the microlevel.

Furthermore, despite being chemically inert in terms of its potential to directly react during cement hydration,[12,13,17-19] NT can generally improve the mechanical performance and durability, as well as decrease the rigidity of cementitious materials.[4,20-23] Moreover, the flexural fatigue performance and abrasion resistance of concretes were reported to be remarkably improved with the use of TiO_2 nanoparticles.[24] The gain in strength in this case might be related to the microstructural modification and the hydration acceleration effects of NT by providing additional surface area for product nucleation (that is, the boundary nucleation effect).[19,24-27] The addition of TiO_2 nanoparticles leads to greater homogeneity, better compaction, and reduction in the pore volume and the pore size of cementitious materials, which results in a remarkable reduction in permeability.[3,8,16,28,29] Titania nanoparticles have been also found to behave as an activator to accelerate the pozzolanic reaction, increase the rate of cement hydration, increase the intensity of the heat peak, and reduce the initial and final setting times and freezing-and-thawing damage. The mechanical properties were also enhanced with the use of NT. The addition of NT to cement-based materials can help them overcome some of their shortcomings, such as low tensile strength and resistance to harmful chemical penetration.

The effect of using NT in cementitious composites on their fresh properties, mechanical properties, and durability is demonstrated in this section.[30] In addition, the microstructural properties of nano-titania-incorporated mortar and concrete are investigated using scanning electron microscopy (SEM) images. Because the final performance of cementitious composites is directly related to their strength and permeability,[31] this section will concentrate on the effect of NT on the mechanical properties and permeability of cement mortar and concrete.

RESEARCH SIGNIFICANCE

The effects of NT on the strength, durability, and microstructure of ordinary portland cement (OPC) are investigated in this paper. The compressive, splitting tensile, and flexural strengths were used to determine the mechanical properties. Water absorption, capillary absorption, and chloride penetration tests were used to determine the transport properties. The pore structure and microstructure of the concrete were examined using SEM. The sorptivity, chloride penetration, and ultrasonic pulse velocity (UPV) characteristics of endurance materials were investigated. The authors believe that this study will demonstrate that it is possible to obtain good-quality concrete at a slight cost increase by using novel materials.

Table 2—Chemical properties of OPC (Grade 53), %

Loss on ignition	CaO	SiO_2	Al_2O_3	Fe_2O_3	MgO	K_2O	Na_2O
2.75	66.52	18.33	4.37	4.70	0.73	0.75	0.12

Because NT improves the overall performance of cement-based materials, as well as their durability and sustainability, it reduces construction maintenance and repair costs. Furthermore, NT endows cement-based materials with new properties such as self-cleaning properties, resulting in lower routine cleaning and maintenance costs.[20] According to some reports,[24,32,33] NT can extend the service life of cement-based materials and, as a result, constructions, resulting in long-term economic benefits.

EXPERIMENTAL PROCEDURE

Materials

The following materials were used in the experimental procedure. The materials, along with their physical and chemical properties, are given in the following tables.

Cement—OPC Grade 53 conforming to IS 12269:2013[34] was used in this work. The physical properties of the cement used in the construction of slabs are presented in Table 1.

The chemical properties following IS 12269:2013[34] were also evaluated and are presented in Table 2.

Aggregates—Basalt with a particle size of less than 20 mm that satisfied IS 2386-1963[25] was used. These were cleaned and dried in the open air for 24 hours after being thoroughly washed with tap water. Silt, dust, and unsound particles were removed from the concrete. The properties of the aggregates used are presented in Table 3.[12]

In this study, river sand that met the requirements of IS 383:2016[35] was employed for the particle-size distribution.

Water—All the concrete mixtures were mixed and cured with municipally supplied portable tap water that was free of organic contaminants, as proven by IS 456:2000[36] and IS 10500:2012.[37] Table 4 shows the qualities of the tap water.

TiO_2 nanoparticles—A company in India supplied the NT powder directly. The properties of the TiO_2 nanoparticles are provided in Table 5.

Mixture proportions and preparation of specimens

According to IS 10262:2019,[38] the nomenclature and proportions of the concrete mixtures are presented in Table 6.

The concrete was mixed using a pan mixer with a capacity of 26.41 gal. (100 L). The surface of all of the particles used in the concrete mixture was saturated and dry. All of the combinations were created by substituting cement in the following weight percentages: 0, 0.5, 1, 1.5, 2.0, 2.5, and 3.0%.

The dispersing agent sodium tripolyphosphate (STPP) for dispersing the nanoparticles, which works as a high-range water-reducing admixture (HRWRA) as well, was mixed with half the amount of water. The workability, strength, and durability of numerous concrete combinations were tested using cube, beam, and cylinder specimens. For curing, the test specimens were immersed in water at 80.6 ± 3.6°F (27 ± 2°C) until they achieved the testing age. Table 7 summarizes all of the experiments, including the specimen age, specimen size, testing apparatus, and the standard code used throughout testing.

Testing methods

Compressive strength—Cubes sized 5.91 in. (150 mm) were made and evaluated at 7, 28, and 56 days after curing for the five different replacements under IS 516-1959.[26] A steady force of 458.87 kp/s (4.5 kN/s) was applied during compression testing until the cube disintegrated and no higher load could be sustained. After 28 days, SEM and energy-dispersive spectroscopy (EDS) investigations were conducted on the broken samples from each replacement.

Splitting tensile test—Splitting tensile tests were conducted following IS 5816:1999,[40] which required the preparation of 5.91 in. (150 mm) diameter and 11.81 in.

Table 3—Properties of coarse aggregate and fine aggregate conforming to IS 2386-1963 (Revision 2016)[25]

Coarse aggregate			Fine aggregate		
S.No.	Property	Values	S.No.	Property	Values
1	Aggregate crushing value, %	19.62	1	Bulk density, kg/m^3	1582
2	Aggregate impact value, %	10.88	2	Fineness modulus	2.58
3	Los Angeles abrasion value, %	12.58	3	Water absorption, %	0.57
4	Bulk density, kg/m^3	1643	4	Specific gravity	2.63
5	Fineness modulus	6.35			
6	Water absorption, %	0.49			
7	Flakiness index, %	6.8			
8	Elongation index, %	11.8			
9	Specific gravity	2.68			

Table 4—Tap water characteristics

S.No.	Parameter	Value
1	Chloride	0.0014 lb/gal. (168 mg/L)
2	pH	7.6
3	Fluoride	0.000003 lb/gal. (0.4 mg/L)
4	Dissolved oxygen	0.00008 lb/gal. (10.15 mg/L)
5	Chemical oxygen demand	0
6	Biological oxygen demand	0
7	Free residual chlorine	8.34×10^{-7} lb/gal. (0.1 mg/L)

Table 5—Properties of TiO_2 nanoparticles

S.No	Properties	Observed values
1	Type	TiO_2 (rutile)
2	Diameter, in. (nm)	3.93×10^{-7} to 7.87×10^{-7} (10 to 20)
3	Surface volume ratio, m^2/g	163
4	Density, lb/in.^{3} (g/cm^3)	0.135 (3.74)
5	Purity, %	>99.9%

Table 6—Nomenclature and mixture proportions of NT-added concrete

		Mixture proportions, lb/yd^3 (kg/m^3)				
Concrete mixture nomenclature	Cement replacement, %	Cement	Fine aggregate	Coarse aggregate	NT	Water
NT0	0	648.93 (385)	1172.42 (695.57)	1913.82 (1135.43)	0	323.62 (192)
NT0.5	0.5	645.68 (383.07)	1172.42 (695.57)	1913.82 (1135.43)	3.23 (1.92)	323.62 (192)
NT1	1	642.44 (381.15)	1172.42 (695.57)	1913.82 (1135.43)	6.48 (3.85)	323.62 (192)
NT1.5	1.5	639.21 (379.23)	1172.42 (695.57)	1913.82 (1135.43)	9.72 (5.77)	323.62 (192)
NT2	2	635.95 (377.30)	1172.42 (695.57)	1913.82 (1135.43)	12.97 (7.70)	323.62 (192)
NT2.5	2.5	632.70 (375.37)	1172.42 (695.57)	1913.82 (1135.43)	16.21 (9.62)	323.62 (192)
NT3	3	629.47 (373.45)	1172.42 (695.57)	1913.82 (1135.43)	19.46 (11.55)	323.62 (192)

Table 7—Details of experiments carried out

Test	Age of concrete, days	Specimen size, in. (mm)	Apparatus/instrument	Reference
Slump	Fresh concrete	—	Standard slump cone	IS 1199-1959[39]
Compressive strength	7, 28, 56, and 90	5.9 x 5.9 x 5.9 (150 x 150 x 150) (cube)	Compression testing machine/universal testing machine	IS 516-1959[26]
Splitting tensile strength	7, 28, 56, and 90	3.93 diameter and 7.87 height (100 diameter and 200 height) (cylinder)	Compression testing machine/universal testing machine	IS 5816:1999[40]
Flexural strength	7, 28, 56, and 90	3.93 x 3.93 x 19.68 (100 x 100 x 500) (beam)	Flexure testing machine	IS 516-1959[26]
Sorptivity	90	5.9 x 5.9 x 5.9 (150 x 150 x 150) (cube)	Weighing machine	—
Water absorption	28	5.9 diameter x 11.81 height (150 diameter x 300 height) (cylinder)	Extensometers	IS 516-1959[26]
Scanning electron microscopy	28	Samples of SEM	Scanning electron microscope	—

(300 mm) height cylinders and their testing at 7, 28, and 56 days. The specimens were tested using universal testing equipment capable of withstanding a force of 203,943.2426 kip (2000 kN). Without using a shock, a steady load was introduced and gradually increased over time at a rate of 1.2 to 2.4 N/(mm^2/min).

Flexural strength—According to Nazari,[7] the specimens containing NT were tested for 28 days under four-point loads using flexural testing equipment. The experiment was conducted using a constant loading system with a shear span of 11.81 in. (300 mm) and a depth ratio of 3.0 for the shear span. Following production, the examples were positioned on the supporting bearing blocks with one side in proportion to the other. At a quarter distance from the ends of the supports, the upper surface of the test specimen was brought into contact with the load-applying block.[41] The load-bearing block is brought into complete contact with the beam surface as a result of this technique. The beam was tested for uniform contact between the bearing and load-bearing blocks. The specimen was loaded repeatedly until it failed and the dial ceased to spin.[41] The maximum applied load was indicated and recorded by the testing equipment. The following equation is used to determine the flexural strength

$$R = \frac{3FL}{4bd^2}$$

where R is the flexural strength in N/mm^2; F is the applied load at failure; L is the beam span measured in mm; b is the beam breadth measured in mm; and d is the beam depth measured in mm.

Sorptivity—Three 30 mm slices were cut from three concrete cubes measuring 3.93 x 3.93 x 2.75 in. (100 x 100 x 70 mm) to conduct the sorptivity test.[12] These cubes have a life span of 90 days. The specimens were dried in an oven at a temperature of 131°F (55°C) for 3 days before being chilled in desiccators. Water absorption from the sides was blocked by coating the sidewalls with epoxy resin, allowing absorption only from the bottom. The specimens were immersed in tap water in pans with a water level of 0.19 in. (5 mm) above the pan's bottom. The experimental

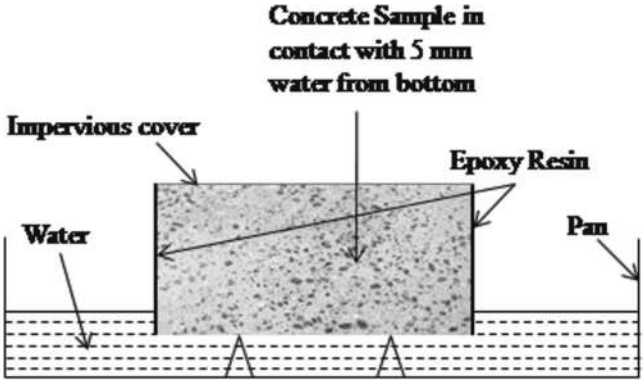

Fig. 1—Experimental setup for sorptivity measurements.

setup is depicted schematically in Fig. 1. After draining extra water with an absorbent cloth, the mass of these specimens was accurately determined at regular intervals. The slope of a line fitted to the plot of the cumulative absorbed volume of water per unit area of inflow surface versus the square root of time was obtained using data on the absorbed volume of water.[42] The sorptivity coefficient is calculated using the following formula

$$f_{sc} = i/\sqrt{t}$$

where f_{sc} is the sorptivity coefficient in mm/√min; i is the cumulative absorbed volume of water per unit area of inflow surface in mm; and t is the elapsed time in minutes. For each test, the readings up to 960 seconds (16 minutes) were ignored to find the slope of the best-fit curve.

Characterization using SEM and EDS

The microstructure and morphology of NT concrete were investigated using EDS and SEM.[3,12] After 28 days, the sample strength was determined and minute fragments of the core were removed. Before SEM analysis, the samples were placed in a desiccator and dried at 1472°F (800°C) overnight to remove moisture. Broken fragments from tested concrete specimens were mounted on brass stabs with carbon ribbons, gold-coated, and viewed under a scanning electron microscope for their microstructure.[27] The samples were analyzed

using a 78.74 in. (2 μm) diameter probe, a 15 kV accelerating voltage, and a 50 mA probe current. The SEM results are projected to be accurate to within a margin of error of ±2%. Figure 2 shows the microstructure of the NT concrete.

RESULTS AND DISCUSSION

In this experimental program, the durability properties of the mixtures were measured by slump flow *D* (mm). Figure 3 presents the results of the tests performed on fresh concrete.

Slump flow

The fresh properties of all replacements are depicted in Fig. 3 (with and without NT). All of the concrete mixtures included the same quantity of water.[27] When NT was added to the concrete, it resulted in a new material that was hard but cohesive and sticky. As a result, the specimen workability decreased in direct proportion to the amount of cement replaced with NT. NT2, roughly 1.42 in. (36 mm), had the lowest slump value. NT has a limited lubricating effect and thus low workability due to its fast water absorption rate and low water content.[43] As a result of the mixing technique, the porous NT particles absorbed more water internally than the natural fine aggregate in the mixture. The rough texture and uneven shape of the material enhance interlocking and hardness, hence minimizing the ball-bearing effect.[44] As a result of all of these factors, concrete containing NT has a lower slump and a higher water requirement. When the slump test results were compared to those from earlier research,[45,46] it was determined that there was a high degree of agreement that increasing NT decreased slump value.[3,5,10]

Although the addition of TiO_2 nanoparticles in various volume fractions reduced flowability characteristics, the nanoparticles increased the consistency of the concrete mixtures.[47] In the mixtures containing TiO_2 nanoparticles, there was less bleeding and segregation.

Mechanical properties

Figures 4 to 6 show the compressive, splitting tensile, and flexural strength of each combination as an average of three specimens at 7, 28, 56, and 90 days. At 7 days of age, NT0's compressive strength was tested to be 3237.24 psi (22.32 MPa). When NT0.5, NT1, and NT1.5 were compared to the control mixture (that is, NT0), the compressive strength increased nominally by 2.15%, 5.15%, and 18.67%, respectively. The percentage increase in strength of NT2 and NT2.5 was determined to be 6.67% and 3.34%, respectively. The maximum gain in compressive strength was found at a replacement level of 1.5%.

As shown in Fig. 5, splitting tensile strength was tested with NT substitution in various percentages. The splitting tensile strength of the NT1, NT1.5, and NT2 concrete mixtures increased on all days when compared to the control mixture. On the 28th day, the splitting tensile strength improved significantly when compared to the seventh day. When 1.5% of the cement in concrete was substituted with NT, the splitting tensile strength rose.

The effect of nominal pozzolanic activity of NT and the filler effect could be some of the probable explanations for the improvement in strength up to 1.5% of NT. The type of cement paste produced and the interfacial transition zone (ITZ), both of which affect tensile strength, are also influenced by NT properties. At 7 days, the splitting tensile strength of NT0 was 2.2 MPa, whereas the splitting tensile strength of the other mixtures NT0.5, NT1.0, NT1.5, NT2, NT2.5, and NT3 were 333.58 psi (2.3 MPa), 362.59 (2.5 MPa),

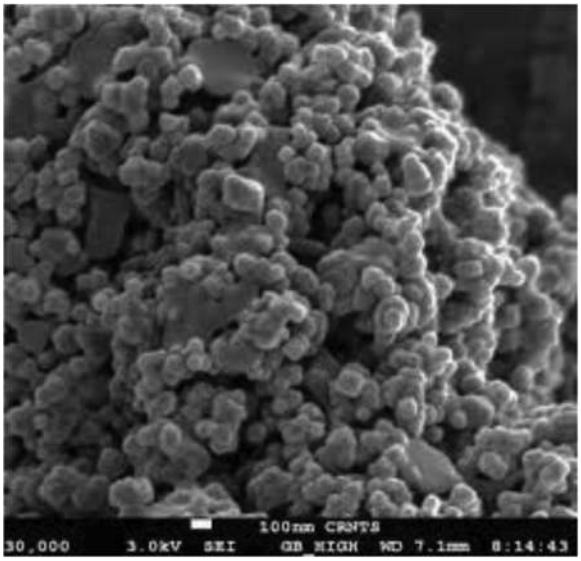

Fig. 2—Microstructure of NT.

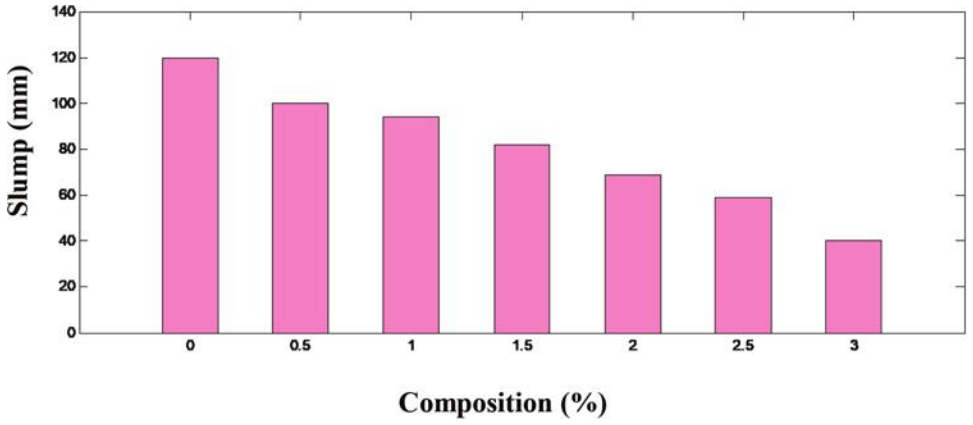

Fig. 3—Slump values of concrete with varying NT percentage.

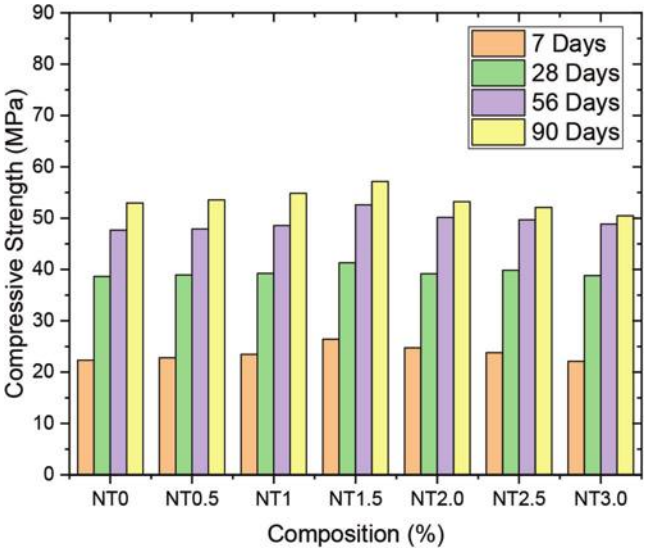

Fig. 4—Compressive strength of concrete containing NT.

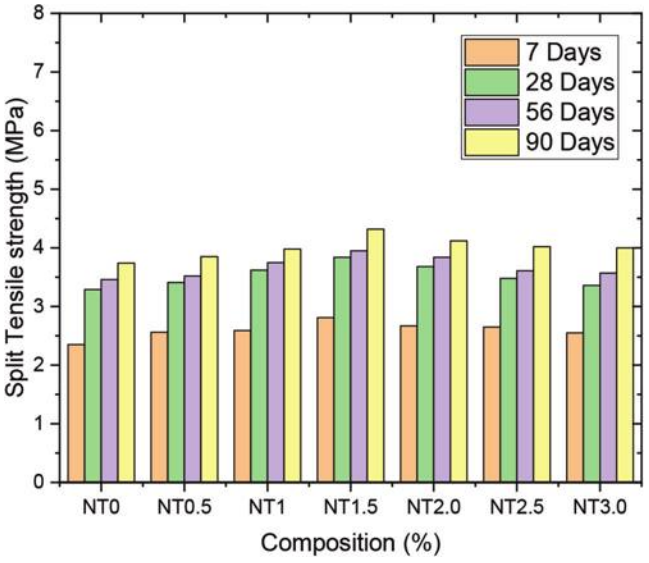

Fig. 5—Splitting tensile strength concrete containing NT.

406.10 psi (2.8 MPa), 390.15 psi (2.69 MPa), 384.35 psi (2.65 MPa), and 359.69 psi (2.48 MPa), respectively.

The beam flexural strength after 7, 28, 56, and 90 days is shown in Fig. 6. The strength parameters are comparable to those of splitting tensile strength, with low strength at 7 days and a significant increase at 28 days.

At 56 and 90 days, a minor increase in strength is also observed while the hydration process continues. At 1.5% replacement, flexural strength, like compressive and splitting tensile strength, reaches a maximum value.

Sorptivity

All samples were tested for capillary suction after curing for 28 days using a sorptivity test. Sorptivity is the slope of the straight line that displays the relationship between absorption and the square root of time.[7,29] In Table 8, the absorption as a function of time and the square root of the absorption coefficient are presented for the NT concrete mixtures.[21] The concrete mixtures with NT3.0 have the lowest sorptivity, followed by NT2.5, NT2, NT1.5, NT1, NT0.5, and NT0. Pore characteristics can be related to differences in sorptivity levels.

Table 8—Sorptivity and water absorption of concrete containing NT

NT, %	Sorptivity, mm/sec$^{0.5}$	Water absorption, %	Apparent porosity, %
NT	0.0477	4.96	25.45
NT0.5	0.0409	4.89	23.62
NT1.0	0.0359	4.74	21.65
NT1.5	0.0369	4.64	19.27
NT2.0	0.0327	4.59	16.31
NT2.5	0.0231	4.45	14.08
NT3.0	0.0102	4.36	10.63

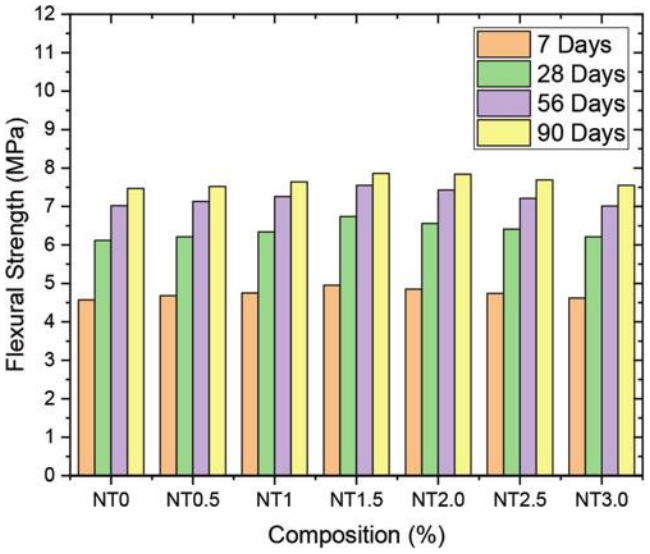

Fig. 6—Flexural strength of concrete containing NT.

The smaller particle size of NT results in the low sorptivity, and increasing the production of calcium-silicate-hydrate (C-S-H) gel shrinks the pores, hence decreasing the sorptivity.[4] Due to the presence of NT in the C-S-H gel, samples containing a higher concentration of NT demonstrated lower sorptivity.[48,49] As a result, the pores become less connected, resulting in decreased absorption.[38] These findings are consistent with those reported in previous research on water absorption (Table 8).

Water absorption

Water absorption was determined using soaking tests, and the findings are reported in Table 8. Water absorption increased throughout 24 hours. Water absorption reduced as the fraction of NT increased, owing to the increase in smaller particles.[25] This is in addition to the results obtained for sorptivity and apparent porosity. Sorptivity and apparent porosity diminish when the NT content increases.

Apparent porosity

Three cubes from each series were oven-dried for 24 hours at 185°F (85°C) to determine the water absorption capacity of mortar specimens, and their weight served as the starting

weight. After 24 hours of immersion in water, the saturated surface-dry weight of the samples was determined to be the final weight. The weight loss of specimens that have absorbed water is expressed as a percentage.[46] The specimens were dried at 185°F (85°C) because higher temperatures could disturb the microstructure of mortar specimens, resulting in erroneous water absorption measurements.[50,51] The third set of three samples was used to determine the apparent porosity.

The following equation was used to find the apparent porosity

$$\text{Apparent porosity} = [(M_w - M_d)/(M_w - NT)] \times 100\%$$

where M_w is the weight of the specimen after immersion in water for 48 hours; M_d is the weight of the specimen after oven drying at 185°F (85°C) for 24 hours; and NT is the weight of the specimen suspended in water.

UPV and dynamic modulus of elasticity

The UPV test is a nondestructive technique for measuring the dynamic modulus of elasticity of concrete specimens as well as their quality and homogeneity.[52] Additionally, this test can be used to discover concrete fractures, defects, and pores. In the current investigation, concrete cube samples cast for compressive strength were subjected to a UPV test before being evaluated for compression on the 28th day. After coating the test surface with petroleum jelly to ensure good acoustic coupling, the pulse velocity was applied through the direct transmission method.[53] The variability of the results for each specimen was reduced by dividing the cube surface into three 3 x 3 grids, as the test is dependent on a variety of variables, including aggregate density and modulus; physical and mechanical properties of cement; the presence of voids; moisture; temperature; and the mixture, shape, and size of concrete.[15] UPV measurements were obtained and averaged at each junction location. The wave velocity was calculated using Erdogan's proposed equation[31]

$$V = (h/t) \times 10^6$$

where V is the ultrasonic wave speed (m/s); h is the distance between the surface of the concrete specimen from which the ultrasonic wave is sent and the surface where the wave is received (m); and t is the time passed from the concrete surface from which the ultrasonic wave is sent and the surface wave is received (μs).

The UPV of concrete containing varying concentrations of NT after 28 days is illustrated in Table 9. In general, when the NT content increases, the UPV values fall. However, all concrete containing NT falls within the category of good concrete, as defined by IS 13311-2:1992,[53] with UPV values of more than 5000 m/s. Additionally, all concrete can be regarded as being of high-quality NT of uniformity and integrity.[54] As a result, it can be inferred that the addition of NT to concrete improves its UPV testing quality. The decrease in voids and microcracks observed as the NT concentration increased could be attributed to NT filler action, which lowers voids and microcracks.[43]

Table 9—UPV at 28 days

S. No.	Mixture	UPV, m/s
1	NT0	6173.44
2	NT0.5	6126.42
3	NT1.0	6052.05
4	NT1.5	5918.63
5	NT2.0	5812.55
6	NT2.5	5699.91
7	NT3.0	5602.58

Işıkdağ and Topçu[55] provided formulas for calculating the dynamic modulus of elasticity (E_d). The formula is as follows

$$E_d = V^2\gamma(1 + \mu)(1 - 2\mu) \times 10^{-6}/(1 - \mu)$$

where μ is the dynamic Poisson's ratio for concrete and is taken as 0.23; and γ is the unit weight (kg/m^3).

Figure 7 shows the dynamic modulus of elasticity in GPa versus the percentage of NT.

Chloride penetration

Cubic specimens 150 x 150 x 150 mm were immersed in a 3% NaCl solution for 90 days after a 90-day curing period. Then specimens were oven-dried for 24 hours. After that, to prepare some pulverized concrete samples (powder samples) for the test, all six faces of the cubic specimens were drilled to depths of 0 to 0.19 in. (0 to 5 mm), 0.19 to 0.39 in. (5 to 10 mm), 0.39 to 0.59 in. (10 to 15 mm), 0.59 to 0.78 in. (15 to 20 mm), and 0.78 to 1.81 in. (20 to 30 mm). The concrete powder samples obtained from all six faces for each depth were blended, and the samples were ready for the next step of the test (ASTM C1218/C1218M-15).[56]

The total chloride content of pulverized concrete is determined using a potentiometric titration of chloride with silver nitrate (ASTM C114)[57] in this test procedure. The produced crushed concrete sample is dissolved in nitric acid, and if the solution is acidic, a small amount of $NaHCO_3$ is added until the pH value reaches 6 or 7. The K_2CrO_4 indicator is then added, resulting in a light yellow color change in the solution. Eventually, 0.05 N $AgNO_3$ is added until the solution turns orange-yellow (weak brown) in color, and the volume of the $AgNO_3$ solution is measured. To determine the Cl ion percentage, the volume of the $AgNO_3$ solution is substituted in the following equation

$$Cl^- (\%) = \frac{3.5453(V \cdot N)}{W}$$

where W is the weight of pulverized (powder) concrete prepared from the sample; N is the normality of $AgNO_3$ solution; and V is the volume of $AgNO_3$ solution.

In this study, the chloride penetration was calculated as a fraction of the weight of the concrete sample.[58] The chloride percentages at various depths of the concrete samples are shown in Fig. 8.

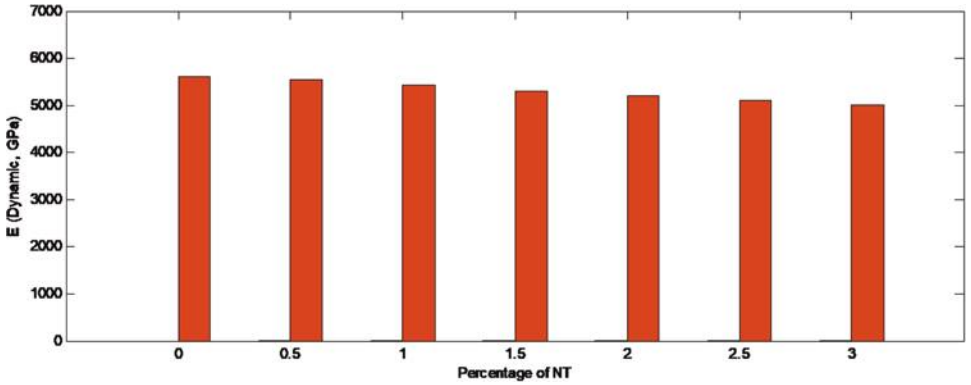

Fig. 7—Dynamic modulus of elasticity (GPa) versus percentage of NT.

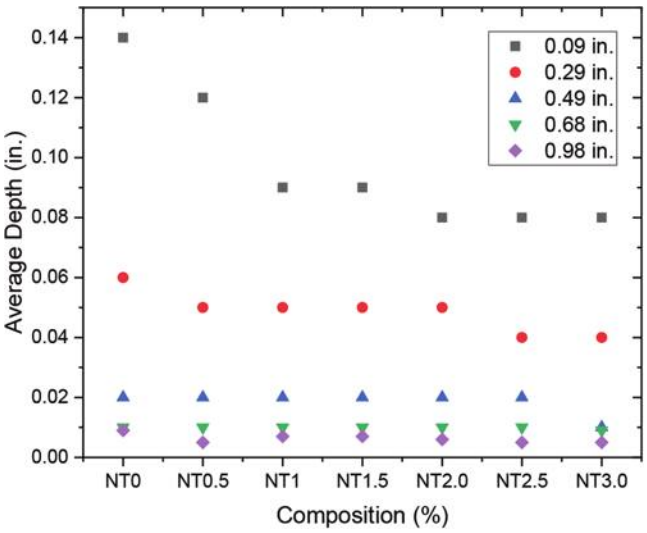

Fig. 8—Chloride penetration depth versus percentage of NT.

The results show a general decrease in chloride percentage by the depth of the concrete sample, indicating that the concrete components, particularly aggregates, are free of chloride ions.

According to the results obtained, increasing the TiO_2 nanoparticles to a concentration of 3 wt. % results in a decrease in chloride penetration. The findings of this study corroborate those of other researchers.[58,59] For instance, Detwiler et al.[1] investigated the efficacy of using supplementary cementitious materials to improve the chloride resistance of accelerated cured concrete and discovered that concretes containing supplementary cementitious materials outperformed portland cement concrete. Additionally, the use of supplementary cementitious materials can help prevent detrimental expansions caused by both delayed ettringite formation and the alkali-silica reaction.[60]

Regarding the beneficial effect of TiO_2 nanoparticles as supplementary cementitious materials on chloride penetration through concrete, this could be because the nanoparticles located in the cement paste as the kernel can further promote cement hydration due to their high activity, resulting in a more homogeneous and compact cement paste.[58] As a result, the pore structure of concrete is significantly improved. When the nanoparticle content is increased above 3% by weight, the improvement in the pore structure of concrete is weakened.[60] This is because the distance between nanoparticles decreases as the nanoparticle content increases, and the $Ca(OH)_2$ crystal quantity decreases as a result.[61] This results in a low ratio of crystal to strengthening gel, increased shrinkage and creep of the cement matrix, and a looser pore structure of the cement matrix, which could result in increased chloride penetration.[51]

Figure 8 shows the percentage of chloride penetration at different average depths of the concrete samples.

MICROSTRUCTURE

The SEM images at 50 μm magnification for all the samples are presented in Fig. 9. While the matrix of the control mixture and 1% NT showed relatively larger (approximately 10 μm) pores unevenly distributed, the 2% NT showed smaller-sized pores (approximately 2 to 3 μm) more uniformly distributed, and 3% NT showed relatively lesser pores. The 2% NT and 3% NT also exhibited the formation of more C-S-H gel. Thus, it is inferred that the higher the percentage of NT, the lesser the pores.

SEM aids in the characterization of concrete's microstructure and the identification of the components that affect its mechanical properties and durability.[62] The concrete microstructure is made up of C-S-H gel, calcium hydroxide, calcium sulfoaluminate hydrate (ettringite and monosulfate), coarse and fine aggregate, and an ITZ between the aggregate and cement hydration products. In EDS spot analysis results, calcium, silica, and alumina content in NT were discovered in percentages of 35.24, 29.3, and 12.87, respectively. Figures 9(a) and (b) show the microstructure of NT0 and NT1.0 concrete.

The microstructure of the specimens changed after 28 days of curing in all of the replacements. The main hydration product, C-S-H gel, which was responsible for improved mechanical properties, is present in significant quantity. Hence, a sharp rise in the value of strength parameters was observed at 28 days. A pozzolanic reaction and the production of a C-S-H gel were observed after 28 days of curing. Figure 9 shows the microstructure of NAC, NT1.0, NT2, and NT3 at 50 μm magnification. Figure 9(a) shows the microstructure of the control mixture. Micropores up to 5 μm are seen scattered along with the matrix. NT1.0 (Fig. 9(b)) and NT2 (Fig. 9(c)) show a progressively improving microstructure with smaller voids and less in number. The ITZ is intact, as seen in NT2 (Fig. 9(c)). In the case of NT3 (Fig. 9(d)), EDS spot analysis revealed a

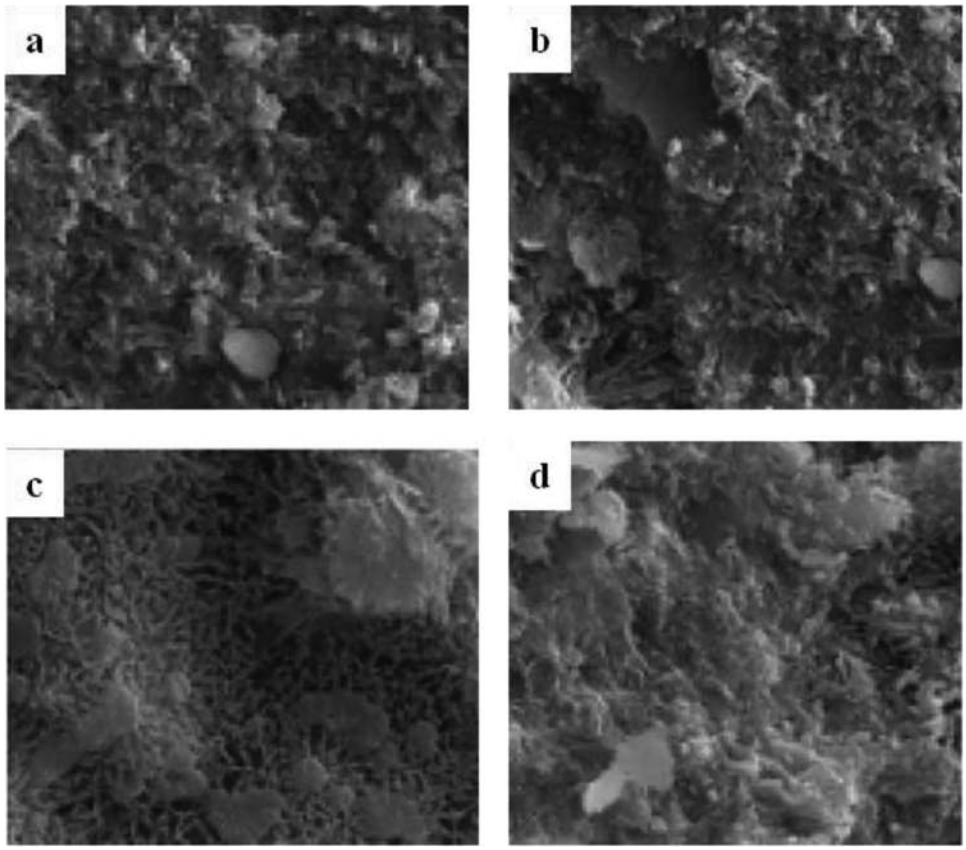

Fig. 9—Microstructure of mortar containing: (a) control mixture; (b) 1% NT; (c) 2% NT; and (d) 3% NT.

dense microstructure and minimal voids. This is consistent with the findings of compressive strength and further establishes the two-wall effect. The aggregates of NT3 are well covered with the matrix and exhibit an excellent bond with the matrix. Microcracks and micropores are nearly absent in this sample.[1] The presence of NT thus reduces the voids in the concrete.

CONCLUSIONS

Experimental investigations to study the effect of partial replacement of cement with nano-titanium dioxide (nano-TiO_2 [NT]) are attempted in this research work. The physical and chemical properties of NT and its viability to be used as a replacement for cement are studied. The results obtained in this study can be summarized as follows:

- Increases in the fraction of nanoparticles often enhanced the durability of the resulting concrete, which might be attributed to finer particles in the cement mixture and the nanoparticles' filler effect.
- TiO_2 nanoparticles as a partial replacement for cement up to 1.5% could accelerate the formation of calcium-silicate-hydrate (C-S-H) gels due to increased crystalline $Ca(OH)_2$ concentration at an early stage of hydration, thereby increasing the flexural and splitting tensile strengths of concrete specimens even at early stages of hydration. The presence of more than 1.5% of TiO_2 nanoparticles results in decreased flexural and splitting tensile strengths because of the decreased crystalline $Ca(OH)_2$ content necessary for C-S-H gel formation.
- Both water absorption and apparent porosity were significantly reduced with the addition of TiO_2 nanoparticles, as the nanoparticles act as nanofillers and improve the concrete resistance to water permeability.
- Ultrasnoic pulse velocity (UPV) tests revealed that when TiO_2 nanoparticles are added, the number of pores in the concrete decreases, indicating that the density of the concrete is raised and the pore structure is improved.
- Chloride penetration decreased with the inclusion of nanoparticles, which could be due to the more packed microstructure created by the nanoparticles and the increased volume of the paste.

AUTHOR BIOS

Garima Rawat *is a PhD Scholar at Jaypee University of Engineering and Technology, Guna, Madhya Pradesh, India, where she received her BTech and MTech in civil engineering in 2015 and 2017, respectively. Her research interests include the cathodic protection of marine structures, strength and durability properties of structures, and chloride diffusivity in concrete structures.*

Sumit Gandhi *is an Associate Professor and Head. He received his BTech in civil engineering from Kavayitri Bahinabai Chaudhari North Maharashtra University, Jalgaon, Maharashtra, India, in 2001; his MTech in water resource engineering from Motilal Nehru National Institute of Technology Allahabad, Prayagraj, Uttar Pradesh, India, in 2004; and his PhD from Motilal Nehru National Institute of Technology Allahabad in 2009. His area of work during his PhD was flow behavior in prismatic and nonprismatic open channels. He has extensive teaching and research experience in the field of civil engineering.*

Yogesh Iyer Murthy *received his BE in civil engineering from Dayananda Sagar College of Engineering, Bengaluru, Karnataka, India, in 2002, with honors; his ME in structural engineering from Shri Govindram Seksaria Institute of Technology and Science, Indore, Madhya Pradesh, India, in 2010; and his PhD from Jaypee University of Engineering and Technology*

in 2021. His ME thesis was on the transient dynamics of laminated fiber-reinforced composite plates using quadrilateral flat-facet shell elements, and the focus of his PhD work was on corrosion mitigation of structures using magnesium alloys as sacrificial anodes.

REFERENCES

1. Detwiler, R. J.; Fapohunda, C. A.; and Natale, J., "Use of Supplementary Cementing Materials to Increase the Resistance to Chloride Ion Penetration of Concretes Cured at Elevated Temperatures," *ACI Materials Journal*, V. 91, No. 1, Jan-Feb. 1994, pp. 63-66.

2. Luna, F. J.; Fernández, Á.; and Alonso, M. C., "The Influence of Curing and Aging on Chloride Transport through Ternary Blended Cement Concrete," *Materiales de Construcción*, V. 68, No. 332, Oct.-Dec. 2018, Article No. e171. doi: 10.3989/mc.2018.11917

3. Saloma; Nasution, A.; Imran, I.; and Abdullah, M., "Improvement of Concrete Durability by Nanomaterials," *Procedia Engineering*, V. 125, 2015, pp. 608-612. doi: 10.1016/j.proeng.2015.11.078

4. Jayapalan, A. R.; Lee, B. Y.; and Kurtis, K. E., "Effect of Nano-sized Titanium Dioxide on Early Age Hydration of Portland Cement," *Nanotechnology in Construction: Proceedings of the NICOM3*, Z. Bittnar, P. J. M. Bartos, J. Němeček, V. Šmilauer, and J. Zeman, eds., Springer-Verlag, Berlin, Germany, 2009, pp. 267-273. doi: 10.1007/978-3-642-00980-8_35

5. Du, S.; Wu, J.; AlShareedah, O.; and Shi, X., "Nanotechnology in Cement-Based Materials: A Review of Durability, Modeling, and Advanced Characterization," *Nanomaterials (Basel)*, V. 9, No. 9, Sept. 2019, Article No. 1213. doi: 10.3390/nano9091213

6. Khataee, R.; Heydari, V.; Moradkhannejhad, L.; Safarpour, M.; and Joo, S. W., "Self-Cleaning and Mechanical Properties of Modified White Cement with Nanostructured TiO_2," *Journal of Nanoscience and Nanotechnology*, V. 13, No. 7, July 2013, pp. 5109-5114. doi: 10.1166/jnn.2013.7586

7. Nazari, A., "The Effects of Curing Medium on Flexural Strength and Water Permeability of Concrete Incorporating TiO_2 Nanoparticles," *Materials and Structures*, V. 54, No. 4, 2021, Article No. 174.

8. Nazari, A., and Riahi, S., "TiO_2 Nanoparticles' Effects on Properties of Concrete Using Ground Granulated Blast Furnace Slag as Binder," *Science China Technological Sciences*, V. 64, No. 9, Sept. 2021, p. 2066.

9. Wang, L.; Zhang, H.; and Gao, Y., "Effect of TiO_2 Nanoparticles on Physical and Mechanical Properties of Cement at Low Temperatures," *Advances in Materials Science and Engineering*, V. 2018, 2018, 12 pp. doi: 10.1155/2018/8934689

10. Shekari, A. H., and Razzaghi, M. S., "Influence of Nano Particles on Durability and Mechanical Properties of High Performance Concrete," *Procedia Engineering*, V. 14, 2011, pp. 3036-3041. doi: 10.1016/j.proeng.2011.07.382

11. Shen, W.; Zhang, C.; Li, Q.; Zhang, W.; Cao, L.; and Ye, J., "Preparation of Titanium Dioxide Nano Particle Modified Photocatalytic Self-Cleaning Concrete," *Journal of Cleaner Production*, V. 87, Jan. 2015, pp. 762-765. doi: 10.1016/j.jclepro.2014.10.014

12. Abdalla, J. A.; Thomas, B. S.; Hawileh, R. A.; Yang, J.; Jindal, B. B.; and Ariyachandra, E., "Influence of Nano-TiO_2, Nano-Fe_2O_3, Nanoclay and Nano-$CaCO_3$ on the Properties of Cement/Geopolymer Concrete," *Cleaner Materials*, V. 4, June 2022, Article No. 100061. doi: 10.1016/j.clema.2022.100061

13. Han, B.; Sun, S.; Ding, S.; Zhang, L.; Yu, X.; and Ou, J., "Review of Nanocarbon-Engineered Multifunctional Cementitious Composites," *Composites Part A: Applied Science and Manufacturing*, V. 70, Mar. 2015, pp. 69-81. doi: 10.1016/j.compositesa.2014.12.002

14. Vittoriadiamanti, M., and Pedeferri, M. P., "Concrete, Mortar and Plaster Using Titanium Dioxide Nanoparticles: Applications in Pollution Control, Self-Cleaning and Photo Sterilization," *Nanotechnology in Eco-Efficient Construction: Materials, Processes and Applications*, F. Pacheco-Torgal, M. V. Diamanti, A. Nazari, and C-G. Granqvist, eds., Woodhead Publishing, Sawston, UK, 2013, pp. 299-326. doi: 10.1533/9780857098832.3.299

15. Lee, B. Y., "Effect of Titanium Dioxide Nanoparticles on Early Age and Long Term Properties of Cementitious Materials," PhD dissertation, Georgia Institute of Technology, Atlanta, GA, Aug. 2012, 227 pp.

16. Meng, T.; Yu, Y.; Qian, X.; Zhan, S.; and Qian, K., "Effect of Nano-TiO_2 on the Mechanical Properties of Cement Mortar," *Construction and Building Materials*, V. 29, Apr. 2012, pp. 241-245. doi: 10.1016/j.conbuildmat.2011.10.047

17. Mohammadi, M.; Hesaraki, S.; and Hafezi-Ardakani, M., "Investigation of Biocompatible Nanosized Materials for Development of Strong Calcium Phosphate Bone Cement: Comparison of Nano-Titania, Nano-Silicon Carbide and Amorphous Nano-Silica," *Ceramics International*, V. 40, No. 6, July 2014, pp. 8377-8387. doi: 10.1016/j.ceramint.2014.01.044

18. Raki, L.; Beaudoin, J.; Alizadeh, R.; Makar, J.; and Sato, T., "Cement and Concrete Nanoscience and Nanotechnology," *Materials (Basel)*, V. 3, No. 2, 2010, pp. 918-942. doi: 10.3390/ma3020918

19. Senff, L.; Tobaldi, D. M.; Lucas, S.; Hotza, D.; Ferreira, V. M.; and Labrincha, J. A., "Formulation of Mortars with Nano-SiO_2 and Nano-TiO_2 for Degradation of Pollutants in Buildings," *Composites Part B: Engineering*, V. 44, No. 1, Jan. 2013, pp. 40-47. doi: 10.1016/j.compositesb.2012.07.022

20. Lazaro, A.; Yu, Q. L.; and Brouwers, H. J. H., "Nanotechnologies for Sustainable Construction," *Sustainability of Construction Materials*, second edition, J. M. Khatib, ed., Woodhead Publishing, Sawston, UK, 2016, pp. 55-78. doi: 10.1016/b978-0-08-100370-1.00004-4

21. Chen, J.; Kou, S.-C.; and Poon, C.-S., "Hydration and Properties of Nano-TiO_2 Blended Cement Composites," *Cement and Concrete Composites*, V. 34, No. 5, May 2012, pp. 642-649. doi: 10.1016/j.cemconcomp.2012.02.009

22. Nazar, S.; Yang, J.; Thomas, B. S.; Azim, I.; and Ur Rehman, S. K., "Rheological Properties of Cementitious Composites with and without Nano-Materials: A Comprehensive Review," *Journal of Cleaner Production*, V. 272, Nov. 2020, Article No. 122701. doi: 10.1016/j.jclepro.2020.122701

23. Yan, D.; Wu, C.; Lin, Z.; Leventis, N.; and Mahadik, S., "Concrete Surface with Nano-Particle Additives for Improved Wearing Resistance to Increasing Truck Traffic," Report No. MATC-MST: 441, Mid-America Transportation Center, Lincoln, NE, 2012, 53 pp.

24. Noorvand, H.; Abang Ali, A. A.; Demirboga, R.; Farzadnia, N.; and Noorvand, H., "Incorporation of Nano TiO_2 in Black Rice Husk Ash Mortars," *Construction and Building Materials*, V. 47, Oct. 2013, pp. 1350-1361. doi: 10.1016/j.conbuildmat.2013.06.066

25. IS 2386-1963(R2016), "Methods of Test for Aggregates for Concrete (Part I to Part VIII) (Revision 2016)," Bureau of Indian Standards, New Delhi, India, 2016.

26. IS 516-1959(R2004), "Method of Tests for Strength of Concrete (Reaffirmed 2004)," Bureau of Indian Standards, New Delhi, India, 2004, 30 pp.

27. Lucas, S. S.; Ferreira, V. M.; and Barroso de Aguiar, J. L., "Incorporation of Titanium Dioxide Nanoparticles in Mortars – Influence of Microstructure in the Hardened State Properties and Photocatalytic Activity," *Cement and Concrete Research*, V. 43, Jan. 2013, pp. 112-120. doi: 10.1016/j.cemconres.2012.09.007

28. Konsta-Gdoutos, M. S.; Metaxa, Z. S.; and Shah, S. P., "Highly Dispersed Carbon Nanotube Reinforced Cement Based Materials," *Cement and Concrete Research*, V. 40, No. 7, July 2010, pp. 1052-1059. doi: 10.1016/j.cemconres.2010.02.015

29. Saleem, H.; Zaidi, S. J.; and Alnuaimi, N. A., "Recent Advancements in the Nanomaterial Application in Concrete and Its Ecological Impact," *Materials (Basel)*, V. 14, No. 21, Nov. 2021, Article No. 6387. doi: 10.3390/ma14216387

30. Yu, X.; Kang, S.; and Long, X., "Compressive Strength of Concrete Reinforced by TiO_2 Nanoparticles," *AIP Conference Proceedings*, V. 2036, No. 1, 2018, Article No. 030006. doi: 10.1063/1.5075659

31. Jalal, M., "Durability Enhancement of Concrete by Incorporating Titanium Dioxide Nanopowder into Binder," *The Journal of American Science*, V. 8, No. 4, 2012, pp. 289-294.

32. Mulenga, D. M., and Robery, P. C., "Can Nanotechnology Address Today's Civil Engineering Challenges?" *Structures Congress 2010*, S. Senapathi, K. Casey, and M. Hoit, eds., Orlando, FL, 2010, pp. 609-621. doi: 10.1061/41130(369)5610.1061/41130(369)56

33. Du, Y.; Yang, J.; Skariah Thomas, B.; Li, L.; Li, H.; Mohamed Shaban, W.; and Tung Chong, W., "Influence of Hybrid Graphene Oxide/Carbon Nanotubes on the Mechanical Properties and Microstructure of Magnesium Potassium Phosphate Cement Paste," *Construction and Building Materials*, V. 260, Nov. 2020, Article No. 120449. doi: 10.1016/j.conbuildmat.2020.120449

34. IS 12269:2013, "Ordinary Portland Cement, 53 Grade — Specification (First Revision)," Bureau of Indian Standards, New Delhi, India, 2013, 14 pp.

35. IS 383-2016, "Specification for Coarse and Fine Aggregates from Natural Sources for Concrete," Bureau of Indian Standards, New Delhi, India, 2016, 24 pp.

36. IS 456:2000, "Plain and Reinforced Concrete — Code of Practice (Fourth Revision) (Reaffirmed 2005)," Bureau of Indian Standards, New Delhi, India, 2000, 114 pp.

37. IS 10500:2012, "Drinking Water — Specification (Second Revision)," Bureau of Indian Standards, New Delhi, India, 2012, 18 pp.

38. IS 10262:2019, "Concrete Mix Proportioning — Guidelines (Second Revision)," Bureau of Indian Standards, New Delhi, India, 2019, 21 pp.

39. IS 1199-1959, "Methods of Sampling and Analysis of Concrete (Reaffirmed 2004)," Bureau of Indian Standards, New Delhi, India, 1959, 49 pp.

40. IS 5816:1999, "Splitting Tensile Strength of Concrete — Method of Test (Reaffirmed 2004)," Bureau of Indian Standards, New Delhi, India, 1999, 14 pp.

41. Salman, M. M.; Eweed, K. M.; and Hameed, A. M., "Influence of Partial Replacement TiO_2 Nanoparticles on the Compressive and Flexural Strength of Ordinary Cement Mortar," *Al-Nahrain University, College of Engineering Journal (NUCEJ)*, V. 19, No. 2, 2016, pp. 265-270.

42. Ur Rehman, A.; Qudoos, A.; Kim, H. G.; and Ryou, J.-S., "Influence of Titanium Dioxide Nanoparticles on the Sulfate Attack upon Ordinary Portland Cement and Slag-Blended Mortars," *Materials (Basel)*, V. 11, No. 3, Mar. 2018, Article No. 356. doi: 10.1016/j.enbuild.2010.12.025

43. Feng, D.; Xie, N.; Gong, C.; Leng, Z.; Xiao, H.; Li, H.; and Shi, X., "Portland Cement Paste Modified by TiO_2 Nanoparticles: A Microstructure Perspective," *Industrial & Engineering Chemistry Research*, V. 52, No. 33, Aug. 2013, pp. 11575-11582. doi: 10.1021/ie4011595

44. Essawy, A. A., and Abd El.Aleem, S., "Physico-Mechanical Properties, Potent Adsorptive and Photocatalytic Efficacies of Sulfate Resisting Cement Blends Containing Micro Silica and Nano-TiO_2," *Construction and Building Materials*, V. 52, Feb. 2014, pp. 1-8. doi: 10.1016/j.conbuildmat.2013.11.026

45. Isfahani, F. T.; Redaelli, E.; Lollini, F.; Li, W.; and Bertolini, L., "Effects of Nanosilica on Compressive Strength and Durability Properties of Concrete with Different Water to Binder Ratios," *Advances in Materials Science and Engineering*, V. 2016, 2016, 16 pp. doi: 10.1155/2016/8453567

46. Nazari, A., and Riahi, S., "The Effect of TiO_2 Nanoparticles on Water Permeability and Thermal and Mechanical Properties of High Strength Self-Compacting Concrete," *Materials Science and Engineering: A*, V. 528, No. 2, Dec. 2010, pp. 756-763. doi: 10.1016/j.msea.2010.09.074

47. Soleymani, F., "Assessments of the Effects of Limewater on Water Permeability of TiO_2 Nanoparticles Binary Blended Palm Oil Clinker Aggregate-Based Concrete," *The Journal of American Science*, V. 8, No. 5, 2012, pp. 698-702.

48. Zhang, R.; Cheng, X.; Hou, P.; and Ye, Z., "Influences of Nano-TiO_2 on the Properties of Cement-Based Materials: Hydration and Drying Shrinkage," *Construction and Building Materials*, V. 81, Apr. 2015, pp. 35-41. doi: 10.1016/j.conbuildmat.2015.02.003

49. Iyappan, A. P.; Srikanthan, L.; Franklin, F. S.; Bhuvaneswari, J.; and Preethika, A., "Replacement of Cement by Using Nano Titanium Dioxide in Concrete," *IJSRD-International Journal for Scientific Research & Development*, V. 5, No. 7, 2017, pp. 499-503.

50. Zhao, L.; Chen, R.; Pang, L. X.; Zhang, W.; and Tan, X., "Study on Photo-Catalytic Efficiency and Durability of Nano-TiO_2 in Permeable Concrete Pavement Structure," *IOP Conference Series: Earth and Environmental Science*, V. 371, No. 4, 2019, Article No. 042011. doi: 10.1088/1755-1315/371/4/042011

51. Zhang, M.-H., and Li, H., "Pore Structure and Chloride Permeability of Concrete Containing Nano-Particles for Pavement," *Construction and Building Materials*, V. 25, No. 2, Feb. 2011, pp. 608-616. doi: 10.1016/j.conbuildmat.2010.07.032

52. Bleszynski, R.; Hooton, R. D.; Thomas, M. D. A.; and Rogers, C. A., "Durability of Ternary Blend Concrete with Silica Fume and Blast-Furnace Slag: Laboratory and Outdoor Exposure Site Studies," *ACI Materials Journal*, V. 99, No. 5, Sept.-Oct. 2002, pp. 499-508.

53. IS 13311-2:1992, "Non-Destructive Testing of Concrete — Methods of Test: Part 2: Rebound Hammer (Reaffirmed 2004)," Bureau of Indian Standards, New Delhi, India, 1992, 12 pp.

54. Senff, L.; Hotza, D.; Lucas, S.; Ferreira, V. M.; and Labrincha, J. A., "Effect of Nano-SiO_2 and Nano-TiO_2 Addition on the Rheological Behavior and the Hardened Properties of Cement Mortars," *Materials Science and Engineering: A*, V. 532, Jan. 2012, pp. 354-361. doi: 10.1016/j.msea.2011.10.102

55. Işıkdağ, B., and Topçu, İ. B., "The Effect of Ground Granulated Blast-Furnace Slag on Properties of Horasan Mortar," *Construction and Building Materials*, V. 40, Mar. 2013, pp. 448-454. doi: 10.1016/j.conbuildmat.2012.11.016

56. ASTM C1218/C1218M-15, "Standard Test Method for Water-Soluble Chloride in Mortar and Concrete," ASTM International, West Conshohocken, PA, 2015, 3 pp.

57. Bouchard, B., "ASTM C-114 Accreditation for Cement Analysis by Fusion," SPEX SamplePrep, Metuchen, NJ.

58. Bassuoni, M. T.; Nehdi, M. L.; and Greenough, T. R., "Enhancing the Reliability of Evaluating Chloride Ingress in Concrete Using the ASTM C 1202 Rapid Chloride Penetrability Test," *Journal of ASTM International*, V. 3, No. 3, 2006, 13 pp. doi: 10.1520/jai13403

59. Ribeiro, D. V.; Labrincha, J. A.; and Morelli, M. R., "Chloride Diffusivity in Red Mud-Ordinary Portland Cement Concrete Determined by Migration Tests," *Materials Research*, V. 14, No. 2, 2011, pp. 227-234. doi: 10.1590/S1516-14392011005000026

60. Gailius, A., and Kosior-Kazberuk, M., "Monitoring of Concrete Resistance to Chloride Penetration," *Materials Science (Medžiagotyra)*, V. 14, No. 4, 2008, pp. 350-355.

61. Özyurt, N.; Söylev, T. A.; Özturan, T.; Pehlivan, A. O.; and Niş, A., "Corrosion and Chloride Diffusivity of Reinforced Concrete Cracked under Sustained Flexure," *Teknik Dergi*, V. 31, No. 6, 2020, pp. 10315-10337. doi: 10.18400/tekderg.430536

62. Ramirez-Meneses, E.; Dominguez-Crespo, M. A.; and Torres-Huerta, A. M., "Stabilized Metal Nanoparticles from Organometallic Precursors for Low Temperature Fuel Cells," *Recent Patents on Nanotechnology*, V. 7, No. 1, 2012, pp. 13-25. doi: 10.2174/1872210511307010013

TECHNOLOGY FORUM

29 - 31 AUGUST 2023

PORTLAND, OR

THE BENSON PORTLAND, CURIO COLLECTIONS BY HILTON

SAVE THE DATE

The **Technology Forum** is an industry-exclusive educational and networking event for concrete professionals **powered by ACI Foundation's Concrete Innovation Council**.

Whether you are an emerging professional or a seasoned veteran, the ACI Foundation Technology Forum is the place to learn about **current trends, emerging technologies, and discoveries within the concrete industry**.

Join us for an exciting and insightful event featuring thought leaders and technology innovators to discuss the future of the concrete industry.

acifoundation.org

aci Foundation
Building the Future

ACI MATERIALS JOURNAL TECHNICAL PAPER

Title No. 120-M24

Evaluation of Sulfate Resistance of One-Part Alkali-Activated Materials Prepared by Mechanochemistry

by Wenda Wu, Shilong Ma, Yuanda Wang, Xuefang Wang, Liwei Xu, and Shichang Ye

In this paper, the resistance of mechanically prepared one-part alkali-activated materials to external sulfuric acid attack was investigated by simulating realistic erosion environments in terms of sulfate type, concentration, and erosion mode. The macroscopic properties of the specimens were measured at different ages. Microscopic analyses were performed by Fourier-transform infrared spectroscopy (FTIR), X-ray diffraction (XRD), mercury intrusion porosimetry (MIP), and other techniques to obtain the effect of different erosion environments on the mechanical-force chemically prepared one-part alkali-activated materials against sulfate erosion. The study shows that the mechanical properties of the specimens showed a trend of increasing and then decreasing with the extension of erosion time. Compared with Na_2SO_4 erosion, the erosion damage was greatest when the sulfate containing Mg^{2+} was eroded in a wetting-and-drying cycle; the erosion products of Na_2SO_4 solution coexist in the form of calcite and gypsum, while the erosion products of $MgSO_4$ solution mainly consist of gypsum.

Keywords: mechanochemistry; one-part alkali-activated materials; sulfate attack.

INTRODUCTION

One-part alkali-excited cementitious material refers to an inorganic nonmetallic material with cementitious activity that is prepared by mixing a solid alkaline exciter with a mineral material with volcanic ash activity according to a certain process.[1,2] This one-part alkali-initiated gelling material is similar to ordinary portland cement (OPC) and can be used by adding water. Alkali-excited gelling materials have attracted great attention from academic authors worldwide for their excellent performance. In the 1940s, Purdon[3] experimentally prepared a geopolymer mixture by simply mixing slag with solid sodium hydroxide and successfully prepared a gelling mixture. At the beginning of the twenty-first century, Duxson and Provis[4] outlined various potential methods for tuning the precursor chemistry and particle behavior of geopolymers and proposed a one-part geopolymer that exceeded the potential of conventional two-part (solid plus alkaline-activator solution) hybrid designs. Peng et al.[5] prepared a one-part geopolymer with excellent compressive strength by a process of calcined bentonite and the addition of solid alkali, which exceeded the compressive strength of a two-part geopolymer with the same ratio and achieved a higher softening factor of 0.93. Additionally, in terms of environmental protection and economy, the raw material sources of alkali-inspired cementitious materials are mostly fly ash, slag, and other industrial waste. These substances have a low cost, simple preparation process, less energy consumption, and only 26 to 45% of the carbon emissions of OPC and are therefore recognized as green cementitious materials.[6-8]

In recent years, researchers have found that the treatment of alkali-excited precursors using mechanical-force chemistry enables the effective release of volcanic ash activity from the precursors, leading to the improvement of various properties, such as the efficiency of curing toxic heavy metal ions and thermal stabilities.[9] The study by Temuujin et al.[10] showed that mechanical-force chemistry changed the physical properties of fly ash and directly affected the volcanic ash reaction of alkali-excited materials. Also, the 28-day compressive strength of alkali-excited fly ash net slurry specimens subjected to mechanical-force chemistry increased by 80%. Kumar et al.[11] proposed that mechanical activation can enhance the reactivity of alkali-excited slag cement net slurry, enabling it to react with water directly and harden, and suggested that the volcanic ash reactivity of slag cement is related to its specific surface area. Zhao et al.[12] found that mechanical activation resulted in optimized particle-size distribution, superior pore structure of alkali-excited fly ash mortar, and reduced aggregation of SiO_4 tetrahedra and AlO_4 tetrahedra in the gel. These studies show that the preparation of single-part alkali-excited gelling materials using mechanical-force chemistry has been recognized by a wide range of researchers and has become a research hot spot in the field of new green building materials.

The issue of durability of concrete has been a decisive factor in the service life of buildings, and the erosion damage of concrete by sulfate is one of the reasons for the serious reduction of durability.[13,14] Previous studies[15-17] have shown that sulfate erosion will cause the expansion of the cementitious material and produce cracks and peeling, which has a great negative impact on its strength and durability. Global maintenance and repair costs due to corrosion alone exceed $150 billion annually.[18,19] The environments in which buildings are located have contributed to diversity in sulfate erosion.[20-22] For example, inland saline areas contain high concentrations of mirabilite ($Na_2SO_4 \cdot 10H_2O$), and sulfate erosion is dominated by salt (Na^+). In contrast, the sulfate ($MgSO_4$) in seawater mainly causes building erosion in coastal areas. In addition, some buildings are partially submerged in seawater for a long period, as well

ACI Materials Journal, V. 120, No. 2, March 2023.

MS No. M-2022-108.R5, doi: 10.14359/51738491, received October 8, 2022, and reviewed under Institute publication policies.

Table 1—Chemical composition of materials, wt. %

Mineral composition	SiO_2	Al_2O_3	Fe_2O_3	MgO	CaO	Na_2O	K_2O	MnO	TiO_2	Loss
Fly ash	45.9	34	5	0.8	6.9	0.2	0.9	0.1	1.7	4.5
Slag	28.7	14	0.4	9.9	41.2	0.5	0.4	0.3	1.4	3.2

as wetting-and-drying circulation areas in splash zones and tidal zones. Therefore, it is necessary to test the sulfate resistance of single-component alkali-initiated gelling materials before they are widely used in practical engineering.

To more closely simulate the authentic environments in which the building is located, Mg^{2+} and Na^{+}, which are more widely distributed, were selected as the metal cations of sulfate erosion solution in this paper. Realistic sulfate erosion environments were simulated by adjusting sulfate solution concentrations (that is, 5 and 10%) and erosion methods (that is, wetting-and-drying cycles and full immersion). At the same time, the sulfate resistance performance was compared with that of OPC to make a comprehensive evaluation of the sulfate resistance of single-part alkali-excited materials prepared by mechanical-force chemistry.

RESEARCH SIGNIFICANCE

The preparation process of one-part alkali-activated materials by mechanical-force ball milling is simple, does not require a high-temperature calcination process, consumes less energy, and has only one-third of the carbon emissions of OPC, which is recognized as a green cementitious material. The investigation of the sulfuric acid resistance of the single-component alkali-initiated material prepared by a mechanical-force ball mill is important preparation for the promotion of the material in practical engineering applications. It is also an effective measure to replace the use of portland cement (PC) and reduce carbon emissions, thereby exhibiting significant research significance.

MATERIALS AND EXPERIMENTS

Raw materials

Material preparation—For this study, fly ash and slag were purchased from the same Chinese mining company. They were used as alkali-excited precursors, where the average particle size of raw fly ash was approximately 63.72 μm, the water requirement was 80%, the 45 μm sieve margin was 15.15%, the average particle size of raw mineral powder was approximately 15.7 μm, and the 28-day activity index reached 98%. Table 1 and Fig. 1 display the chemical composition and crystal composition, respectively. According to Fig. 1, the main crystalline phases in fly ash are mullite and quartz, which also contain amorphous glass phases. Slag is mainly composed of an amorphous glass phase and calcium oxide, and a small amount of calcite.

For the experimental control group, P.O42.5R OPC produced by a cement factory in China was purchased, with a density of 3150 kg/m^3 and a specific surface area of 352 m^2/kg. The cement met the requirements of EN 197-1:2011. Table 2 presents the chemical composition of the cement.

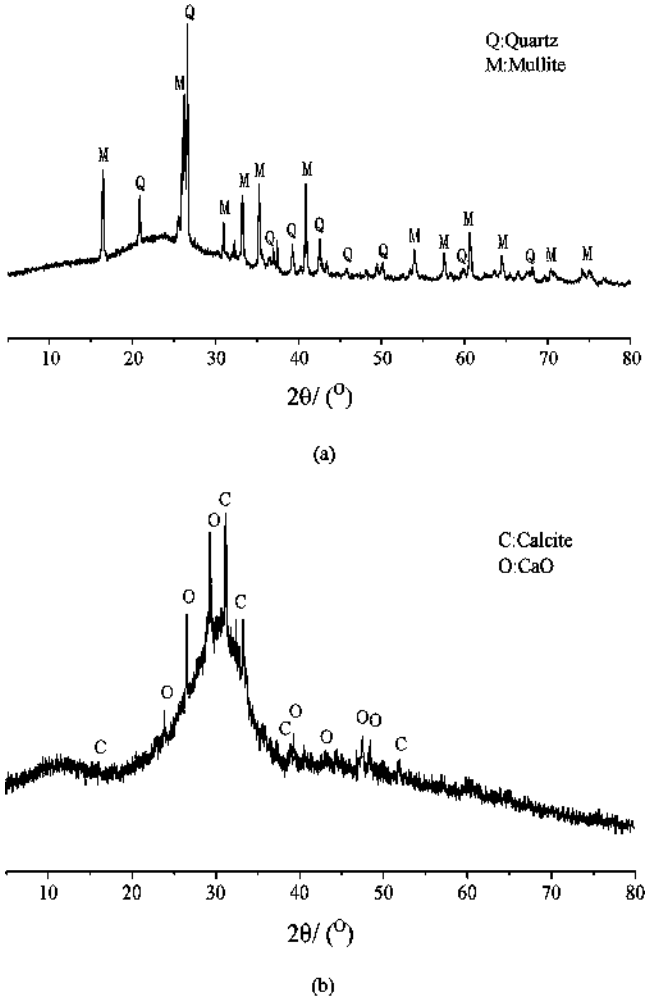

Fig. 1—(a) XRD spectra of original fly ash; and (b) XRD spectra of original slag.

Furthermore, in this study, analytical pure barium chloride was used as a retarder and International Organization for Standardization (ISO) standard sand as mixed sand.

Preparation of alkali-activated materials and sulfate solution—The preparation method of one-part alkali-activated material prepared by mechanochemistry is as follows: first, heat the slag powder and fly ash in an oven at 100 ± 5°C for 2 hours to remove the moisture. Remove the slag powder and fly ash and cool to room temperature. Place the slag powder, fly ash, and solid activator together into a ball mill tank. Use the ball mill to mill the mixture for 30 minutes. Finally, store the milled powder in a sealed bag to inhibit moisture and carbonization. The size of the steel balls in the ball mill was 30, 20, and 10 mm in diameter, the mass ratio was 1:1:1, and the packing density of the steel balls was 4640 kg/m^3. In this experiment, anhydrous NaOH and Na_2SiO_3 were used as alkali activators, where the purity of NaOH was over 96% and the purity of Na_2SiO_3 with SiO_2:Na_2O of 1.4 was over 99%.

Table 2—Chemical compositions of cement, wt. %

Mineral composition	SiO_2	Al_2O_3	CaO	Fe_2O_3	SO_3	MgO	f-CaO	Other	Ignition loss
Value	21.7	4.4	62.5	3.3	2.9	2.1	0.6	0.9	1.6

Table 3—Specimen mixture proportions

Material	Fly ash, %	Slag, %	Portland cement, %	*w/c*	Sand-glue ratio	Alkali-excitation agent, %	Retarder, %
Alkali-activated materials	75	25	—	0.4	0.5	4	1
OPC	—	—	100	0.4	0.5	—	—

Table 4—Test design scheme

Numbering	Sulfate species	Sulfate concentration, %	Erosion mode
M5F	$MgSO_4$	5	Full immersion
M10F	$MgSO_4$	10	Full immersion
N5F	Na_2SO_4	5	Full immersion
N10F	Na_2SO_4	10	Full immersion
M5DW	$MgSO_4$	5	Wetting-and-drying cycles
N5DW	Na_2SO_4	5	Wetting-and-drying cycles
S-M5F	$MgSO_4$	5	Full immersion
O-M5F	$MgSO_4$	5	Full immersion

Note: M is $MgSO_4$; N is Na_2SO_4; F is full immersion; DW is wetting-and-drying cycles; S is simple mixing; O is OPC; numbers denote sulfate solution concentration. (For example, O-M5F denotes full-immersion erosion of specimen prepared with OPC under 5% $MgSO_4$.)

The sulfates used in this experiment were analytically pure anhydrous Na_2SO_4 and anhydrous $MgSO_4$, and the purity of both sulfates exceeded 99%. The configuration steps are as follows: First, weigh an appropriate amount of solid sulfate and deionized water, as required. Then, prepare the sulfate attack solution, according to the configuration standard of the sulfate solution.

Experimental scheme and specimen preparation

Experimental scheme—Table 3 presents the mixture proportions selected in this study (the percentages in the table are quality percentages).

To facilitate accuracy, the test scheme adopted the single control variable method to create erosion tests of various influencing factors, as Table 4 illustrates. At the same time, two control groups were established, which were simple mixing mortar (simple mixing of precursor and alkali activator without mechanical grinding) and OPC mortar specimens. Then, the authors compared the resistance to sulfate attack of the various one-part alkali-activated slag-fly ash mortar specimens prepared by mechanochemistry.

After 28 days of standard curing, the specimens were placed in various pieces of equipment according to the different erosion methods. The full-immersion specimens were placed in a constant temperature and humidity curing box, as Fig. 2(a) illustrates. For the wetting-and-drying cycles, the samples were placed in a self-made automatic wetting-and-drying cycle device, shown in Fig. 2(b). The automatic wetting-and-drying cycle device was maintained at a constant temperature (20°C) and humidity (40%). The wetting-and-drying cycle mode is 16 hours of full immersion and 8 hours of drying, followed by a complete wetting-and-drying cycle for 24 hours. The sulfate erosion solutions were changed monthly during the experiment to reduce errors caused by changes in concentration. When the age of erosion reached 30, 60, and 90 days, the specimens were analyzed for appearance, compressive and flexural strengths, and microscopic variations. Ultimately, the mechanism of the effects of different erosion environments on the one-part alkali-activated materials prepared by mechanochemistry against sulfate erosion was obtained.

Specimen preparation—When the mortar specimen reaches the age of erosion (that is, 30, 60, and 90 days of erosion), the mortar sample from 0 to 5 mm from the surface of the specimen was removed by a cutting machine. The removed samples were crushed into pieces and placed in reagent bottles containing anhydrous ethanol to terminate the volcanic ash reaction. The instruments used for each microscopic test are as follows:

1. Fourier-transform infrared spectroscopy (FTIR): The instrument used in this study is a Fourier-transform infrared spectrometer produced in the United States. The wave number range of the instrument was set from 4000 to 400 cm^{-1} with a resolution of 12.5 px^{-1} and a wave number accuracy of 0.25 px^{-1}. The KBr compression method was used as follows: first, the oven was set to 120°C for drying the potassium bromide powder. Then, 1 mg of sample powder and 100 mg of potassium bromide powder were weighed with an accuracy of 0.1 mg. Subsequently, the mixed powder was ground in an agate mortar and a tablet pressing mechanism was used to make a disc without cracks and with a certain degree of translucency. Finally, the discs were put into the machine to start the test.

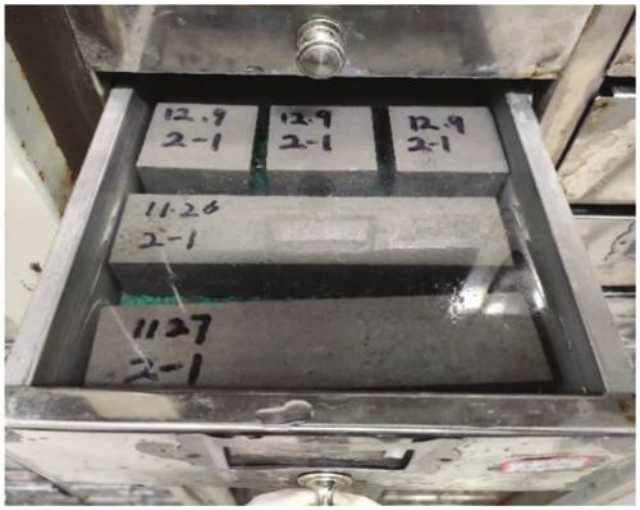

(a)

(b)

Fig. 2—(a) Full-immersion erosion in mortar specimen curing box; and (b) drying-and-wetting erosion of mortar specimens.

2. X-ray diffraction analysis (XRD): The instrument used in this study is an X-ray polycrystalline diffractometer. The 2θ angle range of the test instrument is –110 to 162 degrees, and the resolution full width at half maximum (FWHM) is 0.028 degrees. Before grinding, anhydrous ethanol was poured into the mortar to prevent carbonization of the mortar sample during the grinding process. After grinding, the paste-like samples were loaded into an aluminum box. The aluminum box was placed in a vacuum drying oven and baked at 50°C for 24 hours. The coarse particles in the dried powder were removed with a sieve disc of 0.08 mm aperture, and the sieved powder was put into a sealed bag.

3. Pore structure analysis (that is, mercury intrusion porosimetry [MIP]): The instrument used in this study is a mercury-pressure instrument. The aperture range of the instrument is 0.003 to 1080 μm. A 1.5 g sample was used for the test and was put into the expander and then vacuumed until $p <$ 6.67 Pa. The whole test must go through two stages of low pressure (1.03 to 25 psi) and high pressure (5 to 50,000 psi) to obtain two sets of data, respectively, after which these two sets of data are processed to obtain the analytical data of the sample pore structure.

RESULTS AND DISCUSSION

Effect of different erosion conditions on specimen strength

Figures 3 and 4 display the changes in compressive and flexural strength of the specimens under different erosion conditions. It includes changes in strength and strength loss rate, which is the loss rate of specimen strength at the next phase compared to the strength in the previous phase. It was found that the strength of the test specimens exhibits three phases with increasing erosion time. In the first stage from 0 to 30 days—namely, the growth stage—the strength of the specimens gradually increases with erosion time. In the second stage, which is the transition period at 30 to 60 days, specimen strength growth slows and stabilizes. Then, there is a transition from strength growth to loss. In the third stage, which is the declining stage between 60 to 90 days, the strength of the specimens gradually decreases with erosion.

During the initial growth phase in the first 30 days, the growth in strength of the specimens is mainly caused by two aspects. First, volcanic ash-active substances in the slag and fly ash lead to the hydration of alkali-excited materials. It can be hypothesized that silica-aluminous salts with volcanic ash activity and C-S-H undergo volcanic ash reactions to produce the denser $Ca(SiO_4)_2$,[23] and the accumulation of $Ca(SiO_4)_2$ fills the pores in the concrete. The other factor is the erosion of sulfate, which means that gypsum and ettringite form and accumulate in the micropore structure when the specimen is eroded by sulfate.[24,25] The accumulation of erosion products such as gypsum and ettringite causes expansion, which is beneficial to the strength of the specimen in the early stage of erosion. Figures 3 and 4 illustrate that the compressive strength loss rate of the N5DW specimen is the highest in the initial stage, reaching –19.1%. In contrast, the compressive strength loss rate of the corresponding $MgSO_4$ wetting-and-drying cycle erosion specimen M5DW is only –8.4%. The influence of the wetting-and-drying cycle erosion modes of two sulfates on the compressive strength of the specimens is greater than full-immersion erosion under the same conditions. Compared with sulfate concentration, the compressive strength and flexibility strength of the N5F specimens increases significantly under Na_2SO_4 erosion at low concentrations, and the loss rates are –12.2 and –4.9%, while the N10F specimens present losses of –3.0 and –2.2%. Conversely, the compressive and flexural strengths of the M10F specimens changed significantly under $MgSO_4$ erosion, with loss rates of –5.5% and –13.5%, respectively, while the loss rates of M5F specimens are –2.0% and –7.9%, respectively. The compressive strength loss rates of the S-M5F and O-M5F specimens in the control group are –11.2% and –10.5%, respectively, while the flexural strength loss rates are –10.7 and –10.6%.

In the second stage, the strength transition period at 30 to 60 days, the secondary hydration of alkali-activated materials decreases.[26,27] The accumulation of sulfate erosion products reaches a certain degree, which weakens the strength growth of the specimen. Sulfate erosion products

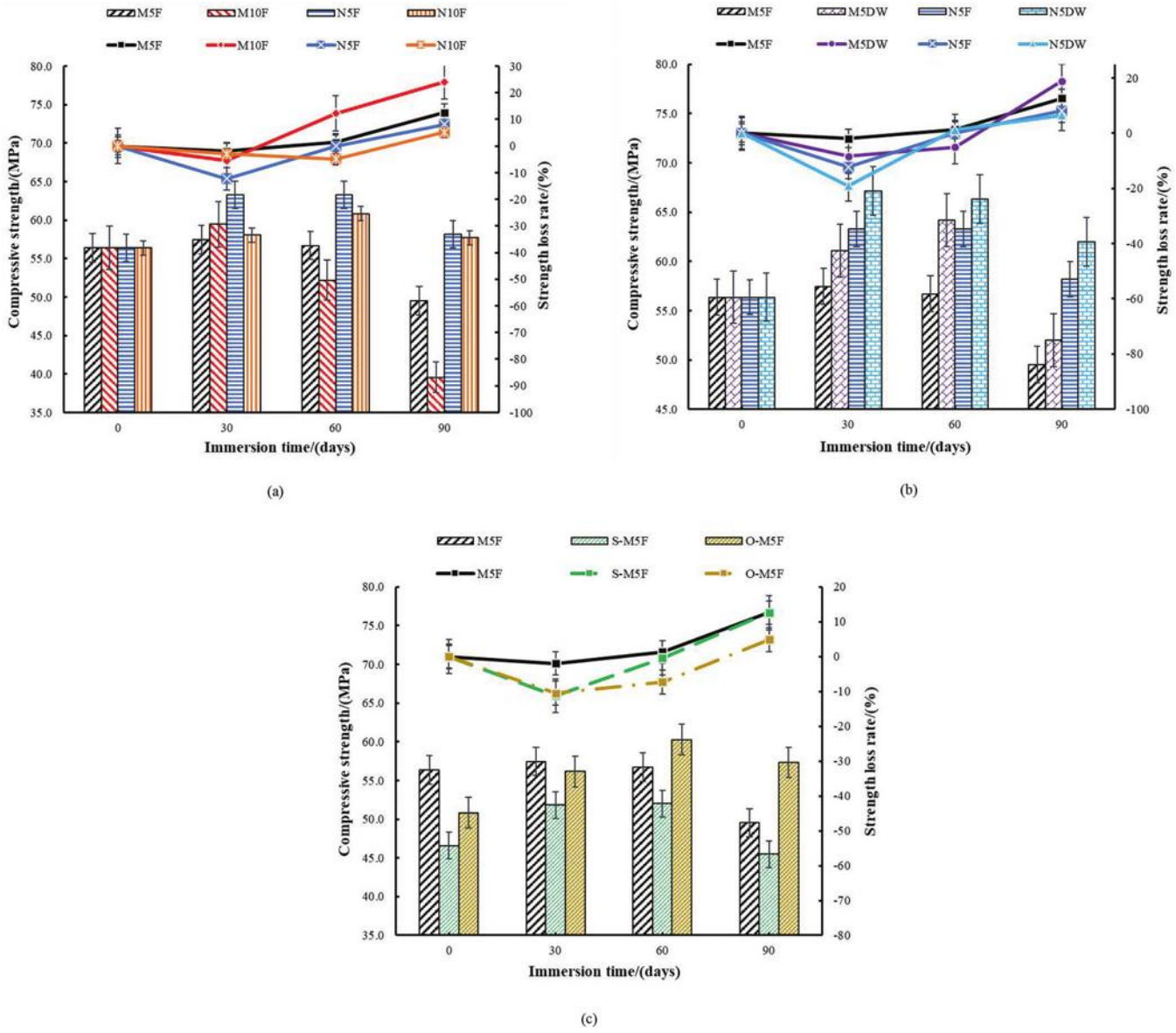

Fig. 3—(a) Effect of different sulfate concentrations on compressive strength; (b) effect of different erosion methods on compressive strength; and (c) effect of control group on compressive strength at different erosion times.

accumulate continuously, adhere to the inner walls of the pores, fill the pores, and increase pore wall pressure.[28] In addition to increasing pore pressure, it also effectively hinders the corrosion progress of the sulfate solution. At this stage, the compactness of the specimen increases, while the pore structure decreases. Figures 3 and 4 reveal that the N5DW and M10F specimens present the greatest degree of strength variation in the transition phase, which is consistent with the first stage. The compressive and flexural strength loss rates for N5DW increase from –19.1 and –2.2% to 1.2 and 6.2%, while the loss rates for M10F increase from –5.5 and –13.5% to 12.3 and 16.2%. In contrast to the strength change of each specimen in the control group, the strength of the M5F and S-M5F specimens in the alkali-activated group complete the transition from growth to loss. However, the strength of the O-M5F specimens still grows steadily, and the compressive and flexural strength loss rates change from –10.5 and –10.6% to –7.3 and –4.6%. These results display some similarities with the findings of Ganjian and Pouya.[29]

In the final 30 days, the decreasing strength stage, the erosion products in the pores of the specimens accumulate continuously, and the expansion stress of the pore walls increases continuously. At the same time, microcracks appear and develop, leading to a rapid decrease in the strength of the specimen. Under certain conditions, the activity of the slag and fly ash is slightly lower than cement and is characterized by early strength and rapid hardening. It is easy for relatively large pores to form between the mortars of the specimens, resulting in a weakening of the bonding force. Therefore, the compressive strength increases rapidly in the early stages, while corrosion damage is more obvious in the later stages. By observing the strength change of each specimen in Fig. 3 and 4, it can be observed that the strength loss of the M10F and M5DW specimens are the largest. The loss rates of compressive strength are 24.1 and 19.0%, while the loss rates of flexural strength are 6.3 and 2.4%. In the control group, the strength of the O-M5F samples did not change significantly, with a loss in compressive strength

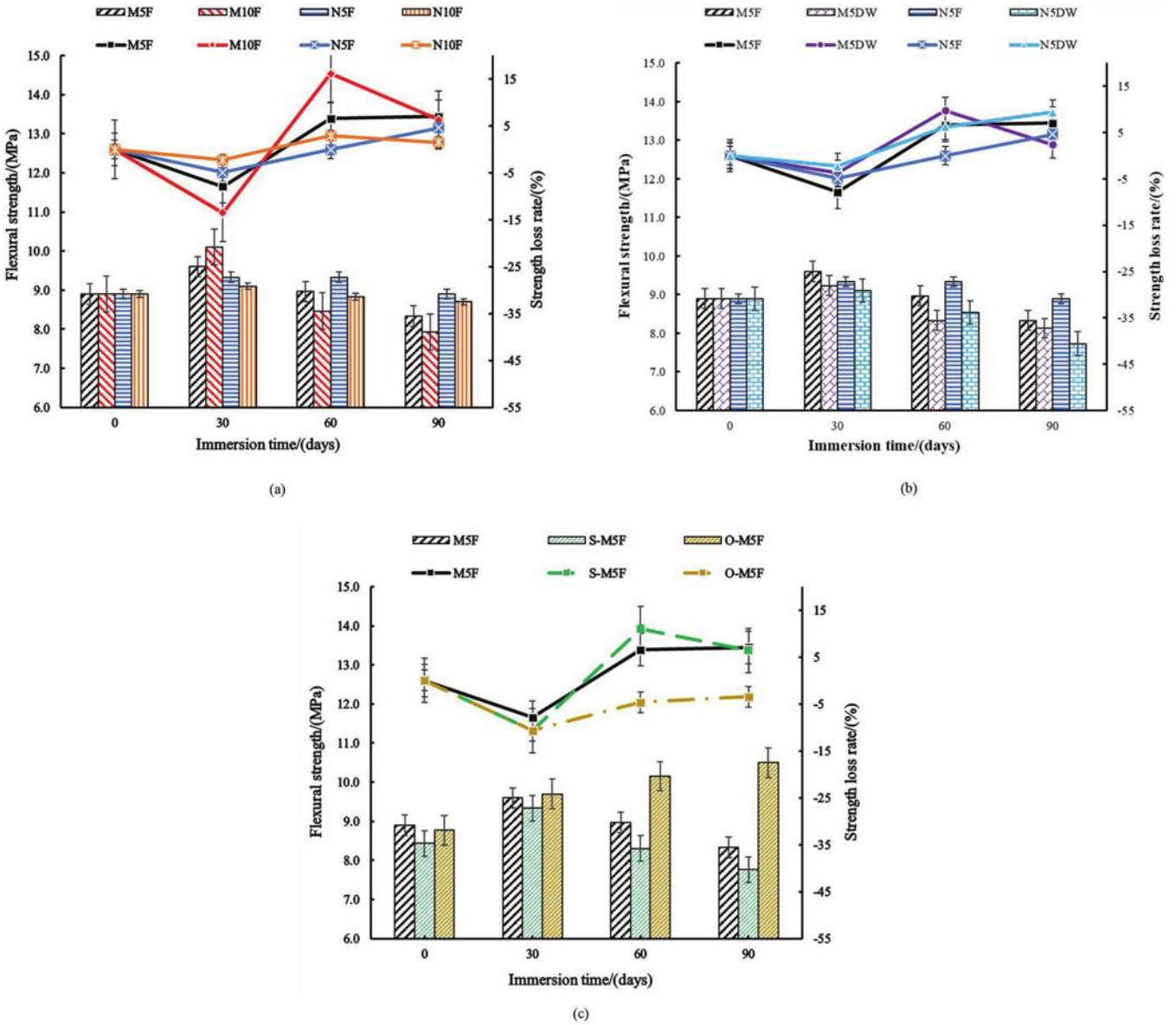

Fig. 4—(a) Effect of different sulfate concentrations on flexural strength; (b) effect of different erosion methods on flexural strength; and (c) effect of control group on flexural strength at different erosion times.

from –7.3 to –4.6% and a loss of flexural strength between 4.9 and –3.4%. The compressive and flexural strengths of M5F and S-M5F continued to decrease, with 12.6 and 12.6% losses in compressive strength, and 7.1 and 6.4% losses in flexural strength.

In summary, from the perspective of sulfate species, concentration, and erosion mode, the erosion of $MgSO_4$ is significantly greater than Na_2SO_4. Besides, high-concentration sulfate experiences greater erosion than low-concentration sulfate, and the erosion mode of the sulfate wetting-and-drying cycle is greater than full immersion. Concerning the sulfate erosion resistance of the three materials, after 90 days of erosion, the sulfate-resistance ability of the mechanically ground alkali-activated cementitious material is stronger than the sample prepared by simple mixing but is still less resistant than OPC. In contrast to the experimental findings of this study, Karakoç et al.[30] and Alcamand et al.[31] concluded that although the strength of alkali-excited materials decreases with increasing sulfate concentration and erosion time in the early stages of erosion, the strength decreases to a lesser extent in the later stages of erosion.

Analysis of erosion products and erosion mechanism

Fourier-transform infrared spectroscopy—To reduce the error of the test results, a fragment 5 mm away from the surface of the mortar specimens was chosen as the microscopic test sample. Figure 5 presents the schematic diagram of the experiment. Based on the change rule of chemical composition and functional groups of erosion products, the influence mechanism of sulfate type, sulfate concentration, and erosion mode on sulfate erosion of the mortar specimens was explored. Figures 6 to 8 display the FTIR curves of the specimens under different erosion conditions.

Existing research[32-34] shows that according to different sulfate erosion products, sulfate erosion types are divided into the following three types: ettringite ($3CaO{\cdot}Al_2O_3{\cdot}3CaSO_4{\cdot}32H_2O$), gypsum ($CaSO_4$), and thaumasite

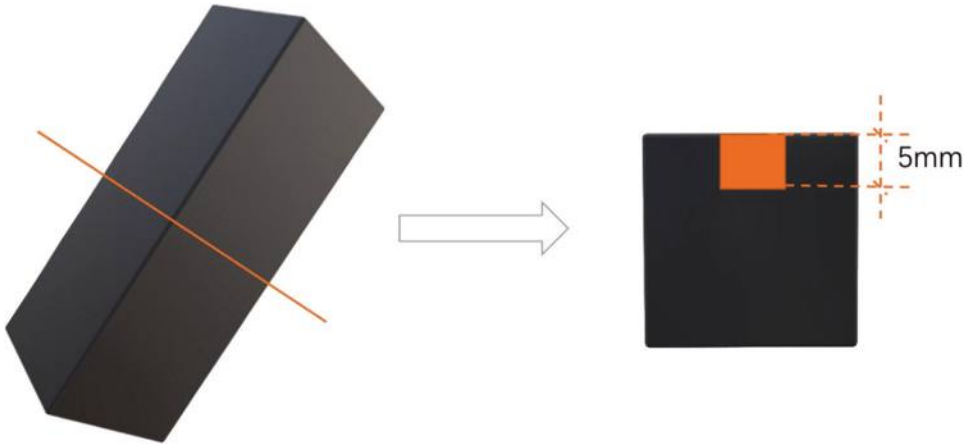

Fig. 5—Diagram of test sample sampling.

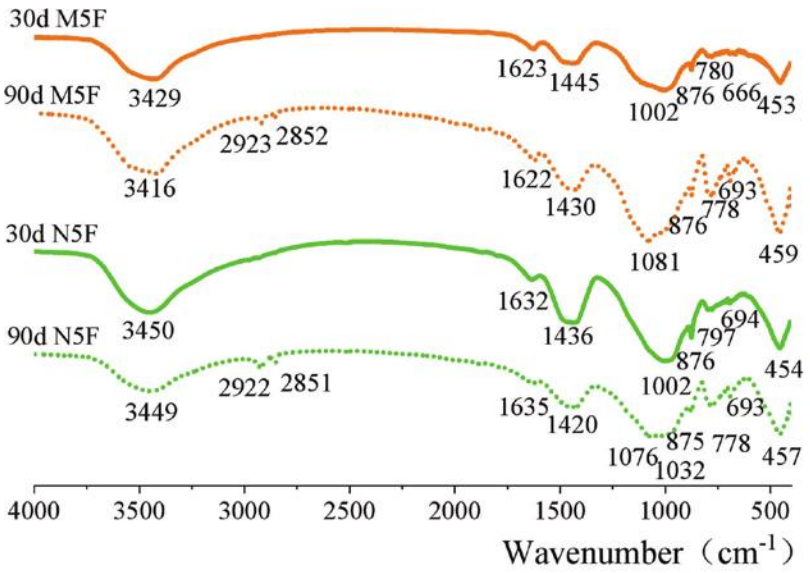

(a)

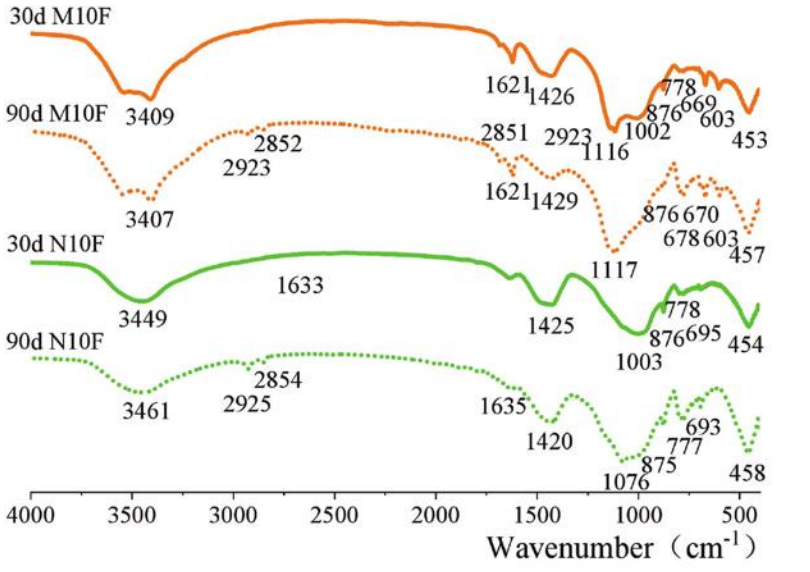

(b)

Fig. 6—(a) FTIR spectra at 5% erosion concentration; and (b) FTIR spectra at 10% erosion concentration.

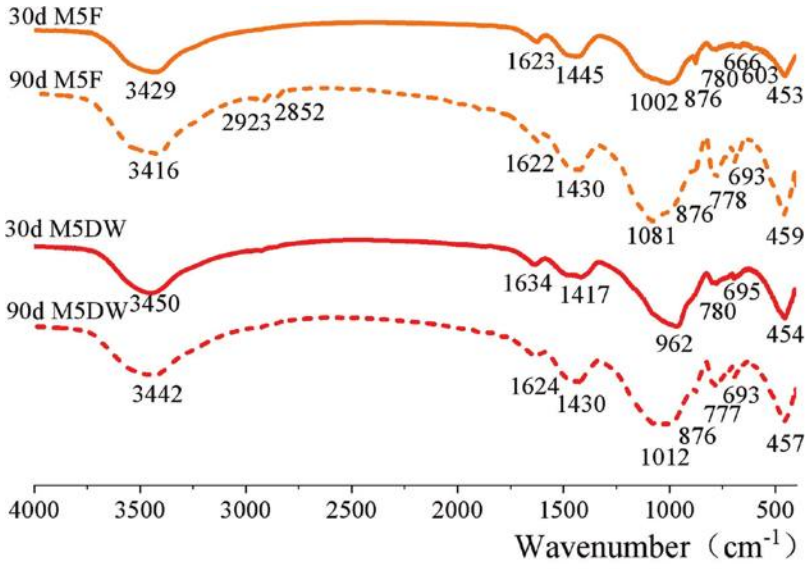

(a)

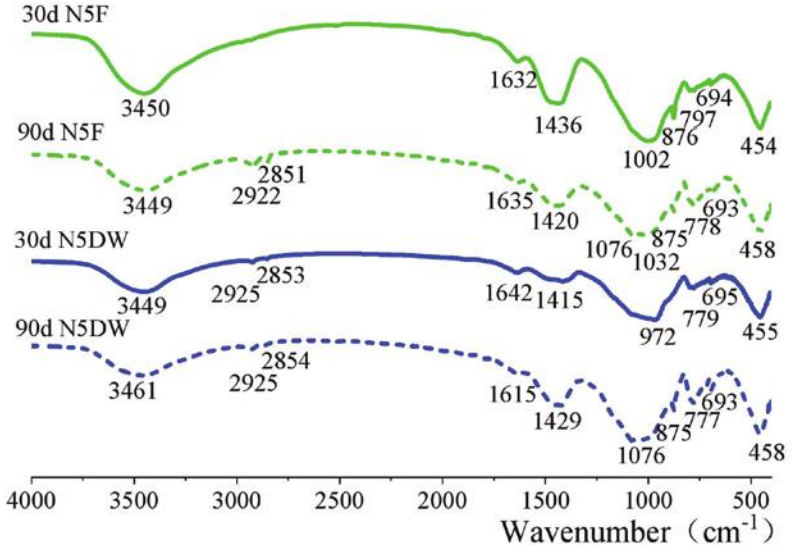

(b)

Fig. 7—(a) FTIR spectra of $MgSO_4$ solution under erosion conditions; and (b) FTIR spectra of Na_2SO_4 solution under erosion conditions.

($CaCO_3 \cdot CaSiO_3 \cdot CaSO_4 \cdot 15H_2O$). According to the FTIR curves in Fig. 6 to 8, the stretching vibration of the S-O bond at 1080 cm^{-1} and the bending vibration peak at 603 cm^{-1} appear, indicating that SO_4^{2-} exists in the sample. The characteristic peaks at 660 and 460 cm^{-1} indicate that gypsum crystals also exist in the sample,[35] but the stretching vibration characteristic peaks of the Al-O bond and SiO_6 are not observed at 550 and 750 cm^{-1}. Therefore, it can be preliminarily speculated that the mechanochemical one-part alkali-activated material mostly experiences gypsum-type erosion damage under sulfate attack. Additionally, there are obvious characteristic peaks at 876 and 1458 cm^{-1} bands in the sulfate attack specimens. These are caused by bending vibration and stretching vibration of the O-C-O bond,[36] indicating that carbonate is present in the sample. With the erosion of sulfate into the interior of the specimen, the content of metal cations (Mg^{2+} and Na^+) in the pore solution of the specimen increases significantly. There is a certain concentration of OH^- in the pore solution, so Mg^{2+} and OH^- can easily combine to form $Mg(OH)_2$ with lower solubility, as Eq. (1) shows. This subsequently leads to aggregation of the O-H bond, which is confirmed by the characteristic peaks of O-H bonds causing stretching and bending vibrations in the 3410 and 1620 cm^{-1} bands.[37]

$$Ca(OH)_2 + Mg^{2+} + SO_4^{2-} \rightarrow CaSO_4 + Mg(OH)_2 \quad (1)$$

$$C(\text{-A})\text{-S-H} + Mg^{2+} + SO_4^{2-} + 2H_2O \rightarrow M(\text{-A})\text{-S-H} + 2H_2O \cdot CaSO_4 \quad (2)$$

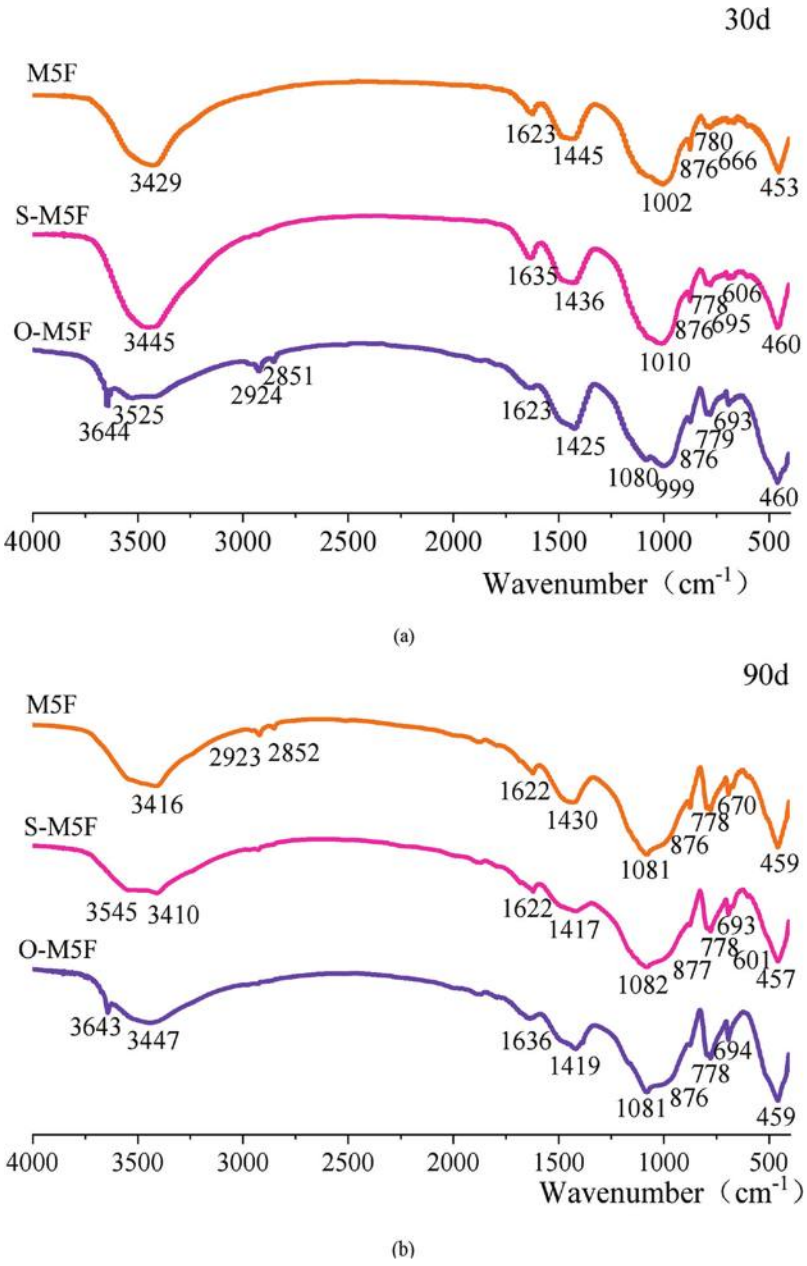

Fig. 8—(a) FTIR spectra of eroded 30-day specimens; and (b) FTIR spectra of eroded 90-day specimens.

Figure 6 presents the FTIR change of sulfate species and concentrations on the erosion products of mortar specimens. Compared with Na_2SO_4 erosion, under the action of $MgSO_4$ erosion, the FTIR curve has more characteristic peaks of gypsum at the 603 and 660 cm^{-1} bands. At the same concentration, the gypsum content after 90 days is higher than at 30. At the same stage, the characteristic peak of gypsum on M10F is more obvious than for M5F, indicating that the gypsum content increases with erosion time and concentration. With larger Mg^{2+} concentrations in the solution, Ca^{2+} is removed from C-S-H and C-A-S-H and Mg^{2+} replaces Ca^{2+} to form new M-S-H and M-A-S-H without bond strength.[38,39] Subsequently, the dissociated Ca^{2+} combines with SO_4^{2-} to form expansive gypsum, such as in Eq. (2). The volume of $2H_2O{\cdot}CaSO_4$ formed with pore water increases by a factor of 1.24. Besides, the pores of the specimens are subjected to expansion and extrusion pressure on the pore walls due to an increase in the volume of erosion products, resulting in the generation of microcracks. The width of the cracks grows with increased concentrations and erosion time, and the strength of the specimen also decreases rapidly. The phenomenon of specimen edges falling off also becomes more serious with increased concentrations. Figure 9(a) illustrates the appearance of the specimens. Characteristic peaks near 2925 cm^{-1} appear on the FTIR curve, revealing that calcite is produced by $MgSO_4$ and Na_2SO_4 solution erosion. The characteristic peaks of calcite produced by sodium salt are more obvious. Compared with $MgSO_4$ salt erosion, sodium salt erosion also has its unique erosion products. The characteristic peak intensities of the Na_2SO_4 erosion specimens at 876 cm^{-1} and 1458 cm^{-1} bands are more obvious, indicating that more carbonates are generated in the Na_2SO_4 erosion specimens. This carbonate does not result in excessive volume expansion, and the integrity of

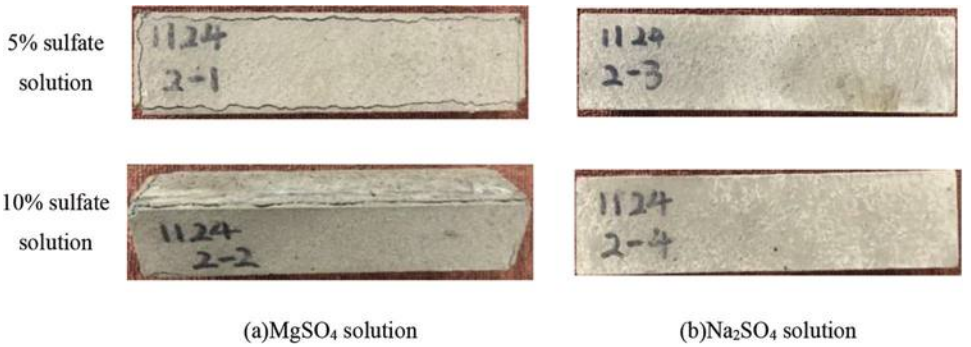

Fig. 9—Appearance effect of sulfate type and concentration on appearance of specimens after 90 days of corrosion.

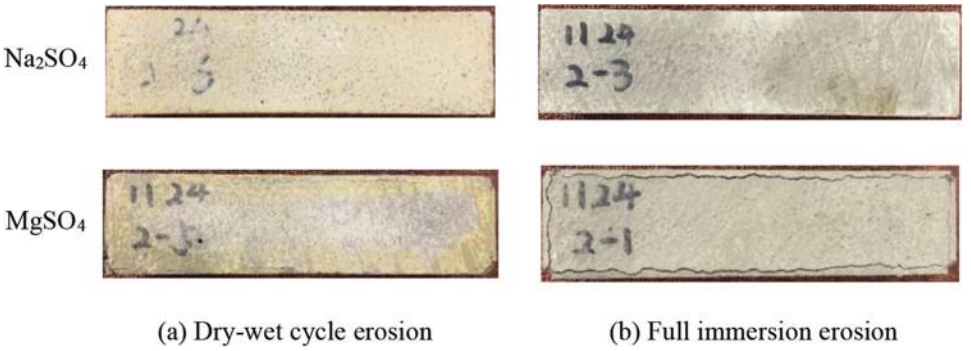

Fig. 10—Appearance effect of different erosion modes on specimens after 90 days of corrosion.

the specimen appears strong, without any obvious cracks, as Fig. 9(b) shows. This is consistent with the research results of Ismail et al.,[39] which stated that Na^+ ions are useful in maintaining the chemical stability of the pore solution of alkali-activated mortar specimens, while Mg^{2+} ions destroy C-S-H condensation.

Figure 7 represents FTIR changes of the erosion products of mortar specimens by sulfate erosion. Under $MgSO_4$ erosion, a weak characteristic peak at the 603 cm^{-1} band appears in the M5F specimen at 30 days, but a characteristic peak was not observed in the wetting-and-drying cycle erosion specimen. For specimens at the 90-day stage, characteristic peaks appear near 660 and 460 cm^{-1} in the two erosion modes. The characteristic peak of the specimen under full immersion is more obvious, indicating that gypsum is more likely to be produced by full-immersion erosion. Under the action of Na_2SO_4 solution erosion, the characteristic peak intensity of the N5DW specimen at 876 and 2925 cm^{-1} is greater than the N5F specimen, indicating that there is higher carbonate content in the wetting-and-drying cycle erosion specimen, which is in contact with the air for 8 hours when drying. The CO_2 in the air dissolves very easily in the surface adsorption water of the specimen. When the surface adsorption water gradually evaporates, it permeates the specimen through the liquid in the capillaries and promotes the carbonization of the specimen to produce calcium carbonate minerals. Observations indicate that the corners of the specimens subjected to wetting-and-drying cycle erosion appear to be detached, and their surfaces become rough and softened. For specimens subjected to full-immersion erosion, angular shedding is not obvious, but serious cracks occurred around the specimens corroded by $MgSO_4$ solution. Figure 10 shows the details.

Figure 8 presents the FTIR changes in erosion products of the one-part alkali-activated fly ash-slag mortar specimens prepared by the mechanochemical method, as well as the control group. Compared with O-M5F, the characteristic peak intensity of the S-M5F specimen at the 603 and 1100 cm^{-1} bands is more obvious, indicating that the gypsum content in the S-M5F specimen is higher. The stretching vibration frequency of O-H is in the range of 3550 to 3720 cm^{-1}, and the characteristic peak of 3644 cm^{-1} in the FTIR curve of the O-M5F corresponds to $Ca(OH)_2$. In contrast to the hydration products of traditional PC, the cohesive cementing of alkali-activated materials is mainly achieved by C-S-H and C-A-S-H. Thus, $Ca(OH)_2$ is not produced, which is consistent with the results of Komljenović et al.[40] The bond energy of C-O is lower than the C-S bond and is easier to break. Therefore, when $MgSO_4$ erodes, it preferentially reacts with $Ca(OH)_2$. The presence of $Ca(OH)_2$ effectively protects the stability of the C-S-H gel, while the alkali-activated material does not contain $Ca(OH)_2$. Compared to N-A-S-H, C-S-H and C-A-S-H are less resistant to sulfate,[41,42] causing a greater destructive effect. $MgSO_4$ erosion may destroy C-S-H and C-A-S-H gel, resulting in a more damaging effect. This is why the resistance of traditional PC to sulfate attack is better than the other two groups of alkali-activated materials, and the apparent compactness of traditional PC specimens is superior. The apparent compactness of the main part of the specimens prepared by mechanochemistry and simple mixing is satisfactory, but cracks appeared at the edge of the specimens, as Fig. 11 illustrates.

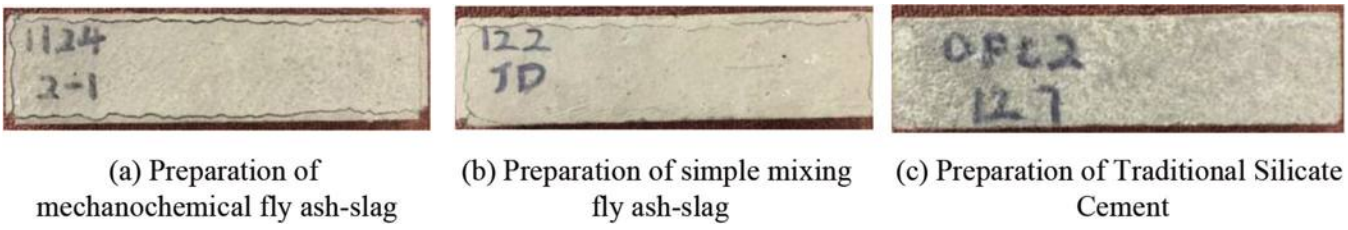

Fig. 11—Appearance effect of control specimen after 90 days of 5% $MgSO_4$ solution erosion.

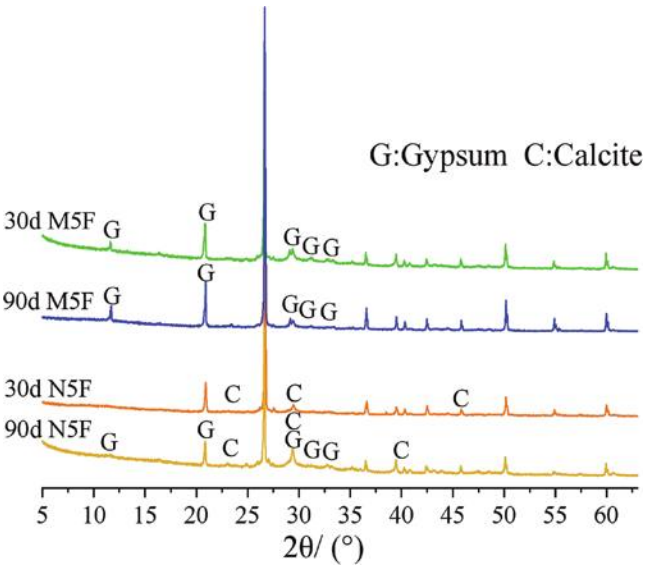

Fig. 12—XRD spectra of different sulfate attack specimens.

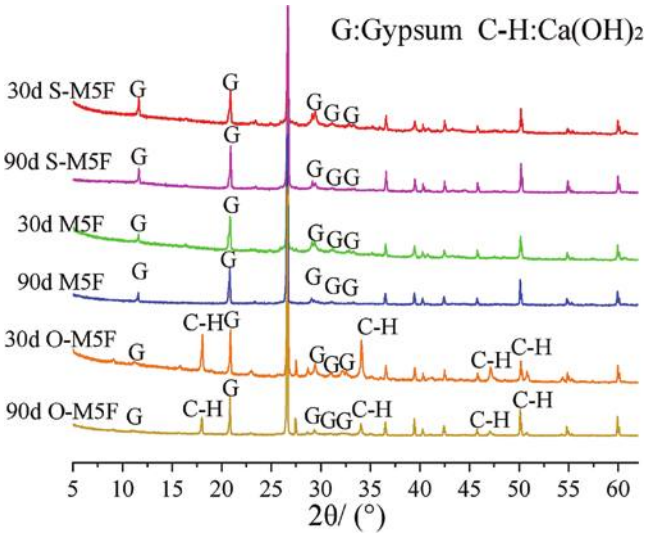

Fig. 13—XRD spectra of control immersion specimens.

X-ray diffraction analysis—XRD is the most powerful method for studying inorganic crystal structures and is suitable for the phase analysis of crystalline materials. According to differences in the diffraction spectrum of the crystal in the number, angle position, relative intensity order, and shape of the diffraction peak, the constituent elements or groups of crystalline substances can be determined.

Figures 12 and 13 present XRD images of the sulfate attack specimens. For the XRD of mortar specimens, the diffraction peak intensity of quartz crystal at 25 to 28 degrees is extremely high, and this high diffraction peak masks the weak diffraction peaks of other crystals. At the positions of 25 to 30 degrees, a wide dispersion peak appears in the spectra, which indicates the existence of amorphous substances, mostly comprising N-A-S-H and C-A-S-H. Additionally, C-S-H gel causes the peaks at 32 to 40 degrees and 45 to 50 degrees.[43] In this study, the corrosion products of sulfate attack mortar specimens were analyzed using XRD analysis technology and compared with the results of the corrosion products obtained by FTIR analysis to obtain more accurate experimental results. According to the XRD analysis, the crystals in the erosion products mainly contain gypsum, $Ca(OH)_2$, and calcite.

Figure 12 displays XRD spectra of different sulfate attack specimens. The product of $MgSO_4$ solution erosion is mainly gypsum, while Na_2SO_4 solution erosion contains parts of gypsum, but mostly calcite. With increased erosion times from 30 to 90 days, the diffraction peak intensity of gypsum crystals in the XRD specimens increases moderately for $MgSO_4$ solution erosion. However, the types of erosion products do not change. Comparing the erosion products of the Na_2SO_4 solution and the $MgSO_4$ solution, after 30 days, only the diffraction peak of calcite crystal was found in the XRD specimens of the Na_2SO_4 solution erosion products. At 90 days, there are many weak diffraction peaks of gypsum crystal in the XRD specimens, and the diffraction peak of calcite is also enhanced. This phenomenon further illustrates that $MgSO_4$ solution erosion produces a large amount of gypsum and results in severe gypsum-type erosion damage. For Na_2SO_4 solution erosion, in the early stage of erosion, the damage is mainly carbonized. However, in the later stage of erosion, carbonation degradation and gypsum erosion damage occur simultaneously. Nevertheless, sodium sulfate solution erosion produced less gypsum-type damage than magnesium sulfate solution erosion, which is consistent with the FTIR analysis results.

Figure 13 shows the XRD diagram of the immersed specimens from the control group. Compared with the one-part alkali-activated specimens prepared by mechanochemistry, the sulfate attack products all contain gypsum crystal diffraction peaks. When the erosion time is 30 days, the gypsum crystal diffraction peak intensity of the S-M5F specimen is greater than the M5F specimen, while the gypsum diffraction peak of the O-M5F specimen is not obvious. After 90 days, the diffraction peaks of gypsum in the control group were enhanced, indicating an increased accumulation of gypsum from erosion. Besides, the specimens exhibit expansion cracking, as Fig. 11 illustrates. In the XRD specimens, the O-M5F sample has an obvious $Ca(OH)_2$ diffraction peak, which is produced by the hydration of traditional silicate

cement. However, it could not be determined whether they are erosion products or not. In Fig. 13, the intensity of the $Ca(OH)_2$ diffraction peak of the O-M5F specimen decreases with longer invasion times. It is possible that the decrease in $Ca(OH)_2$ content is caused by resistance to sulfate attack. Sulfate invades the pore solution with high alkalinity, while Mg^{2+} and OH^- combine to form $Mg(OH)_2$. This substance is insoluble in water, and consequently reduces the alkalinity of the pore solution. To maintain the alkaline balance of the pore solution, the slightly soluble $Ca(OH)_2$ solid constantly dissolves in water, resulting in a continuous decrease of $Ca(OH)_2$ and causing a softening of colloidal sand and reduction in strength.[44] The hydration products of alkali-activated cementitious materials are mainly C-S-H and C-A-S-H, while almost no $Ca(OH)_2$ and stable bonded aluminum phases are produced.[45] Therefore, no $Ca(OH)_2$ diffraction peak was observed in the alkali-activated material specimens.

Mercury intrusion porosimetry—The pore structure connects the microstructure and macrostructure of the mortar, which is an important factor affecting mechanical properties and durability. There is a wide range of hole structure size distributions, the pore shape varies, and the system is complex. The pore structure may be divided into gel pores (<10 nm), transition pores (10 to 100 nm), capillary pores (100 to 1000 nm), and large pores (>1000 nm), according to the pore size.[46,47] Some scholars[48,49] believe that the strength and durability of concrete mainly depend on harmful pores larger than 100 nm, while pores smaller than 100 nm have a limited influence. In this section, MIP was used to analyze the porosity of mortar specimens against sulfate attack. This method measures pores with diameters of 0.005 to 1000 μm and provides valuable information regarding the pore structure analysis of concrete, as Fig. 14 displays.

Figure 14(a) shows the pore structure parameters of mortar specimens subjected to different types of sulfate attack. With increased erosion time, the pore structure distribution becomes homogenized, thus increasing the harmful pores and decreasing the porosity of the specimen. Taking $MgSO_4$ corrosion as an example, the porosity, gel pores, transition pores, capillary pores, and macropores of the 90-day specimens change by –24.55%, 11.75%, –49.80%, 18.61%, and 31.01%, respectively, compared with the 30-day specimens. For the $MgSO_4$ erosion specimens, in the early stage of erosion, new C-A-S-H and C-S-H gels are generated. This is due to the secondary volcanic ash reaction of fly ash, which may effectively fill the pores of specimens and increase the compactness. At the same time, the surplus gypsum produced by $MgSO_4$ erosion may fill the pores further. However, with an increase in the invasion time, the pozzolanic effect decreases, but the gypsum produced by erosion continues to increase. Excessive gypsum accumulation is certain to exert tremendous pressure on the pores, which increases the size of the small pores as well as the number of harmful pores. It also weakens erosion resistance and allows the large pores to progress into microfractures. When the microcracks connect, the specimen may suffer acute damage and the strength of the specimen may decrease rapidly. In the early stage of erosion of the Na_2SO_4 specimen, the calcium carbonate minerals produced by Na_2SO_4 erosion fill the pores and make them denser, thus enhancing the strength of the specimen. Furthermore, continuous accumulation of calcium carbonate minerals generates huge extrusion pressure on the pore walls, leading to microcracks inside the specimen and prompting a rapid reduction in strength. Therefore, a much more obvious reduction in strength occurs in the later stages of sulfate invasion.

Figure 14(b) illustrates the pore structure parameters of the control group mortar specimens. It was observed that the pore structure of O-M5F was not significantly different after 30 and 90 days of erosion, with harmless gel pores and transition pores accounting for 71.19% of the total pore structure at 30 days and 69.85% at 90 days. The main pore structures of S-M5F and M5F are also predominantly gel pores and transition pores, accounting for 71.53% and 61.91% of the total pore structure, respectively. Previous reports have shown that the pore size of alkali slag materials is mainly distributed between 1 and 20 nm, while the pore size of OPC is between 10 and 100 nm.[50,51] The O-M5F specimen has small porosity, and the C-S-H gel produced by conventional PC fills the pore structure and microcracks, leading to a reduction in the proportion of large pores and cracks with high compactness. This effectively prevents the sulfate erosion solution from entering the interior of the specimen and slows down the replacement reaction of Mg^{2+} and SO_4^{2-} with Ca^{2+} in C-S-H, thus reducing the damage caused by sulfate erosion.

The gel pore occupancy of the alkali-excited material is greater, and the water absorption rate is two to three times higher than OPC,[52,53] which provides Mg^{2+} and SO_4^{2-} with excellent channels for erosion, allowing them to gradually migrate to the interior of the specimen with the pore solution. Additionally, the concentration of alkali metal ions in the pore solution of the alkali slag material is high, exceeding OPC by nearly 10 times.[54] The high alkalinity of the pore solution provides suitable reaction conditions for Mg^{2+}, OH^-, and SO_4^{2-} to combine with Ca^{2+} in C(-A)-S-H, destroying the C(-A)-S-H gel bonds and making the pore structure of the specimen flimsy. However, the flimsy pore structure further contributes to the accelerated erosion rate, and the alkali-excited material specimens suffer severe erosion damage. Mechanical-force chemistry not only further activates the volcanic ash activity of the precursors, but also allows the precursors and alkali excipients to mix sufficiently for a stable and effective volcanic ash reaction, resulting in higher strength, less porosity, and superior resistance to sulfate in M5F than in S-M5F.

CONCLUSIONS

In this paper, the mechanochemical preparation of one-part alkali-excited mortars for resistance to sulfate attack was systematically studied. Based on macro and micro experimental data and experimental results, the following conclusions were obtained:

1. The tests in this paper show that highly concentrated $MgSO_4$ solution damages the strength of the specimens most severely under wetting-and-drying cyclic conditions. This is probably because the $MgSO_4$ solution not only provides

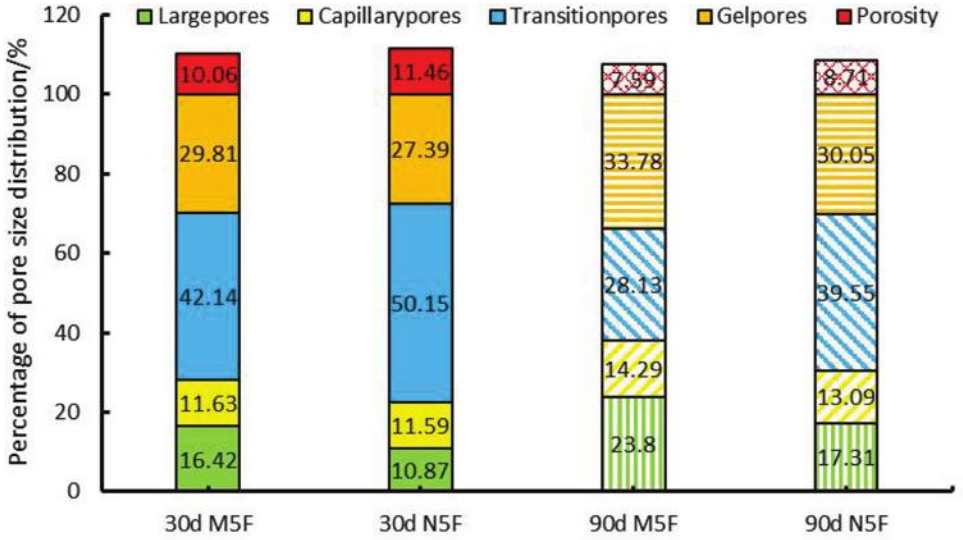

(a)

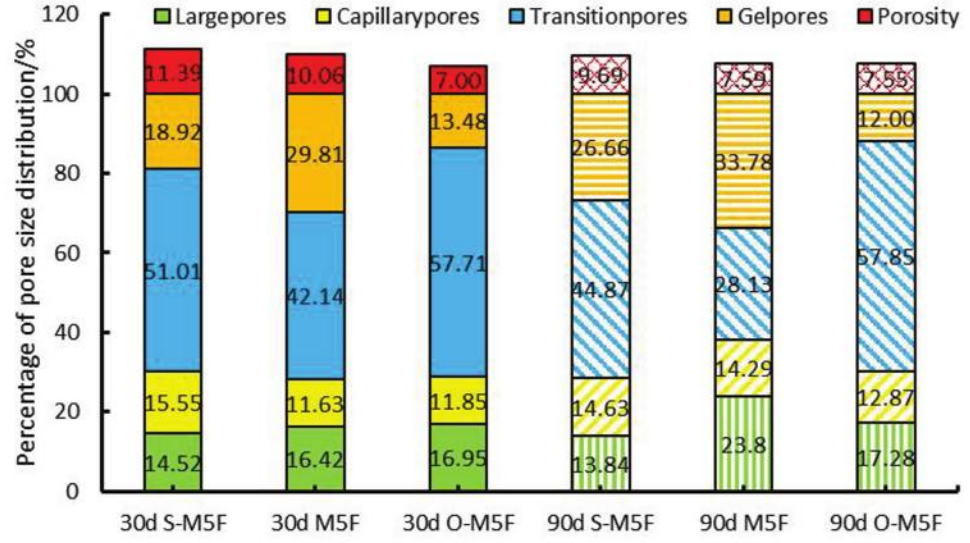

(b)

Fig. 14—(a) Pore structure changes under different kinds of sulfate erosion conditions; and (b) changes in pore structure of control group under different erosion time conditions.

erosive SO_4^{2-} ions, but Mg^{2+} ions are also involved in the erosion process. Moreover, there are variations in the sensitivity of flexural and compressive strength to different types of sulfate erosion. The compressive strength of specimens is more sensitive to $MgSO_4$ solution erosion, and the flexural strength is more sensitive to Na_2SO_4 solution erosion.

2. The mechanical-force chemical activation of gelling material precursors promotes the fine release of precursor particles with the promotion of volcanic ash activity and allows full mixing of the precursors and solid alkali-excitation agent. The adequate mixing of single-part alkali-excited materials provides a guarantee for stable and effective volcanic ash reactions. This is reflected in both porosity and strength, because M5F has lower porosity than S-M5F, while M5F has higher strength than S-M5F.

3. Under different types of sulfate erosion, the erosion products vary. According to Fourier-transform infrared spectroscopy (FTIR) and X-ray diffraction (XRD) analysis, it was observed that under Na_2SO_4 solution erosion, the erosion products of the specimen are mainly calcite in the early stage and a combination of calcite and gypsum in the later stage. For $MgSO_4$ solution erosion, the erosion products generated inside the specimen are gypsum, which indicates gypsum-type swelling erosion damage.

4. The mechanism of resistance to sulfate attack varies between alkali-stimulated cementitious materials and ordinary portland cement (OPC). The Ca^{2+} in C-A-S-H in alkali-excited cementitious materials is replaced by Na^+ and Mg^{2+} ions, and free Ca^{2+} combines with SO_4^{2-} to produce gypsum. Conventional silicate cements contain large amounts of $Ca(OH)_2$, which provides Ca^{2+} and slows the rate of C-S-H gel destruction, resulting in silicate cement samples that maintain some steady-state strength loss and pore structure

damage at 90 days of erosion, with less damage than alkali-excited specimens.

5. In this paper, the three aspects of sulfate type, concentration, and erosion mode were studied to simulate a genuine erosion environment. However, real environments are very complex and factors such as load size, temperature change, and sulfate type all have an impact on erosion. Therefore, further investigations are required to understand the mechanism of sulfate erosion from other aspects, which will help to improve the study of the sulfate erosion of alkali-excited materials.

AUTHOR BIOS

Wenda Wu *is an Associate Researcher, Master Supervisor, and Quanzhou Talent Harbor High-Level Talent in Quanzhou, Fujian, China. He attended the School of Advanced Manufacturing at Fuzhou University, Fuzhou, Fujian, China. His research interests include alkali-excited cements/concrete, self-consolidating concrete materials/structural properties, and recycled concrete materials/structural properties.*

Shilong Ma *is a Graduate Student in the School of Advanced Manufacturing at Fuzhou University. His research interests include one-part alkali-excited materials.*

Yuanda Wang *is a Graduate Student in the College of Civil Engineering at Fuzhou University. His research interests include the durability performance of alkali-excited materials.*

Xuefang Wang *is an Associate Researcher and Master Supervisor in Fujian, China. She received her PhD in engineering from the School of Advanced Manufacturing at Fuzhou University. Her research interests include the research and application of self-consolidating high-performance concrete and its structure, research on volume stability and durability of high-performance concrete and its ratio optimization design, and environmentally friendly and energy-saving cement-based materials.*

Liwei Xu *is a Professor, Senior Engineer, Master's Degree Supervisor, and was a Visiting Scholar at Michigan State University, East Lansing, MI, in 2016, and at the University of Applied Sciences, Cologne, Germany, in 2011.*

Shichang Ye *is an Engineer at Sanming Yiyuan Electric Power Survey and Design Co., Ltd.*

ACKNOWLEDGMENTS

The authors would like to thank the China Postdoctoral Science Foundation for providing equipment and funding for this work. This work was supported by the National Outstanding Youth Science Fund Project of the National Natural Science Foundation of China (Grant No. 51808124), the Innovative Research Group Project of the National Natural Science Foundation of China (Grant No. 2019M652246), and the Fujian Provincial Department of Science and Technology (Grant No. 2019HZ07011). The authors declare that they have no known competing financial interests or personal relationships that might affect the work reported in this paper.

REFERENCES

1. Shi, C; Krivenko, P. V.; and Roy, D., *Alkali-Activated Cements and Concretes*, Taylor & Francis, London, UK, 2006.

2. Pacheco-Torgal, F.; Castro-Gomes, J.; and Jalali, S., "Alkali-Activated Binders: A Review: Part 1. Historical Background, Terminology, Reaction Mechanisms and Hydration Products," *Construction and Building Materials*, V. 22, No. 7, 2008, pp. 1305-1314. doi: 10.1016/j.conbuildmat.2007.10.015

3. Purdon, A. O., "The Action of Alkalis On Blast-Furnace Slag," *Journal of the Society of Chemical Industry*, V. 59, No. 9, 1940, pp. 191-202.

4. Duxson, P., and Provis, J. L., "Designing Precursors for Geopolymer Cements," *Journal of the American Ceramic Society,* V. 91, No. 12, 2008, pp. 3864-3869. doi:10.1111/j.1551-2916.2008.02787.x

5. Peng, M. X.; Wang, Z. H.; Shen, S. H.; Xiao, Q. G.; Li, L. J.; Tang, Y. C.; and Hu, L. L., "Alkali Fusion of Bentonite to Synthesize One-Part Geopolymeric Cements Cured at Elevated Temperature by Comparison With Two-Part Ones," *Construction and Building Materials*, V. 130, 2017, pp. 103-112 doi: 10.1016/j.conbuildmat.2016.11.010

6. Habert, G.; d'Espinose de Lacaillerie, J. B.; and Roussel, N., "An Environmental Evaluation of Geopolymer Based Concrete Production: Reviewing Current Research Trends," *Journal of Cleaner Production,* V. 19, No. 11, 2011, pp. 1229-1238. doi: 10.1016/j.jclepro.2011.03.012

7. McLellan, B. C.; Williams, R. P.; Lay, J.; van Riessen, A.; and Corder, G. D., "Costs and Carbon Emissions For Geopolymer Pastes in Comparison to Ordinary Portland Cement," *Journal of Cleaner Production*, V. 19, No. 9-10, 2011, pp. 1080-1090. doi: 10.1016/j.jclepro.2011.02.010

8. Davidovits, J.; Comrie, D. C.; Paterson, J. H.; and Ritcey, D. J., "Geopolymeric Concretes for Environmental Protection," *Concrete International*, V. 12, No. 7, July 1990, pp. 30-40.

9. Stellacci, P.; Liberti, L.; Notarnicola, M.; and Bishop, P. L., "Valorization of Coal Fly Ash by Mechano-Chemical Activation: Part I. Enhancing Adsorption Capacity," *Chemical Engineering Journal,* V. 149 No. 1-3, 2009, pp. 11-18. doi: 10.1016/j.cej.2008.06.043

10. Temuujin, J.; Williams, R. P.; and van Riessen, A., "Effect of Mechanical Activation of Fly Ash on the Properties of Geopolymer Cured at Ambient Temperature," *Journal of Materials Processing Technology,* V. 209, No. 12-13, 2009, pp. 5276-5280. doi: 10.1016/j.jmatprotec.2009.03.016.10.1016

11. Kumar, R.; Kumar, S.; Badjena, S.; and Mehrotra, S. P., "Hydration of Mechanically Activated Granulated Blast Furnace Slag," *Metallurgical and Materials Transactions B*, V. 36, No. 6, 2005, pp. 873-883. doi: 10.1007/s11663-005-0089-x

12. Zhao, J.; Wang, D.; and Liao, S., "Effect of Mechanical Grinding on Physical and Chemical Characteristics of Circulating Fluidized Bed Fly Ash From Coal Gangue Power Plant," *Construction and Building Materials*, V. 101, Part 1, 2015, pp. 851-860. doi: 10.1016/j.conbuildmat.2015.10.144

13. Feng, P.; Garboczi, E. J.; Miao, C.; and Bullard, J. W., "Microstructural Origins of Cement Paste Degradation by External Sulfate Attack," *Construction and Building Materials*, V. 96, 2015, pp. 391-403. doi: 10.1016/j.conbuildmat.2015.07.186

14. Ikumi, T.; Cavalaro, S. H. P.; Segura, I.; de la Fuente, A.; and Aguado, A., "Simplified Methodology to Evaluate the External Sulfate Attack in Concrete Structures," *Materials & Design*, V. 89, 2016, pp. 1147-1160. doi: 10.1016/j.matdes.2015.10.084

15. Torres, S. M.; Sharp, J. H.; Swamy, R. N.; Lynsdale, C. J.; and Huntley, S. A., "Long Term Durability of Portland-Limestone Cement Mortars Exposed to Magnesium Sulfate Attack," *Cement and Concrete Composites*, V. 25, No. 8, 2003, pp. 947-954. doi: 10.1016/S0958-9465(03)00160-4

16. Lothenbach, B.; Bary, B.; Le Bescop, P.; Schmidt, T.; and Leterrier, N., "Sulfate Ingress in Portland Cement," *Cement and Concrete Research*, V. 40, No. 8, 2010, pp. 1211-1225. doi: 10.1016/j.cemconres.2010.04.004

17. Al-Amoudi, O. S. B., "Attack on Plain and Blended Cements Exposed to Aggressive Sulfate Environments," *Cement and Concrete Composites*, V. 24, No. 3-4, 2002, pp. 305-316. doi: 10.1016/S0958-9465(01)00082-8

18. Comanescu, I.; Melchers, R.E.; and Taxén, C., "Corrosion and Durability of Offshore Steel Water Injection Pipelines," *Ships and Offshore Structures*, V. 11, No. 4, 2016, pp. 424-437. doi: 10.1080/17445302.2015.1014249

19. Rabeh, M.; Petersen, J.; and O'Hearn, S., "Insulation Optimization Improves Safety, Reduces Corrosion Risks," *Offshore*, V. 78, No. 2, 2018, pp. 32-33. doi: 10.14359/51663865

20. Tan, L.; Wang, F.; Liang, M.; Wang, X.; Das, R.; Mao, D.; and Luo, Y., "Antibiotic Resistance Genes Attenuated With Salt Accumulation in Saline Soil," *Journal of Hazardous Materials*, V. 374, 2019, pp. 35-42. doi: 10.1016/j.jhazmat.2019.04.020

21. Wang, X.; Xue, Z.; Lu, X.; Liu, Y.; Liu, G.; and Wu, Z., "Salt Leaching of Heavy Coastal Saline Silty Soil by Controlling the Soil Matric Potential," *Soil and Water Research*, V. 14, No. 3, 2019, pp. 132-137. doi: 10.17221/106/2018-SWR

22. Rui, H.; Zheng, S.; Gan, V. J. L.; Wang, Z.; Fang, J.; and Shao, Y., "Damage Mechanism and Interfacial Transition Zone Characteristics of Concrete under Sulfate Erosion and Dry-Wet Cycles," *Construction and Building Materials*, V. 255, 2020, Article No. 119340. doi: 10.1016/j.conbuildmat.2020.119340

23. Cao, M. L.; Yao, H.; and Cui, S. C., "Experimental Study on Impact Resistance of $CaCO_3$ Whisker-Reinforced Cement Mortar," *Applied Mechanics and Materials*, V. 99-100, Sept. 2011, pp. 706-710. doi: 10.4028/www.scientific.net/AMM.99-100.706

24. Ikumi, T., and Segura, I., "Numerical Assessment of External Sulfate Attack in Concrete Structures. A Review," *Cement and Concrete Research*, V. 121, 2019, pp. 91-105. doi: 10.1016/j.cemconres. 2019.04.010

25. Sun, D.; Wu, K.; Shi, H.; Zhang, L.; and Zhang, L., "Effect of Interfacial Transition Zone on the Transport of Sulfate Ions in Concrete," *Construction and Building Materials*, V. 192, Dec. 2018, pp. 28-37 doi: 10.1016/j.conbuildmat. 2018.10.140

26. Kong, L.; Ge, Y.; Zhang, B.; and Zhang, W., "Effect of Water Release of Lightweight Aggregate on Secondary Hydration of Fly Ash," *Kuei*

Suan Jen Hsueh Pao/Journal of the Chinese Ceramic Society, V. 37, 2009, pp. 1239-1243.

27. Quan, X.; Wang, S.; Liu, K.; Zhao, N.; Xu, J.; Xu, F.; and Zhou, J., "The Corrosion Resistance of Engineered Cementitious Composite (ECC) Containing High-Volume Fly Ash and Low-Volume Bentonite against the Combined Action of Sulfate Attack and Dry-Wet Cycles," *Construction and Building Materials*, V. 303, No. 11, Oct. 2021, Article No. 124599

28. Wang, K.; Guo, J.; Liu, X.; Yang, L.; and Zhang, P., "Effect of Dry–Wet Ratio on Pore-Structure Characteristics of Fly Ash Concrete under Sulfate Attack," *Materials and Structures*, V. 54, No. 3, 2021, Article No. 100. doi: 10.1617/s11527-021-01700-2

29. Ganjian, E., and Pouya, H. S., "The Effect of Persian Gulf Tidal Zone Exposure on Durability of Mixes Containing Silica Fume and Blast Furnace Slag," *Construction and Building Materials*, V. 23, No. 2, 2009, pp. 644-652. doi: 10.1016/j.conbuildmat.2008.02.009

30. Karakoç, M. B.; Türkmen, I.; Maraş, M. M.; Kantarci, F.; and Demirboğa, R., "Sulfate Resistance of Ferrochrome Slag Based Geopolymer Concrete," *Ceramics International*, V. 42, No. 1, Part B, 2016, pp. 1254-1260. doi: 10.1016/j.ceramint.2015.09.058

31. Alcamand, H. A.; Borges, P. H. R.; Silva, F. A.; and Trindade, A. C. C., "The Effect of Matrix Composition and Calcium Content on the Sulfate Durability of Metakaolin and Metakaolin/Slag Alkali-Activated Mortars," *Ceramics International*, V. 44, No. 5, 2018, pp. 5037-5044. doi: 10.1016/j.ceramint.2017.12.102

32. Rozière, E.; Loukili, A.; El Hachem, R.; and Grondin, F., "Durability of Concrete Exposed to Leaching and External Sulphate Attacks," *Cement and Concrete Research*, V. 39, No. 12, 2009, pp. 1188-1198. doi: 10.1016/j.cemconres.2009.07.021

33. Kunther, W.; Lothenbach, B.; and Scrivener, K. L., "On the Relevance of Volume Increase for the Length Changes of Mortar Bars in Sulfate Solutions," *Cement and Concrete Research*, V. 46, 2013, pp. 23-29. doi: 10.1016/j.cemconres.2013.01.002

34. Müllauer, W.; Beddoe, R. E.; and Heinz, D., "Sulfate Attack Expansion Mechanisms," *Cement and Concrete Research*, V. 52, 2013, pp. 208-215. doi: 10.1016/j.cemconres.2013.07.005

35. Chang, J.; Gu, Y.; and Ansari, W. S., "Mechanism of Blended Steel Slag Mortar With CO_2 Curing Exposed to Sulfate Attack," *Construction and Building Materials*, V. 251, 2020, Article No. 118880. doi: 10.1016/j.conbuildmat.2020.118880

36. Yusuf, M. O., "Performance of Slag Blended Alkaline Activated Palm Oil Fuel Ash Mortar in Sulfate Environments," *Construction and Building Materials*, V. 98, 2015, pp. 417-424. doi: 10.1016/j.conbuildmat.2015.07.012

37. Lecomte, I.; Henrist, C.; Liégeois M.; Maseri, F.; Rulmont, A.; and Cloots, R., "(Micro)-Structural Comparison between Geopolymers, Alkali-Activated Slag Cement and Portland Cement," *Journal of the European Ceramic Society*, V. 26, No. 16, 2005, pp. 3789-3797. doi: 10.1016/j.jeurceramsoc.2005.12.021

38. Aydın, S., and Baradan, B., "Sulfate Resistance of Alkali-Activated Slag and Portland Cement Based Reactive Powder Concrete," *Journal of Building Engineering*, V. 43, 2021, Article No. 103205. doi: 10.1016/j.jobe.2021.103205

39. Ismail, I.; Bernal, S. A.; Provis, J. L.; Hamdan, S.; and van Deventer, J. S. J., "Microstructural Changes in Alkali Activated Fly Ash/Slag Geopolymers with Sulfate Exposure," *Materials and Structures*, V. 46, No. 3, 2013, pp. 361-373. doi: 10.1617/s11527-012-9906-2

40. Komljenović, M.; Baščarević, Z.; Marjanović, N.; and Nikolić, V., "External Sulfate Attack on Alkali-Activated Slag," *Construction and Building Materials*, V. 49, 2013, pp. 31-39. doi: 10.1016/j.conbuildmat.2013.08.013

41. Thokchom, S.; Ghosh, P.; and Ghosh, S., "Performance of Fly Ash Based Geopolymer Mortars in Sulphate Solution," *Journal of Engineering Science and Technology Review*, V. 3, No. 1, 2010, pp. 36-40.

42. Duan, P.; Yan, C.; and Zhou, W., "Influence of Partial Replacement of Fly Ash by Metakaolin on Mechanical Properties and Microstructure of Fly Ash Geopolymer Paste Exposed to Sulfate Attack," *Ceramics International*, V. 42, No. 2, Part B, 2016, pp. 3504-3517. doi: 10.1016/j.ceramint.2015.10.154

43. Aboulayt, A.; Riahi, M.; Ouazzani Touhami, M.; Hannache, H.; Gomina, M.; and Moussa, R., "Properties of Metakaolin Based Geopolymer Incorporating Calcium Carbonate," *Advanced Powder Technology*, V. 28, No. 9, 2017, pp. 2393-2401. doi: 10.1016/j.apt.2017.06.022

44. Chen, J.-K.; Qian, C.; and Song, H., "A New Chemo-Mechanical Model of Damage in Concrete under Sulfate Attack," *Construction and Building Materials*, V. 115, 2016, pp. 536-543. doi: 10.1016/j.conbuildmat.2016.04.074

45. Myers, R. J.; Bernal, S. A.; Gehman, J. D.; van Deventer, J. S. J.; and Provis, J. L., "The Role of Al in Cross-Linking of Alkali-Activated Slag Cements," *Journal of the American Ceramic Society*, V. 98, No. 3, 2015, pp. 996-1004. doi: 10.1111/jace.13360

46. Ozturk, A. U., and Baradan, B., "A Comparison Study of Porosity and Compressive Strength Mathematical Models with Image Analysis," *Computational Materials Science*, V. 43, No. 4, 2008, pp. 974-979. doi: 10.1016/j.commatsci.2008.02.011

47. Olsen, R. A.; Neubauer, C. M.; and Jennings, H. M., "Damage to the Pore Structure of Hardened Portland Cement Paste by Mercury Intrusion," *Journal of the American Ceramic Society*, V 80, No. 9, 1997, pp. 2454-2458. doi: 10.1111/j.1151-2916.1997.tb03144.x

48. Mehta, P. K., and Monteiro, P. J. M., *Concrete: Microstructure, Properties, and Materials*, McGraw-Hill, New York, 2006.

49. Jin, S.; Zhang, J.; and Han, S., "Fractal Analysis of Relation between Strength and Pore Structure of Hardened Mortar," *Construction and Building Materials*, V. 135, 2017, pp. 1-7. doi: 10.1016/j.conbuildmat.2016.12.152

50. Babaee, M., and Castel, A., "Water Vapor Sorption Isotherms, Pore Structure, and Moisture Transport Characteristics of Alkali-Activated and Portland Cement-Based Binders," *Cement and Concrete Research*, V. 113, 2018, pp. 99-120. doi: 10.1016/j.cemconres.2018.07.006

51. Li, Q.; Yang, Y.; Yang, K.; Chao, Z.; Tang, D.; Tian, Y.; Wu, F.; Basheer, M.; and Yang, C., "The Role of Calcium Stearate on Regulating Activation to Form Stable, Uniform and Flawless Reaction Products in Alkali-Activated Slag Cement," *Cement and Concrete Composites*, V. 103, 2019, pp. 242-251. doi: 10.1016/j.cemconcomp.2019.05.009

52. Li, Q.; Yang, K.; and Yang, C., "An Alternative Admixture to Reduce Sorptivity of Alkali-Activated Slag Cement by Optimising Pore Structure and Introducing Hydrophobic Film," *Cement and Concrete Composites*, V. 95, 2019, pp. 183-192. doi: 10.1016/j.cemconcomp.2018.11.004

53. Yang, K.; Yang, C.; Magee, B.; Nanukuttan, S.; and Ye, J., "Establishment of a Preconditioning Regime for Air Permeability and Sorptivity of Alkali-Activated Slag Concrete," *Cement and Concrete Composites*, V. 73, 2016, pp. 19-28. doi: 10.1016/j.cemconcomp.2016.06.019

54. Puertas, F.; Fernández-Jiménez, A.; Blanco-Varela, M. T., "Pore Solution in Alkali-Activated Slag Cement Pastes. Relation to the Composition and Structure of Calcium Silicate Hydrate," *Cement and Concrete Research*, V. 34, No. 1, 2004, pp. 139-148. doi: 10.1016/S0008-8846(03)00254-0

CALL FOR ACTION

ACI Invites You To...

Share your expertise

Do you have EXPERTISE in any of these areas?

- BIM
- Chimneys
- Circular Concrete Structures Prestressed by Wrapping with Wire and Strand
- Circular Concrete Structures Prestressed with Circumferential Tendons
- Concrete Properties
- Demolition
- Deterioration of Concrete in Hydraulic Structures
- Electronic Data Exchange
- Insulating Concrete Forms, Design, and Construction
- Nuclear Reactors, Concrete Components
- Pedestal Water Towers
- Pipe, Cast-in-Place
- Strengthening of Concrete Members
- Sustainability

Then become a REVIEWER for the *ACI Structural Journal* or the *ACI Materials Journal*.

Become a Reviewer for the ACI Journals

How to become a Reviewer:

1. Go to: **http://mc.manuscriptcentral.com/aci**;
2. Click on "Create Account" in the upper right-hand corner; and
3. Enter your E-mail/Name, Address, User ID and Password, and Area(s) of Expertise.

Update your Manuscript Central user account information

Did you know that the database for MANUSCRIPT CENTRAL, our manuscript submission program, is separate from the ACI membership database?

How to update your user account:

1. Go to **http://mc.manuscriptcentral.com/aci**;
2. Log in with your current User ID & Password; and
3. Update your E-mail/Name, Address, User ID and Password, and Area(s) of Expertise.

QUESTIONS?

E-mail any questions to Journals.Manuscripts@concrete.org.

American Concrete Institute

Always advancing

ACI MATERIALS JOURNAL TECHNICAL PAPER

Title No. 120-M25

Preparatory Study about Effect of Feldspar on Properties of Alkali-Activated Slag Concrete

by Alaa M. Rashad, Youssef A. Mosleh, and Mahmoud Gharieb

In spite of feldspars being the most plentiful components in the crust of the earth, their uses in alkali-activated materials are still too limited. In this work, for the first time, the effect of different ratios of potassium feldspar on the properties of alkali-activated slag (AAS) concrete was studied. The slag was partially replaced with 10 to 50% feldspar with a stride of 10 wt. %. The effects of feldspar on the workability, compressive strength, splitting tensile strength, water absorption, and total porosity of AAS concrete were investigated. Different techniques were applied to investigate the crystalline phases, hydration products, and microstructures of the critical samples. The results showed a positive effect of feldspar on workability, of which the workability increased with increasing feldspar ratio. The incorporation of 10% feldspar has a positive effect on compressive strength, splitting tensile strength, water absorption, total porosity, and refining the microstructure, while higher ratios than 10% have a negative effect.

Keywords: alkali-activated slag (AAS); compressive strength; feldspar; splitting strength; total porosity; water absorption.

INTRODUCTION

Recently, there is no material in existence more widely used than concrete. After water, it is the second most-used material on the planet. Currently, the global production of concrete is approximately 4.4 billion tons per year. This number is expected to increase to reach approximately 5.5 billion tons by 2025.[1] Because portland cement (PC) is the primary ingredient of concrete, a huge amount of cement is produced per year. Unfortunately, cement is the source of approximately 8% of global carbon dioxide (CO_2) emissions.[2] These recent high CO_2 emissions have led to an increase in the global temperature by an average of 1°C. It is expected that by 2025, the CO_2 emissions may increase as high as 450 to 550 ppm. This means that the average worldwide temperature may increase by approximately 1.4 to 5.8°C, leading to a negative effect on the economy, health of humanity, and environment.[3] The cement sector is the third-largest industrial pollution source, generating approximately 500,000 tons annually of nitrogen oxide (NO_x), sulfur dioxide (SO_2), and carbon monoxide (CO). Cement production consumes 12 to 15% of global energy resources per year.[4] At the same pace, the production of cement consumes a large amount of natural raw materials. One strategy to limit the consumption of cement is replacing some cement with cementitious materials such as fly ash (FA),[5] metakaolin (MK),[6] and slag.[7] Another more effective strategy to hinder cement production is producing new types of binders that are free from PC, such as alkali-activated materials (AAMs). Using the former materials have a positive effect on reducing CO_2 emissions and can reduce the energy consumption and virgin materials required for the PC industry. AAMs are produced by activating materials rich with aluminosilicate such as MK, FA, and slag. Through the different precursors used for AAMs, slag is the most widely used due to its availability and simple curing, which does not need heat curing.[8] Since the first use of alkali-activated slag (AAS) in 1930, when Kull investigated the setting time of slag powder activated with potash solution,[9] the development of AAS properties is still ongoing. The wide option to improve AAS systems is blended slag with a suitable amount of other material(s) such as quartz powder,[10] silica fume (SF), MK, FA, and so on.[11]

Feldspars are the most considerable mineral in the oceanic and continental earth crust. More than half of the earth's crust is made up of feldspar minerals.[12] They are an aluminosilicate based on the three-dimensional framework of linked Si and Al-O tetrahedral, and are mostly gray, pink, or white in color. Plagioclase and potassium feldspars are the two primary groups of feldspars.[13] Potassium feldspars have a wide range of applications, of which they play a crucial role in the production of fillers for rubber, paints, and the plastic and adhesive industries. In addition to these applications, they are also used as fluxes in ceramics and glass. Generally, there are numerous uses of feldspars on a daily basis, such as shower basins in bathrooms, floor tiles, fiberglass, drinking glasses, dishes, and tableware. In the field of cementitious materials, feldspar can be used as a pozzolanic material in PC systems. Yao et al.[14] showed that the pozzolanic activity of feldspar increased when decreasing its crystallization degree and vice versa. Khoshkbijari et al.[15] reported that the incorporation of 10 to 30% feldspar by weight in mortars as a cement substitution enhanced the residual strength and decreased water absorption of the mortars after being exposed to 600°C. Enríquez et al.[16] found better reflectance, whiteness, and thermal conductivity of pastes by partially replacing cement with 15 and 25% feldspar by weight. Constantiner and Diamond[17] reported that employing feldspar as a fine aggregate in cement mortars released alkali ions into the pore solution. These releases can contribute to alkali-silica reaction (ASR) activity if ASR-reactive aggregate was incorporated. For AAMs, there are too limited

ACI Materials Journal, V. 120, No. 2, March 2023.

MS No. M-2022-113.R1, doi: 10.14359/51737345, received August 16, 2022, and reviewed under Institute publication policies.

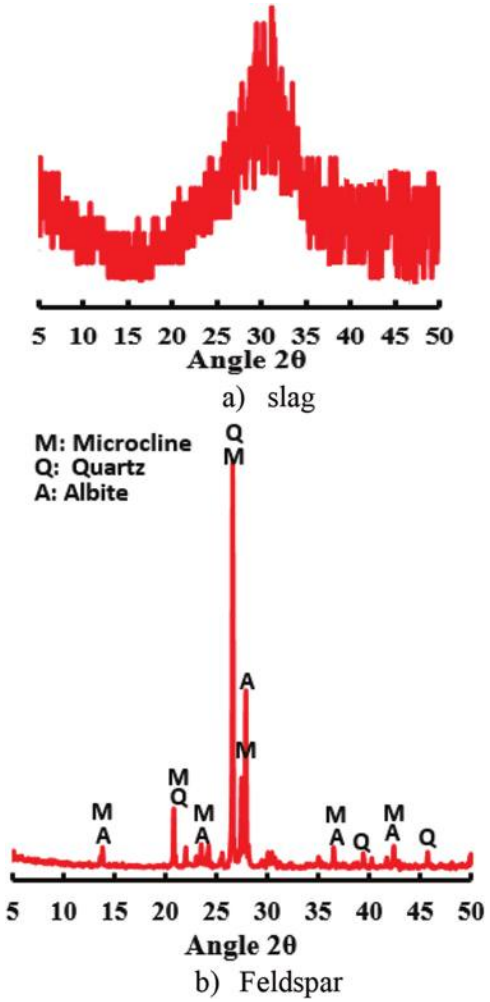

Fig. 1—XRD patterns of: (a) slag; and (b) feldspar.

studies using feldspar as a precursor or a part of a precursor. In this regard, Xu and van Deventer[18] reported that feldspar (sodium and potassium) showed high dissolution in an alkali solution and a high aptitude for geopolymerization. Tian et al.[19] used K-feldspar/quartz as aggregates, MK as the precursor, and NaOH and water-glass solution as the alkaline activators to manufacture geopolymer bricks. They concluded that NaOH can be reduced in the mixture with the inclusion of K-feldspar due to its solubility in the alkaline solution. González-García et al.[20] used plagioclase feldspar as a precursor. NaOH and sodium silicate solution were used as alkaline activators. The results showed that a compressive strength of 13.2 MPa at the age of 28 days can be obtained for specimens cured at room temperature. Abdel-Gawwad and Khalil[21] prepared a one-part geopolymer cement from 60% cement kiln dust and 40% feldspar activated with soda ash. They reported that the vitrification temperature and its duration, as well as the concentration of soda ash, have a major effect on the obtained compressive strength.

RESEARCH SIGNIFICANCE

As shown in the aforementioned survey, there are too limited studies focused on employing feldspar as a cementitious material, and hitherto, there is no publication focused on the effect of feldspar on the main properties of AAS concrete. Thus, for the first time, the effects of different ratios of feldspar on AAS concrete properties were investigated. For this purpose, the slag was partially replaced with feldspar at ratios oscillating from 10 to 50 wt. % with a stride of 10 wt. %. After mixing, workability was determined. After room-temperature curing, compressive strength, splitting strength, water absorption, and total porosity were determined. After 28 days of curing, critical samples were examined by X-ray diffraction (XRD), thermogravimetric analysis (TGA), and scanning electronic microscopy (SEM) to investigate the change in the crystalline phases, hydration products, and microstructure morphologies, respectively. This investigation can add new data about new uses for a suitable ratio of feldspar in the field of AAS systems.

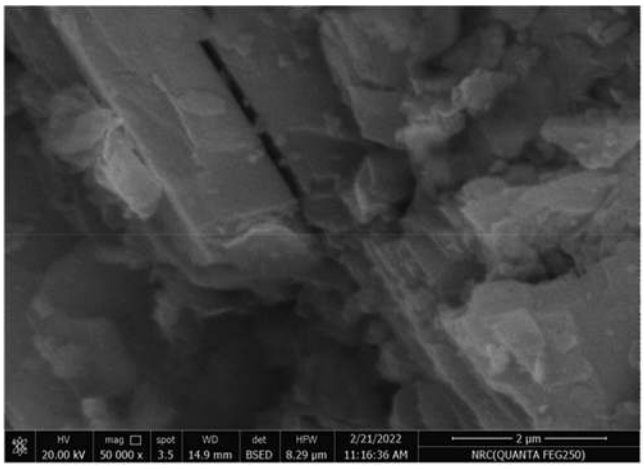

Fig. 2—Morphology of feldspar.

EXPERIMENTAL DETAILS

Materials

The main precursor was a slag. It was delivered from a factory in Cairo, Egypt, in water quenching fine grains. The delivered slag was then ground by a special ball mill to reach a Blaine surface area of 300 m^2/kg. Its specific gravity was 2.9. Potassium feldspar was delivered from local Egyptian quarries. Its Blaine surface area was 500 m^2/kg, while its specific gravity was 2.57. An amorphous slag phase is shown in Fig. 1(a), which is assured by a broad swelling at 25 to 35 degrees 2θ, while the feldspar shows crystalline phases of microcline, quartz, and albite (Fig. 1(b)). Feldspar morphology is plate-like, crystal grains with a compact configuration (Fig. 2), while slag morphology shape is irregular, jagged, and angular, as reported in a previous work.[22] The chemical composition of the precursors and aggregates analyzed by an X-ray fluorescence (XRF) spectrometer is given in Table 1. Local commercial liquid sodium silicate solution (38.2% SiO_2, 11.3% Na_2O, and 50.5% water) was used as a part of the alkaline activator. High-purity (99%) NaOH pellets were delivered from a chemicals company in Cairo and employed as a part of the alkaline activator. A high-range water reducer (HRWR) in the form of an aqueous solution of modified polycarboxylates was also used; it complies with the requirements of ASTM C494/C494M-19 Type F.[23] The fine aggregate was natural siliceous sand. Its particle-size distribution (ES 1109/2021[24]) is placed within

Table 1—Chemical composition of precursors and aggregates

Oxide, %	Slag, %	Feldspar, %	Coarse aggregate, %	Fine aggregate, %
SiO_2	33	74.6	1.67	93.4
Al_2O_3	16	12.2	0.07	2.03
Fe_2O_3	1.5	1.38	0.01	0.98
CaO	37.39	1.86	35.54	0.71
MgO	6.19	0.28	17.51	0.25
K_2O	0.93	5.66	0.02	0.64
Na_2O	1.84	2.83	0.04	0.38
SO_3	1.86	0.28	0.13	0.3
MnO	0.53	0	—	0.03
TiO_2	0.83	0.12	0.01	0.17
BaO	0.3	0.05	—	—
SrO	0.14	0	—	—
ZrO_2	0.07	0	—	—
P_2O_5	0.02	0.03	0.01	0.06
Cl^-	0.18	0.12	—	0.08
Cr_2O_3	0	0.05	—	—
ZnO	0	0.03	—	—
LOI	0.51	0.5	44.99	0.74

Note: LOI is loss on ignition.

the range of the medium grading zone. Its water absorption (ASTM C128-15[25]) and fineness modulus (ASTM C136/C136M-14[26]) were 1.5% and 2.75, respectively. The coarse aggregate was a natural crushed stone, with more than 90% of the coarse aggregate particles having a size of 10 mm. Its water absorption and fineness modulus were 0.95% and 6.8, respectively. Figure 3 shows the general view of the raw materials used in this investigation.

Mixture preparation and methods

The neat slag concrete mixture without any ratio of feldspar was used as a reference. This mixture was designated as F0. The remaining mixtures were prepared by partially replacing slag with feldspar at ratios of 10, 20, 30, 40, and 50 wt. %. These mixtures were designated as F10, F20, F30, F40, and F50, respectively. NaOH pellets were dissolved in water to obtain a 14 M concentration. This solution was left for 24 hours before use to get rid of the rising of solution temperature. After that, one part of NaOH (14 M) was mixed with 2.2 parts of sodium silicate to prepare the alkaline solution. The concentration of this solution was fixed at 35 wt. % of the powders (slag and feldspar). A fixed level of HRWR at a dosage of 3% was used. This dosage was premixed with the extra water. A fixed ratio of extra water/powders of 0.14 was used. The coarse-to-fine aggregate ratio was 1.5 by weight. Table 2 summarizes the ingredients of the designed concrete mixtures. Similar mixtures without aggregates (pastes) for F0, F10, and F50 were prepared for XRD and TGA tests.

The mixing operations sequenced were as follows: the powders, fine aggregate, and coarse aggregate were carefully

Fig. 3—Optical view of starting materials.

mixed in a drum electrical mixer for 5 minutes. The alkaline solution and HRWR premixed with extra water were added and mixed for 5 minutes. After reaching a homogenous mixture, a sample of fresh concrete was employed for the slump test to measure the workability according to ASTM C143/C143M-12[27] at the same time the different molds were filled in three equal layers. The filled molds were vibrated on a special shake table for 1 minute. The top surface was leveled and covered with a thin plastic sheet to prevent water evaporation. After 24 hours of casting, the specimens were demolded and cured at room temperature until the age of testing. Figure 4 shows live photos during mixing.

Cube specimens with dimensions of 100 x 100 x 100 mm were used for compressive strength measurements in agreement with BS EN 12390-3:2019.[28] Three specimens from each mixture were tested in compression at the ages of 7, 28, and 56 days and the average was determined. Cylinder specimens with a diameter of 100 mm and a height of 200 mm

Table 2—Concrete mixture proportions

ID	Ingredients, kg/m^3							
	Slag	Feldspar	NaOH (14 M)	Sodium silicate	Extra water	HRWR	Fine aggregate	Coarse aggregate
F0	550	0	60	132.5	78	16.5	592.6	888.92
F10	495	55	60	132.5	78	16.5	592.6	888.92
F20	440	110	60	132.5	78	16.5	592.6	888.92
F30	385	165	60	132.5	78	16.5	592.6	888.92
F40	330	220	60	132.5	78	16.5	592.6	888.92
F50	275	275	60	132.5	78	16.5	592.6	888.92

Fig. 4—Live photos during mixing.

were used for splitting tensile strength measurements in agreement with BS EN 12390-6:2009.[29] Three specimens from each mixture were tested at the age of 28 days and the average was determined. A testing machine with a capacity of 5000 kN (Fig. 5) was used for this purpose. Cubes specimens with dimensions of 100 x 100 x 100 mm (Fig. 6) were used for water absorption and total porosity measurements. After curing for 28 days, the water absorption and total porosity of different concrete specimens were measured following ASTM C642-21.[30] For each test, three specimens were tested and the average was determined. To measure XRF (Fig. 7), the sample was pressed into pellets. The sample was exposed to X-ray light, which excites the elements present in the sample. The elements release light as they return to their ground state. The light released as the elements relax is identifiable to the particular element present in the sample, and measuring the fluorescence makes it possible to calculate the exact chemical composition of

Fig. 5—Optical view of testing machine.

the sample. After curing for 28 days, the cast pastes (for F0, F10, and F50) were prepared and tested under XRD and TGA in a similar way reported in Rashad and Essa,[31] while the extracted samples from selected concrete cubes (F0, F10, and F50) after crushing at the age of 28 days were prepared and tested under SEM. Each extracted sample (with a suitable size) was cleaned and coated with a thin layer of gold to make it conductive. Each sample was dried before placing in the testing machine. In this investigation, the SEM analysis was performed by scanning electron microscope, similar to Rashad and Essa.[31]

RESULTS AND DISCUSSION

Workability

Figure 8 shows live photos during measuring the slump, while Fig. 9 shows the effect of various ratios of feldspar on the slump. As can be observed, the slump of the mixtures strongly depends on the ratio of feldspar. Despite the fact that slag particles are less fine (coarser) than feldspar ones, the incorporation of feldspar in the mixture has a positive effect on the workability, which increased with increasing the ratio of feldspar. Introducing only 10% feldspar in the mixture (F10) led to an increase in the slump by 25% compared to the control (F0). Increasing the feldspar ratio

Fig. 6—Optical view of cube testing specimens.

to 20 to 40% led to an additional increase in the workability, of which the slump was increased by 50 to 112.5%. The highest slump (125%) was achieved when 50% of the slag was replaced by feldspar (F50). The higher workability with the inclusion of feldspar, even though its surface area is higher than that of slag, could be attributed to its fine particles that can fill the voids between slag particles. Filling these voids led to less water demand needed to fill the voids. In addition, increasing the feldspar ratio in the mixtures led to increasing the silica ratio and decreasing the calcium ratio (Table 3), which have a positive effect on the workability. It was reported that the workability increased with increasing the silica modulus of the geopolymer.[32,33] Rashad and Sadek[34] reported that a higher calcium ratio in the geopolymer mixture led to lower workability. It is worth mentioning that the results obtained by Puertas et al.[35] revealed that the silica ratio increased in the AAS paste mixtures as the workability increased. In such a way, Ramezanianpour and Moeini[36] found higher flowability of AAS/SF mortar mixtures with increasing silica ratio. Yaseri et al.[32] observed a higher spread diameter of MK/SF geopolymer paste mixtures with increasing Si/Al ratio.

Mechanical strength

Figure 10 shows the compressive strength at 7, 28, and 56 days. As can be noted, the compressive strength is affected by the hydration time and the feldspar ratio. As is known, the compressive strength increased with increasing hydration time. The specimens free from feldspar (F0) show a good deal of compressive strength, with strengths of 29.9, 34.5, and 39.17 MPa at 7, 28, and 56 days, respectively. The incorporation of feldspar has a major effect on compressive strength, of which it may increase or decrease.

Fig. 7—Optical view of XRF tool.

Fig. 8—Live photos during slump measuring.

This mainly depends on the feldspar ratio. The incorporation of 10% feldspar can efficiently enhance the compressive strength by 25.77%, 18.48%, and 15.48% at 7, 28, and 56 days, respectively. The highest ratio of enhancement was observed at 7 days (25.77%) compared to those at 28 (18.48%) or 56 days (15.48%). This means that the suitable ratio of feldspar has a pronounced effect on the early-age strength. The enhancement of the compressive strength could be attributed to more than one reason. One reason is the fine feldspar particles can act as microaggregates. These microaggregates can help in blocking the pores between the slag skeleton, decreasing total porosity, refining the microstructure, and can act as nuclei sites.[22] Another reason for enhancing the strength is increasing the Si/Al molar ratio with the incorporation of 10% feldspar from 4.48 for F0

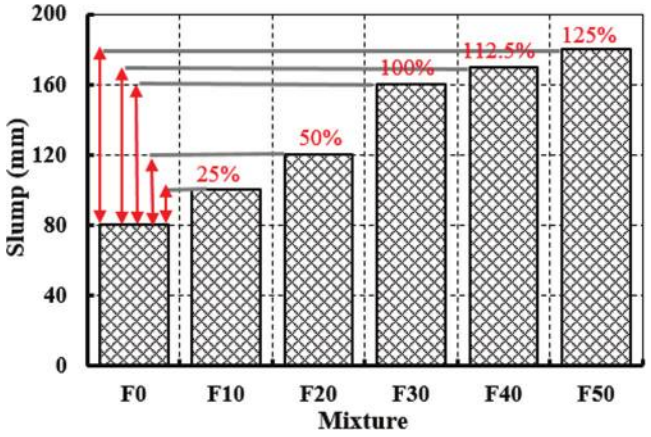

Fig. 9—Slump value variations as function of feldspar content.

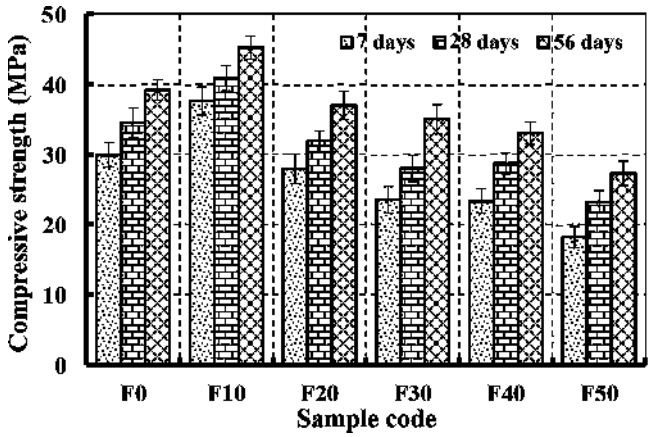

Fig. 10—Compressive strength variations as function of feldspar content.

to 5 for F10 (Table 3). A higher Si/Al ratio, up to a certain level, led to prevailing structures of polysialatedisiloxo and poly(sialate-siloxo) (Si-O-Si) in geopolymer lattice rather than structures of polysialate (Si-O-Al).[37,38]

The incorporations of feldspar at ratios higher than 10% did not show any positive effect on the compressive strength, but strength degradation was obtained. The incorporations of 20%, 30%, 40%, and 50% feldspar decreased the strength by an average of 6.59%, 16.96%, 18.21%, and 34.1%, respectively. This reduction could be attributed to the higher silica ratio than required. This further increase in silica ratio can decrease the solubility/formation of the gel, which can lead to an increase in the number of unreacted particles,[39,40] leading to a porous and weak structure.[41,42] The previous results revealed that the compressive strength of AAS/FA/SF mortars[43] or pastes[44] increased with increasing silica ratio up to a certain level, then decreased with a further increase in this ratio. Similarly, an increase in the compressive strength of AAS/SF pastes[44-46] and mortars[36] was found when increasing the silica ratio up to a certain level, then a reduction was observed with a further increase in this ratio. Another reason for the reduction in the compressive strength with ratios of feldspar higher than 10% is increasing the crystalline phases and reducing the amorphization degree, which will be discussed later.

Table 3—Effect of feldspar on SiO_2/Al_2O_3 and CaO/SiO_2 ratios

Mixture ID	SiO_2/Al_2O_3	CaO/SiO_2
F0	4.48	0.95
F10	5.04	0.78
F20	5.63	0.64
F30	6.25	0.52
F40	6.90	0.42
F50	7.59	0.33

Fig. 11—Live photos during splitting strength measuring.

Figure 11 shows live photos during measuring of the splitting strength, while Fig. 12 shows the results of splitting strength at the age of 28 days. The specimens without feldspar show a reasonable value of splitting strength (2.51 MPa). This value is higher than that mentioned in Hammad et al.[47] and lower than that reported in Mithun and Narasimhan.[48] The splitting strength was enhanced by approximately 9.5% with the incorporation of 10% feldspar (F10). Further increasing the feldspar ratios to 20%, 30%, 40%, and 50% resulted in a reduction in the splitting strength by 2.4%, 7.7%, 14.34%, and 20.32%, respectively. The reasons for increasing or decreasing splitting strength with the variation of feldspar ratios are similar to those of compressive strength.

Water absorption and total porosity

A matrix's ability to absorb water is an important factor in determining its durability and the presence of shrinkage cracks. In water absorption, structural pores as well as

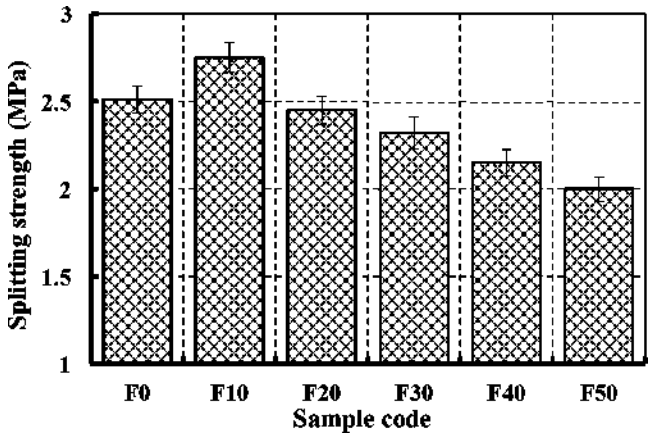

Fig. 12—Splitting tensile strength variations as function of feldspar content.

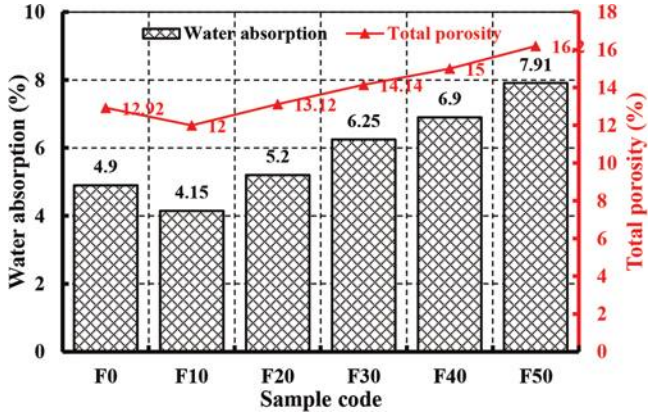

Fig. 13—Water absorption and total porosity variations as function of feldspar content.

capillary pores are directly associated with internal porosity volume. A specimen's surface porosity can be estimated by measuring the absorption of water. The porosity of a matrix can be detected by measuring the volume of voids. With implications for durability and structural performance, porosity affects the efficiency of mass transport and matrix strength. Figure 13 shows the effect of different ratios of feldspar on the water absorption and total porosity of the specimens. The specimens free from feldspar (F0) show water absorption of 4.9%. This ratio of water absorption is acceptable, and is comparable to that reported in Mengasini et al.[49] (4.1%); higher than that reported in Mithun and Narasimhan[48] (~3.8%), Huang et al.[50] (3.53%), and Rostami and Behfarnia[51,52] (2.68%); and lower than that reported by Bai et al.[53] (~7.8%) and Nanayakkara et al.[54] (8.6%). Similarly, these specimens show a total porosity of 12.92%. The incorporation of 10% feldspar has a noteworthy effect on water absorption and porosity, of which both were reduced. The incorporation of only 10% feldspar decreases water absorption from 4.9% (from F0) to 4.15% (for F10) and the porosity from 12.92% (for F0) to 11.9% (for F10). These reductions (improvements) in both water absorption and total porosity could be attributed to the packing effect of fine feldspar particles. These particles are thought to decrease water absorption and porosity due to their packing effect, which reduces capillary pores and prevents water molecules from sticking

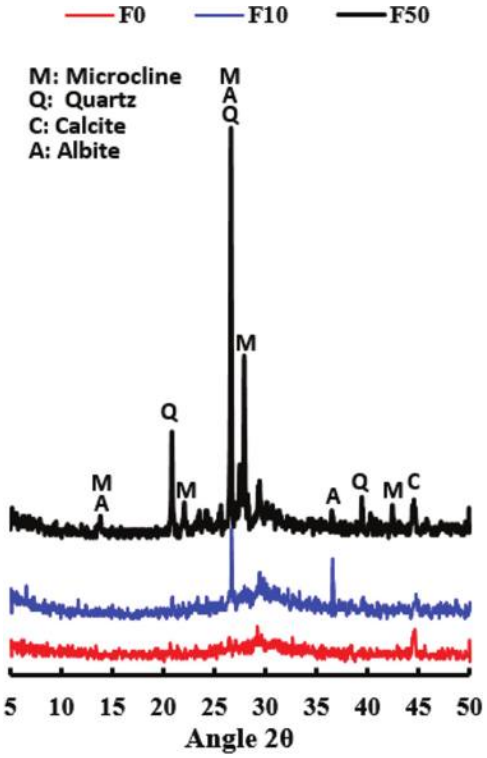

Fig. 14—XRD patterns of F0, F10, and F50 samples.

to the samples.[22,55] This packing effect can contribute to the formation of a dense structure.[56] Increasing the proportion of feldspar higher than 10% results in an adverse effect on the water absorption and porosity, which increase gradually with increasing feldspar ratio. The incorporation of 20%, 30%, 40%, and 50% feldspar ratio led to increasing water absorption from 4.15% (for F10) to 5.2% (for F20), 6.25% (for F30), 6.9% (for F40), and 7.91% (for F50), respectively. In that way, the total porosity of specimens containing 20%, 30%, 40%, and 50% feldspar show an increase from 12% (for F10) to 13.12% (for F20), 14.14% (for F30), 15% (for F40), and 16.2% (for F50), respectively. This higher water absorption and porosity could be attributed to the porous microstructure that excessive ratios of feldspar (silica ratio) caused. This excessive ratio can reduce the solubility and formation of the gel, resulting in an increase in the number of unreacted particles,[39,40] and a porous and weak structure.[41,42] The high crystallinity/low amorphization degree of specimens containing ratios of feldspar higher than the optimum is another reason for the higher water absorption and porosity. The increase of incomplete dispersion of excessive feldspar particles than the optimum can lead to higher porosity, which is clearly shown in the microstructure. It is worth mentioning that Shariati et al.[57] found a reduction in water absorption of AAS or AAS/SF pastes with increasing silica ratio up to a certain level, then an increasing rate with increasing this ratio was obtained.

Crystalline phases

Figure 14 shows the XRD patterns of the F0 (the control), F10 (the optimum), and F50 (the worst) samples after curing for 28 days. The generalized view shows crystalline and amorphous phases coexisting. The samples show

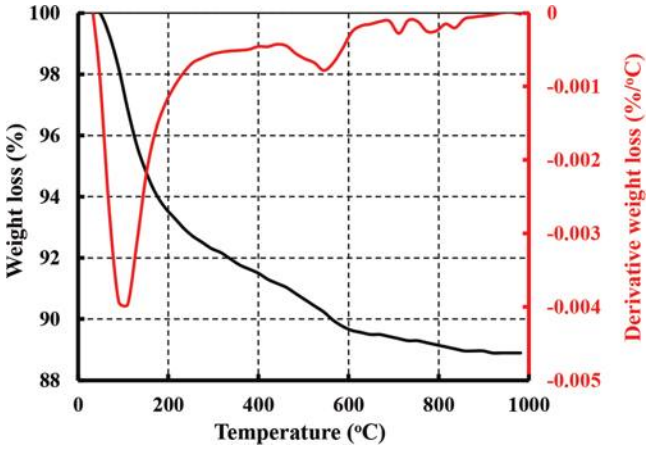

Fig. 15—TGA curves of F0 sample.

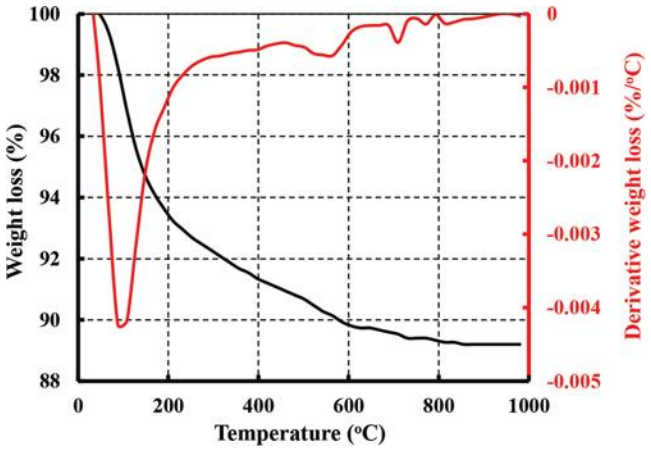

Fig. 16—TGA curves of F10 sample.

a wide broad hump between 25 and 35 degrees 2θ, which is attributed to C-S-H for the F0 sample, and C-S-H and N-A-S-H for the F10 and F50 samples. The appearance of this hump indicates an amorphous phase. The amorphous hump of the F0 sample was slightly increased with the inclusion of 10% feldspar (F10), then decreased with the inclusion of 50% feldspar (F50). This difference in the amorphous hump is a part of the explanation for the higher strength of F10 over F0 and the lower strength of F50 compared to F0. The samples of F10 and F50 show the crystalline phases of microcline, calcite, albite, and quartz. The intensity of these peaks rapidly increases with increasing feldspar ratio from 10% (F10) to 50% (F50).

Thermogravimetric analysis

Figures 15, 16, and 17 show the TGA curves of the F0 (the control), F10 (the optimum), and F50 (the worst) samples after curing for 28 days. The general view of the TGA of the F0 sample presented in Fig. 15 shows three weight losses corresponding to three TGA endothermic peaks. One of them is large and main, while the others are minor. The main weight loss can be seen at a temperature lower than 200°C. This loss is attributed to dehydration of free water and C-S-H gel. There is a minor weight loss at 573°C, which is attributed to the decomposition of quartz. The minor weight

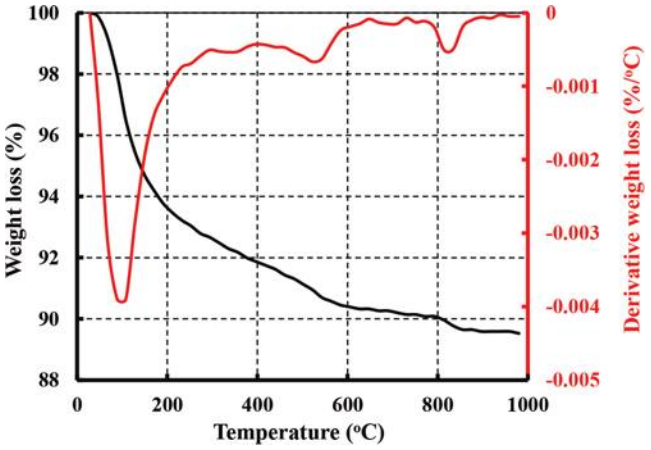

Fig. 17—TGA curves of F50 sample.

loss between 600 and 800°C is attributed to the decomposition of calcite. The samples of F10 (Fig. 16) and F50 (Fig. 17) show similar weight losses at approximately 573°C and between 600 and 800°C, while the main weight loss before 200°C is attributed to the coexistence of C-S-H and N-A-S-H. Comparing the main weight loss (before 200°C) for each sample (F0, F10, and F50), it can be observed that F10 shows the highest weight loss, which explains its highest strength in Fig. 10 and 12 and its lowest water absorption/total porosity in Fig. 13, while F50 shows the lowest weight loss, which explains its lowest strength in Fig. 10 and 12 and highest water absorption/porosity in Fig. 13.

Microstructure analysis

Figure 18 shows the SEM images of the F0 (the control), F10 (the optimum), and F50 (the worst) samples after curing for 28 days. Apparently, the sample free from feldspar (F0) shows a somewhat homogenous microstructure with few unreacted particles that are identifiable by their angular, jagged, and irregular shapes with a bright appearance (Fig. 18(a)). This microstructure also shows a limited number of pores dispersed between slag particles (Fig. 18(a)), which correlated to its reasonable strength. Partially replacing slag with only 10% feldspar (F10) results in a denser, more compact, and more homogenous microstructure and interfacial transition zone (Fig. 18(b)). The filler and packing effect of a suitable ratio of feldspar (10%) can block the pores and play an important role in enhancing strength, reducing the water absorption, and total porosity. The view of this microstructure confirms that a suitable ratio of silica (Table 3) has a positive effect on the homogeneity and compactness of the microstructure. Partially replacing slag with 50% feldspar results in an important change in the microstructure: a porous microstructure can be observed with a high number and size of pores, featured with their black color (Fig. 18(c)). In addition, several unreacted particles and microcracks can be observed (Fig. 18(c)) that are responsible for the degradation of strength, the higher water absorption, and the total porosity. The view of this microstructure confirms that a higher silica ratio than the optimum can produce numerous pores[41,42] and unreacted particles.[39,40]

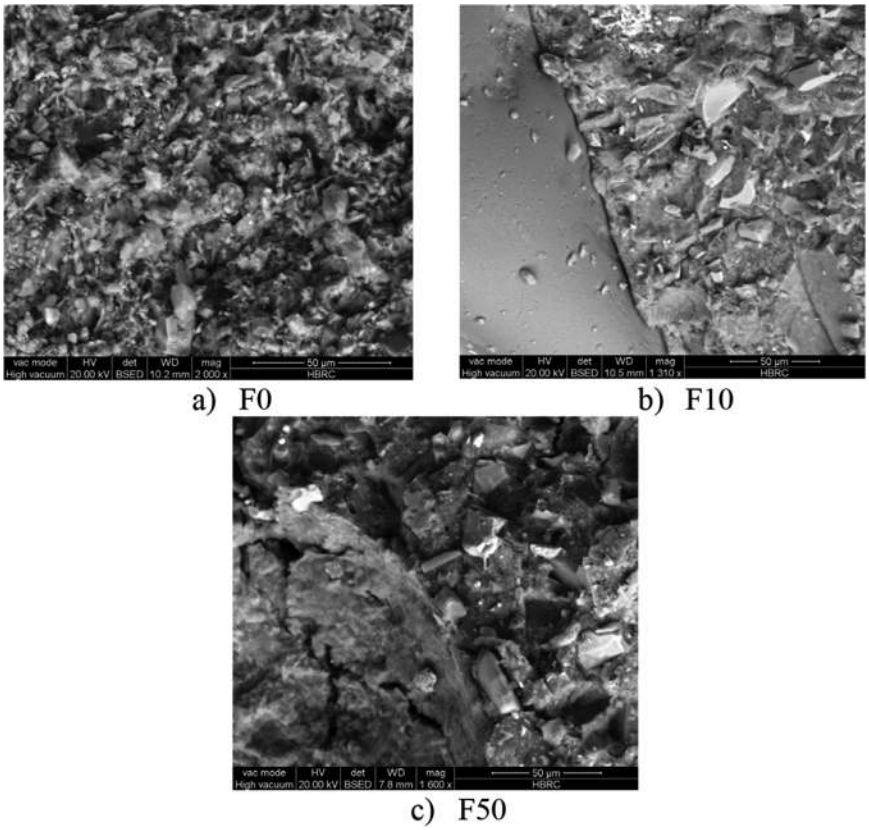

Fig. 18—SEM images of F0, F10, and F50 samples.

CONCLUSIONS

This study aims to investigate the possibility of modifying the properties of alkali-activated slag (AAS) concrete with feldspar. Tests on the effects of different ratios of feldspar on the workability, compressive strength, splitting tensile strength, water absorption, total porosity, and microstructure morphology of AAS concrete were conducted. The main outlines of this investigation are listed as follows:

1. It is possible to use a suitable ratio of feldspar to improve the fresh and hardened properties of AAS concrete.

2. The incorporation of feldspar increased the workability of the mixtures due to the increasing silica ratio and decreasing calcium ratio. The ratio of feldspar in the mixture increased as the workability increased. The incorporation of 10 to 50% feldspar increased the slump by 25 to 125%.

3. The incorporation of 10% feldspar improved and enhanced the compressive strength—especially at an early age—and the splitting tensile strength due to its filler and packing effect, as well as increasing the silica ratio. Adversely, a higher ratio of feldspar than 10% decreased both the compressive strength and splitting strength. The strength reduction increased with increasing feldspar ratio.

4. The inclusion of 10% feldspar decreased water absorption and total porosity, while a higher ratio than 10% increased them. The feldspar ratio increased as water absorption and total porosity increased.

5. The inclusion of 10% feldspar led to an increase in the silica ratio in the mixture, which has a positive effect on strength and durability, but a further higher silica ratio than required resulted in a higher number of unreacted particles and a porous and weak microstructure, as confirmed by microstructure analysis.

6. The crystalline phases of microcline, calcite, albite, and quartz, as well as C-S-H and N-A-S-H gels, were detected when feldspar was added to the samples. The incorporation of 10% showed the highest level of the coexistence of C-S-H and N-A-S-H gels, and a dense, more compact microstructure and interfacial transition zone.

This investigation can fill the gap in the literature about the effect of feldspar on some properties of AAS concrete. It is recommended to investigate the effect of feldspar on other properties of AAS concrete such as sulfate resistance, chloride resistance, and acid resistance.

AUTHOR BIOS

Alaa M. Rashad *is a Professor at the Building Materials and Quality Control Research Institute, Housing and Building National Research Center (HBRC), Cairo, Egypt, as well as the Civil Engineering Department, College of Engineering, Shaqra University, Al-Dawadmi, Riyadh, Saudi Arabia. He received his BS, MS, and PhD from the Faculty of Engineering at Cairo University, Cairo, Egypt, and his postdoctoral research associate from the School of Planning, Architecture, and Civil Engineering at Queen's University Belfast, Belfast, UK. His research interests include building materials, nanotechnology, alkali-activated materials, fire resistance, and thermal insulation.*

Youssef A. Mosleh *is a Researcher (Assistant Professor) at the Building Materials and Quality Control Research Institute, Housing and Building National Research Center (HBRC), Cairo, Egypt. He received his BS, MS, and PhD from the Faculty of Engineering at Cairo University. His research interests include building materials, nanotechnology, and geopolymers.*

Mahmoud Gharieb *is a Researcher (Assistant Professor) at the Raw Building Materials and Technology Processing Research Institute, Housing and Building National Research Center (HBRC), Cairo, Egypt. He received his BS and MS from the Faculty of Science at Al-Azhar University, Cairo,*

Egypt, and his PhD from Ain Shams University, Cairo, Egypt. His research interests include building materials and geopolymers.

REFERENCES

1. Hilburg, J., "Concrete Production Produces Eight Percent of the World's Carbon Dioxide Emissions," *The Architect's Newspaper*, Jan. 2, 2019, https://www.archpaper.com/2019/01/concrete-production-eight-percent-co2-emissions/. (last accessed Feb. 10, 2023)

2. Rodgers, L., "Climate Change: The Massive CO2 Emitter You May Not Know About," *BBC News*, Dec. 17, 2018, https://www.bbc.com/news/science-environment-46455844. (last accessed Feb. 10, 2023)

3. Le Quéré, C.; Andrew, R. M.; Friedlingstein, P.; Sitch, S.; Hauck, J.; Pongratz, J.; Pickers, P. A.; Korsbakken, J. I.; Peters, G. P.; Canadell, J. G.; Arneth, A.; Arora, V. K.; Barbero, L.; Bastos, A.; Bopp, L.; Chevallier, F.; Chini, L. P.; Ciais, P.; Doney, S. C.; Gkritzalis, T.; Goll, D. S.; Harris, I.; Haverd, V.; Hoffman, F. M.; Hoppema, M.; Houghton, R. A.; Hurtt, G.; Ilyina, T.; Jain, A. K.; Johannessen, T.; Jones, C. D.; Kato, E.; Keeling, R. F.; Goldewijk, K. K.; Landschützer, P.; Lefèvre, N.; Lienert, S.; Liu, Z.; Lombardozzi, D.; Metzl, N.; Munro, D. R.; Nabel, J. E. M. S.; Nakaoka, S.; Neill, C.; Olsen, A.; Ono, T.; Patra, P.; Peregon, A.; Peters, W.; Peylin, P.; Pfeil, B.; Pierrot, D.; Poulter, B.; Rehder, G.; Resplandy, L.; Robertson, E.; Rocher, M.; Rödenbeck, C.; Schuster, U.; Schwinger, J.; Séférian, R.; Skjelvan, I.; Steinhoff, T.; Sutton, A.; Tans, P. P.; Tian, H.; Tilbrook, B.; Tubiello, F. N.; van der Laan-Luijkx, I. T.; van der Werf, G. R.; Viovy, N.; Walker, A. P.; Wiltshire, A. J.; Wright, R.; Zaehle, S.; and Zheng, B., "Global Carbon Budget 2018," *Earth System Science Data*, V. 10, No. 4, 2018, pp. 2141-2194. doi: 10.5194/essd-10-2141-2018

4. Abriyantoro, D.; Dong, J.; Hicks, C.; and Singh, S. P., "A Stochastic Optimisation Model for Biomass Outsourcing in the Cement Manufacturing Industry with Production Planning Constraints," *Energy*, V. 169, 2019, pp. 515-526. doi: 10.1016/j.energy.2018.11.114

5. Rashad, A. M., "A Brief on High-Volume Class F Fly Ash as Cement Replacement–A Guide for Civil Engineer," *International Journal of Sustainable Built Environment*, V. 4, No. 2, 2015, pp. 278-306. doi: 10.1016/j.ijsbe.2015.10.002

6. Rashad, A. M., "Metakaolin: Fresh Properties and Optimum Content for Mechanical Strength in Traditional Cementitious Materials–A Comprehensive Overview," *Reviews on Advanced Materials Science*, V. 40, No. 1, 2015, pp. 15-44.

7. Rashad, A. M., "An Overview on Rheology, Mechanical Properties and Durability of High-Volume Slag Used as a Cement Replacement in Paste, Mortar and Concrete," *Construction and Building Materials*, V. 187, 2018, pp. 89-117. doi: 10.1016/j.conbuildmat.2018.07.150

8. Rashad, A. M., "A Comprehensive Overview about the Influence of Different Additives on the Properties of Alkali-Activated Slag–A Guide for Civil Engineer," *Construction and Building Materials*, V. 47, 2013, pp. 29-55. doi: 10.1016/j.conbuildmat.2013.04.011

9. Shi, C.; Roy, D.; and Krivenko, P., *Alkali-Activated Cements and Concretes*, CRC Press, Boca Raton, FL, 2003.

10. Rashad, A. M., "Effect of Quartz-Powder on the Properties of Conventional Cementitious Materials and Geopolymers," *Materials Science and Technology*, V. 34, No. 17, 2018, pp. 2043-2056. doi: 10.1080/02670836.2018.1471435

11. Amran, Y. H. M.; Alyousef, R.; Alabduljabbar, H.; and El-Zeadani, M., "Clean Production and Properties of Geopolymer Concrete; A Review," *Journal of Cleaner Production*, V. 251, 2020, Article No. 119679. doi: 10.1016/j.jclepro.2019.119679

12. Loring, J. S.; Miller, Q. R.; Thompson, C. J.; and Schaef, H. T., "Experimental Studies of Reactivity and Transformations of Rocks and Minerals in Water-Bearing Supercritical CO_2," *Science of Carbon Storage in Deep Saline Formations: Process Coupling across Time and Spatial Scales*, P. Newell and A. G. Ilgen, eds., Elsevier, Amsterdam, the Netherlands, 2019, pp. 63-88.

13. Locati, F.; Marfil, S.; Baldo, E.; and Maiza, P., "Na_2O, K_2O, SiO_2 and Al_2O_3 Release from Potassic and Calcic–Sodic Feldspars into Alkaline Solutions," *Cement and Concrete Research*, V. 40, No. 8, 2010, pp. 1189-1196. doi: 10.1016/j.cemconres.2010.04.005

14. Yao, G.; Wang, Z.; Yao, J.; Cong, X.; Anning, C.; and Lyu, X., "Pozzolanic Activity and Hydration Properties of Feldspar after Mechanical Activation," *Powder Technology*, V. 383, 2021, pp. 167-174. doi: 10.1016/j.powtec.2021.01.042

15. Khoshkbijari, R. K.; Samimi, M. F.; Mohammadi, F.; and Talebitaher, P., "Effects of Mica and Feldspar as Partial Cement Replacement on the Rheological, Mechanical and Thermal Durability of Self-Compacting Mortars," *Construction and Building Materials*, V. 263, 2020, Article No. 120149. doi: 10.1016/j.conbuildmat.2020.120149

16. Enríquez, E.; Torres-Carrasco, M.; Cabrera, M. J.; Muñoz, D.; and Fernández, J. F., "Towards More Sustainable Building Based on Modified Portland Cements through Partial Substitution by Engineered Feldspars," *Construction and Building Materials*, V. 269, 2021, Article No. 121334. doi: 10.1016/j.conbuildmat.2020.121334

17. Constantiner, D., and Diamond, S., "Alkali Release from Feldspars into Pore Solutions," *Cement and Concrete Research*, V. 33, No. 4, 2003, pp. 549-554. doi: 10.1016/S0008-8846(02)01001-3

18. Xu, H., and van Deventer, J. S. J., "Factors Affecting the Geopolymerization of Alkali-Feldspars," *Mining, Metallurgy & Exploration*, V. 19, No. 4, 2002, pp. 209-214. doi: 10.1007/BF03403271

19. Tian, L.; Feng, W.; Ma, H.; Zhang, S.; and Shi, H., "Investigation on the Microstructure and Mechanism of Geopolymer with Different Proportion of Quartz and K-Feldspar," *Construction and Building Materials*, V. 147, 2017, pp. 543-549. doi: 10.1016/j.conbuildmat.2017.04.102

20. González-García, D. M.; Téllez-Jurado, L.; Jiménez-Álvarez, F. J.; and Balmori-Ramírez, H., "Structural Study of Geopolymers Obtained from Alkali-Activated Natural Pozzolan Feldspars," *Ceramics International*, V. 43, No. 2, 2017, pp. 2606-2613. doi: 10.1016/j.ceramint.2016.11.070

21. Abdel-Gawwad, H. A., and Khalil, K. A., "Application of Thermal Treatment on Cement Kiln Dust and Feldspar to Create One-Part Geopolymer Cement," *Construction and Building Materials*, V. 187, 2018, pp. 231-237. doi: 10.1016/j.conbuildmat.2018.07.161

22. Rashad, A. M.; Morsi, W. M.; and Khafaga, S. A., "Effect of Limestone Powder on Mechanical Strength, Durability and Drying Shrinkage of Alkali-Activated Slag Pastes," *Innovative Infrastructure Solutions*, V. 6, No. 2, 2021, Article No. 127. doi: 10.1007/s41062-021-00496-y

23. ASTM C494/C494M-19, "Standard Specification for Chemical Admixtures for Concrete," ASTM International, West Conshohocken, PA, 2019, 15 pp.

24. ES 1109/2021, "Aggregate for Concrete," Egyptian Organization for Standards & Quality, Cairo, Egypt, 2021, 52 pp.

25. ASTM C128-15, "Standard Test Method for Density, Relative Density (Specific Gravity), and Absorption of Fine Aggregate," ASTM International, West Conshohocken, PA, 2015, 6 pp.

26. ASTM C136/C136M-14, "Standard Test Method for Sieve Analysis of Fine and Coarse Aggregates," ASTM International, West Conshohocken, PA, 2014, 5 pp.

27. ASTM C143/C143M-12, "Standard Test Method for Slump of Hydraulic-Cement Concrete," ASTM International, West Conshohocken, PA, 2012, 4 pp.

28. BS EN 12390-3:2019, "Testing Hardened Concrete - Part 3: Compressive Strength of Test Specimens," British Standards Institution, London, UK, 2019.

29. BS EN 12390-6:2009, "Testing Hardened Concrete - Part 6: Tensile Splitting Strength of Test Specimens," British Standards Institution, London, UK, 2009.

30. ASTM C642-21, "Standard Test Method for Density, Absorption, and Voids in Hardened Concrete," ASTM International, West Conshohocken, PA, 2021, 3 pp.

31. Rashad, A. M., and Essa, G. M. F., "Effect of Ceramic Waste Powder on Alkali-Activated Slag Pastes Cured in Hot Weather after Exposure to Elevated Temperature," *Cement and Concrete Composites*, V. 111, 2020, Article No. 103617. doi: 10.1016/j.cemconcomp.2020.103617

32. Yaseri, S.; Hajiaghaei, G.; Mohammadi, F.; Mahdikhani, M.; and Farokhzad, R., "The Role of Synthesis Parameters on the Workability, Setting and Strength Properties of Binary Binder Based Geopolymer Paste," *Construction and Building Materials*, V. 157, 2017, pp. 534-545. doi: 10.1016/j.conbuildmat.2017.09.102

33. Khalil, M. G.; Elgabbas, F.; El-Feky, M. S.; and El-Shafie, H., "Performance of Geopolymer Mortar Cured under Ambient Temperature," *Construction and Building Materials*, V. 242, 2020, Article No. 118090. doi: 10.1016/j.conbuildmat.2020.118090

34. Rashad, A. M., and Sadek, D. M., "An Exploratory Study on Alkali-Activated Slag Blended with Microsize Metakaolin Particles Under the Effect of Seawater Attack and Tidal Zone," *Arabian Journal for Science and Engineering*, V. 47, No. 4, 2022, pp. 4499-4510. doi: 10.1007/s13369-021-06151-z

35. Puertas, F.; Varga, C.; and Alonso, M. M., "Rheology of Alkali-Activated Slag Pastes. Effect of the Nature and Concentration of the Activating Solution," *Cement and Concrete Composites*, V. 53, 2014, pp. 279-288. doi: 10.1016/j.cemconcomp.2014.07.012

36. Ramezanianpour A. A., and Moeini M. A., "Mechanical and Durability Properties of Alkali Activated Slag Coating Mortars Containing Nanosilica and Silica Fume," *Construction and Building Materials*, V. 163, 2018, pp. 611-621. doi: 10.1016/j.conbuildmat.2017.12.062

37. He, P.; Wang, M.; Fu, S.; Jia, D.; Yan, S.; Yuan, J.; Xu, J.; Wang, P.; and Zhou, Y., "Effects of Si/Al Ratio on the Structure and Properties of Metakaolin Based Geopolymer," *Ceramics International*, V. 42, No. 13, 2016, pp. 14416-14422. doi: 10.1016/j.ceramint.2016.06.033

38. Riahi, S.; Nemati, A.; Khodabandeh, A.; and Baghshahi, S., "The Effect of Mixing Molar Ratios and Sand Particles on Microstructure and Mechanical Properties of Metakaolin-Based Geopolymers," *Materials Chemistry and Physics*, V. 240, 2020, Article No. 122223. doi: 10.1016/j.matchemphys.2019.122223

39. Wang, H.; Li, H.; and Yan, F., "Synthesis and Mechanical Properties of Metakaolinite-Based Geopolymer," *Colloids and Surfaces A: Physicochemical and Engineering Aspects*, V. 268, No. 1-3, 2005, pp. 1-6. doi: 10.1016/j.colsurfa.2005.01.016

40. De Silva, P.; Sagoe-Crenstil, K.; and Sirivivatnanon, V., "Kinetics of Geopolymerization: Role of Al_2O_3 and SiO_2," *Cement and Concrete Research*, V. 37, No. 4, 2007, pp. 512-518. doi: 10.1016/j.cemconres.2007.01.003

41. Lahoti, M.; Narang, P.; Tan, K. H.; and Yang, E.-H., "Mix Design Factors and Strength Prediction of Metakaolin-Based Geopolymer," *Ceramics International*, V. 43, No. 14, 2017, pp. 11433-11441. doi: 10.1016/j.ceramint.2017.06.006

42. Pouhet, R.; Cyr, M.; and Bucher, R., "Influence of the Initial Water Content in Flash Calcined Metakaolin-Based Geopolymer," *Construction and Building Materials*, V. 201, 2019, pp. 421-429. doi: 10.1016/j.conbuildmat.2018.12.201

43. Cheah, C. B.; Tan, L. E.; and Ramli, M., "The Engineering Properties and Microstructure of Sodium Carbonate Activated Fly Ash/Slag Blended Mortars with Silica Fume," *Composites Part B: Engineering*, V. 160, 2019, pp. 558-572. doi: 10.1016/j.compositesb.2018.12.056

44. Liu, Y.; Shi, C.; Zhang, Z.; Li, N.; and Shi, D., "Mechanical and Fracture Properties of Ultra-High Performance Geopolymer Concrete: Effects of Steel Fiber and Silica Fume," *Cement and Concrete Composites*, V. 112, 2020, Article No. 103665. doi: 10.1016/j.cemconcomp.2020.103665

45. Rashad, A. M., and Khalil, M. H., "A Preliminary Study of Alkali-Activated Slag Blended with Silica Fume under the Effect of Thermal Loads and Thermal Shock Cycles," *Construction and Building Materials*, V. 40, 2013, pp. 522-532. doi: 10.1016/j.conbuildmat.2012.10.014

46. Wetzel, A., and Middendorf, B., "Influence of Silica Fume on Properties of Fresh and Hardened Ultra-High Performance Concrete Based on Alkali-Activated Slag," *Cement and Concrete Composites*, V. 100, 2019, pp. 53-59. doi: 10.1016/j.cemconcomp.2019.03.023

47. Hammad, N.; El-Nemr, A.; and Hasan, H. E.-D., "The Performance of Fiber GGBS Based Alkali-Activated Concrete," *Journal of Building Engineering*, V. 42, 2021, Article No. 102464. doi: 10.1016/j.jobe.2021.102464

48. Mithun, B. M., and Narasimhan, M. C., "Performance of Alkali Activated Slag Concrete Mixes Incorporating Copper Slag as Fine Aggregate," *Journal of Cleaner Production*, V. 112, Part 1, 2016, pp. 837-844. doi: 10.1016/j.jclepro.2015.06.026

49. Mengasini, L.; Mavroulidou, M.; and Gunn, M. J., "Alkali-Activated Concrete Mixes with Ground Granulated Blast Furnace Slag and Paper Sludge Ash in Seawater Environments," *Sustainable Chemistry and Pharmacy*, V. 20, 2021, Article No. 100380. doi: 10.1016/j.scp.2021.100380

50. Huang, J.; Zou, C.; Sun, D.; Yang, B.; and Yan, J., "Effect of Recycled Fine Aggregates on Alkali-Activated Slag Concrete Properties," *Structures*, V. 30, 2021, pp. 89-99. doi: 10.1016/j.istruc.2020.12.064

51. Rostami, M., and Behfarnia, K., "The Effect of Silica Fume on Durability of Alkali Activated Slag Concrete," *Construction and Building Materials*, V. 134, 2017, pp. 262-268. doi: 10.1016/j.conbuildmat.2016.12.072

52. Behfarnia, K., and Rostami, M., "Mechanical Properties and Durability of Fiber Reinforced Alkali Activated Slag Concrete," *Journal of Materials in Civil Engineering*, ASCE, V. 29, No. 12, 2017, p. 04017231. doi: 10.1061/(ASCE)MT.1943-5533.0002073

53. Bai, Y.-H.; Yu, S.; and Chen, W., "Experimental Study of Carbonation Resistance of Alkali-Activated Slag Concrete," *ACI Materials Journal*, V. 116, No. 3, May 2019, pp. 95-104. doi: 10.14359/51715585

54. Nanayakkara, O.; Gunasekara, C.; Sandanayake, M.; Law, D. W.; Nguyen, K.; Xia, J.; and Setunge, S., "Alkali Activated Slag Concrete Incorporating Recycled Aggregate Concrete: Long Term Performance and Sustainability Aspect," *Construction and Building Materials*, V. 271, 2021, Article No. 121512. doi: 10.1016/j.conbuildmat.2020.121512

55. Bayiha, B. N.; Billong, N.; Yamb, E.; Kaze, R. C.; and Nzengwa, R., "Effect of Limestone Dosages on Some Properties of Geopolymer from Thermally Activated Halloysite," *Construction and Building Materials*, V. 217, 2019, pp. 28-35. doi: 10.1016/j.conbuildmat.2019.05.058

56. Kim, T., and Kang, C., "The Mechanical Properties of Alkali-Activated Slag-Silica Fume Cement Pastes by Mixing Method," *International Journal of Concrete Structures and Materials*, V. 14, No. 1, 2020, Article No. 41. doi: 10.1186/s40069-020-00416-x

57. Shariati, M.; Shariati, A.; Trung, N. T.; Shoaei, P.; Ameri, F.; Bahrami, N.; and Zamanabadi, S. N., "Alkali-Activated Slag (AAS) Paste: Correlation between Durability and Microstructural Characteristics," *Construction and Building Materials*, V. 267, 2021, Article No. 120886. doi: 10.1016/j.conbuildmat.2020.120886

ACI in Your Classroom

Integrate ACI into your classroom!

To support future leaders, ACI has launched several initiatives to engage students in the Institute's activities and programs – select programs that may be of interest to Educators are:

- **Free student membership –** encourage students to sign up
- **Special student discounts on *ACI 318 Building Code Requirements for Structural Concrete*, *ACI 530 Building Code Requirements and Specification for Masonry Structure*, & *Formwork for Concrete* manual.**
- **Access to *Concrete International* –** free to all ACI student members
- **Access to *ACI Structural Journal* and *ACI Materials Journal* –** free to all ACI student members
- **Free sustainability resources –** free copies of Sustainable Concrete Guides provided to universities for use in the classroom
- **Student competitions –** participate in ACI's written and/or team-based competitions
- **Scholarships and fellowships –** students who win awards are provided up to $15,000 and may be offered internships and paid travel to attend ACI's conventions
- **ACI Award for University Student Activities –** receive local and international recognition for your University's participation in concrete-related activities
- **Free access to the *ACI Collection of Concrete Codes, Specifications, and Practices* –** in conjunction with ACI's chapters, students are provided free access to the online ACI Collection
- **ACI online recorded web sessions and continuing education programs –** online learning tools ideal for use as quizzes or in-class study material

https://www.concrete.org/educatorsandresearchers/aciinyourclassroom.aspx

ACI MATERIALS JOURNAL TECHNICAL PAPER

Title No. 120-M26

Effect of Polyphosphates on Properties of Alkali-Activated Slag/Fly Ash Concrete

by Youssef A. Mosleh, Mahmoud Gharieb, and Alaa M. Rashad

Polyphosphate materials such as sodium tripolyphosphate (STPP) and sodium hexametaphosphate (SHMP) are usually used as a dispersion agent for the ceramic industry, auxiliary materials in high-range water-reducing admixtures, and retarders in traditional cement systems. Until now, however, no comprehensive study has been performed on the effect of STPP or SHMP on the properties of alkali-activated materials (AAMs). Thus, in this paper, the effect of different concentrations (2 to 8 wt. %) of STPP and SHMP on the properties of alkali-activated slag/fly ash concrete was investigated. The variations in workability, compressive strength, water absorption, and total porosity with the incorporation of either STPP or SHMP at levels of 2, 4, 6, and 8%, by weight, were conducted. Modern techniques were employed to investigate the crystalline phases and microstructure morphologies. The primary results showed that both STPP and SHMP can increase workability. Each type of polyphosphate showed a positive effect on the compressive strength, but 4% was the optimum concentration. Both water absorption and total porosity were reduced with the incorporation of each type of polyphosphate, but 4% was the optimum. The incorporation of a suitable concentration of each type of polyphosphate can enhance the dispersion and deagglomeration of the particles and refine the microstructure.

Keywords: alkali-activated slag/fly ash concrete; hardened properties; microstructure; sodium hexametaphosphate (SHMP); sodium tripolyphosphate (STPP); workability.

INTRODUCTION

In construction and civil engineering, concrete is the most typically used material due to its ease of configuration and implementation, good durability, and versatility. Recently, approximately 4.4 billion tonnes of concrete are produced annually. The requirement for concrete in different fields is increasing at a rapid rate. It is expected that by 2025, approximately 5.5 billion tonnes of concrete will be produced.[1] Portland cement (PC) is still the popular binder material for concrete. This has led to an increase in the production of cement from 3.31 billion tonnes in 2010 to 4.1 and 4.4 billion tonnes in 2020 and 2021,[2,3] respectively. Cement production is accused of releasing huge amounts of toxic gases, consuming intensive amounts of fuel and raw materials. This industry alone emits approximately 8% of global CO_2 emissions. By 2050, it is expected that direct CO_2 releases from this industry will increase by 4%.[4] The cement industry is not only accused of emitting a high amount of CO_2 but also accused of releasing other toxic gases such as CO, SO_2, and NO_x. Unfortunately, this industry furiously devours approximately 12 to 15% of global annual energy.[5] It is urgent to find a suitable solution for these problems. One scenario to reduce cement consumption is substituting a part of cement with supplementary cementitious materials (SCMs) such as slag,[6] metakaolin,[7] and fly ash (FA).[8] An alternative, more effective scenario for hindering cement production is replacing cement with a new binder material based on alkali activation. As a result of using alkali-activated materials (AAMs) as an alternative to cement, CO_2 emissions, energy, and raw materials consumption can be reduced. Materials rich with aluminosilicate such as FA,[9] metakaolin,[10] and slag[11] are commonly used as precursors for AAMs. Using by-product materials such as slag and FA in AAMs not only reduces the problems of the cement industry but also reduces the industry wastes.[12] Starting from 1930, with the first use of slag powder activated with KOH,[13] the development and improvement of these materials are continuous. One of the most common scenarios to improve the properties of AAMs is adding suitable ratios of SCMs,[12,14] fibers,[15-17] nanoparticles,[18,19] chemical admixtures,[20] and so on.

Sodium tripolyphosphate (STPP) and sodium hexametaphosphate (SHMP) are two types of polyphosphate. STPP is an inorganic compound. It is a sodium salt of the phosphate penta-anion. It is a white powder that has a variety of uses. It can be used as an additive for food, as a preservative material, and as a treated material for animal feed and pet food.[21] Furthermore, STPP can be used in dishwashing and laundry detergents, as a tanning leather agent, for metallurgy, petroleum refining, water treatment, and mining applications. In the construction field, it can be added directly to the dry mixture or dissolved into mixing water. It is commonly used as a dispersing agent in the processing of ceramics[22,23] and making refractory castables.[24,25] It can be used as an additive for PC,[26-30] magnesium phosphate cement,[31,32] and gypsum,[33] and as an alkalinity source to control the interstitial pH value.[22] It can be used as an effective anticorrosive pigment for waterborne epoxy coatings[34] and an effective inhibitor against steel corrosion in concrete.[35] SHMP is an inorganic compound, which is a white powder or block solid or colorless transparent glass flake. It is a very hygroscopic material. Similar to STPP, SHMP has a different variety of uses. It can be used as an additive for food, textiles, dyeing, washing, rinsing, water treatment and papermaking, an effective ingredient in toothpaste for tartar prevention, and as an anti-staining agent. In the construction field, it can be used as a retarding agent for cement,[30,36] an additive for calcium aluminate cement[37,38] and refractory materials,[38] a

ACI Materials Journal, V. 120, No. 2, March 2023.

MS No. M-2022-125.R1, doi: 10.14359/51738460, received August 17, 2022, and reviewed under Institute publication policies.

water reducer for MgO/silica fume (SF) systems,[39] a modifying agent for the ceramic industry,[40] a corrosion inhibitor,[41] and a deflocculant in clay-based ceramic particles production.[42,43] It can also be used as a dispersing agent to break down clay and other types of soil.[44]

RESEARCH SIGNIFICANCE

Despite there being numerous uses of STPP and SHMP, there is no trial study to investigate the effect of STPP or SHMP on the properties of AAMs. Thus, it is useful to know the behaviors of AAMs when STPP or SHMP was added. Consequently, the properties of alkali-activated slag/FA concrete after adding 2 to 8% with a step of 2 wt. % of STPP and SHMP were investigated. These properties included workability, compressive strength, water absorption, total porosity, crystalline phases, and microstructure morphologies. This investigation can be considered an initial study in this field, and more studies are needed to cover the effect of STPP and SHMP on the remaining properties of AAMs.

EXPERIMENTAL DETAILS

Materials

The main precursors used in the current investigation were slag and FA. The slag was obtained from Helwan Steel and Iron Factory in Cairo, Egypt. The obtained slag was powdered in a special machine to obtain 300 kg/m^2 Blaine surface area. Its specific gravity was 2.9. The used FA can be classified as Class F according to ASTM C618-08. It was obtained from a local company. Its specific gravity and Blaine surface area were 2.2 and 400 kg/m^2, respectively. The chemical composition of both the slag and FA analyzed by X-ray fluorescence (XRF) is presented in Table 1. The X-ray diffraction (XRD) patterns of the precursors are plotted in Fig. 1. The NaOH, sodium silicate, STPP, and SHMP were delivered from a chemicals company in Cairo. The NaOH pellets with 98% purity were used as a part of the alkali activator. The properties of the sodium silicate used herein were similar to those reported in Rashad and Essa.[45] The STPP used herein has 0.023% water-insoluble matter, 0.006% Fe, 89.53% whiteness, 94.21 $Na_5P_3O_{10}$, 56.7% P_2O_5, 0.57 g/cm^3 density, and 9.8 pH value. The SHMP used herein has 68% total P_2O_5, 7.5% inactive P_2O_5, 0.03% Fe, 0.03% water insolubility, 8.6 pH value, 2.48 g/cm^3 density, and 90% whiteness. Natural sand with a maximum grain size, water absorption, and fineness modulus of 4.75 mm, 1.5%, and 2.75, respectively, was used as a fine aggregate. The natural crushed stone has a fineness modulus and water absorption of 6.8 and 0.95%, respectively, and was used as a coarse aggregate. The prevailing size (more than 90%) of the coarse aggregate was 10 mm. Figure 2 shows the optical view of the raw materials used herein.

Table 1—Chemical composition of precursors

Oxide, %	Slag, %	FA, %
SiO_2	33	58.12
Al_2O_3	16	31.90
Fe_2O_3	1.5	1.74
CaO	37.39	1.32
MgO	6.19	2.20
K_2O	0.93	0.42
Na_2O	1.84	0.64
SO_3	1.86	0.32
MnO	0.53	—
TiO_2	0.83	0.67
BaO	0.3	—
SrO	0.14	—
ZrO_2	0.07	—
P_2O_5	0.02	0.33
Cl^-	0.18	0.04
Cr_2O_3	0	—
ZnO	0	—
Loss on ignition	0.51	2.12

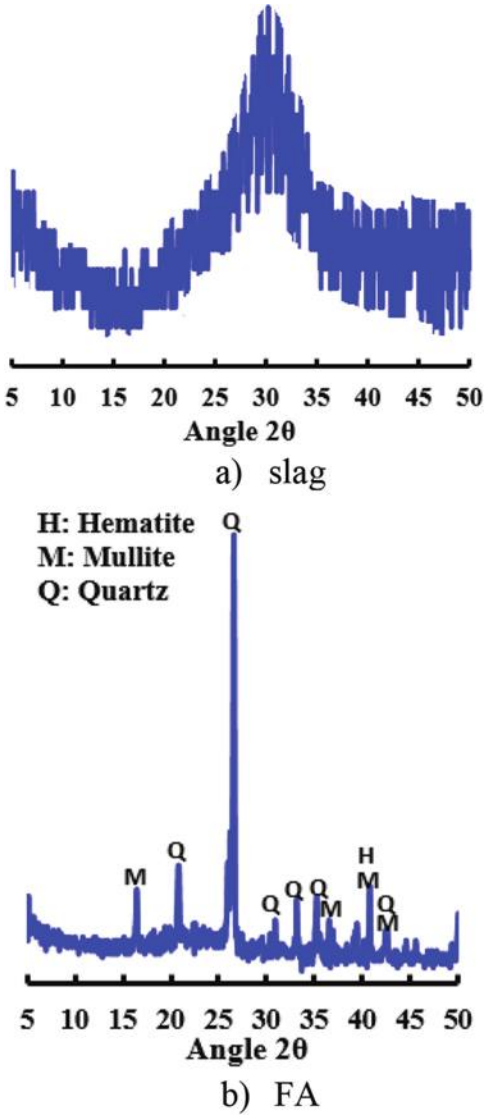

Fig. 1—XRD patterns of: (a) slag; and (b) FA.

Mixture preparation and methods

The control concrete mixture with the target compressive strength of 30 MPa free from any addition of STPP or SHMP was labeled as C0. An additional eight concrete mixtures were prepared by adding either STPP or SHMP at levels of 2, 4, 6, and 8% by weight. These mixtures were labeled as T2, T4, T6, T8, H2, H4, H6, and H8, respectively. The NaOH pellets were added to water and dissolved to prepare a solution with a 12 M concentration.[46] This solution was prepared 1 day before use. The alkaline activator solution (40 wt. % of the powders) was made from one part of NaOH to 2.5 parts of sodium silicate. A fixed extra water-powders ratio of 0.15 was used. The required concentration from each type of polyphosphate (that is, STPP or SHMP) was dissolved in mixing water. Table 2 briefs the components of each concrete mixture. Similar mixtures free from aggregates were prepared for the XRD test.

The mixing sequence was as follows: The solid ingredients (that is, slag/FA and aggregates) were dry-mixed in a drum mixer for 5 minutes. The activator solution and STPP or SHMP (if any) premixed with additional water were poured into the solid ingredients and mixed for 5 minutes. When the homogeneous mixture was reached, the workability was measured according to ASTM C143; simultaneously, the molds were filled with fresh concrete and vibrated for 1 minute, and leveled and covered with a polypropylene sheet to enhance the curing condition by eliminating water evaporation. The specimens were demolded after 24 hours from casting, then cured at room temperature to simulate actual curing.[47] Figure 3 shows optical photos during mixing conditions. The compressive strength at the ages of 7, 28, and 56 days were measured according to BS 1881: Part 120:1983 using cube specimens with 100 mm long sides. The total porosity and water absorption at the same ages were measured according to ASTM C642 using 100 mm cube specimens. For each test, at least three specimens were tested and the average was determined. The selected samples were prepared and analyzed for XRD and scanning electron microscope (SEM) analyses in a similar way reported in Rashad and Essa.[45]

RESULTS AND DISCUSSION

Workability

Figure 4 shows optical photos during the measurement of the slump of the mixtures, while Fig. 5 shows the effect of various concentrations of STPP on the slump. As can be seen, the slump of the mixtures depends on the concentration of STPP. The incorporation of STPP in the mixture has a positive effect on the workability: the higher the STPP

Fig. 2—View of starting materials.

Table 2—Concrete mixture proportions, kg/m³

ID	Slag	FA	NaOH (12 M)	Sodium silicate	Extra water	STPP	SHMP	Fine aggregate	Coarse aggregate
C0	240	240	55	137	74	0	0	580	1015
T2	240	240	55	137	74	9.6	0	580	1015
T4	240	240	55	137	74	19.2	0	580	1015
T6	240	240	55	137	74	28.8	0	580	1015
T8	240	240	55	137	74	38.4	0	580	1015
H2	240	240	55	137	74	0	9.6	580	1015
H4	240	240	55	137	74	0	19.2	580	1015
H6	240	240	55	137	74	0	28.8	580	1015
H8	240	240	55	137	74	0	38.4	580	1015

Fig. 3—Optical photos during mixing.

Fig. 4—Optical photos during slump measuring.

concentration, the higher the workability of the mixture. The inclusion of only 2% STPP in the concrete mixture (T2) can increase the slump from 80 mm for the control mixture (T0) to 100 mm with a higher ratio of 20%. Increasing STPP concentrations to 4, 6, and 8% resulted in an additional increase in the slump from 100 mm for T2 to 110, 130, and

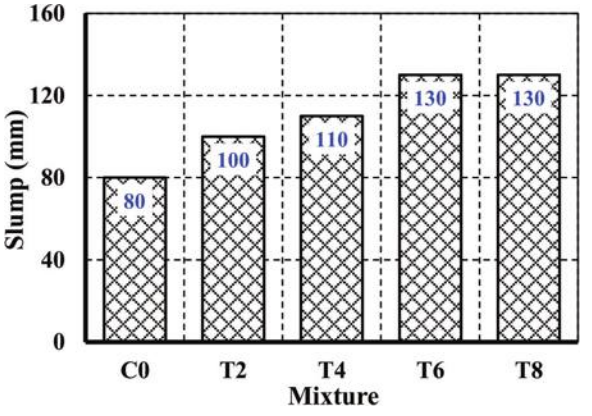

Fig. 5—Variation of slump with STPP concentration. (Note: 1 in. = 25.4 mm.)

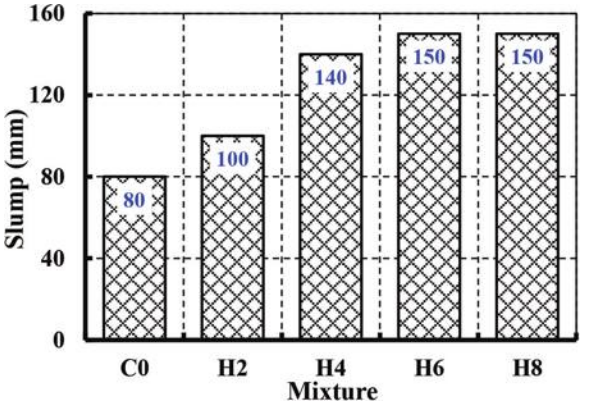

Fig. 6—Variation of slump with SHMP concentration. (Note: 1 in. = 25.4 mm.)

130 mm for T4, T6, and T8, respectively. The incorporation of STPP not only has a positive effect on the workability herein but also showed a positive effect on the workability in other systems. In this regard, Tan et al.[48] found higher fluidity of cement-montmorillonite paste mixture with the incorporation of 0.05 to 0.15% STPP. Ltifi et al.[27] confirmed higher fluidity of cement paste mixtures during a very short period by adding small amounts of STPP. The fluidity results obtained by Tan et al.[49] revealed that the incorporation of 0.05 to 0.2% STPP into cement paste mixtures increased their fluidity. Li[50] confirmed higher fluidity of sulfoaluminate

cement/aluminate cement/FA/ultrafine slag mortar mixtures with the incorporation of STPP.

Figure 6 shows the effect of various concentrations of SHMP on the slump. As can be seen, a similar trend of the workability results to those of STPP was observed when various concentrations of SHMP were added, but with a higher rate. The incorporations of 2%, 4%, 6%, and 8% SHMP increase the slump by 25%, 75%, 87.5%, and 87.5%, respectively, compared to the control. The incorporation of SHMP not only increases the workability herein but also increased it in other systems. Cheng et al.[38] reported higher workability of calcium aluminate cement paste mixtures with the incorporation of SHMP up to 0.2%. Wei et al.[51] incorporated 2% SHMP into the MgO/microsilica paste mixture aiming to improve its fluidity. Zhang et al.,[39] as well as Tan et al.,[49] found that the addition of 1% SHMP into the MgO/SF mixture led to a reduction in water requirement. Bu et al.[52] confirmed that 2.5% SHMP can be used as an additive for phosphoaluminate cement to limit fluid loss.

The main feature of Fig. 5 and 6 is increased workability as the concentration of STPP or SHMP increased up to 8%. The incorporation of SHMP showed higher workability than that of STPP. This observation was also previously observed by Otroj et al.,[53] who found higher flowability of Al_2O_3-SiC-C castable mixtures containing 0.01 to 0.1% SHMP compared to those containing the same dosages of STPP. The higher workability with the incorporation of these two types of polyphosphate (that is, STPP and SHMP) could be related to the higher repulsion forces that they caused. These repulsion forces can reduce the viscosity and increase workability.[53,54]

Compressive strength

Figure 7 shows optical photos during measurement of the slump of the compressive strength, while Fig. 8 shows the development results of compressive strength during the ages of 7, 28, and 56 days for concrete specimens containing different concentrations of STPP. Exactly as expected, the compressive strength was enhanced with a longer hydration period. The control specimens (C0) show good compressive strength, of which the obtained compressive strength reaches 25, 28.7, and 33.3 MPa at the ages of 7, 28, and 56 days, respectively. The incorporation of STPP has a substantial effect on compressive strength. This mainly is contingent on its concentration. The incorporation of only 2% STPP (T2) can marginally enhance the strength at all ages by an average of 5.9%. Increasing STPP concentration to 4% (T4) results in an additional strength enhancement, of which the strength reaches its highest value with an average enhancement of 38.8%. The incorporations of higher concentrations of STPP than 4% do not show additional improvement, but a slight degradation in strength was observed. In comparison with T4, the incorporations of 6% (T6) and 8% (T8) STPP decrease the strength by an average of 10.32% and 17.76%, respectively, while they show an average increase of 24.4% and 18.34% compared to the control (C0), respectively. The incorporation of STPP can not only increase the compressive strength of this system used herein but can also increase the strength of other systems. Hall et al.[31] found higher 24-hour and 7- and 28-day flexural strength of magnesia-phosphate

Fig. 7—Optical photos during measurement of compressive strength.

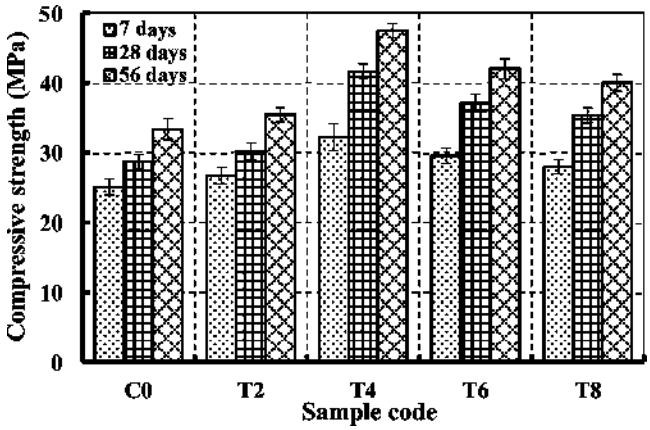

Fig. 8—Variation of compressive strength with STPP concentration. (Note: 1 MPa = 145.032 psi.)

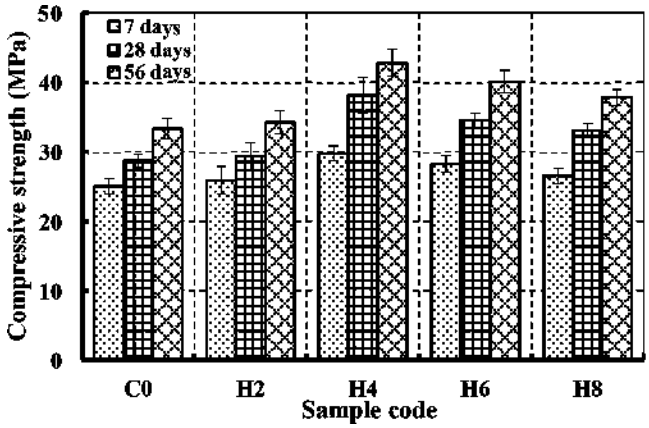

Fig. 9—Variation of compressive strength with SHMP concentration. (Note: 1 MPa = 145.032 psi.)

cement mortars with the incorporation of 25, 35, and 45 g of STPP/kg mortar batch. A higher amount of STPP slightly decreased it, but it was still higher than the control Pan and Wang[55] showed: a higher 2-hour compressive strength of α-calcium sulfate hemihydrate with adding 0.025% STPP.

Figure 9 shows the effect of various concentrations of SHMP on compressive strength development. As can be seen, a similar trend of the strength results to those of STPP

was observed when various concentrations of SHMP were added, but with a lower rate of enhancement. The incorporations of 2% (H2), 4% (H4), 6% (H6), and 8% (H8) SHMP increase the strength at all ages by an average of 2.9%, 26.77%, 17.82%, and 11.86%, respectively. The incorporation of SHMP can not only increase the compressive strength of this system used herein but can also increase the strength of other systems. The results obtained by Palou et al.[37] showed a higher 2 to 365-day compressive strength of high alumina cement with the incorporation of SHMP and calcium hydroxide. Jia et al.[56] reported higher compressive strength of MgO/SF cement with the incorporation of 2% SHMP.

The main features of Fig. 8 and 9 show using STPP or SHMP as an additive in alkali-activated slag/FA concrete has a positive effect on the compressive strength. The optimum ratio was 4%. Higher ratios than 4% (that is, 6 and 8%) did not show more strength enhancement compared to that of 4%, but a slight reduction in strength was obtained. Even though the incorporation of 6 and 8% STPP or SHMP slightly decreased the compressive strength compared to that of 4%, it is still higher than the control. The enhancement in the compressive strength with the inclusion of suitable concentrations of each type of polyphosphate (that is, STPP or SHMP) could be related to increasing the alkalinity of the matrix. Increasing the alkalinity up to a certain level has an important effect on the hydration[57,58] and mechanical strength[58-60] of AAMs. The measured pH value of the control sample (C0) was 10.95; when 4% STPP was added, this pH value was increased to reach 11.25. In such a way, when 4% SHMP was added, the pH value of C0 was increased to reach 11.0. It was reported that a higher pH value led to a higher compressive strength of MgO/SF cement.[56]

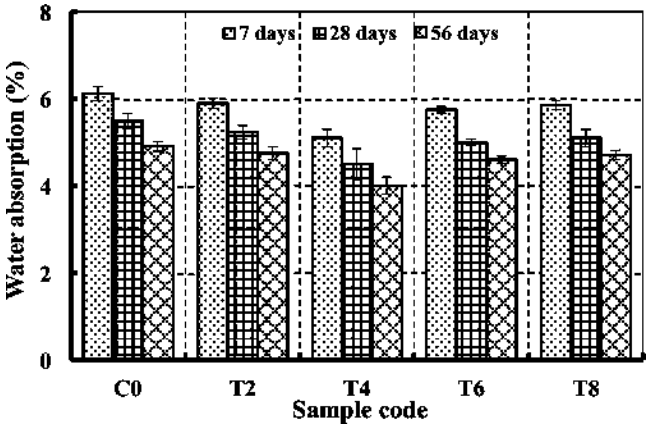

Fig. 10—Variation of water absorption with STPP concentration.

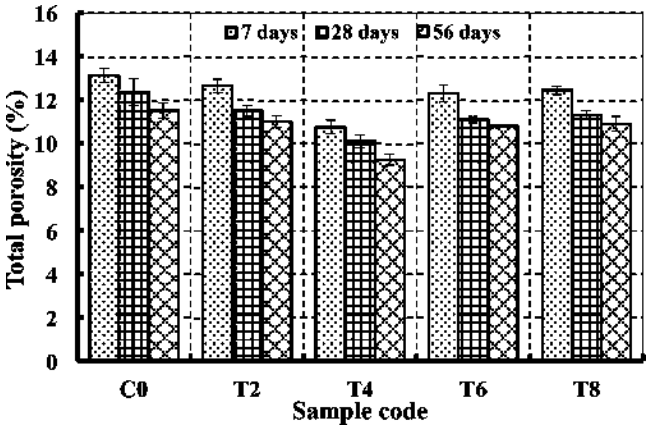

Fig. 11—Variation of total porosity with STPP concentration.

In addition, the incorporation of STPP or SHMP has an important role in supporting wet-mix compaction, which has a positive effect on the compressive strength.[31] This enhancement also could be related to the stabilization and filling effect of SHMP.[37] On the other hand, higher concentrations of STPP or SHMP than the optimum can somewhat increase the degree of heterogeneity (refer to Fig. 16 later) and resulted in a reduction in the strength compared with that containing the optimum concentration.[31] The same trend was also observed in other systems. Ltifi et al.[26] found an enhancement in the 7-day compressive strength of cement pastes with the incorporation of 1 and 5 g/L STPP, while the incorporation of 50 g/L decreased it. Fan and Chen[32] confirmed an increase in the 1-hour, 3-hour, 1-day, 7-day, and 28-day compressive strength of magnesium phosphate cement specimens with the incorporation of 0.5 to 2% STPP, while the incorporation of 2.5% STPP decreased it but was still higher than the control. Finally, as visible from comparing Fig. 8 and 9, the compressive strength of STPP specimens is somewhat higher than that of SHMP specimens. This could be related to the higher pH value of STPP (9.8) compared to that of SHMP (8.6). The higher pH value can dissolve the precursor and produce higher strength.[61,62]

Water absorption and total porosity

A matrix's ability to absorb water is one of the most important indicators of its durability, as well as the formed cracks caused by shrinkage. Water absorption is directly proportional to structural pores, capillary pores, and volume of internal porosity. Estimation of surface porosity can be made by measuring water absorption.[63] The volume of voids in the matrix is an indication of its porosity. It affects the matrix strength, mass transport process, and can be used as an indicator of its performance and durability. Figures 10 through 13 show the variation of water absorption and total porosity at different ages with the incorporation of different

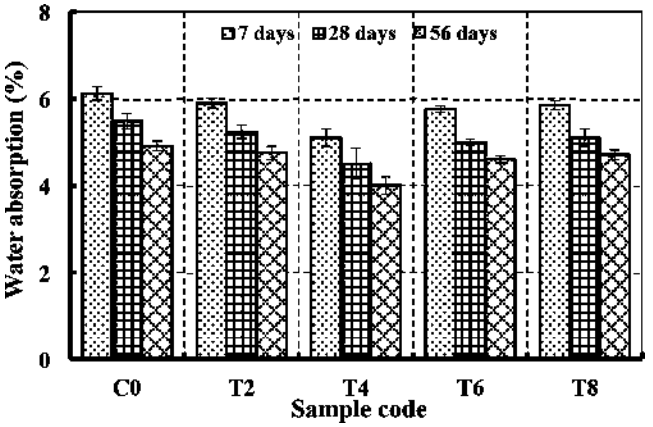

Fig. 12—Variation of water absorption with SHMP concentration.

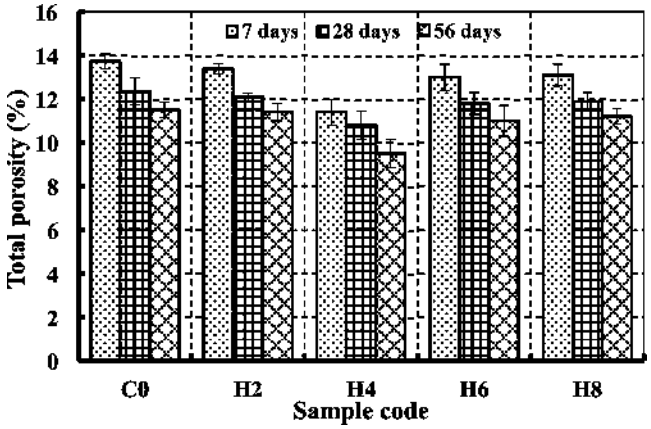

Fig. 13—Variation of total porosity with SHMP concentration.

concentrations of STPP and SHMP. The general view of the results confirms the remarkable effect of each type of polyphosphate as well as hydration time on both water absorption and total porosity. The control specimens show the highest water absorption and porosity. At the age of 7 days, the control specimens show 6.1% water absorption. This ratio was reduced with increasing hydration time, due to the improvement of pore structure,[64] to reach 5.5% and 4.91% at the ages of 28 and 56 days, respectively. The obtained results at the age of 28 days herein are higher than those of alkali-activated slag concrete reported in References 65 through 68, lower than those reported in References 69 through 72, and comparable to those reported in Reference 73. Similarly, the specimens free from any type of polyphosphate show the highest total porosity of 13.7%, 12.4%, and 11.5% at the ages of 7, 28, and 56 days, respectively. The obtained results are acceptable: the porosity at the age of 28 days is higher than what was reported in References 47, 65, and 67 and lower than what was reported in References 74 and 75.

The incorporation of STPP has a remarkable effect on water absorption and porosity (Fig. 10 and 11). This mainly depends on its concentration. The incorporation of only 2% STPP (T2) can marginally reduce water porosity at all ages by an average of 3.83%. Increasing STPP concentration to 4% (T4) results in an additional water absorption reduction, which accounts for an average of 17.65% lower than the control. The incorporations of higher concentrations of STPP than 4% do not show additional reduction, but a slight increase in water absorption was observed (Fig. 10). Compared to T4, the inclusions of 6% (T6) and 8% (T8) STPP increase water absorption by an average of 12.9% and 15.23%, respectively. Compared to C0, the inclusions of 6% (T6) and 8% (T8) STPP reduce water absorption by an average of 7.1% and 5.1%, respectively. Similarly, the inclusion of 2% (T2), 4% (T4), 6% (T6), and 8% (T8) STPP can reduce the total porosity from an average of 12.33% to an average of 11.72%, 10%, 11.4%, and 11.55%, respectively (Fig. 11).

Figures 12 and 13 show the effect of various concentrations of SHMP on water absorption and total porosity development. As can be noted, these results show a similar trend to those obtained with the inclusion of STPP but with

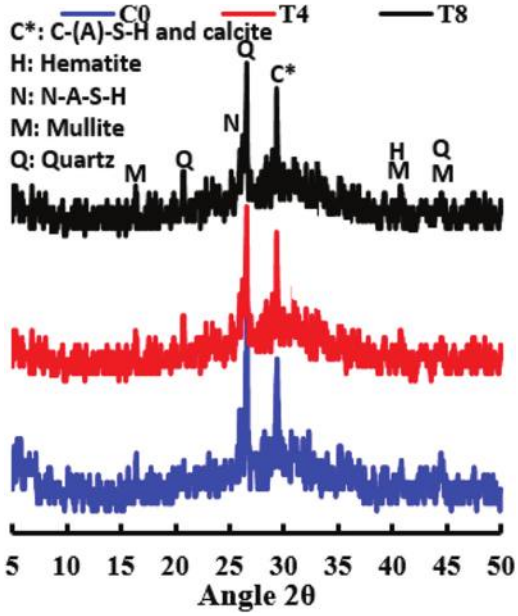

Fig. 14—XRD patterns for C0, T4, and T8 samples.

a slightly higher rate. The incorporations of 2% (H2), 4% (H4), 6% (H6), and 8% (H8) SHMP reduce water absorption by an average of 2.27%, 13.5%, 4.9%, and 3.42%, respectively, while the obtained total porosity was 12.3%, 10.57%, 11.93%, and 12.1%, respectively. The main features of Fig. 10 through 13 are using STPP or SHMP as an additive in alkali-activated slag/FA concrete has a positive effect on reducing water absorption and total porosity. The optimum ratio was 4%. This reduction could be attributed to the increased repulsive force between powder particles caused by each type of polyphosphate. This force can enhance the dispersion[38,56,76] and deagglomeration[77] of the particles, producing a refined microstructure (refer to Fig. 16 later). In addition, each type of polyphosphate has a deflocculating characteristic. It was reported that deflocculating characteristics can improve the wet-mix compaction, which led to lower porosity of the hardened matrix.[78]

Crystalline phases

Figure 14 shows the XRD patterns of the control sample (C0) as well as those containing 4% STPP (T4) and 8% STPP (T8) after hydration for 28 days. The sample of C0 shows the existence of a diffusive hump, which is attributed to the amorphous gels in both raw precursors and hydration products. This hump is centered between 25 and 35 degrees 2θ. The coexistence of semi-crystalline phases of C-(A)-S-H and N-A-S-H can be detected. This detection is consistent with what was previously described by Aboulayt et al.,[79] who reported that replacing slag with 20 to 40% FA in an alkali-activated slag/FA system resulted in a predominate C-A-S-H phase concerted with N-A-S-H. The mineralogical characterization of this sample (C0) shows the dominant peaks of quartz, which is an indication that quartz in the starting material did not participate in the reaction.[80] The crystalline peaks of mullite and hematite also can be detected.[81] As observed, there is no remarkable change in the different phases for T4 and T8 samples compared to C0.

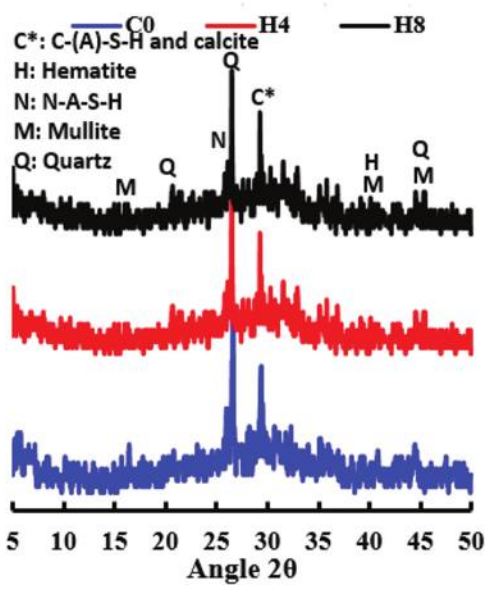

Fig. 15—XRD patterns for C0, H4, and H8 samples.

Similar peak identifications can be observed for the samples containing 4% SHMP (H4) and 8% SHMP (T8) (Fig. 15).

Microstructure analysis

Figure 16 shows the SEM images of the reference sample (C0) as well as samples containing different concentrations of STPP (T4, T8) and SHMP (H4, H8) after hydration for 28 days. As is clear from Fig. 16(a), the C0 sample shows some unreacted FA particles that can be identified by their spherical shape as well as slag particles that can be identified by their irregular, jagged, and angular shapes with light gray color. This image shows a somewhat heterogeneous microstructure with a small number of pores. The incorporation of 4% STPP or 4% SHMP has a remarkable effect on the microstructure of the sample (Fig. 16(b) and (c)): the microstructure of each sample seems to be relatively dense and more homogenous compared to the control (C0). The dispersion stability was increased due to increasing electrostatic repulsion between particles.[38,76] These features are in agreement with the results of enhanced compressive strength, reduced water absorption, and reduced total porosity. In another

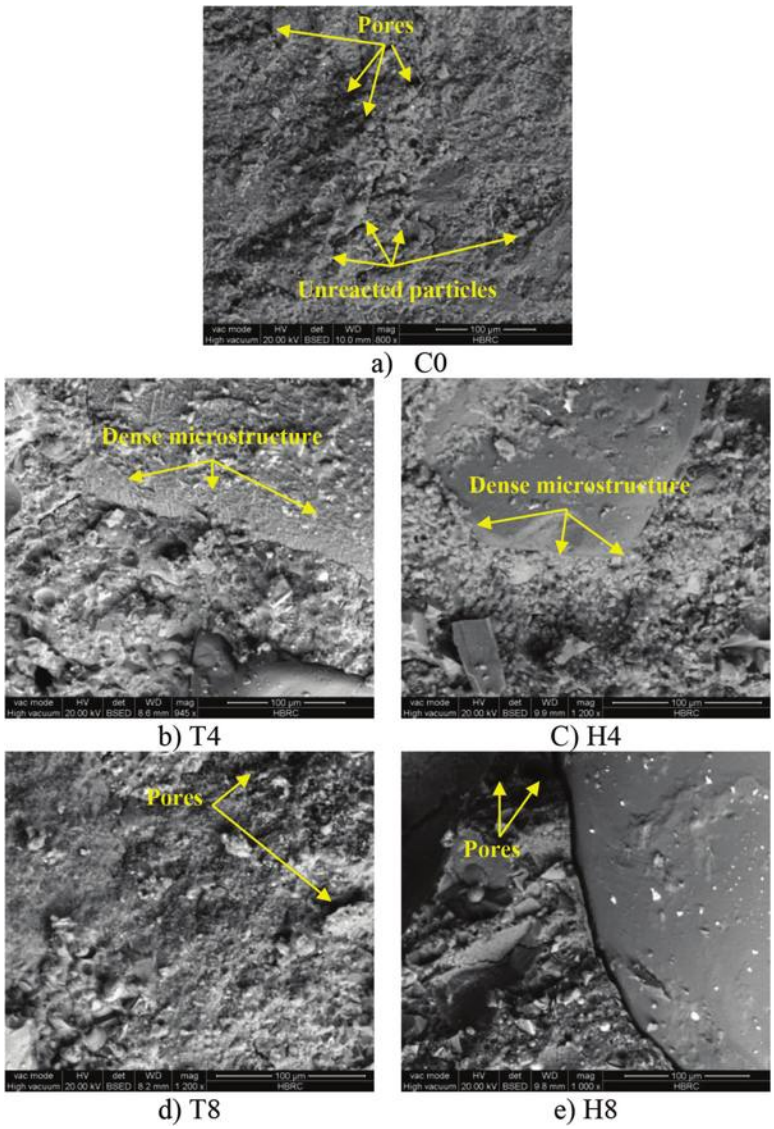

Fig. 16—SEM images of: (a) C0; (b) T4; (c) H4; (d) T8; and (e) H8.

system, Song et al.[76] reported that the incorporation of SHMP into gas-sealing coating filler resulted in a homogenous and dense microstructure. Increasing the concentration of STPP or SHMP to 8% results in an increase in the heterogeneity degree (Fig. 9(d) and (e)). This increase in heterogeneity or decreased homogeneity is the main reason for variation in the compressive strength. In another system, Hall et al.[31] reported that the incorporation of lower or higher ratios of STPP in magnesium phosphate cement than the optimum resulted in an increase in the heterogeneity degree.

CONCLUSIONS

In this paper, the possibility of improving some properties of alkali-activated slag/fly ash (FA) concrete by incorporating different concentrations of different types of polyphosphate named sodium tripolyphosphate (STPP) and sodium hexametaphosphate (SHMP) was studied. The effects of different concentrations of STPP and SHMP on workability, compressive strength, water absorption, total porosity, and microstructure morphology were investigated. The main conclusions extracted from this study are listed as follows:

1. The incorporation of STPP and SHMP increased workability.

2. The compressive strength at all ages was enhanced with the incorporation of STPP or SHMP due to the increase in the alkalinity as well as the stabilization and filling effect of STPP and SHMP.

3. The concentration of 4% from STPP or SHMP exhibited the highest strength. Increasing the concentrations over 4% did not show additional improvement in the strength, but a slight reduction was observed.

4. The incorporation of STPP or SHMP in the matrix showed a positive effect in reducing water absorption and total porosity, of which 4% showed the highest reduction. This positive effect is attributed to enhancing the dispersion and deagglomeration of the particles and refining the microstructure. In addition, the deflocculating characteristics of each type of polyphosphate can improve the wet-mix compaction, which led to lower porosity of the hardened matrix.

5. The incorporation of 4% STPP or SHMP in the matrix resulted in a relatively dense and more homogenous microstructure compared to the control, of which the dispersion stability was increased due to increasing electrostatic repulsion between particles.

6. This study can be considered as an initial or a preliminary study, and more studies are required.

AUTHOR BIOS

Youssef A. Mosleh *is a Researcher (Assistant Professor) at the Building Materials and Quality Control Research Institute, Housing and Building National Research Center (HBRC), Cairo, Egypt. He received his BS, MS, and PhD from the Faculty of Engineering at Cairo University, Cairo, Egypt. His research interests include building materials, nanotechnology, and geopolymers.*

Mahmoud Gharieb *is a Researcher (Assistant Professor) at the Raw Building Materials and Technology Processing Research Institute, Housing and Building National Research Center (HBRC), Cairo, Egypt. He received his BS and MS from the Faculty of Science at Al-Azhar University, Cairo, Egypt, and his PhD from Ain Shams University, Cairo, Egypt. His research interests include building materials and geopolymers.*

Alaa M. Rashad *is a Professor at the Building Materials and Quality Control Research Institute, Housing and Building National Research Center (HBRC), Cairo, Egypt, as well as the Civil Engineering Department, College of Engineering, Shaqra University, Al-Dawadmi, Riyadh, Saudi Arabia. He received his BS, MS, and PhD from the Faculty of Engineering at Cairo University. He received his postdoctoral research associate from the School of Planning, Architecture, and Civil Engineering, Queen's University Belfast, Belfast, UK. His research interests include building materials, nanotechnology, alkali-activated materials, fire resistance, and thermal insulation.*

REFERENCES

1. Hilburg, J., "Concrete Production Produces Eight Percent of the World's Carbon Dioxide Emissions," *The Architect's Newspaper*, Jan. 2, 2019, https://www.archpaper.com/2019/01/concrete-production-eight-percent-co2-emissions/. (last accessed Feb. 13, 2023)

2. U.S. Geological Survey, "Mineral Commodity Summaries: 2012," Reston, VA, 2012.

3. U.S. Geological Survey, "USGS: Reston," Reston, VA, 2021, 200 pp.

4. Zhongming Z.; Linong, L.; Xiaona, Y.; Wangqiang, Z.; and Wei, L., "Cement Technology Roadmap Shows How the Path to Achieve CO2 Reductions Up to 24% by 2050," International Energy Agency, Paris, France, Apr. 6, 2018, https://www.iea.org/news/cement-technology-roadmap-plots-path-to-cutting-co2-emissions-24-by-2050. (last accessed Feb. 13, 2023)

5. Abriyantoro, D.; Dong, J.; Hicks, C.; and Singh, S. P., "A Stochastic Optimisation Model for Biomass Outsourcing in the Cement Manufacturing Industry with Production Planning Constraints," *Energy*, V. 169, 2019, pp. 515-526. doi: 10.1016/j.energy.2018.11.114

6. Rashad, A. M., "An Overview on Rheology, Mechanical Properties and Durability of High-Volume Slag Used as a Cement Replacement in Paste, Mortar and Concrete," *Construction and Building Materials*, V. 187, 2018, pp. 89-117. doi: 10.1016/j.conbuildmat.2018.07.150

7. Rashad, A. M., "Metakaolin: Fresh Properties and Optimum Content for Mechanical Strength in Traditional Cementitious Materials—A Comprehensive Overview," *Reviews on Advanced Materials Science*, V. 40, No. 1, 2015, pp. 15-44.

8. Rashad, A. M., "A Brief on High-Volume Class F Fly Ash as Cement Replacement—A Guide for Civil Engineer," *International Journal of Sustainable Built Environment*, V. 4, No. 2, 2015, pp. 278-306. doi: 10.1016/j.ijsbe.2015.10.002

9. Rashad, A. M., "A Comprehensive Overview about the Influence of Different Admixtures and Additives on the Properties of Alkali-Activated Fly Ash," *Materials & Design*, V. 53, 2014, pp. 1005-1025. doi: 10.1016/j.matdes.2013.07.074

10. Rashad, A. M., "Alkali-Activated Metakaolin: A Short Guide for Civil Engineer—An Overview," *Construction and Building Materials*, V. 41, 2013, pp. 751-765. doi: 10.1016/j.conbuildmat.2012.12.030

11. Rashad, A. M., "A Comprehensive Overview about the Influence of Different Additives on the Properties of Alkali-Activated Slag—A Guide for Civil Engineer," *Construction and Building Materials*, V. 47, 2013, pp. 29-55. doi: 10.1016/j.conbuildmat.2013.04.011

12. John, S. K.; Nadir, Y.; and Girija, K., "Effect of Source Materials, Additives on the Mechanical Properties and Durability of Fly Ash and Fly Ash-Slag Geopolymer Mortar: A Review," *Construction and Building Materials*, V. 280, 2021, Article No. 122443. doi: 10.1016/j.conbuildmat.2021.122443

13. Shi, C.; Roy, D.; and Krivenko, P. V., *Alkali-Activated Cements and Concretes*, CRC Press, Boca Raton, FL, 2003.

14. Rashad, A. M., "Effect of Quartz-Powder on the Properties of Conventional Cementitious Materials and Geopolymers," *Materials Science and Technology*, V. 34, No. 17, 2018, pp. 2043-2056. doi: 10.1080/02670836.2018.1471435

15. Rashad, A. M., "The Effect of Polypropylene, Polyvinyl-Alcohol, Carbon and Glass Fibres on Geopolymers Properties," *Materials Science and Technology*, V. 35, No. 2, 2019, pp. 127-146. doi: 10.1080/02670836.2018.1514096

16. Rashad, A. M., "Effect of Steel Fibers on Geopolymer Properties—The Best Synopsis for Civil Engineer," *Construction and Building Materials*, V. 246, 2020, Article No. 118534. doi: 10.1016/j.conbuildmat.2020.118534

17. Ranjbar, N., and Zhang, M., "Fiber-Reinforced Geopolymer Composites: A Review," *Cement and Concrete Composites*, V. 107, 2020, Article No. 103498. doi: 10.1016/j.cemconcomp.2019.103498

18. Rashad, A. M., "Effect of Nanoparticles on the Properties of Geopolymer Materials," *Magazine of Concrete Research*, V. 71, No. 24, 2019, pp. 1283-1301. doi: 10.1680/jmacr.18.00289

19. Li, Z.; Fei, M.-E.; Huyan, C.; and Shi, X., "Nano-Engineered, Fly Ash-Based Geopolymer Composites: An Overview," *Resources,*

Conservation and Recycling, V. 168, 2021, Article No. 105334. doi: 10.1016/j.resconrec.2020.105334

20. Tong, S.; Yuqi, Z.; and Qiang, W., "Recent Advances in Chemical Admixtures for Improving the Workability of Alkali-Activated Slag-Based Material Systems," *Construction and Building Materials*, V. 272, Feb. 2021, Article No. 121647. doi: 10.1016/j.conbuildmat.2020.121647

21. Schrödter, K.; Bettermann, G.; Staffel, T.; Wahl, F.; Klein, T.; and Hofmann, T., "Phosphoric Acid and Phosphates," *Ullmann's Encyclopedia of Industrial Chemistry*, Wiley-VCH Verlag GmbH & Co. KGaA, Weinheim, Germany, 2000.

22. Papo, A.; Piani, L.; and Ricceri, R., "Sodium Tripolyphosphate and Polyphosphate as Dispersing Agents for Kaolin Suspensions: Rheological Characterization," *Colloids and Surfaces A: Physicochemical and Engineering Aspects*, V. 201, No. 1-3, 2002, pp. 219-230. doi: 10.1016/S0927-7757(01)01024-X

23. Slyusar, A. A.; Slyusar, O. A.; and Zdorenko, N. M., "Rheological Properties and Critical Structure-Forming Concentration of Kaolin Suspensions with Complex Additives," *Glass and Ceramics*, V. 65, No. 7-8, 2008, pp. 285-286.

24. Goberis, S., and Stonis, R., "Advantageous Features of Sodium Silicate as the Plasticizer for Low-Cement Refractory Castables," *Refractories and Industrial Ceramics*, V. 45, No. 6, 2004, pp. 446-449. doi: 10.1007/s11148-005-0031-4

25. Goberis, S.; Pundene, I.; and Antonovich, V., "The Effect of Sodium Tripolyphosphate on the Properties of Medium-Cement Refractory Castables Based on Gorkal-40 Cement," *Refractories and Industrial Ceramics*, V. 46, No. 6, 2005, pp. 403-408. doi: 10.1007/s11148-006-0035-8

26. Ltifi, M.; Guefrech, A.; and Mounanga, P., "Effects of Sodium Tripolyphosphate Addition on Early-Age Physico-Chemical Properties of Cement Pastes," *Procedia Engineering*, V. 10, 2011, pp. 1457-1462. doi: 10.1016/j.proeng.2011.04.242

27. Ltifi, M.; Guefrech, A.; and Mounanga, P., "Effects of Sodium Tripolyphosphate on the Rheology and Hydration Rate of Portland Cement Pastes," *Advances in Cement Research*, V. 24, No. 6, 2012, pp. 325-335. doi: 10.1680/adcr.11.00028

28. Tan, H.; Ma, B.; Li, X.; Jian, S.; and Yang, H., "Effect of Competitive Adsorption between Sodium Tripolyphosphate and Naphthalene Superplasticizer on Fluidity of Cement Paste," *Journal of Wuhan University of Technology-Materials Science Edition*, V. 29, No. 2, 2014, pp. 334-340. doi: 10.1007/s11595-014-0917-4

29. Tan, H.; Zou, F.; Ma, B.; Liu, M.; Li, X.; and Jian, S., "Effect of Sodium Tripolyphosphate on Adsorbing Behavior of Polycarboxylate Superplasticizer," *Construction and Building Materials*, V. 126, 2016, pp. 617-623. doi: 10.1016/j.conbuildmat.2016.09.077

30. Tan, H.; Zou, F.; Liu, M.; Ma, B.; Guo, Y.; and Jian, S., "Effect of the Adsorbing Behavior of Phosphate Retarders on Hydration of Cement Paste," *Journal of Materials in Civil Engineering*, ASCE, V. 29, No. 9, 2017, p. 04017088. doi: 10.1061/(ASCE)MT.1943-5533.0001929

31. Hall, D. A.; Stevens, R.; and El-Jazairi, B., "The Effect of Retarders on the Microstructure and Mechanical Properties of Magnesia-Phosphate Cement Mortar," *Cement and Concrete Research*, V. 31, No. 3, 2001, pp. 455-465. doi: 10.1016/S0008-8846(00)00501-9

32. Fan, S., and Chen, B., "Experimental Study of Phosphate Salts Influencing Properties of Magnesium Phosphate Cement," *Construction and Building Materials*, V. 65, 2014, pp. 480-486. doi: 10.1016/j.conbuildmat.2014.05.021

33. Tan, H.; Deng, X.; Gu, B.; Ma, B.; Luo, S.; Zhi, Z.; Guo, Y.; and Zou, F., "Effect of Borax and Sodium Tripolyphosphate on Fluidity of Gypsum Paste Plasticized by Polycarboxylate Superplasticizer," *Construction and Building Materials*, V. 176, 2018, pp. 394-402. doi: 10.1016/j.conbuildmat.2018.05.005

34. Wang, N.; Yin, X.; Zhang, J.; Gao, H.; Diao, X.; and Yao, H., "Preparation and Anti-Corrosive Properties of Waterborne Epoxy Composite Coating Containing Graphene Oxide Grafted with Sodium Tripolyphosphate," *Coatings*, V. 10, No. 4, 2020, Article No. 307. doi: 10.3390/coatings10040307

35. Paulson, B. M.; Joby Thomas, K.; Raphael, V. P.; Shaju, K.; and Ragi, K., "Mitigation of Concrete Reinforced Steel Corrosion by Penta Sodium Triphosphate: Physicochemical and Electrochemical Investigations," *SN Applied Sciences*, V. 2, No. 11, 2020, Article No. 1813. doi: 10.1007/s42452-020-03586-1

36. Zhang, Y.; Liu, H.; Liu, J.; and Tong, R., "Effect of Sodium Hexametaphosphate and Trisodium Phosphate on Dispersion of Polycarboxylate Superplasticizer," *Materials (Basel)*, V. 12, No. 24, 2019, Article No. 4190. doi: 10.3390/ma12244190

37. Palou, M.; Kuzielová, E.; Žemlička, M.; and Živica, V., "The Influence of Sodium Hexametaphosphate ($Na_6P_6O_{18}$) on Hydration of Calcium Aluminate Cement under Hydrothermal Condition," *Procedia Engineering*, V. 151, 2016, pp. 119-126. doi: 10.1016/j.proeng.2016.07.371

38. Cheng, B.; Yao, C.; Xiong, J.; Liu, X.; Zhang, H.; and Zhang, S., "Effects of Sodium Hexametaphosphate Addition on the Dispersion and Hydration of Pure Calcium Aluminate Cement," *Materials (Basel)*, V. 13, No. 22, 2020, Article No. 5229. doi: 10.3390/ma13225229

39. Zhang, T.; Vandeperre, L. J.; and Cheeseman, C. R., "Formation of Magnesium Silicate Hydrate (M-S-H) Cement Pastes Using Sodium Hexametaphosphate," *Cement and Concrete Research*, V. 65, 2014, pp. 8-14. doi: 10.1016/j.cemconres.2014.07.001

40. Vitali, S., and Giorgini, L., "Overview of the Rheological Behaviour of Ceramic Slurries," *FME Transactions*, V. 47, No. 1, 2019, pp. 42-7.

41. Baia, X.; Wanga, Y.; Lib, R.; Chena, J.; Raoc, Q.; and Shud, S., "Corrosion Control and Inhibition Mechanism of Sodium Polyphosphate on Highly Eroded Cement Coating Pipe Surfaces," *Desalination and Water Treatment*, V. 113, 2018, pp. 81-87. doi: 10.5004/dwt.2018.22305

42. Andreola, F.; Castellini, E.; Manfredini, T.; and Romagnoli, M., "The Role of Sodium Hexametaphosphate in the Dissolution Process of Kaolinite and Kaolin," *Journal of the European Ceramic Society*, V. 24, No. 7, 2004, pp. 2113-2124. doi: 10.1016/S0955-2219(03)00366-2

43. Otroj, S.; Nilforushan, M. R.; Daghighi, A.; and Marzban, R., "Impact of Dispersants on the Mechanical Strength Development of Alumina-Spinel Self-Flowing Refractory Castables," *Ceramics-Silikáty*, V. 54, No. 3, 2010, pp. 284-289.

44. ASTM D422-63, "Standard Test Method for Particle-Size Analysis of Soils (Withdrawn 2016)," ASTM International, West Conshohocken, PA, 1963, pp. 10-16.

45. Rashad, A. M., and Essa, G. M. F., "Effect of Ceramic Waste Powder on Alkali-Activated Slag Pastes Cured in Hot Weather after Exposure to Elevated Temperature," *Cement and Concrete Composites*, V. 111, 2020, Article No. 103617. doi: 10.1016/j.cemconcomp.2020.103617

46. Gopalakrishnan, R., and Chinnaraju, K., "Durability of Ambient Cured Alumina Silicate Concrete Based on Slag/Fly Ash Blends against Sulfate Environment," *Construction and Building Materials*, V. 204, 2019, pp. 70-83. doi: 10.1016/j.conbuildmat.2019.01.153

47. Kuranlı, Ö. F.; Uysal, M.; Abbas, M. T.; Cosgun, T.; Niş, A.; Aygörmez, Y.; Canpolat, O.; and Al-mashhadani, M. M., "Evaluation of Slag/Fly Ash Based Geopolymer Concrete with Steel, Polypropylene and Polyamide Fibers," *Construction and Building Materials*, V. 325, 2022, Article No. 126747. doi: 10.1016/j.conbuildmat.2022.126747

48. Tan, H.; Guo, Y.; Ma, B.; Huang, J.; Gu, B.; and Zou, F., "Effect of Sodium Tripolyphosphate on Clay Tolerance of Polycarboxylate Superplasticizer," *KSCE Journal of Civil Engineering*, V. 22, No. 8, 2018, pp. 2934-2941. doi: 10.1007/s12205-017-2017-4

49. Tan, H.; Huang, J.; Ma, B.; and Li, X., "Effect of Superplasticiser and Sodium Tripolyphosphate on Fluidity of Cement Paste," *Magazine of Concrete Research*, V. 66, No. 23, 2014, pp. 1194-1200. doi: 10.1680/macr.14.00091

50. Li, X., "Effect of Chemical Admixtures on the Properties of Grouting Materials with High-Volume Mineral Materials," *Composites and Advanced Materials*, V. 28, 2019.

51. Wei, J.; Yu, Q.; Zhang, W.; and Zhang, H., "Reaction Products of MgO and Microsilica Cementitious Materials at Different Temperatures," *Journal of Wuhan University of Technology-Materials Science Edition*, V. 26, No. 4, 2011, pp. 745-748. doi: 10.1007/s11595-011-0304-3

52. Bu, Y.; Liu, H.; Nazari, A.; He, Y.; and Song, W., "Amphoteric Ion Polymer as Fluid Loss Additive for Phosphoaluminate Cement in the Presence of Sodium Hexametaphosphate," *Journal of Natural Gas Science and Engineering*, V. 31, 2016, pp. 474-480. doi: 10.1016/j.jngse.2016.03.062

53. Otroj, S.; Bahrevar, M. A.; Mostarzadeh, F.; and Nilforoshan, M. R., "The Effect of Deflocculants on the Self-Flow Characteristics of Ultra Low-Cement Castables in Al_2O_3–Sic–C System," *Ceramics International*, V. 31, No. 5, 2005, pp. 647-653. doi: 10.1016/j.ceramint.2004.06.023

54. Studart, A. R.; Zhong, W.; and Pandolfelli, V. C., "Rheological Design of Zero-Cement Self-Flow Castables," *American Ceramic Society Bulletin*, V. 78, No. 5, 1999, pp. 65-72.

55. Pan, W., and Wang, P., "Effect of Compounding of Sodium Tripolyphosphate and Super Plasticizers on the Hydration of α-Calcium Sulfate Hemihydrate," *Journal of Wuhan University of Technology-Materials Science Edition*, V. 26, No. 4, 2011, pp. 737-744. doi: 10.1007/s11595-011-0303-4

56. Jia, Y.; Wang, B.; Wu, Z.; Han, J.; Zhang, T.; Vandeperre, L. J.; and Cheeseman, C. R., "Role of Sodium Hexametaphosphate in MgO/SiO_2 Cement Pastes," *Cement and Concrete Research*, V. 89, 2016, pp. 63-71. doi: 10.1016/j.cemconres.2016.08.003

57. Song, S.; Sohn, D.; Jennings, H. M.; and Mason, T. O., "Hydration of Alkali-Activated Ground Granulated Blast Furnace Slag," *Journal of Materials Science*, V. 35, No. 1, 2000, pp. 249-257. doi: 10.1023/A:1004742027117

58. Rashad, A. M.; Bai, Y.; Basheer, P. A. M.; Milestone, N. B.; and Collier, N. C., "Hydration and Properties of Sodium Sulfate Activated

Slag," *Cement and Concrete Composites*, V. 37, 2013, pp. 20-29. doi: 10.1016/j.cemconcomp.2012.12.010

59. Song, S., and Jennings, H. M., "Pore Solution Chemistry of Alkali-Activated Ground Granulated Blast-Furnace Slag," *Cement and Concrete Research*, V. 29, No. 2, 1999, pp. 159-170. doi: 10.1016/S0008-8846(98)00212-9

60. Rashad, A. M., and Ezzat, M., "A Preliminary Study on the Use of Magnetic, Zamzam, and Sea Water as Mixing Water for Alkali-Activated Slag Pastes," *Construction and Building Materials*, V. 207, 2019, pp. 672-678. doi: 10.1016/j.conbuildmat.2019.02.162

61. Sakulich, A. R., and Bentz, D. P., "Mitigation of Autogenous Shrinkage in Alkali Activated Slag Mortars by Internal Curing," *Materials and Structures*, V. 46, No. 8, 2013, pp. 1355-1367. doi: 10.1617/s11527-012-9978-z

62. Song, C.; Choi, Y. C.; and Choi, S., "Effect of Internal Curing by Superabsorbent Polymers–Internal Relative Humidity and Autogenous Shrinkage of Alkali-Activated Slag Mortars," *Construction and Building Materials*, V. 123, 2016, pp. 198-206. doi: 10.1016/j.conbuildmat.2016.07.007

63. Rashad, A. M.; Khafaga, S. A.; and Gharieb, M., "Valorization of Fly Ash as an Additive for Electric Arc Furnace Slag Geopolymer Cement," *Construction and Building Materials*, V. 294, 2021, Article No. 123570. doi: 10.1016/j.conbuildmat.2021.123570

64. Hu, X.; Shi, C.; Shi, Z.; and Zhang, L., "Compressive Strength, Pore Structure and Chloride Transport Properties of Alkali-Activated Slag/Fly Ash Mortars," *Cement and Concrete Composites*, V. 104, 2019, Article No. 103392. doi: 10.1016/j.cemconcomp.2019.103392

65. Mithun, B. M., and Narasimhan, M. C., "Performance of Alkali Activated Slag Concrete Mixes Incorporating Copper Slag as Fine Aggregate," *Journal of Cleaner Production*, V. 112, Part 1, 2016, pp. 837-844. doi: 10.1016/j.jclepro.2015.06.026

66. Behfarnia, K., and Rostami, M., "Mechanical Properties and Durability of Fiber Reinforced Alkali Activated Slag Concrete," *Journal of Materials in Civil Engineering*, ASCE, V. 29, No. 12, 2017, p. 04017231. doi: 10.1061/(ASCE)MT.1943-5533.0002073

67. Hammad, N.; El-Nemr, A.; and Hasan, H. E.-D., "The Performance of Fiber GGBS Based Alkali-Activated Concrete," *Journal of Building Engineering*, V. 42, 2021, Article No. 102464. doi: 10.1016/j.jobe.2021.102464

68. Huang, J.; Zou, C.; Sun, D.; Yang, B.; and Yan, J., "Effect of Recycled Fine Aggregates on Alkali-Activated Slag Concrete Properties," *Structures*, V. 30, 2021, pp. 89-99.

69. Bai, Y.-H.; Yu, S.; and Chen, W., "Experimental Study of Carbonation Resistance of Alkali-Activated Slag Concrete," *ACI Materials Journal*, V. 116, No. 3, May 2019, pp. 95-104., doi: 10.14359/51715585

70. Ren, P.; Li, B.; Yu, J.-G.; and Ling, T.-C., "Utilization of Recycled Concrete Fines and Powders to Produce Alkali-Activated Slag Concrete Blocks," *Journal of Cleaner Production*, V. 267, 2020, Article No. 122115. doi: 10.1016/j.jclepro.2020.122115

71. Nanayakkara, O.; Gunasekara, C.; Sandanayake, M.; Law, D. W.; Nguyen, K.; Xia, J.; and Setunge, S., "Alkali Activated Slag Concrete Incorporating Recycled Aggregate Concrete: Long Term Performance and Sustainability Aspect," *Construction and Building Materials*, V. 271, 2021, Article No. 121512. doi: 10.1016/j.conbuildmat.2020.121512

72. El-Hassan, H.; Shehab, E.; and Al-Sallamin, A., "Effect of Curing Regime on the Performance and Microstructure Characteristics of Alkali-Activated Slag-Fly Ash Blended Concrete," *Journal of Sustainable Cement-Based Materials*, V. 10, No. 5, 2021, pp. 289-317. doi: 10.1080/21650373.2021.1883145

73. Thunuguntla, C. S., and Rao, T. D. G., "Effect of Mix Design Parameters on Mechanical and Durability Properties of Alkali Activated Slag Concrete," *Construction and Building Materials*, V. 193, 2018, pp. 173-188. doi: 10.1016/j.conbuildmat.2018.10.189

74. Lee, W.-H.; Wang, J.-H.; Ding, Y.-C.; and Cheng, T.-W., "A Study on the Characteristics and Microstructures of GGBS/FA Based Geopolymer Paste and Concrete," *Construction and Building Materials*, V. 211, 2019, pp. 807-813. doi: 10.1016/j.conbuildmat.2019.03.291

75. Cai, Y.; Yu, L.; Yang, Y.; Gao, Y.; and Yang, C., "Effect of Early Age-Curing Methods on Drying Shrinkage of Alkali-Activated Slag Concrete," *Materials (Basel)*, V. 12, No. 10, 2019, Article No. 1633. doi: 10.3390/ma12101633

76. Song, H.; Cao, Z.; Xie, W.; Cheng, F.; Gasem, K. A. M.; and Fan, M., "Improvement of Dispersion Stability of Filler Based on Fly Ash by Adding Sodium Hexametaphosphate in Gas-Sealing Coating," *Journal of Cleaner Production*, V. 235, 2019, pp. 259-271. doi: 10.1016/j.jclepro.2019.06.332

77. Hesaraki, S.; Zamanian, A.; and Moztarzadeh, F., "Effect of Adding Sodium Hexametaphosphate Liquefier on Basic Properties of Calcium Phosphate Cements," *Journal of Biomedical Materials Research Part A*, V. 88, No. 2, 2009, pp. 314-321. doi: 10.1002/jbm.a.31836

78. Abdelrazig, B., *Chemical Reactions in Magnesia-Phosphate Cement*, 1984, 141 pp.

79. Aboulayt, A.; Souayfan, F.; Roziere, E.; Jaafri, R.; El Idrissi, A. C.; Moussa, R.; Justino C.; and Loukili A., "Alkali-Activated Grouts Based on Slag-Fly Ash Mixtures: From Early-Age Characterization to Long-Term Phase Composition," *Construction and Building Materials*, V. 260, 2020, Article No. 120510. doi: 10.1016/j.conbuildmat.2020.120510

80. Fan, J.; Zhu, H.; Shi, J.; Li, Z.; and Yang, S., "Influence of Slag Content on the Bond Strength, Chloride Penetration Resistance, and Interface Phase Evolution of Concrete Repaired with Alkali Activated Slag/Fly Ash," *Construction and Building Materials*, V. 263, 2020, Article No. 120639. doi: 10.1016/j.conbuildmat.2020.120639

81. Li, Z.; Zhang, S.; Liang, X.; Granja, J.; Azenha, M.; and Ye, G., "Internal Curing of Alkali-Activated Slag-Fly Ash Paste with Superabsorbent Polymers," *Construction and Building Materials*, V. 263, 2020, Article No. 120985. doi: 10.1016/j.conbuildmat.2020.120985

JOIN AN ACI Chapter!

The American Concrete Institute has Chapters and Student Chapters located throughout the world. Participation in a local chapter can be extremely rewarding in terms of gaining greater technical knowledge and networking with leaders in the concrete community.

Because chapters are distinct and independent legal entities, membership includes both ACI members and non-ACI members and is made up of a diverse blend of architects, engineers, consultants, contractors, educators, material suppliers, equipment suppliers, owners, and students—basically anyone interested in concrete. Many active ACI members initially became involved in ACI through their local chapter. In addition to technical programs and publications, many chapters sponsor ACI Certification programs, ACI educational seminars, project award recognition programs, and social events with the goal of advancing concrete knowledge.

Check out the Chapters Special Section from the November 2020 *Concrete International*: www.concrete.org/publications/concreteinternational.aspx

---

Student Chapters

Join or form an ACI Student Chapter to maximize your influence, knowledge sharing, and camaraderie! ACI has 240+ student chapters located throughout the world, each providing opportunities for students to:

- Connect with their peers and participate in concrete-related activities such as: student competitions, ACI Conventions, ACI Certification Programs, ACI Educational Seminars, local chapter meetings, social events, and community service projects;
- Network with members of local chapters, many of whom have been in the industry for decades and can help to develop professional relationships and offer career advice;
- Win recognition for their universities through the University Award; and
- Learn about the many scholarships and fellowships offered by the ACI Foundation and by ACI's local chapters.

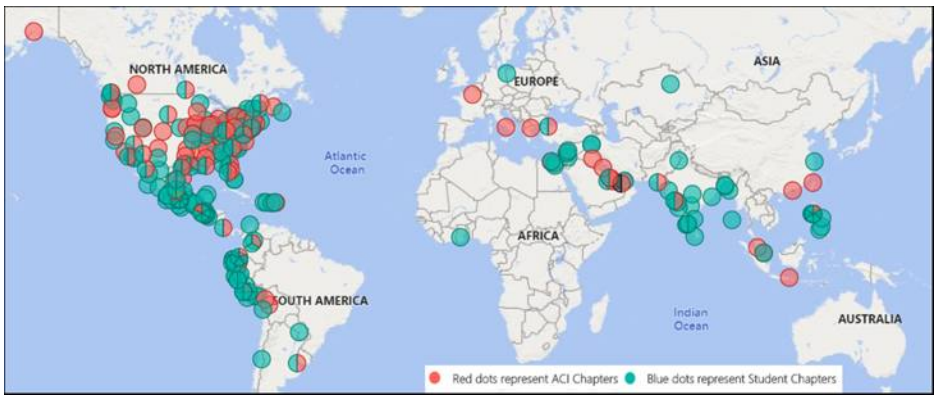

American Concrete Institute

www.concrete.org/chapters

ACI MATERIALS JOURNAL TECHNICAL PAPER

Title No. 120-M27

Critical Bending Strain and Mechanical Properties of Corroded Reinforcing Bars

by Victor Calderon, Moe Pourghaz, and Mervyn Kowalsky

Corrosion of reinforcing steel increases the probability of the fracturing of longitudinal reinforcing bars and leads to the loss of load-carrying capacity in reinforced concrete (RC) members. Twenty-four reinforcing steel bars were subjected to the buckled bar tension (BBT) test, and the critical bending strain was obtained at different corrosion levels. The specimens were passivated reinforcing steel bars that were corroded through accelerated electrolytic corrosion. The results show that the critical bending strain decreases as the corrosion level increases. The critical bending strain influences the post-buckling bar fracture limit state and reduces the displacement capacity of columns as the corrosion level in the longitudinal reinforcing bar increases. In addition, the degradation of yield strength, ultimate strength, and uniform axial elongation for corroded reinforcing steel bars were observed.

Keywords: buckled bar tension (BBT); buckling; corrosion; fractures; ultimate limit state.

INTRODUCTION

Reinforcing steel corrosion is one of the principal causes of the deterioration of reinforced concrete (RC) structures. The corrosion of reinforcing steel affects serviceability and structural safety by decreasing the load-bearing and displacement capacities of RC members due to the loss of bar section and bond between reinforcing steel and concrete.

Prior research has shown the structural degradation of corroded RC columns subjected to cyclic quasi-static tests.[1-3] For example, Meda et al.[1] showed that a column with longitudinal steel exhibiting a mass loss or corrosion level (*CL*) of 20% had a strength reduction of 33%, while the maximum displacement capacity decreased by 50% compared to a control specimen in pristine conditions.

Past studies on the material properties of corroded reinforcing steel bars have shown that the reinforcing steel bars' effective yield strength and elongation decrease with increasing levels of corrosion.[4-6] These studies have been conducted on bars subjected to accelerated electrolytic corrosion and have reported equations that correlate the yield strength, ultimate strength, and uniform elongation to the level of corrosion. However, these studies have used high current densities, and in other studies, the bar was not passivated.[1,3] In addition, the presence of a passive layer affects the corrosion morphology at the bar's surface, which translates into characteristics of produced flows, affecting fracture growth and propagation. Recent advances in studying the cyclic behavior of structures have led to the development of the buckled bar tension (BBT) test.[7] The BBT test has been used to assess the embrittlement of reinforcing bars due to changes in the chemical composition, manufacturing process, and rib radii of reinforcing steel bars.[7] The embrittlement was measured through the critical bending, which has been shown to correlate well with the onset of bar fracture in RC columns subjected to cyclic loading.[8]

Corrosion directly affects the geometry of the longitudinal steel bars and the effective mechanical properties of corroded reinforcing steel bars, such as yield strength, ultimate strength, uniform axial elongation, and critical bending strain. Therefore, it is hypothesized that corrosion results in the formation of surface flows that penetrate the reinforcing bar; these flows act as initial fractures, resulting in an increased stress concentration. During cyclic loading in BBT, the fracture can propagate and reduce the ductility of the reinforcing bar.

In this study, passivated specimens using a pore solution were prepared to levels of corrosion ranging from 5 to 20%. Then, three-dimensional (3-D) scanning was used to precisely measure the corrosion level. Next, the specimens were subjected to tension and BBT tests. In addition, scanning electron microscope (SEM) observations were used to detect if chlorides were present at the microstructural level on the fracture surfaces and to study the morphology of the fracture surface. Finally, turned-down specimens from corroded reinforcing bars were prepared to prove that the observed degradation did not change the material itself but was caused by the geometrical imperfections produced by the corrosion process.

RESEARCH SIGNIFICANCE

The material tests described in this paper confirm that the critical bending strain of reinforcing bars decreases as the corrosion level of the reinforcing steel increases. The bending strain has implications for the definition of performance limit states for columns containing corroded reinforcement and is the first step toward quantifying those limits.

EXPERIMENTAL PROGRAM

The experimental program evaluated the behavior of buckled reinforcing steel bars at corrosion levels from 5 to 20%. The *CL* is defined as the mass loss due to corrosion divided by the initial mass of the specimen. A total of 24 BBT

ACI Materials Journal, V. 120, No. 2, March 2023.

MS No. M-2022-139.R2, doi: 10.14359/51738461, received September 20, 2022, and reviewed under Institute publication policies.

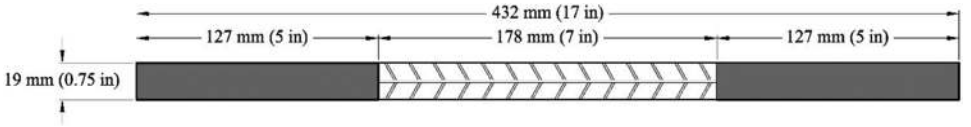

Fig. 1—Specimen geometry, gauge length, and grip area.

Table 1—Testing matrix for 20 mm (0.75 in.) at different corrosion levels

Corrosion level, %	Number of tension tests	Number of BBT tests
5	3	6
10	3	6
15	0	6
20	3	6

tests and nine tension tests were conducted on ASTM A706 Grade 80, 20 mm (0.75 in.) diameter reinforcing steel bars. First, the specimens were corroded through an electrochemical process explained as follows. A summary of the testing matrix is provided in Table 1. In addition, 3-D scanning was used to capture the volumetric imperfections on the surface of the corroded reinforcing steel bars to identify the equivalent diameter and compare it with the expected diameter for a uniformly corroded reinforcing steel bar. Finally, SEM observations of six fracture surfaces were performed to study the fractography to determine if chlorides had penetrated the fracture surface at the microstructural level.

Test specimen geometry

The specimens consisted of reinforcing steel bars 432 mm (17 in.) in length. A total gauge length of 178 mm (7 in.) was provided, as shown in Fig. 1. The ends of the specimens were protected against corrosion with three layers. The first layer consisted of two-part epoxy, the second layer consisted of electroplating tape, and the third layer consisted of shrink tubing.[9] These layers ensured that no corrosion occurred in the grip areas of the reinforcing steel bars, as shown in Fig. 2.

Corrosion methodology

In this study, before subjecting the specimens to corrosion, the reinforcing steel bars were allowed to develop a passive layer by submerging them in synthetic concrete pore solution following Ghods et al.[10] The pore solution included other salts that are present in the cement matrix, such as calcium, sodium, potassium, and sulfate oxide. The pore solution was generated with the following concentrations[10]: 4 g/L saturated calcium hydroxide ($Ca(OH)_2$), sodium hydroxide (Na(OH)), 11.22 g/L potassium hydroxide (KOH), and 13.77 g/L of calcium sulfate dihydrate ($CaSO_4 + 2H_2O$). The specimens were submerged in synthetic pore solution for 8 days to allow the development of the passive layer following the findings by Ghods et al.[10] on the minimum required duration for the formation of a stable passive layer. During the exposure, the synthetic pore solution was protected against exposure to air to avoid carbonation of the pore solution.

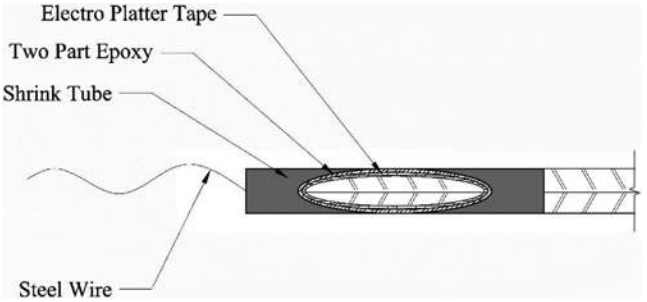

Fig. 2—Grip protective layers.

The accelerated corrosion process of the reinforcing steel bars started after generating the passive layer. Then, the accelerated corrosion was performed through an electrochemical process. In the electrochemical process, the anode consisted of the reinforcing bar, the cathode consisted of the stainless steel mesh, the electrolytic solution of 0.3 M of NaCl solution was added to the pore solution, and an impressed electric current of 0.15 A was used. The setup used to accelerate corrosion is shown in Fig. 3.

Faraday's law was used to estimate the time required to achieve the intended corrosion level in terms of mass loss. Faraday's law is shown in Eq. (1), where Δm_{loss} corresponds to the mass loss; I is the current in amperes (I = 150 mA); t is the time the current is sustained in seconds; and A_M is the atomic mass of the oxidizing component. The oxidizing component was the iron (Fe) in the reinforcing steel bars. Hence, A_M = 54.845 g/mol, where n is the number of electrons lost per atom oxidized (the number of electrons for iron [Fe] is 2), and F is Faraday's number; F = 96,485 C. Solving Eq. (1) for t and assuming uniform corrosion, the time to corrosion was calculated.

$$\Delta m_{loss} = \frac{It\left(A_M\right)}{nF} \tag{1}$$

The resulting corroded reinforcing steel bars for all the corrosion levels are shown in Fig. 4.

Corrosion-level measurement

The corrosion on the specimens was uniform throughout the gauge length. After the specimens had been subjected to the depassivation process, the specimens were cleaned from the corrosion using hydrochloric acid (HCl). The corrosion level was calculated as the ratio of mass loss to initial mass in the gauge length, expressed as follows

$$CL_m = \frac{\Delta m_{loss}}{m_0} = \frac{m_f - m_0}{m_0} \times 100\% \tag{2}$$

where m_0 is the weight of reinforcement prior to corrosion; and m_f is the weight of the same reinforcement after it was

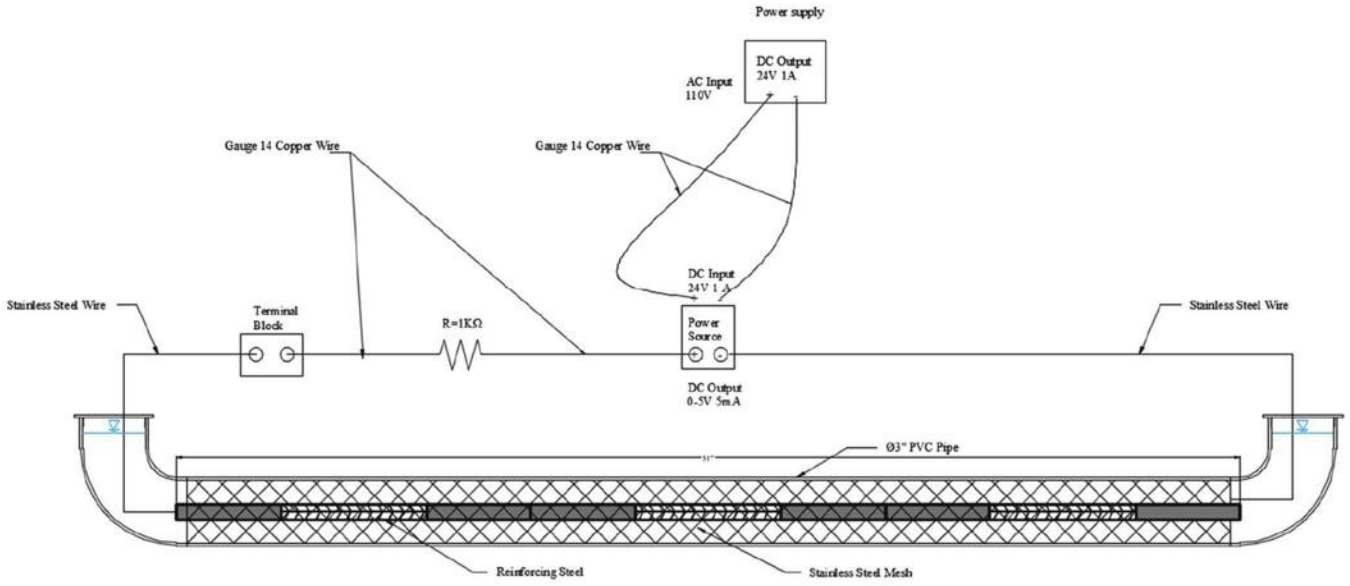

Fig. 3—Specimen accelerated electrolytic corrosion setup.

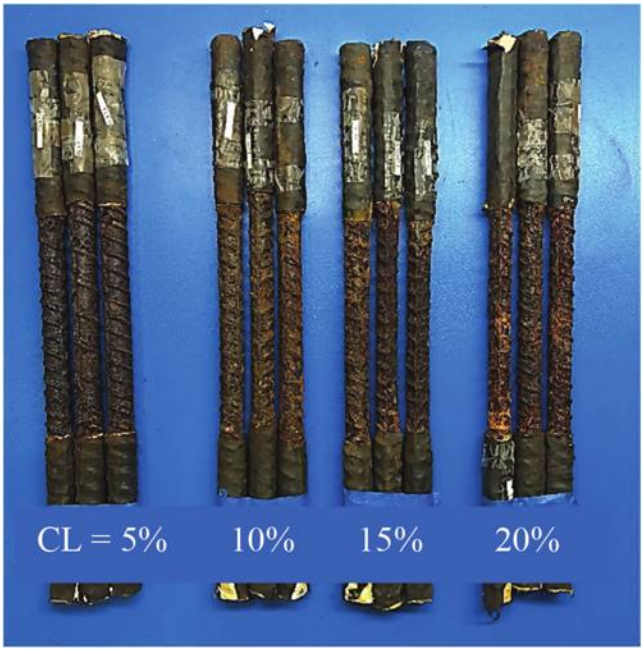

Fig. 4—Sample of resulting corroded reinforcing bars.

corroded and cleaned in the acid solution. The corrosion on the specimens was uniform throughout the gauge length. Therefore, each specimen was weighed before and after the accelerated electrolytic corrosion. The corrosion level was calculated as the ratio of mass loss to initial mass in the gauge length, as expressed in the following sections.

Measurement of corrosion level using 3-D scanning

The corroded reinforcing steel bars were scanned using a coordinate-measuring machine.[11] The 3-D scans were performed along the gauge length with a resolution of 0.024 mm (0.001 in.). A sample of the 3-D scans is shown in Fig. 5. From the 3-D scans, the volume (V) of the gauge length with the imperfection induced by the corrosion was

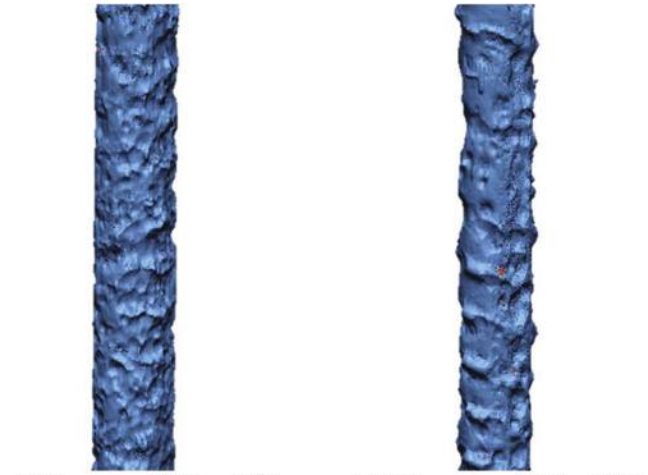

Fig. 5—3-D scanning of reinforcing steel bar imperfections.

measured. The effective diameter was calculated, assuming a uniform cylinder, expressed as

$$d_{eff} = \sqrt{\frac{V}{\frac{1}{4}\pi L_o}} \tag{3}$$

With the effective diameter, the level of corrosion was calculated as

$$CL_{3\text{-}D} = \left[1 - \left(\frac{d_{eff}}{d_o}\right)^2\right] \times 100\% \tag{4}$$

Tension tests

The objective of the tension tests was to observe if there were changes in the correlation between effective yield strength and corrosion for ASTM A706 Grade 80 steel. The procedure to perform the tension tests corresponds to ASTM A370. The strains were captured using light-emitting

diode (LED) markers from a dynamic measuring machine.[12] The gauge length between the LED markers was 51 mm (2 in.), as specified in ASTM A370. Figure 6 shows the test setup. The stress was calculated based on the load reading from the universal testing machine (UTM) and divided by the measured area of the corroded reinforcing steel bars.

BBT tests

The BBT test was used to characterize the change in the critical bending strain of corroded reinforcing steel bars. The BBT tests consisted of placing a reinforcing steel bar in a UTM; then, the surface of the reinforcing steel bar specimen was instrumented with LED markers, such that the displaced shape of the bar could be measured. Then, the reinforcing steel bar specimen was compressed to impose a bending strain of a prescribed level. The prescribed level of strain was calculated using the Barcley and Kowalsky[7] model shown as follows

$$\Delta_{axial} = 0.096\left(\frac{L_0}{d_{eff}}\varepsilon_b\right)^2 + 0.329\left(\frac{L_0}{d_{eff}}\varepsilon_b\right) - 0.031 \quad (5)$$

Once buckled to the prescribed curvature, the reinforcing steel bar is loaded in tension until the fracture is observed. This procedure was repeated at different bending strains. The procedure thus described is shown in Fig. 7.

A fourth-order polynomial was fitted to the LED sensors near the buckled region of the bar to obtain the displaced shape (w). Then, the bending strain was calculated per Eq. (6).

$$\varepsilon_b = \frac{d^2w(x)}{dx^2}\left(\frac{d_{eff}}{2}\right) \quad (6)$$

After all the tests were performed, results from elongation at peak force were generated, as shown in Fig. 8. The level of bending strain demand was controlled by monitoring the bar curvature during testing using the calculations described previously. The corroded reinforcing bars were subjected to different bending strain demands from buckling and then pulled to fracture. Two failure modes were observed in the BBT test: 1) ductile failure mode, in which the specimen experienced uniform axial elongation similar to a uniaxial tensile test and exhibited necking prior to fracture, as shown in Fig. 9(a); and 2) brittle failure mode occurred when the uniform axial elongation was a negative value or lower than the typical results of a uniaxial tensile test, and the failure

Fig. 6—Tension test setup on corroded reinforcing steel bar.

Fig. 7—Corroded reinforcing steel bar specimen loaded in BBT test setup.

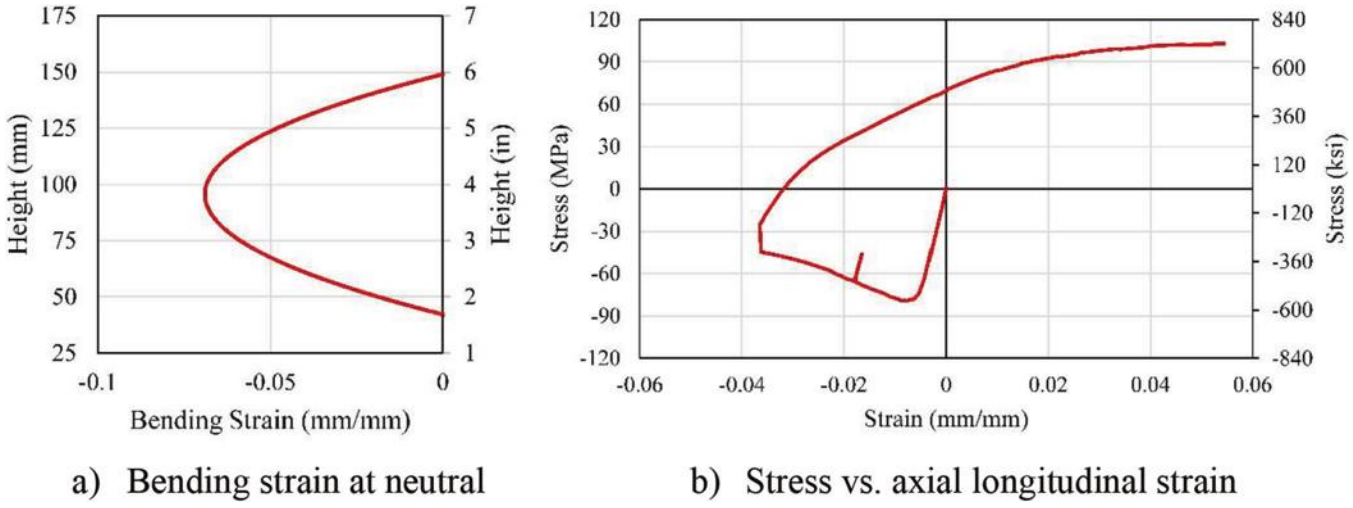

Fig. 8—Processing of data from BBT tests.

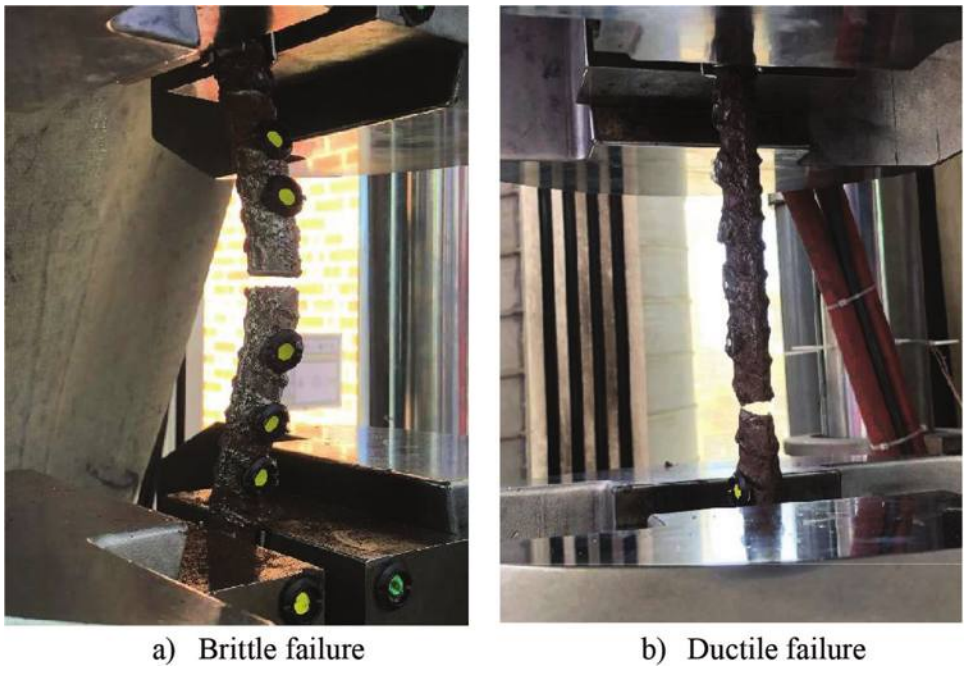

Fig. 9—Types of fractures in BBT tests of corroded reinforcing steel bars.

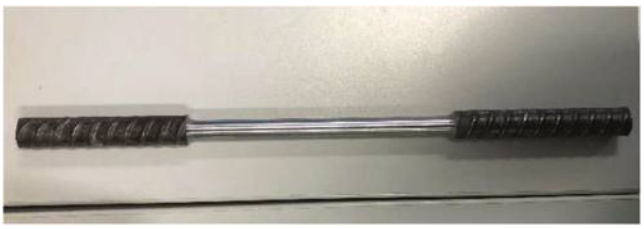

Fig. 10—Turned-down bar sample.

surface was flat, as shown in Fig. 9(b). The critical bending strain (ε_b) is the strain from bending that results in a transition from ductile to brittle fracture.

Tension test and BBT tests on turned-down reinforcing steel bars

Nine corroded specimens of up to a level of corrosion of 20% were turned down in a lathe to remove the imperfections induced by the corrosion and any corroded material. The turned-down reinforcing bars are shown in Fig. 10. The objectives of these tests were to prove that the observed degradation did not change the material itself but was caused by the geometrical imperfections produced by the corrosion process.

SEM analysis of fracture surface

Six fracture surfaces were observed under the variable-pressure scanning electron microscope (VPSEM) to observe the fracture surface of the BBT tests. The information obtained from the VPSEM images was used to determine the effect of corrosion on the fracture surface. In addition, the backscattered electron observations allowed for a chemical analysis of the fracture surface, which allowed the identification of corrosion products on the fracture surface.

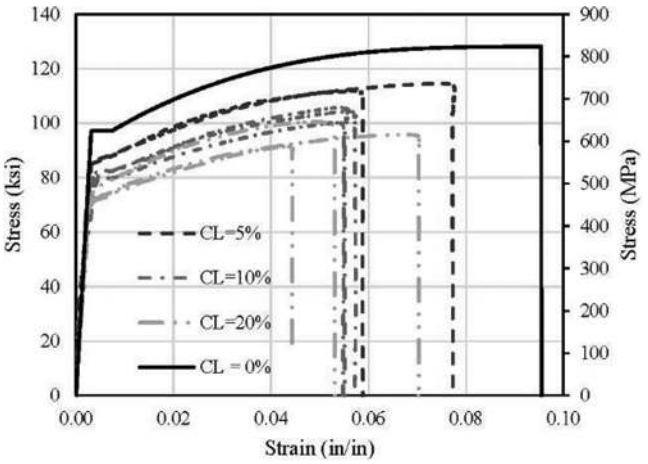

Fig. 11—Tension test results at different corrosion levels.

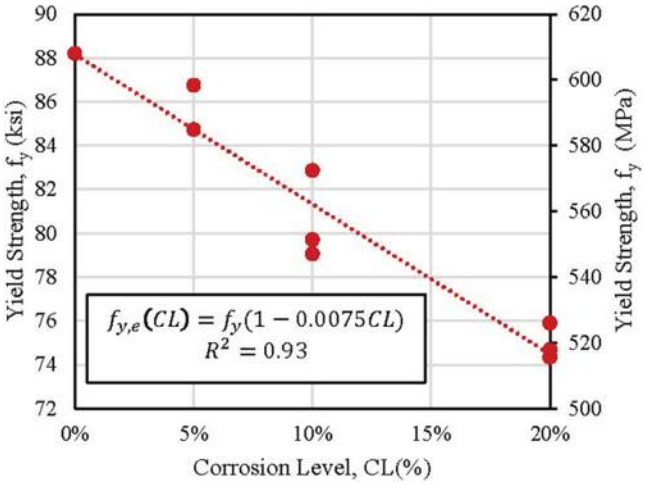

Fig. 12—Yield strength degradation versus corrosion level.

EXPERIMENTAL RESULTS AND DISCUSSION

Measured corrosion level in specimens

The level of corrosion was measured through the mass loss method and the 3-D scans. The results from both methodologies show that the target corrosion level was achieved within a margin of 1% of the expected corrosion level, as shown in Table 2. In addition, the 3-D scan effective diameter was used in the subsequent sections to calculate the stresses and strains.

Effective mechanical properties of corroded reinforcing steel bar

The results of corroded reinforcing bar specimens subjected to tension tests were statistically analyzed through linear regression. The results show a reduction in the corroded reinforcing steel bars' strength and deformation capacity as the corrosion level increases, as seen in Fig. 11. The yield strength is plotted at each corrosion level, and a linear trend between the effective yield strength can be observed, as shown in Fig. 12. The relationship between the effective yield strength and the corrosion level can be expressed as follows

$$f_{ye,CL} = f_{y,o}(1 - 0.0075CL) \quad (7)$$

Table 2—Accelerated corrosion calculated and measured corrosion level

Target corrosion level, %	Number of specimens	Current density, μA/cm²	Exposure time, days	3-D scans, %	Mass loss, %
5	9	370	16	5.1	4.6
10	9	370	31	10.3	9.4
15	6	370	47	15.1	14.9
20	9	370	63	20.5	19.1

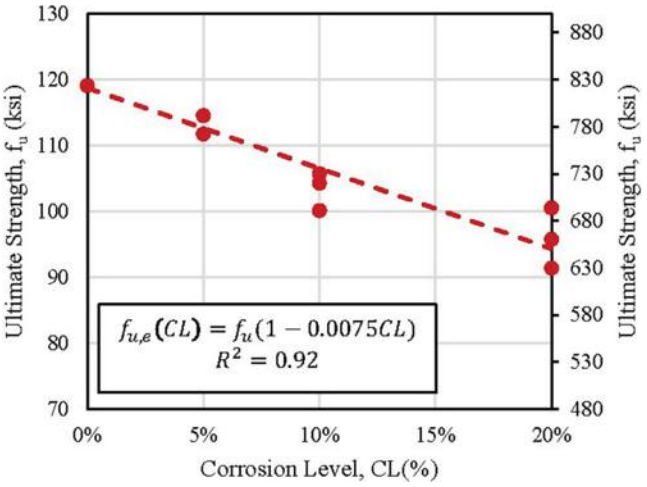

Fig. 13—Ultimate strength degradation versus corrosion level.

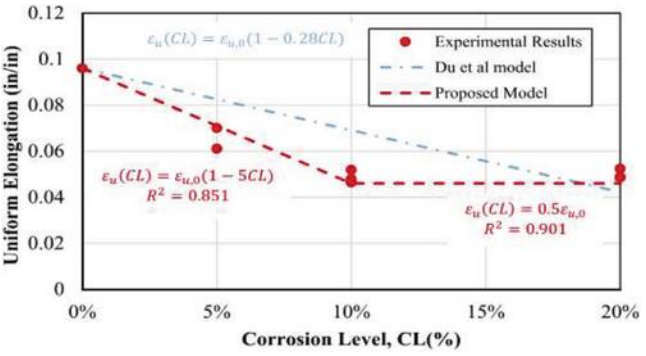

Fig. 14—Uniform elongation degradation versus corrosion level.

Equation (7) was found through regression analysis of the experimental results. Similarly, the ultimate strength degradation was analyzed based on the level of corrosion. The degradation of the ultimate strength was also linear as a function of the corrosion level, as shown in Fig. 13. Therefore, the ultimate strength degradation with the corrosion level can be expressed as

$$f_{ue,CL} = f_{u,o}(1 - 0.0075CL) \quad (8)$$

Likewise, the degradation in the uniform elongation as a function of the corrosion level was linear up to a level of corrosion of 10%, as seen in Fig. 14. However, the uniform elongation remained constant at corrosion levels between 10

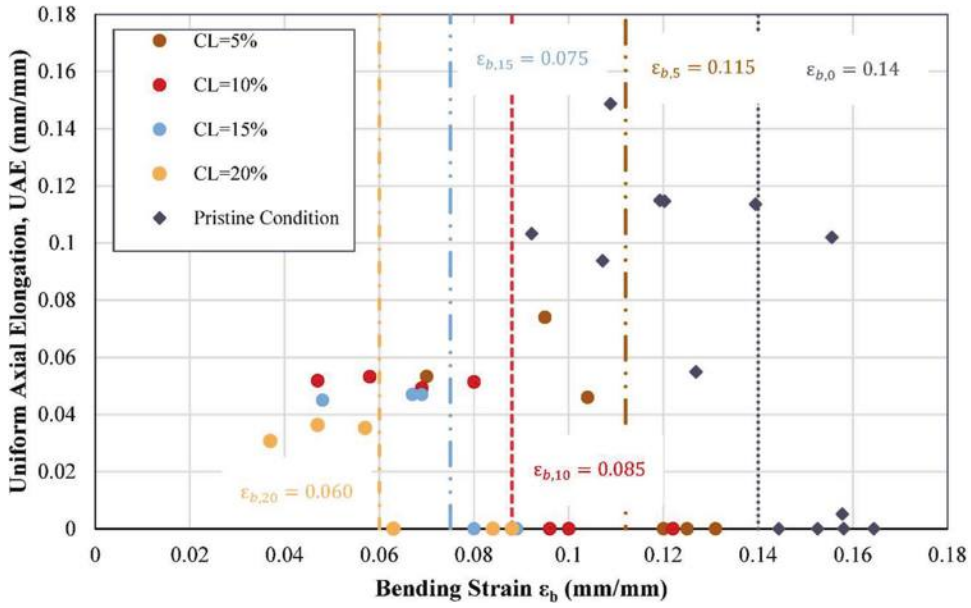

Fig. 15—Determining maximum bending strain for corrosion levels of 0 to 20%.

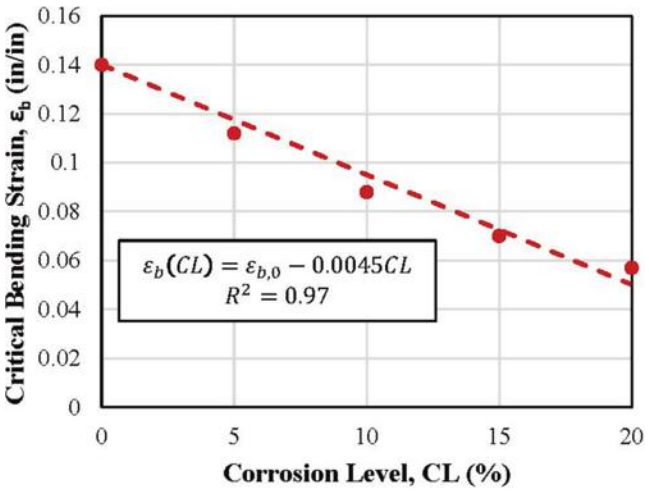

Fig. 16—Maximum bending strain degradation versus corrosion level.

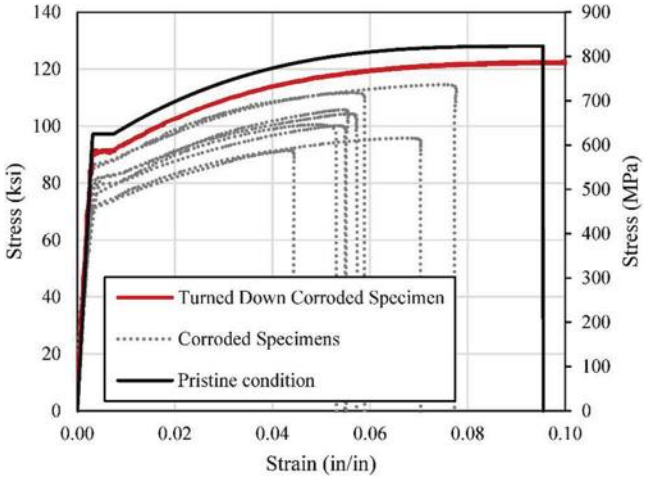

Fig. 17—Tension tests results for turned-down corroded specimens.

and 20%. The relationship can be expressed in the following equations

$$\varepsilon_{ue,CL} = \varepsilon_o - 0.05CL \text{ for } 0\% \le CL \le 10\% \quad (9)$$

$$\varepsilon_{ue,CL} = \varepsilon_o - 0.05 \text{ for } 10\% < CL \quad (10)$$

The uniform elongation, yield, and ultimate strength differ from the Du et al. model.[6] These differences might be caused by microstructural differences on the surface of the reinforcing bars when the passive layer was generated. Past research has shown that the passive layer changes the microstructure of the surface of reinforcing steel.[10]

Critical bending strain and corrosion level relationship

The corroded reinforcing bar specimens subjected to BBT tests were analyzed based on the critical bending strain parameter. The critical bending strain was evaluated at corrosion levels between 0 and 20%. The results from the 24 BBT tests are shown in Fig. 15, which shows that as the corrosion level increases, the critical bending strain decreases. Plotting the critical bending strain against the level of corrosion in Fig. 16, the degradation between the critical bending strain as a function of the corrosion level becomes more evident. It can be seen that the critical bending strain reduces linearly with an increasing level of corrosion and can be expressed as

$$\varepsilon_{be,CL} = \varepsilon_{b,o} - 0.0045CL \quad (11)$$

It is important to note that Eq. (7) to (11) are applicable only to the tests described in this paper and are provided to illustrate the trends. They should not be applied to other

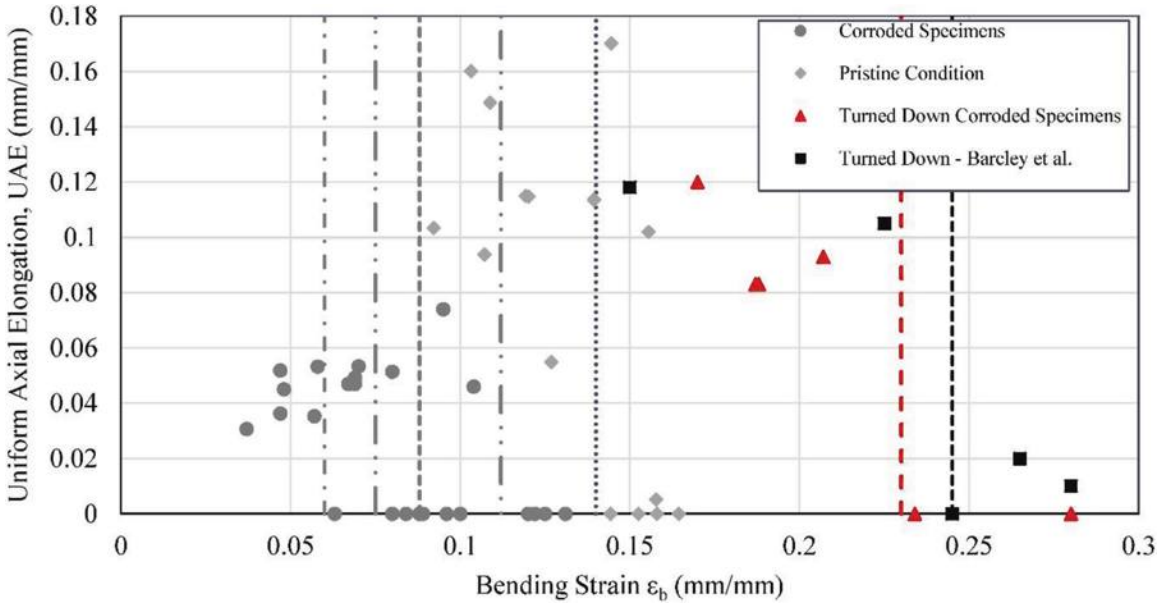

Fig. 18—Maximum bending strain for turned-down corroded specimens.

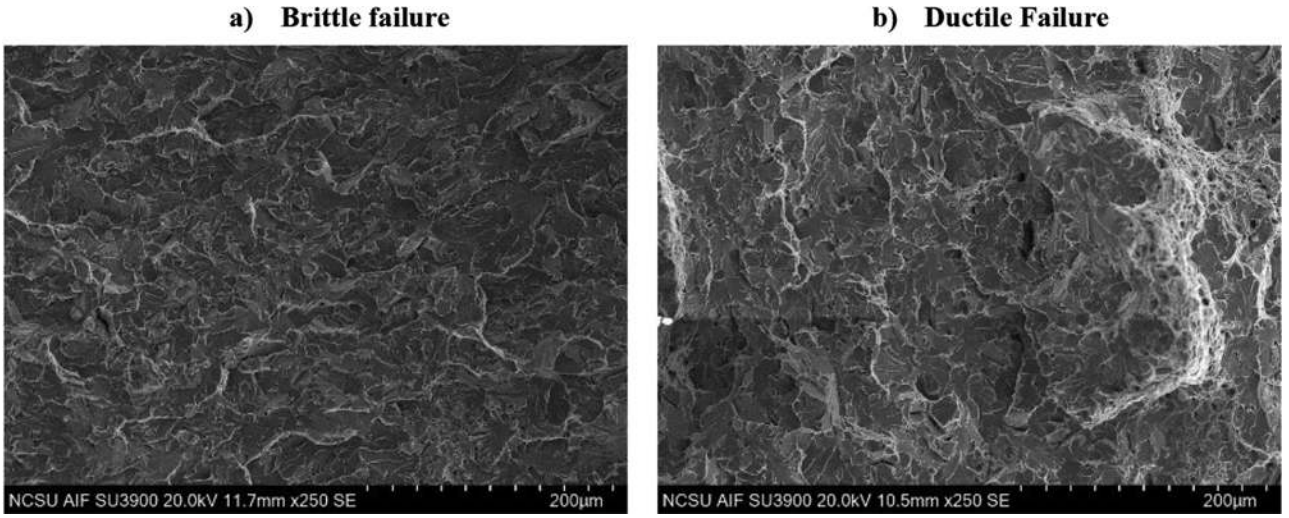

Fig. 19—SEM observations of brittle and ductile fractures.

bar diameters without additional verification. However, perhaps most impactful is the observation that the critical bending strain is impacted by corrosion because this directly correlates to a bar's fracture strain. In the following sections, it will be shown that the effect of corrosion is tied to the geometric imperfections that result from corrosion, as opposed to mechanical changes to the constitutive response.

Results from turned-down corroded reinforcing steel bars

The tension and BBT tests show that the virgin material in the corroded reinforcing steel bars remains unchanged, as shown in Fig. 17 and 18. In Fig. 17, the yield and ultimate strengths of turned-down specimens remain unchanged compared to reinforcing steel bars in pristine conditions. Similarly, in Fig. 18, the BBT test results are compared to pristine-condition reinforcing steel bars with the ribs removed from the study by Barcley and Kowalsky.[7] Again, it can be observed that the results match well. Therefore, it can be concluded that corrosion induces geometrical imperfections along the reinforcing steel bar surfaces, which then reduces the performance of the corroded reinforcing steel bars. However, the intrinsic material properties in the core of the material do not change.

SEM analysis of fracture surface

Six fracture surfaces from the BBT tests were observed with the SEM. In Fig. 19, the images for a brittle fracture and a ductile fracture sample are shown. Brittle fractures had flat fracture surfaces (Fig. 19(a)), and the ductile fracture had dimple features (Fig. 19(b)), typical of each fracture type. These observations indicated no changes to the microstructural composition of the material due to corrosion.

In addition, to rule out the presence of chlorides in the fracture surfaces, energy-dispersive spectroscopy (EDS) spectrum analysis was performed. The EDS analysis allowed

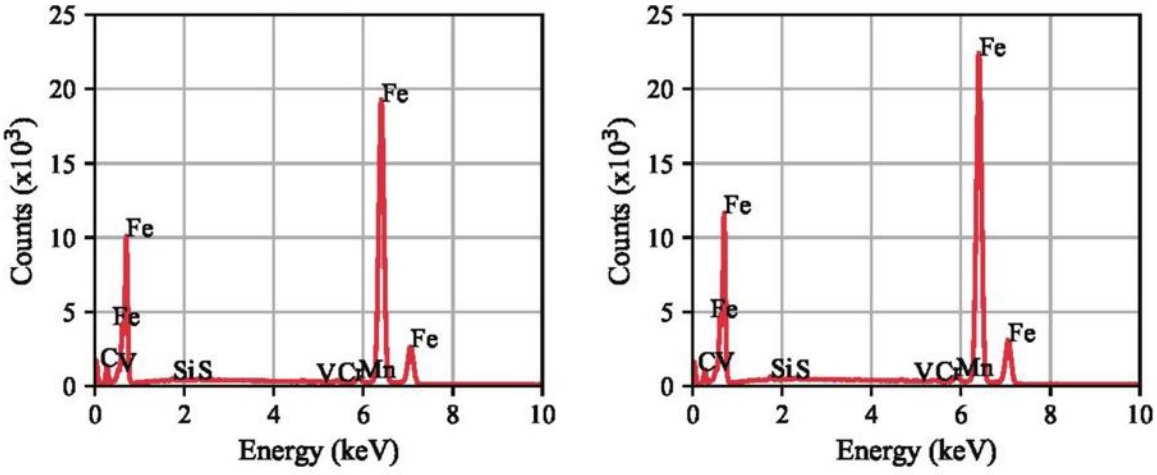

Fig. 20—EDS spectrum analysis of SEM observations shows no chlorides on fracture surface.

the authors to identify which elements were present in the fracture surfaces. As Fig. 20 shows, the EDS analysis results showed no chlorides on the fracture surfaces of brittle and ductile specimens. Thus, it is evident that premature fractures are an effect of the geometrical imperfections on the surface of the specimens due to corrosion.

FUTURE RESEARCH

Based on the research outcomes described in this paper, additional studies are required to evaluate the impact of corrosion level on the performance of RC columns with corrosion in the longitudinal steel subjected to cyclic loading. These tests would confirm the correlation between displacement capacity and critical bending strain of corroded RC columns. In addition, the evaluation of critical bending strains for corroded reinforcing bars of varying diameters and grades should also be conducted.

CONCLUSIONS

The authors considered corroded reinforcing steel specimens using a low-density current and a pore solution that emulated the conditions of bars present in the portland cement matrix. The tension tests performed determined the effective mechanical properties defined as a function of the pristine material properties and the corrosion level.

In addition, the critical bending strain degradation due to corrosion was determined as a function of the corrosion level. Similar to the effective mechanical properties, the critical bending strain decreases as the corrosion level increases.

The results from the turned-down reinforcing bars showed no changes in the intrinsic material properties of the reinforcing steel bars. These results indicate that the observed effect of corrosion on the effective mechanical properties of corroded reinforcing steel is related to the changes in the morphology of the surface of corroded reinforcing bars and the presence of flaws caused by corrosion. Finally, scanning electron microscope (SEM) observations determined that the microstructural composition of the virgin material remains unchanged.

The authors envision that using the critical bending strain and the effective mechanical properties (yield strength, ultimate strength, and uniform elongation) will define the material properties and limit states of corroded reinforced concrete (RC) members for the performance-based design of aging structures.

AUTHOR BIOS

ACI member **Victor Calderon** *received his BS from Universidad Centroamericana José Simeón Cañas (UCA), San Salvador, El Salvador, and his MCE and PhD in structural engineering from North Carolina State University, Raleigh, NC. His research interests include the durability of reinforced concrete structures, earthquake engineering, and resilient design of structures.*

ACI member **Moe Pourghaz** *is a Professor in the Department of Civil, Construction, and Environmental Engineering at North Carolina State University. He received his BS in civil engineering from the University of Tabriz, Tabriz, Iran; his MS from Carleton University, Ottawa, ON, Canada, in 2007; and his PhD from the Lyles School of Civil Engineering at Purdue University, West Lafayette, IN, in 2011. His research interests include service life prediction and health monitoring of concrete infrastructure.*

ACI member **Mervyn Kowalsky** *is the Christopher W. Clark Distinguished Professor at North Carolina State University. He is a member of ACI Committee 341, Earthquake-Resistant Concrete Bridges. His research interests include the seismic behavior of structural systems.*

ACKNOWLEDGMENTS

The authors wish to express their gratitude and sincere appreciation to the Alaska Department of Transportation and Public Facilities (AKDOT&PF) for financing this research work, and the staff and students at the Constructed Facilities Lab (CFL), the Sensing and Materials Research Team (SMART) Lab, the Analytical Instrumentation Facility (AIF), and the Center for Additive Manufacturing and Logistics (CAMAL) at North Carolina State University.

NOTATION

A_M	=	atomic number
CL	=	corrosion level
CL_M	=	corrosion level, mass loss method
$CL_{3\text{-}D}$	=	corrosion level, 3-D scanning method
d_{eff}	=	effective diameter
d_0	=	initial diameter
F	=	Faraday's number
$f_{u,o}$	=	initial ultimate strength
$f_{ue,CL}$	=	effective ultimate strength at corrosion level
$f_{y,o}$	=	initial yield strength
$f_{ye,CL}$	=	effective yield strength at corrosion level

I = current in amperes
L_0 = gauge length
m_f = final mass after corrosion
m_0 = initial mass
n = electron numbers
t = time to obtain mass loss in Faraday's equation
V = volume in gauge length obtained from 3-D scans
w = displaced shape of reinforcing steel bar
Δ_{axial} = axial displacement of universal testing machine
Δm_{loss} = mass loss
ε_b = prescribed bending strain
$\varepsilon_{b,o}$ = pristine condition bending strain
$\varepsilon_{be,CL}$ = effective bending strain at corrosion level
ε_o = uniform axial elongation in pristine condition
$\varepsilon_{ue,CL}$ = effective uniform axial elongation at corrosion level

REFERENCES

1. Meda, A.; Mostosi, S.; Rinaldi, Z.; and Riva, P., "Experimental Evaluation of the Corrosion Influence on the Cyclic Behaviour of RC Columns," *Engineering Structures*, V. 76, Oct. 2014, pp. 112-123. doi: 10.1016/j.engstruct.2014.06.043

2. Yang, S.-Y.; Song, X.-B.; Jia, H.-X.; Chen, X.; and Liu, X.-L., "Experimental Research on Hysteretic Behaviors of Corroded Reinforced Concrete Columns with Different Maximum Amounts of Corrosion of Rebar," *Construction and Building Materials*, V. 121, Sept. 2016, pp. 319-327. doi: 10.1016/j.conbuildmat.2016.06.002

3. Ma, Y.; Che, Y.; and Gong, J., "Behavior of Corrosion Damaged Circular Reinforced Concrete Columns under Cyclic Loading," *Construction and Building Materials*, V. 29, Apr. 2012, pp. 548-556. doi: 10.1016/j.conbuildmat.2011.11.002

4. Cairns, J.; Plizzari, G. A.; Du, Y.; Law, D. W.; and Franzoni, C., "Mechanical Properties of Corrosion-Damaged Reinforcement," *ACI Materials Journal*, V. 102, No. 4, July-Aug. 2005, pp. 256-264.

5. Khan, I.; François, R.; and Castel, A., "Prediction of Reinforcement Corrosion Using Corrosion Induced Cracks Width in Corroded Reinforced Concrete Beams," *Cement and Concrete Research*, V. 56, Feb. 2014, pp. 84-96. doi: 10.1016/j.cemconres.2013.11.006

6. Du, Y. G.; Clark, L. A.; and Chan, A. H. C., "Residual Capacity of Corroded Reinforcing Bars," *Magazine of Concrete Research*, V. 57, No. 3, Apr. 2005, pp. 135-147. doi: 10.1680/macr.2005.57.3.135

7. Barcley, L., and Kowalsky, M., "Critical Bending Strain of Reinforcing Steel and the Buckled Bar Tension Test," *ACI Materials Journal*, V. 116, No. 3, May 2019, pp. 53-61. doi: 10.14359/51715583

8. Barcley, L., and Kowalsky, M., "Seismic Performance of Circular Concrete Columns Reinforced with High-Strength Steel," *Journal of Structural Engineering*, ASCE, V. 146, No. 2, Feb. 2020, p. 04019198. doi: 10.1061/(ASCE)ST.1943-541X.0002452

9. ASTM G5-14, "Standard Reference Test Method for Making Potentiodynamic Anodic Polarization Measurements," ASTM International, West Conshohocken, PA, 2014, 9 pp.

10. Ghods, P.; Isgor, O. B.; McRae, G.; and Miller, T., "The Effect of Concrete Pore Solution Composition on the Quality of Passive Oxide Films on Black Steel Reinforcement," *Cement and Concrete Composites*, V. 31, No. 1, Jan. 2009, pp. 2-11. doi: 10.1016/j.cemconcomp.2008.10.003

11. FARO Technologies, Inc., "FaroArm and FARO Laser ScanArm Quantum Max User Manual," FARO Technologies, Inc., Lake Mary, FL, 2022, 208 pp.

12. Northern Digital Inc., "OPTOTRAK Certus HD Dynamic Measuring Machine," Northern Digital Inc, Waterloo, ON, Canada, 2020, https://www.ndigital.com/products/legacy-products/. (last accessed Feb. 8, 2023)

ACI MATERIALS JOURNAL TECHNICAL PAPER

Title No. 120-M28

A Framework for Determining Direct Tensile Properties of Ultra-High-Performance Concrete

by Rodolfo Bonetti, Oguzhan Bayrak, Kevin Folliard, and Thanos Drimalas

This paper presents a set of procedures and a recently developed direct tension test for determining the uniaxial tensile strength and full stress-strain behavior of ultra-high-performance concrete (UHPC). The proposed set of procedures aim to establish an upper and lower bound for the tensile strength based on preferential casting orientation. Results from this research show that an upper and lower bound of strength could be established when properly executed casting procedures are in place. On the other hand, the proposed direct tension test can capture the full stress-strain behavior of the material at pre- and post-cracking stages, for both strain-hardening and strain-softening samples. Results from the direct tension tests performed during this research favor the use of contactless extensometers to avoid stress concentrations that induce early localization at the regions close to the attachment points when using traditional measuring methods.

Keywords: casting orientation; direct tension test; ultra-high-performance concrete (UHPC).

INTRODUCTION

In structural engineering, the design of new structures and the evaluation of existing ones requires knowledge of the behavior and mechanical properties of the materials used for construction. Ultra-high-performance concrete (UHPC) is a relatively novel concrete material with enhanced tensile strength, offering considerable advantages that are appealing to the precast industry. Nevertheless, this material presents some challenges for determining its uniaxial tensile strength and obtaining meaningful stress-strain information from tensile tests that could be used reliably for structural modeling of UHPC elements. A direct tension test (DTT) is the straightforward solution to the aforementioned challenges. Accordingly, the test should be capable of capturing the full stress-strain behavior in tension of the material while exhibiting a reasonable coefficient of variation within a sample set of tests. Additionally, the tensile test should be relatively easy to implement at in-house quality control (QC) labs, using either existing equipment or with a minimum investment for the acquisition of new equipment. The importance of developing a reliable tensile test resides in the fact that most current tensile tests for concrete materials are inherently indirect in nature, with high intra-test variability and/or the inability to capture the full stress-strain behavior of the material.

In recent years, the development of a DTT for UHPC (Graybeal and Baby[1,2]) represents a great advance toward the standardization of a reliable tensile test for the material. The DTT has been the result of more than 5 years of study and development at the Federal Highway Administration (FHWA) Laboratories. In the DTT, a prismatic 50 x 50 x 430 mm (2 x 2 x 17 in.) specimen is loaded in tension in a displacement-controlled universal testing machine (UTM). The load is transferred by gripping the specimens at their ends through epoxied aluminum plates located at both sides of the test sample. The deformation of the specimen is measured by four linear variable differential transducers (LVDT), each located at one of the four faces of the specimen, and the average of these measurements represents the true deformation in a gauge length set to 100 mm (4 in.) (refer to Fig. 1). Because the load and deformation are recorded simultaneously until failure, the full strain-stress behavior of the material is obtained accordingly. The latter is of upmost importance for the specialized modeling techniques required for UHPC structures.

Another issue of great importance for the determination of the tensile properties of UHPC is the effect of cast/fiber orientation in the strength and ductility in tension of the material. A study by Maya Duque and Graybeal[3] tackling this issue demonstrated a remarkable reduction of strength and ductility before localization for samples extracted at a 90-degree angle from the direction of the cast flow. In contrast, samples that were extracted along the casting direction (at 0 degrees) and those that were mold-cast with induced flow in the longitudinal direction exhibited greater strength values and ductility.

Building on the well-grounded knowledge provided by the FHWA test, the authors propose a new DTT targeting areas identified as having room for improvement from the current FHWA test—among them, the challenges with specimen preparation, alignment, instrumentation, and the possible introduction of significant tensile strains at gripping.[2] Additionally, a set of procedures is presented to address the issue of the influence of cast/fiber orientation on the outcome of the DTTs and establish an upper and lower bound of strength using these casting procedures.

RESEARCH SIGNIFICANCE

The work presented herein introduces a new test method for determining the direct tensile properties of UHPC. The recently developed DTT represents an alternative to dog-bone and the FHWA DTTs. The test can be performed

ACI Materials Journal, V. 120, No. 2, March 2023.

MS No. M-2022-143.R1, doi: 10.14359/51738374, received September 17, 2022, and reviewed under Institute publication policies.

Fig. 1—FHWA direct tension test for UHPC.

with standard laboratory equipment used for the testing of metals and circumvents some of the hurdles existing in other tensile tests related to variable geometry, end boundary conditions, attachment methods, and required specimen preparation. Additionally, a casting procedure is proposed to obtain characteristic upper and lower values of strength in UHPC mixtures. An investigation on the direct tension properties of a nonproprietary mixture showcases the proposed test method.

EXPERIMENTAL PROCEDURE

Materials

A nonproprietary UHPC mixture was developed for the purpose of this investigation. The mixture is a metakaolin-limestone formulation with a 28-day average 50 mm (2 in.) cube compressive strength of 138 MPa (20 ksi) and splitting tensile strength of 16.5 MPa (2.4 ksi). The flexural tensile strength (from ASTM C1609 tests) and modulus of elasticity were measured as 16 MPa (2.33 ksi) and 43,500 MPa (6300 ksi), respectively. Details on the composition of the mixture are presented in Table 1. Figure A1 in the Appendix presents the size distribution of the different mixture dry components and a comparison of the combined grading curve to the modified Andreasen model used for packing optimization. A Type V cement was used for a mixture with a C_3A content of 3.1% and a C_3S/C_2S ratio of 4.6. A limestone powder filler was selected with an average particle size of 100 μm and 30.5% of particles passing a 325 mesh. The steel fibers used for the mixture were 0.2 x 13 mm (0.008 x 0.5 in.) in size with a nominal tensile strength of 2750 MPa (398.5 ksi).

Table 1—Nonproprietary mixture proportions

Material	Quantity, kg/m^3 (lb/yd^3)
Cement, PC Type V	653 (1100)
Metakaolin	196 (330)
Limestone powder	345 (580)
Sand	915 (1540)
Air detrainer	6.53 (11)
HRWR	23.6 (6.25)
Water	212 (357)
Steel fibers*	156 (263)

*Straight, 0.2 x 13 mm, 2% by volume.

Note: PC is portland cement; HRWR is high-range water reducer.

Casting procedure

Tensile specimens were cast in a casting bed in polyvinyl chloride (PVC) tubes 52 mm (2.05 in.) in diameter and 1270 mm (50 in.) in length. These forms were impregnated with form oil prior to casting. A static spread in the range of 254 to 279 mm (10 to 11 in.) from the ASTM C1437 static flow test results was optimal for the type of mixture used with no need for vibration and avoiding segregation of the fibers. The casting was performed in two different orientations intended to generate a preferential fiber alignment on the specimens.

The first casting orientation was horizontal, with induced flow along the longitudinal axis of the casting pipe, intended to produce a prevalent fiber orientation along the longitudinal axis of the specimens. The former was attained by funneling the material through a leading short piece of pipe with a 50 x 75 mm (2 x 3 in.) PVC reducing coupling fitted at its end (refer to Fig. 2). As soon as the material came out at the opposite side, a pipe cap was placed at that end and the PVC pipe was slightly raised from the leading end and tapped several times to complete the filling and remove entrapped air. Later, the mold was turned into a vertical position, the leading pipe removed, and a second pipe cap placed at the leading end to prevent moisture loss. Total casting time was approximately 8 minutes per mold.

A second casting orientation was selected with the intention to produce a disorderly orientation of the fibers at an angle greater than 45 degrees with respect to the longitudinal axis. The most striking differences with the horizontal casting were achieved when a vertical casting was performed by slowly but continuously placing the material in the center of the pipe in such a manner that it did not touch the pipes' wall. As for the horizontal casting, the tubes were sealed with caps after the placement of the material to prevent moisture loss.

Specimen preparation

At 2 days of age, the compressive strength of accompanying 50 mm (2 in.) cubes was obtained with a minimum pre-established strength value of 55 MPa (8 ksi), and the 50 mm (2 in.) diameter specimens were saw-cut to their required 400 mm (16 in.) length. The specimens were cut,

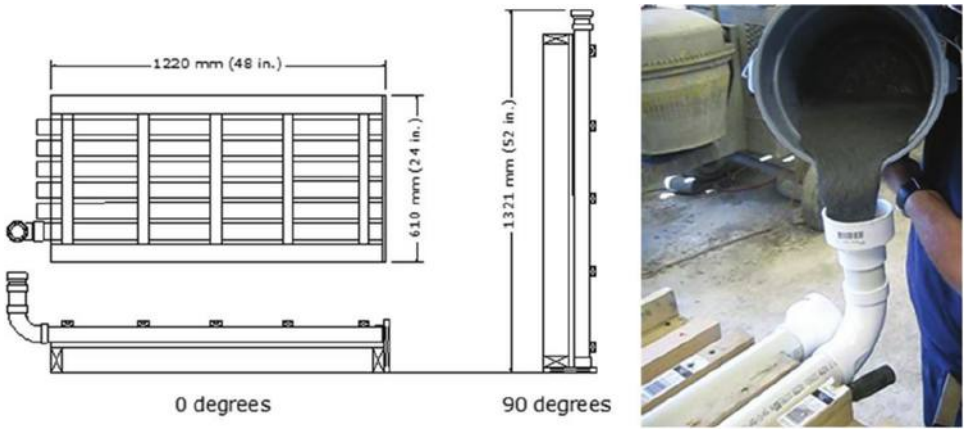

Fig. 2—Tensile test specimens casting procedure.

demolded, and water-cured for 3 additional days, after which they were attached with 50 x 75 mm (2 x 3 in.) half steel nipples at their ends. The procedure for attaching the steel nipples involved the grinding and cleaning of the inside of the nipples, sanding of the specimens' ends, and gluing the steel nipples to the ends with a creep-resistant epoxy. The overall gap between the specimen and the steel nipple was in the order of 0.75 mm (1/32 in.). This gap created enough space for the epoxy glue but was small enough to prevent the introduction of eccentricities at fabrication. During this research, connection failures or slip at the connection ends were not detected.

End conditions and load-transfer mechanism

The singularities of the DTT regarding the influences of the methods of gripping to the test machine, nonsymmetric deformations, and the boundary end conditions of the tensile specimens have been reported in previous research.[4,5] Concerns about the out-of-plane rotations after cracking in rotating-rotating specimens are justified to some extent. Nevertheless, direct gripping of specimens in a fixed-fixed condition can introduce significant bending stresses that are dependent on the specimens' face alignment. A study by Amin et al.[5] on steel fiber-reinforced concrete (SFRC) found that a fixed-fixed end condition resulted in lower cracking strength than their rotating-rotating counterparts, which exhibited increasing out-of-plane rotations with increasing deformation because of the heterogeneous fiber distribution in the specimens. All these factors considered, it was determined that for a material such as UHPC, with multi-cracking, sustained strength, and/or hardening behavior, the rotating-rotating end condition was best suited for the DTT.

The connection of the specimens to the machine was realized through a ball joint-clevis mechanism that allowed for rotation about two axes. A threaded coupling and solid plug with internal threads were attached to the specimen ends prior to testing and the ball joints were attached to the solid plugs to complete the assembly. The threaded connection and the glued steel nipples at the ends of the specimens were intended to transfer the load progressively in a surface bond mechanism resembling the transfer of the tensile load from reinforcing bar to the concrete matrix (refer to Fig. 3(a) and 4).

Direct tension test development

During the development phase of the DTT (Round 1 of tests), the use of an extensometer with two LVDTs for the measurement of the deformation was particularly convenient for attachment to the cylindrical 50 x 400 mm (2 x 16 in.) specimens. Figure 3 shows the general layout and test setup of a tensile specimen. Nevertheless, after the tally and classification of the failure modes on 17 specimens, it was found that approximately two-thirds of them experienced localization in the regions within 13 mm (0.5 in.) of the attachment points of the extensometer. A posterior linear-elastic (E_c = 41,400 MPa [6000 ksi]) finite element analysis corroborated increases of approximately 30% in the tensile stress at those locations.

At the conclusion of Round 1, it was also found that an epoxy transition of 13 mm (0.5 in.) would greatly reduce tensile stresses at the vicinity of the steel-UHPC interface (refer to Fig. 4), diminishing the probability of failures at that location. The normalized stress profile at the specimen surface, with and without the epoxy transition, is presented in Fig. 4. The overall success rate of valid tests in Round 1 was only 17.6%. Furthermore, it was not possible to have any success with strain-softening samples (cast at 90 degrees) in Round 1 due to premature localization outside the gauge length.

A contactless method of measurement using digital image correlation (DIC) was implemented for Round 2 of DTTs. The DIC method required the painting of the specimens with whitewash and the imprinting of a black speckle pattern, as shown in Fig. 5. The complete test setup with the systems' cameras is presented in the same figure. This test setup proved to be effective for the testing of strain-hardening (cast at 0 degrees) and strain-softening samples (cast at 90 degrees) as well. Additionally, the DIC method presented the advantage of permitting a variable and extended gauge length that could be selected by the user. A 200 mm (8 in.) maximum gauge length was established, matching the constant stress region on the finite element analysis (refer to Fig. 4). The overall success rate of the Round 2 DTTs was 67%. The success of a test was defined as localization occurring within the gauge length. All the DTTs carried out in Rounds 1 and 2 were performed in a displacement-control mode at a test speed of 0.152 mm/min (0.006 in./min). For more detailed information on the

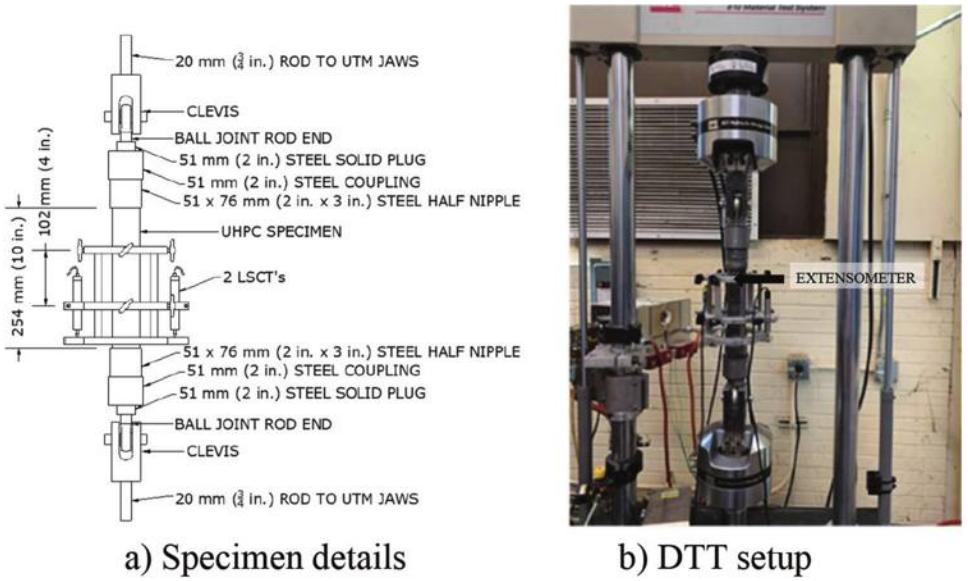

Fig. 3—Specimen details and overview of test setup (Round 1 of tests).

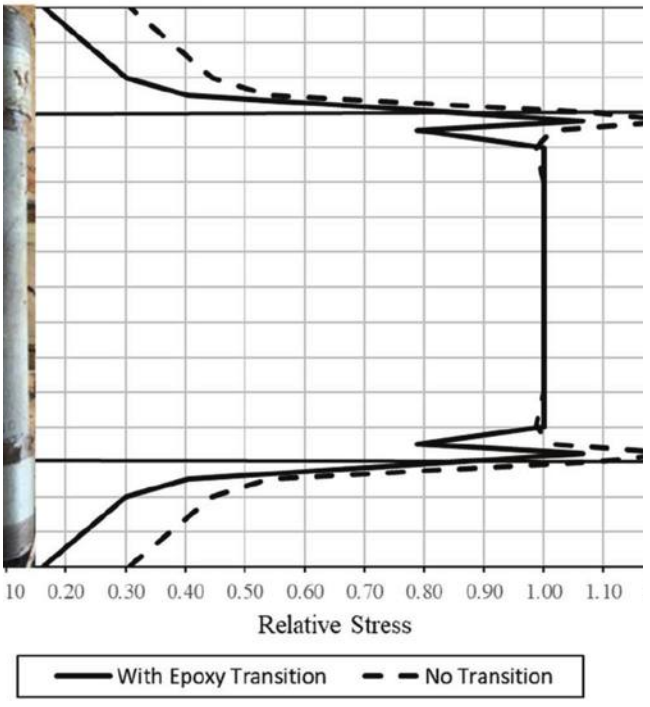

Fig. 4—Relative stress distribution with and without epoxy transition (from finite element analysis).

specimen types, failure modes, and successful test results for both rounds, refer to Tables A1 and A2 in the Appendix.

EXPERIMENTAL RESULTS AND DISCUSSION

Validation of DIC measurements

The validation of the DIC method of measurement was performed by a comparison of valid tests from Round 1 with similar tests executed in Round 2 (refer to Fig. 6). The parameters of comparison were the first cracking strain, overall shape of the stress-strain curve, and the similarities in the strain values at crack localization. It was found that regardless of the difference in test age, the variation in the first cracking strain was no more than 10% from one another,

Fig. 5—Specimen speckle pattern and test setup with DIC system for Round 2.

the overall shape of the stress-strain curves is remarkably similar, and the strain at crack localization was within 5% for the 0-degree casting orientation. Additionally, the slope of the linear portion of the stress-strain diagram obtained with the DIC method of measurement was within 10% of the modulus of elasticity obtained by the ASTM C486 test. In conclusion, the contactless method of strain measurement was considered a valid method for implementation in the direct tension testing of UHPC.

Direct tension tests of 0-degree casting orientation specimens

The behavior of specimens cast horizontally was characterized by an initial linear-elastic behavior with an average limit of proportionality at a rather low stress level of approximately 4.5 MPa (650 psi). The linear-elastic stage was followed by a

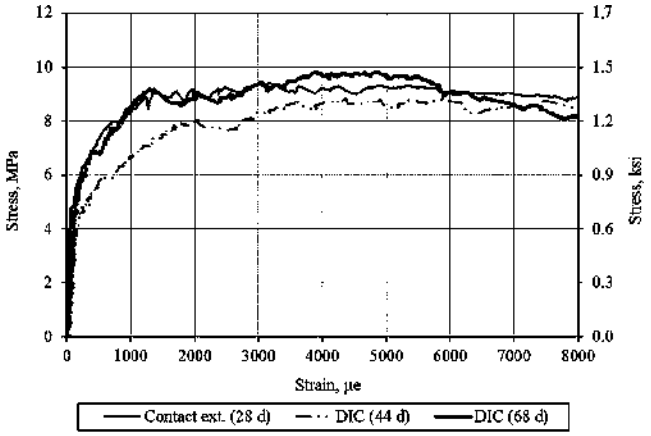

Fig. 6—Stress-strain curves for 0-degree casting orientation.

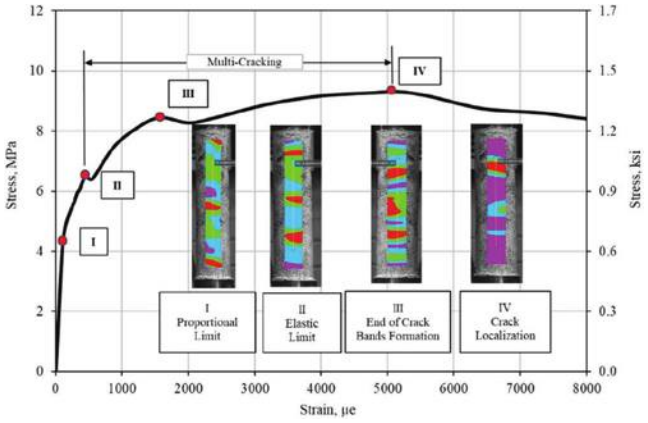

Fig. 7—Idealized stress-strain curve for 0-degree casting orientation.

Fig. 8—Typical crack pattern and fiber orientation for 0-degree casting.

progressive decrease in stiffness and increase in stress until a first local peak occurred at stress and strain levels of 6.5 MPa (950 psi) and 450 με, respectively. This kind of discontinuity in the stress-strain curve was reported previously by Haber et al.[6] as possibly the result of geometric imperfections or most likely, in this case, material heterogeneity. After this first local peak, the trend of decreasing stiffness and increasing stress continued until reaching a second peak in the stress-strain curve at an average stress level of 8.4 MPa (1200 psi) and strain of 1550 με. During this stage, the material experiences the formation of several crack bands, as shown by the DIC mapping of strains (refer to Fig. 7).

The behavior described previously resembles the stress-strain behavior of aluminum with an initial elastic phase immediately followed by a tensile-hardening phase. After the second peak, a pseudo stress plateau starts with the widening of pre-existing microcracks and the formation of new ones. The pseudo stress plateau is typically accompanied by some increase in tensile stress until reaching the crack localization point at an average maximum stress of 9.3 MPa (1350 psi) and strain of 5150 με. The results for this type of material and casting orientation are encouraging because of the high tensile strength obtained and a pseudo stress plateau that starts at a strain level of 1550 με, close to 75% of yielding of Grade 60 reinforcing bar. Additionally, localization occurs at a strain level for tension-controlled sections, guaranteeing an adequate level of ductility in flexure at failure. Figures 6 and 7 show selected stress-strain curves for horizontally cast (0-degree) specimens and the idealized average curve, respectively. The latter contains the typical strain mapping from the DIC post-processing at different conspicuous points in the curve. Figure 8 exhibits the typical crack pattern and fiber orientation for the horizontally cast specimens.

The reason behind the favorable results described previously could be explained by hydrodynamics of viscous suspensions and flow molding theory and has been characterized for UHPC by several authors.[7,8] Essentially, the fibers are embedded in a high-plastic-viscosity, flowable media that, in the case of the 0-degree casting orientation, is subjected to shear flow due to the narrow, long, and confined nature of the casting pipe. Once a shear flow is established in the longitudinal direction, the longer the traveling of the material in the form, the more the tendency of the fibers to align parallel to the form axis.

Direct tension tests of 90-degree casting orientation specimens

A remarkably different behavior in uniaxial tension has been observed in the 90-degree cast test specimens in comparison to the 0-degree specimens. The 90-degree cast (vertical) specimens presented either some tensile stress hardening (H) but limited ductility, or experienced tension softening (S) right after first cracking. In the hardening type (H) specimens, the average limit of proportionality was measured at 6 MPa (850 psi). After this initial linear-elastic stage, the material experienced stiffness degradation with increasing strength, similar to that of the 0-degree specimens, except that the transition to a stress plateau was not as smooth, with the appearance of three to four macrocracks along the way. Nevertheless, the stress plateau was reached at the same stress level of 8.3 MPa (1200 psi) but at a lower strain value of 1000 με. After this point, the material experienced some hardening in a less remarkable fashion than the 0-degree counterparts, until achieving localization at a stress level of 8.6 MPa (1250 psi) and at a strain of 2800 με. A steeper descending branch after localization was also observed (refer to Fig. 9 and 10).

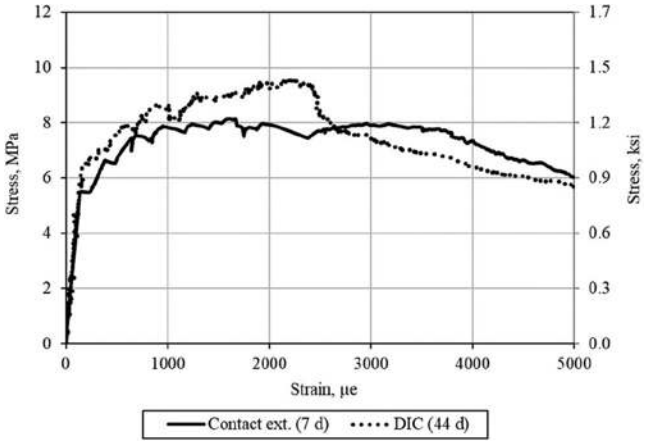

Fig. 9—Stress-strain curves for 90-degree casting orientation (Type H behavior).

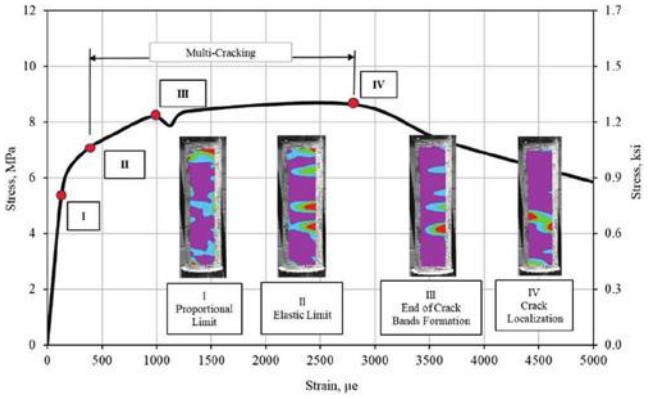

Fig. 10—Idealized stress-strain curve for 90-degree casting orientation (Type H behavior).

On the other hand, several specimens in Rounds 1 and 2 experienced tension-softening (Type S) behavior right after first cracking, which occurred at a strain value very close to the limit of proportionality. The low strength values achieved by those samples were also noted (refer to Fig. 11 and 12), with an average strength of approximately 3.2 MPa (460 psi). Figure 13 shows the typical crack pattern and fiber orientation at the failure surface for 90-degree cast specimens.

These findings are diametrically opposite to the outcomes of the horizontally (0-degree) cast specimens and point out the crucial role that fiber orientation and distribution play in both strength and ductility of UHPC. This issue has also been observed in the work of Maya Duque and Graybeal,[3] but it is more pronounced in this case because of the procedure implemented for the vertical casting in this research. The vertical casting procedure induced a divergent flow (refer to Fig. 14) and the collapse of the fibers under the weight of the material placed above. In a divergent flow, the fibers tend to migrate from the center to the pipes' wall. These mechanisms provoked a prevalent orientation of the fibers at an angle of more than 45 degrees with respect to the longitudinal axis of the pipe form.

Some questions remain open in regard to the possibility of anisotropic behavior induced by casting orientation in actual UHPC elements, and to whether the casting criteria

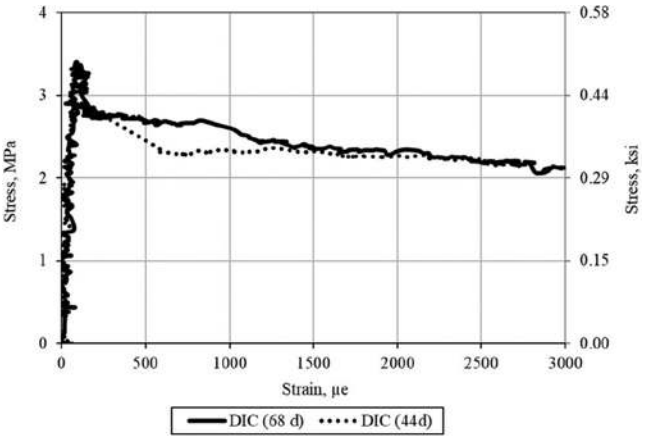

Fig. 11—Stress-strain curves for 90-degree casting orientation (Type S behavior).

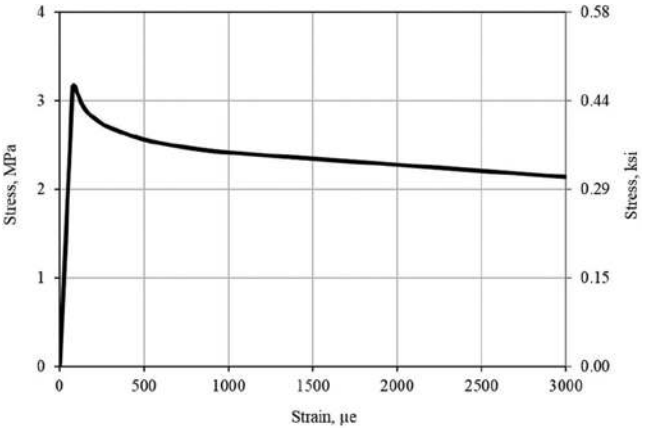

Fig. 12—Idealized stress-strain curve for 90-degree casting orientation (Type S behavior).

used in this work could mimic in-place conditions of full-scale specimens—for instance, in vertically cast, relatively narrow elements. Ultimately, the results from this work and other research found in the literature[3,9,10] should not be left for oblivion, especially in the case of a possible widespread use of UHPC as a standalone material for shear resistance in precast applications.

CONCLUSIONS

From a total of 26 direct tension tests (DTTs) in Rounds 1 and 2, several conclusions are drawn:

1. The casting orientation procedure successfully established two extreme, different behaviors in tension for the ultra-high-performance concrete (UHPC) mixture studied. In one extreme, the 90-degree (vertical) casting orientation produced samples with softening behavior (Type S specimens) and low strength results. In the other extreme, the samples cast at 0 degrees (horizontal) showed strain-hardening behavior and higher tensile strength results.

2. The proposed DTT can capture the full behavior in uniaxial tension of the nonproprietary UHPC mixture studied. Success was achieved in tension-hardening specimens and in tension-softening samples as well. The new test has some advantages over other DTTs regarding specimen preparation and the relative simplicity of its execution.

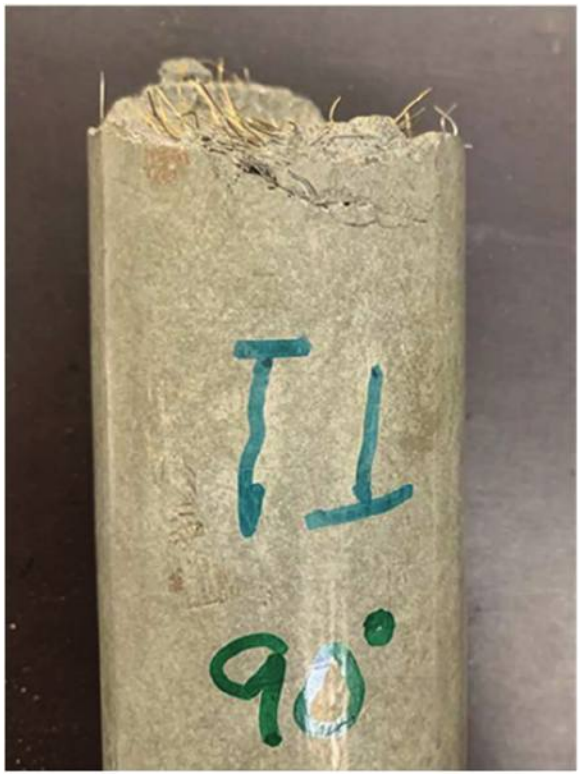

Fig. 13—Typical crack pattern and fiber orientation for 90-degree cast specimens.

3. The new test has a similar success rate (67%) as that of the Federal Highway Administration (FHWA) test (65%) when using digital image correlation (DIC) and proper specimen preparation.

4. When specimens are cast using the 0-degree casting procedure described herein, the limestone-metakaolin nonproprietary mixture exhibits a maximum average tensile strength of 9.3 MPa (1350 psi), tensile-hardening behavior, multi-cracking, and an average crack localization strain of approximately 5150 με.

5. Specimens fabricated using the vertical casting procedure (90 degrees) have either a limited ductility or behave in a tension-softening manner, achieving very low strength values.

6. Casting orientation induces flow and alignment of fibers in a particular preferential direction, which could produce significant variations in the tensile properties of the UHPC material in other directions.

AUTHOR BIOS

ACI member **Rodolfo Bonetti** *received his BS from Pontificia Universidad Católica Madre y Maestra, Santiago, Dominican Republic; his MS from Virginia Tech, Blacksburg, VA; and his PhD in civil engineering from The University of Texas at Austin, Austin, TX, in 2022. His research interests include the characterization of cementitious composites and the behavior of concrete structures.*

Oguzhan Bayrak *is the Phil M. Ferguson Professor in civil engineering at The University of Texas at Austin. His research interests include the behavior, analysis, and design of reinforced and prestressed concrete structures; bridge engineering; evaluation of structures in distress; structural repair; fiber-reinforced polymers; and earthquake engineering.*

Kevin Folliard, *FACI, is the Warren S. Bellows Centennial Professor in civil engineering at The University of Texas at Austin. His research interests include portland cement concrete, concrete durability, high-performance concrete, and controlled low-strength materials.*

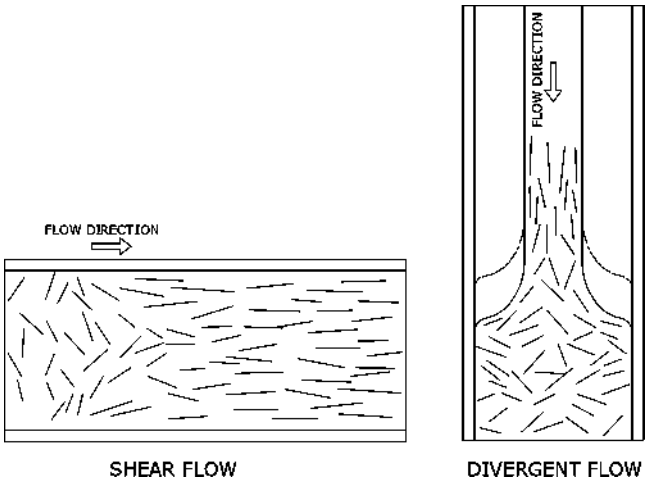

Fig. 14—Difference in flow type in horizontal and vertical casting.

Thanos Drimalas, *FACI, is a Research Associate in the Department of Civil, Architectural and Environmental Engineering at The University of Texas at Austin, where he received his PhD in civil and environmental engineering in 2007. He is a member of ACI Committees 201, Durability of Concrete; 301, Specifications for Concrete Construction; 321, Concrete Durability Code; and 350C, Environmental Engineering Concrete Structure Code. His research interests include concrete durability and the use of supplementary cementitious materials in concrete.*

ACKNOWLEDGMENTS

The authors are appreciative of Burgess, Huber Engineered Materials, Composites One LLC, Bekaert, and Sika USA for providing materials for this research.

NOTATION

E_c = modulus of elasticity in tension of UHPC

REFERENCES

1. Graybeal, B., and Baby, F., "Development of Direct Tension Test Method for Ultra-High-Performance Fiber-Reinforced Concrete," *ACI Materials Journal*, V. 110, No. 2, Mar.-Apr. 2013, pp. 177-186.

2. Graybeal, B., and Baby, F., "Tension Testing of Ultra-High Performance Concrete," Publication No. FHWA-HRT-17-053, Federal Highway Administration, McLean, VA, 2019, 181 pp.

3. Maya Duque, L. F., and Graybeal, B., "Fiber Orientation Distribution and Tensile Mechanical Response in UHPFRC," *Materials and Structures*, V. 50, No. 1, 2017, pp. 1-17.

4. Rots, J., and DeBorst, R., "Analysis of Concrete Fracture in 'Direct' Tension," *International Journal of Solids and Structures*, V. 25, No. 12, 1989, pp. 1381-1394. doi: 10.1016/0020-7683(89)90107-8

5. Amin, A.; Markić, T.; and Kaufmann, W., "Direct Tension Testing of SFRC – Some Peculiar Effects of the End Restraints," *Proceedings, 10th International Conference on Fracture Mechanics of Concrete and Concrete Structures, FraMCoS-X*, G. Pijaudier-Cabot, P. Grassl, and C. La Borderie, eds., Bayonne, France, 2019, pp. 1-9.

6. Haber, Z.; De la Varga, I.; and Graybeal, B., "Properties and Behavior of UHPC-Class Materials," Publication No. FHWA-HRT-18-036, Federal Highway Administration, McLean, VA, 2018, 147 pp.

7. Kang, S., and Kim, J., "Numerical Simulation of the Variation of Fiber Orientation Distribution during Flow Molding of Ultra-High Performance Cementitious Composites (UHPCC)," *Cement and Concrete Composites*, V. 34, No. 2, 2012, pp. 208-217. doi: 10.1016/j.cemconcomp.2011.09.015

8. Huang, H.; Gao, X.; and Teng, L., "Fiber Alignment and Its Effect on Mechanical Properties of UHPC: An Overview," *Construction and Building Materials*, V. 296, 2021, pp. 1-16. doi: 10.1016/j.conbuildmat.2021.123741

9. Shen, X., and Brühwiler, E., "Influence of Local Fiber Distribution on Tensile Behavior of Strain Hardening UHPFRC Using NDT and DIC," *Cement and Concrete Research*, V. 132, 2020, pp. 1-15. doi: 10.1016/j.cemconres.2020.106042

10. Abrishambaf, A.; Pimentel, M.; and Nunes, S., "Influence of Fibre Orientation on the Tensile Behavior of Ultra-High Performance Fibre Reinforced Cementitious Composites," *Cement and Concrete Research*, V. 97, 2017, pp. 28-40. doi: 10.1016/j.cemconres.2017.03.007

APPENDIX

Table A1—Specimen types and failure modes of specimens in this research

DTTs summary				
Test No.	Casting orientation	Epoxy transition?	Localization*, mm (in.)	Failure location
Round 1 (deformations measured with extensometer)				
1	0 degrees	No	0 (0.00)	At steel interface
2	90 degrees	No	51 (2.00)	Close to transition
3	0 degrees	Yes	114 (4.50)	Within gauge length
4	0 degrees	Yes	108 (4.25)	Within gauge length
5	90 degrees	Yes	102 (4.00)	Within gauge length
6	0 degrees	Yes	25 (1.00)	Close to transition
7	0 degrees	Yes	89 (3.50)	At attach points
8	0 degrees	No	83 (3.25)	At attach points
9	90 degrees	No	70 (2.75)	At attach points
10	90 degrees	No	64 (2.50)	At attach points
11	0 degrees	Yes	70 (2.75)	At attach points
12	90 degrees	Yes	76 (3.00)	At attach points
13	0 degrees	No	57 (2.25)	At attach points
14	0 degrees	No	70 (2.75)	At attach points
15	0 degrees	Yes	70 (2.75)	At attach points
16	0 degrees	Yes	95 (3.75)	At attach points
17	90 degrees	No	70 (2.75)	At attach points
Round 2 (deformations measured with DIC)				
1	90 degrees	Yes	114 (4.50)	Within gauge length
2	0 degrees	Yes	127 (5.00)	Within gauge length
3	0 degrees	Yes	95 (3.75)	Within gauge length
4	90 degrees	Yes	76 (3.00)	Within gauge length
5	90 degrees	Yes	102 (4.00)	Within gauge length
6	90 degrees	Yes	76 (3.00)	Within gauge length
7	90 degrees	Yes	25 (1.00)	Close to transition
8	0 degrees	Yes	0 (0.00)	At steel interface
9	90 degrees	Yes	13 (0.50)	Close to transition

*From nearest steel interface.

Table A2—Details of strain and stress data for valid tests in Rounds 1 and 2

Failure within gauge length tensile tests summary					
Test No.	Casting orientation	Elastic limit stress, MPa (ksi)	Elastic limit strain, με	Tensile strength, MPa (ksi)	Localization strain, με
Round 1 (deformations measured with extensometer)					
3	0 degrees	6.4 (0.93)	322	9.3 (1.35)	5304
4	0 degrees	8.0 (1.16)	284	10.1 (1.47)	5229
5	90 degrees	6.7 (0.97)	310	8.0 (1.15)	3224
Round 2 (deformations measured with DIC)					
1	90 degrees	7.0 (1.01)	390	9 (1.30)	2301
2	0 degrees	5.0 (0.73)	370	8.4 (1.22)	5124
3	0 degrees	6.7 (0.98)	360	9.7 (1.42)	4880
4*	90 degrees	3.4 (0.49)	86	3.4 (0.49)	86
5*	90 degrees	3.0 (0.43)	75	3.0 (0.43)	75
6*	90 degrees	8.7 (1.26)	342	8.7 (1.26)	342

*Type S specimens.

Note: 1 MPa = 0.145 ksi.

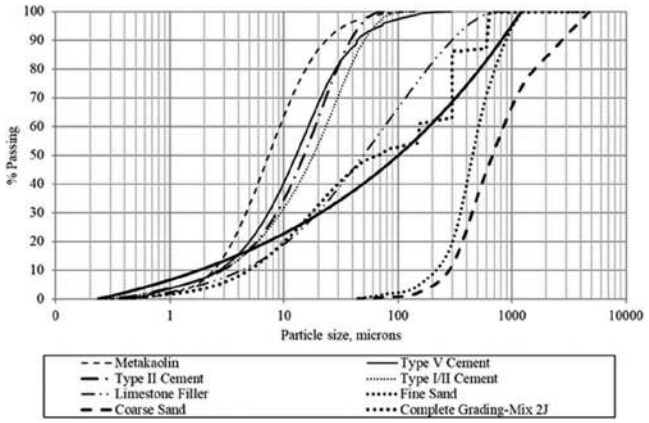

Fig. A1—Particle-size distribution of dry constituents of UHPC mixture.

ARE YOU A RESEARCHER?

SIGN UP FOR ORCID TODAY!

ORCID provides a persistent digital identifier that distinguishes you from every other researcher and, through integration in key research workflows such as manuscript and grant submission, supports automated linkages between you and your professional activities, ensuring that your work is recognized.

Individuals may use ORCID services freely and it's as easy as **1-2-3**:

1. REGISTER
2. ADD YOUR INFO
3. USE YOUR ORCID ID

For more information and to register, visit:

WWW.ORCID.ORG

ACI MATERIALS JOURNAL TECHNICAL PAPER

Title No. 120-M29

Tensile Creep of Metakaolin-Limestone Powder Ultra-High-Performance Concrete

by Rodolfo Bonetti, Oguzhan Bayrak, Kevin Folliard, and Thanos Drimalas

An investigation was performed on the drying shrinkage and tensile drying creep characteristics of a nonproprietary ultra-high-performance concrete (UHPC) mixture. The mixture was formulated using metakaolin as the supplementary cementitious material (SCM) and limestone powder as the mineral filler. Cylindrical specimens with dimensions of 52 x 400 mm (2.05 x 16 in.) were fabricated and loaded at 7 and 11 days from casting to various stress levels for 90 days. Additional specimens were fabricated from a proprietary mixture with a silica fume-ground quartz formulation to study the effects of mixture composition. Simultaneous free drying shrinkage measurements were recorded in accompanying specimens placed in the same room environment. Attention was given to the effect of the casting orientation, age at loading, and mixture composition on the drying shrinkage and drying creep behavior of the samples. These tests show that the metakaolin-limestone powder mixture has significantly lower drying shrinkage and specific drying creep than the silica fume-ground quartz mixture. Additionally, the age at loading influences primary creep behavior while not affecting secondary creep at the same stress level. It seems that fiber orientation plays a significant role in the drying creep behavior of UHPC and that cracked UHPC under constant tensile stress undergoes a significant amount of fiber slip.

Keywords: casting orientation; drying shrinkage; mixture composition; tensile creep; ultra-high-performance concrete (UHPC).

INTRODUCTION

Ultra-high-performance concrete (UHPC) is a cementitious composite offering strength and durability features that could potentially transform the precast concrete industry. Nevertheless, the widespread use of UHPC as a standalone material for shear resistance requires some critical knowledge about its long-term behavior in tension. Creep consists of additional deformations over time in excess of the initial strain at a constant level of stress. In cementitious materials, creep is the result of water movement (microdiffusion) between capillary and gel pores,[1] producing local debonding of the intertwined solid phase of the calcium-silicate-hydrate (C-S-H) gel. Total creep strains are the sum of basic creep, occurring under sealed conditions, and drying creep, occurring under conditions of exposure to the environment. Concurrent deformations (shrinkage) caused by water loss influence the total deformation under constant stress. Internal water loss produces autogenous shrinkage. The loss of water to the environment produces drying shrinkage. These deformations need to be subtracted from the total deformation to obtain basic or drying creep values, as required by each case.

Tensile creep of UHPC is one of those areas where very limited research has been published, in part because of the complexities surrounding the required test methods. Another obstacle has been the lack of a broadly accepted framework for determining the full spectrum of tensile behaviors of the material. Although some of these difficulties persist, various researchers[2,3] have contributed to this knowledge base, mainly studying the tensile creep behavior of proprietary mixtures that have silica fume as the main supplementary cementitious material (SCM), with or without ground quartz as the mineral filler.

Garas Yanni[2] conducted a multiscale investigation on the tensile creep of UHPC, observing that the drying tensile creep of UHPC is several times greater than its compressive creep at the same relative stress level and that the long-term creep behavior is greatly affected by the porosity of the fiber-matrix interface. The researcher favored the use of thermal treatment and proper consolidation of the material if intended for use as shear reinforcement in bridge girders. A tensile creep study by Switek[3] proposed the hypothesis that the nonlinear viscoelasticity observed in tensile creep specimens tested at an early age is mainly caused by the internal moisture changes verified during the incipient hydration process.

The work presented in this paper focuses on several aspects not covered extensively in the current literature related to the tensile creep behavior of nontraditional, nonproprietary UHPC.

RESEARCH SIGNIFICANCE

The use of UHPC for shear resistance constitutes a logical path of application for the material due to its enhanced tensile strength and ductility in comparison with high-strength concrete. However, the long-term behavior in tension of this relatively novel material has not been addressed in detail, which is one of the issues causing some stagnation of the technology. Various aspects have been identified where gaps in the current literature still exist, such as the effects on tensile creep of the age at loading, mixture composition, casting/fiber orientation, and the creep behavior of cracked specimens. This paper provides some answers to these issues.

ACI Materials Journal, V. 120, No. 2, March 2023.

MS No. M-2022-144.R1, doi: 10.14359/51738492, received October 16, 2022, and reviewed under Institute publication policies.

EXPERIMENTAL PROCEDURE

Creep frames

Various test setups have been proposed[2,3] for the long-term tensile creep testing of concrete and UHPC, most of them consisting of a dead load-lever arm system with some similarities to the one proposed by Bissonnette and Pigeon[4] for fiber-reinforced concretes. The moveable creep frames built for the purpose of this study are inspired by the work of Switek[3] with the introduction of several modifications. These modifications were intended to increase stiffness and minimize out-of-plane deformations, and accommodate a lever arm ratio of 6:1 and bigger loading plates for the use of steel weights. Additionally, the frames were made in two sections to make possible their placement and assembly inside the controlled environment room. Figure 1 depicts the steel frames fabricated for this investigation. Calibration of each lever was performed prior to the use of the creep frames. This was achieved by applying incremental step loading at the tip of the lever and measuring the tensile force reaction through a donut load cell located at the top of the frame. The slope of the resulting straight line of the tensile force versus applied load was the value of the lever ratio. All the values of the lever ratio were found to be within ±3% of the theoretical value of 6.

Materials

A nonproprietary mixture was developed for this shrinkage and creep study, with metakaolin as the SCM at an amount of 30% of cement content by weight. Limestone powder was used as the mineral filler with an average particle size of 100 µm. Packing optimization of dry constituents was achieved by using the sum of squares of residuals (SSR) of the total grading curve points, departing from the modified Andreasen and Andersen model with a *k*-value of 0.225. An air detrainer in a 1% dose by cement weight was added to the mixture to curb some of the entrapped air introduced by the high amount of high-range water-reducing admixture (HRWRA) required for workability. Table 1 shows the composition of the mixture described previously. The proprietary mixture used in this study has silica fume as the main SCM and ground quartz as the mineral filler (refer to Graybeal[5]).The mixing of the materials was performed in a horizontal pan mixer in batches of 0.033 m^3 (1.1 ft^3) with a total mixing time of 13 minutes for the nonproprietary mixture and up to 45 minutes for the proprietary mixture.

Specimens

The creep specimens were cast in a casting bed, in clear, polyethylene terephthalate glycol (PETG) plastic tubes of 52 mm (2.05 in.) inside diameter and 1220 mm (48 in.) in length, using two different casting orientations intended to induce different preferential fiber alignment in the specimens. The first set of specimens was cast with the casting bed placed horizontally (0 degrees) and the second set with the casting bed in a vertical position (90 degrees). External vibration was used for the horizontal specimens to facilitate material placement. Figure 2 shows the casting orientations described previously. After casting, the tubes were sealed to prevent moisture loss and placed in an upright position until samples reached at least 55 MPa (8000 psi) of compressive strength, tested from accompanying 50 mm (2 in.) cubes. The specimens were then cut to 400 mm (16 in.) lengths using a concrete saw. Following cutting, the specimens were water cured for 3 additional days, after which their ends were slightly sanded, cleaned, and epoxied to receive the steel nipples that were attached to them.

Table 1—Nonproprietary mixture proportions

Material	Proportions by weight
Cement, PC Type V	1.000
Metakaolin	0.300
Limestone powder	0.523
Sand	1.400
Air detrainer	0.010
HRWRA	0.051
Water	0.325
Steel fibers*	0.239

*Straight, 0.2 x 13 mm, 2% by volume.

Note: PC is portland cement.

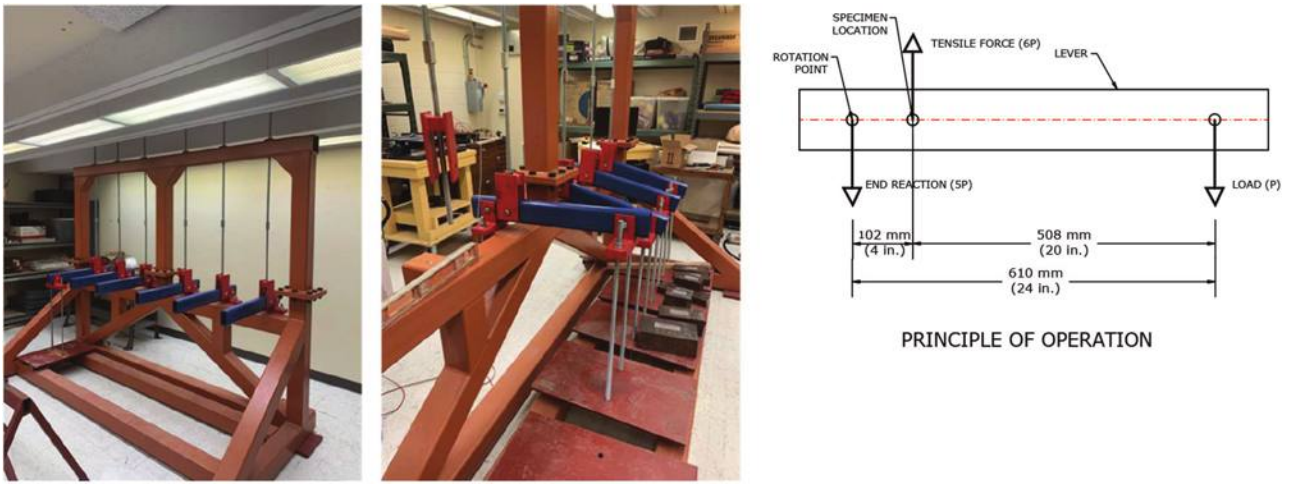

Fig. 1—Overview of creep frames used in research.

Table 2—Summary of specimens in tensile creep test program

Specimen	Mixture	Casting orientation, degrees	Age at loading, days	Applied tensile stress, MPa (ksi)	Stress-strength ratio
L1	Nonproprietary	0	7	4.7 (0.68)	0.84
L2	Nonproprietary	0	7	4.7 (0.68)	0.84
L5	Nonproprietary	0	11	4.9 (0.71)	0.87
L6	Nonproprietary	0	11	4.1 (0.59)	0.72
L7	Proprietary	0	11	4.3 (0.63)	0.59
L9	Nonproprietary	90	11	3.7 (0.53)	0.85
L10	Nonproprietary	90	11	3.7 (0.53)	0.85

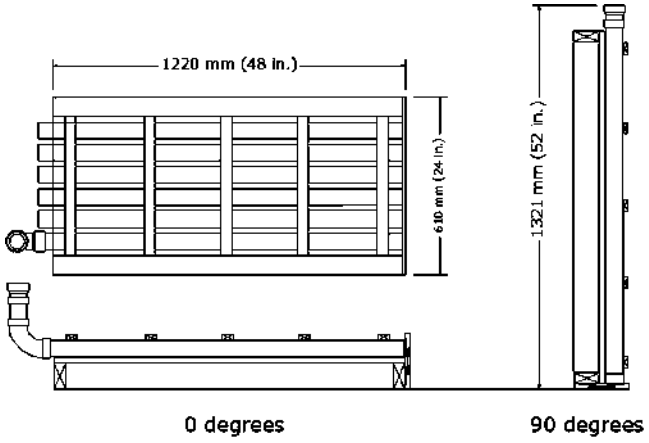

Fig. 2—Casting orientations for shrinkage and creep specimens.

The drying shrinkage specimens followed the same preparation procedure as the creep specimens, except that steel nipples were not attached to their ends. Figure 3(a) shows the shrinkage specimens resting on the free drying shrinkage table.

Instrumentation

Two concrete surface strain gauges 60 mm (2.5 in.) long were glued to opposite sides of all the specimens. Additionally, the tensile creep specimens were instrumented with two 50 mm (2 in.) linear potentiometers located at 90 degrees from the strain gauges and at opposite sides of the specimens. The potentiometers were attached to the specimens with U-bolts, as shown in Fig. 3(b). All sensors were connected to a data acquisition system, and deformation values were recorded at a 5-minute time interval for the first 24 hours and at 30-minute increments afterward, until the end of the tests.

Loading procedure

The tensile strength of each mixture and casting direction was determined by direct tension tests prior to the loading of the creep specimens, as the average strength of two samples. The test method used to determine the tensile strength is a new direct tension test in displacement control at a loading rate of 0.15 mm/min (0.006 in./min).[6] For the nonproprietary and proprietary mixtures cast at 0 degrees, the average tensile strengths were measured at 5.6 and 7.3 MPa (0.81 and 1.06 ksi), respectively. The tensile strength of the

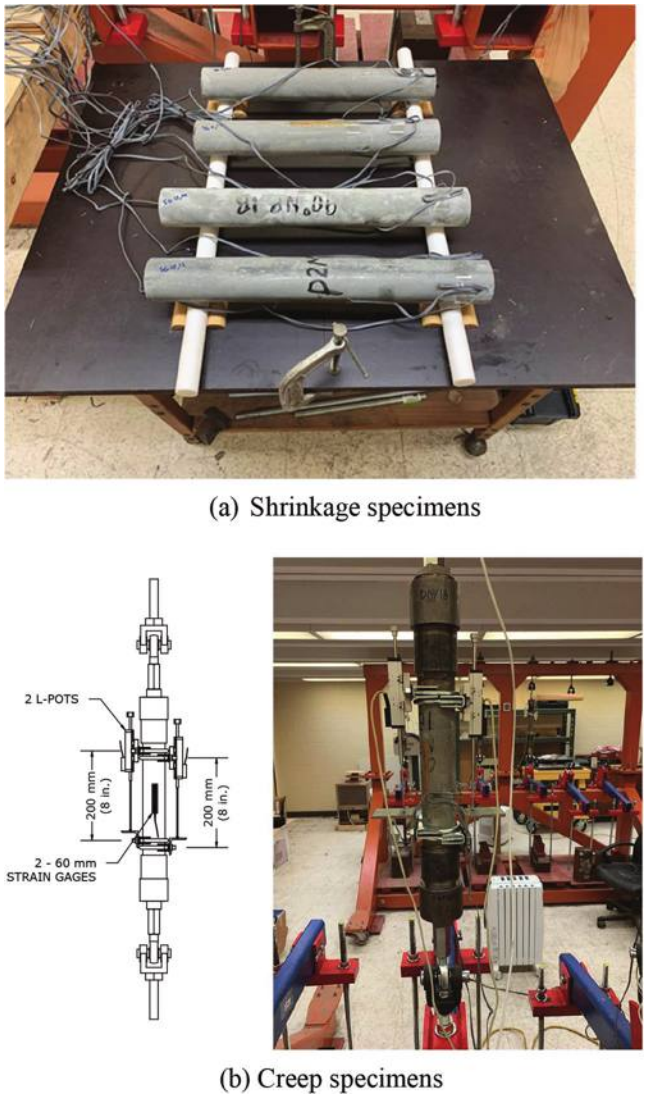

Fig. 3—Test setups for shrinkage and creep specimens.

nonproprietary mixture cast at 90 degrees was 4.3 MPa (0.62 ksi). These strength values served to determine the required amount of steel weights to place on the loading plates for each sample and depended on the target stress level. The calculation of these steel weights included the predetermined weights of hardware, lever, and plate. Table 2 shows the actual stress and stress-strength ratios applied to each of the samples. The specimens were attached and

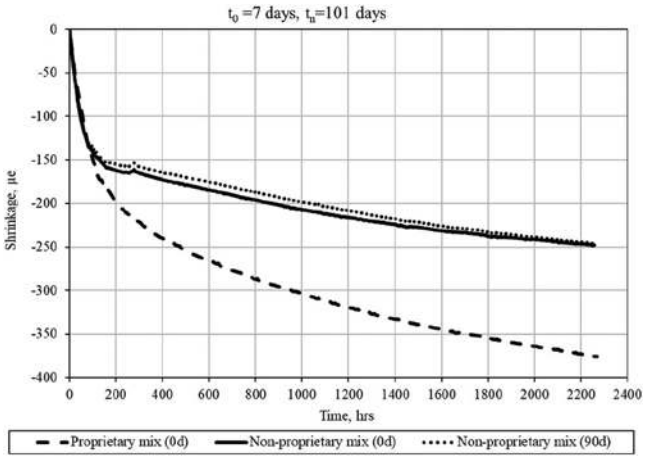

Fig. 4—Free drying shrinkage of proprietary and nonproprietary UHPC mixtures.

aligned to the frame and levers through two ball joints at each end. The load was progressively transferred to the specimens by simultaneously turning the nuts of the two hanging rods supporting the steel plates until the plates were approximately 38 mm (1.5 in.) above the bottom beams of the frames. The load-transfer operation lasted approximately 5 minutes. Additionally, temperature and humidity were controlled over the duration of the tests to 23 ± 1°C (73 ± 2°F) and 50 ± 4% relative humidity, respectively. Table 2 shows a summary of the creep specimens tested in this research program.

EXPERIMENTAL RESULTS AND DISCUSSION

Drying shrinkage specimens

Drying shrinkage deformations from five specimens were recorded starting at 7 days of age and for 94 days afterward. The specimens rested over low-friction rods to prevent any restraint. Figure 4 shows the results of free drying shrinkage deformations as the average of two samples (two gauges each), except for the nonproprietary mixture cast vertically (90 degrees), where only the average of two gauges on one sample was measured. The experimental evidence shows the drying shrinkage behavior to be similar for both mixtures regardless of casting orientation for the first 100 hours, with a slightly steeper slope for the nonproprietary mixture. After this accelerated phase, shrinkage of the nonproprietary mixture progresses at a much lower rate than the proprietary mixture.

At 94 days of testing, the proprietary mixture drying shrinkage strains were 53% higher than those of the nonproprietary mixture. These results are somewhat unexpected because the nonproprietary mixture has a greater water-binder ratio (w/b) of 0.25 in comparison to the 0.20 ratio of the proprietary mixture. A plausible explanation for this behavior resides in the increased sand-powder ratio; a lower cement content; and larger particle size of the sand, mineral filler, and SCM (metakaolin) of the nonproprietary mixture. In terms of the preferential fiber orientation, it is apparent that casting orientation does not affect the drying shrinkage behavior of the nonproprietary mixture.

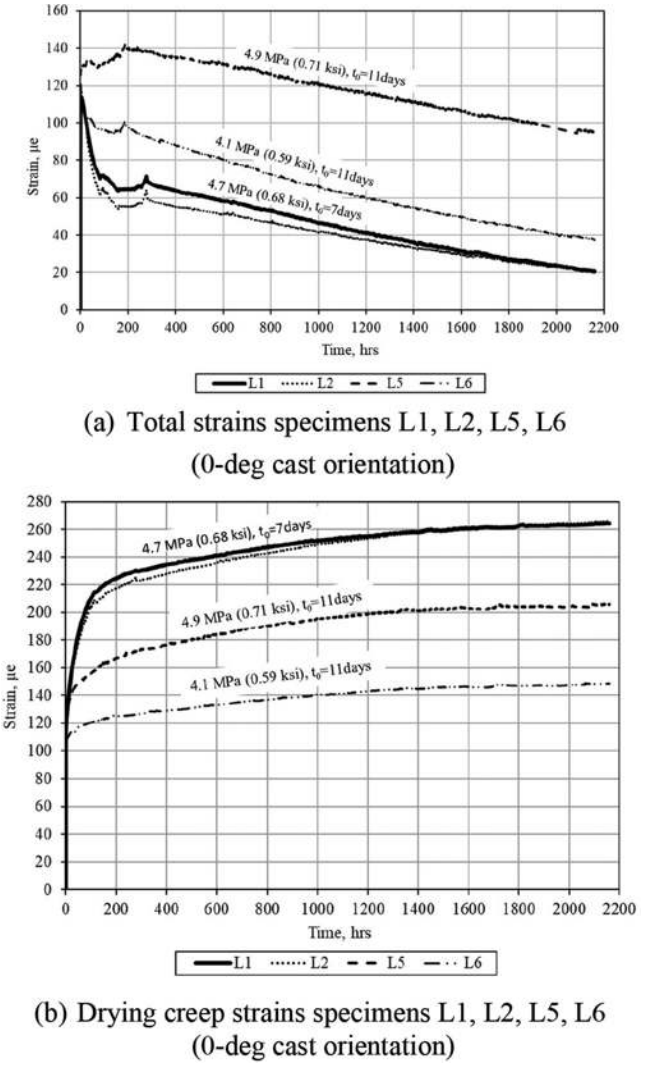

Fig. 5—Total strains and drying creep of nonproprietary mixture (0-degree casting orientation).

Drying creep specimens

The 50 mm (2 in.) cube compressive strength and modulus of elasticity (ASTM C469) of the material at the time of load transfer were 124 MPa (18 ksi) and 41.4 GPa (6000 ksi), respectively. Drying creep deformations were calculated as the result of the total deformations minus the corresponding shrinkage deformations. Basic creep deformations in sealed specimens were not measured during this research because loading started at ages (7 and 11 days) where almost all autogenous shrinkage has taken effect in the specimens (refer to Fig. A.1 in Appendix A). Drying creep strains reported in Fig. 5(b) include the initial elastic strain, ε_o. Table A.1 in Appendix A shows the initial elastic deformation, ε_o, and the drying creep coefficient at 90 days ($\varepsilon_{90}/\varepsilon_o$) for the specimens in this research.

Effect of age at loading

Specimens L1 and L2 were loaded at 7 days from casting at a 4.7 MPa (0.68 ksi) stress level for 90 days. Specimens L5 and L6 were loaded at 11 days at stress levels of 4.9 MPa (0.71 ksi) and 4.1 MPa (0.59 ksi), respectively. Figures 5(a) and (b) show the total strains and drying creep strains for

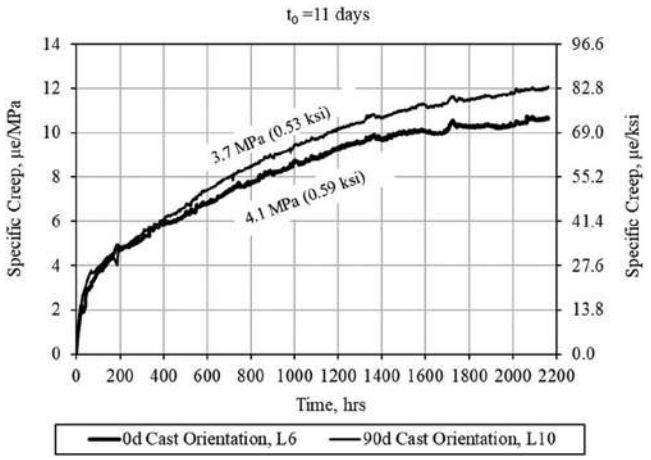

Fig. 6—Effect of casting orientation on specific drying creep of nonproprietary mixture.

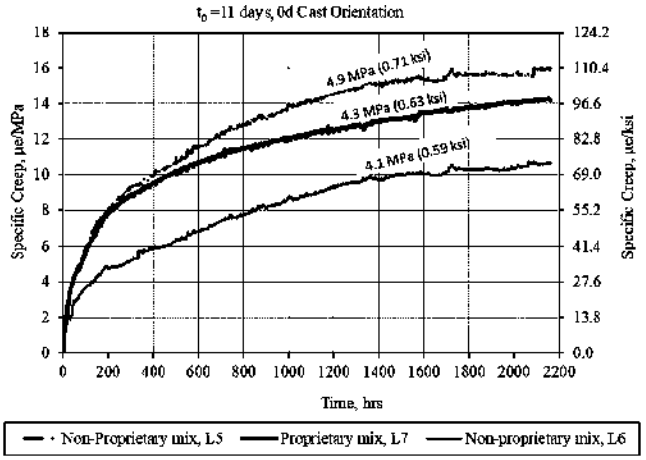

Fig. 7—Effect of mixture composition on specific drying creep.

these four specimens. It is evident that when specimens are loaded in tension at 7 days, the total strains are heavily affected by shrinkage in comparison to the lesser impact shown on those loaded at 11 days of age. Additionally, the age at loading affects the onset of the state of a constant rate of creep deformation (secondary creep). Specimens loaded at 11 days experienced a shortening of the primary creep stage in approximately 100 hours in comparison to those loaded at 7 days. Secondary creep seems to not be affected by the age at loading at approximately the same stress level. These findings are very similar to other results reported in the literature,[3,7] tying a reduction in creep deformation to hydration evolution with time.

Effect of fiber orientation

Specimens L6 and L10 were loaded at 11 days of age at 4.1 and 3.7 MPa (0.59 and 0.53 ksi) stress levels, respectively. Specimen L6 was cast horizontally (0 degrees), whereas Specimen L10 was cast vertically (90 degrees). Specific drying creep for both specimens is presented in Fig. 6. These results show an increase in the specific creep of the specimen cast at 90 degrees in comparison to the specimen cast horizontally regardless of being loaded at a smaller stress level. This behavior could be explained by the microcracking effect theory (Neville et al.[8] and Bissonnette et al.[7]). A preferential fiber orientation along the axis of the creep specimen, where the tensile stress is applied, will prevent the propagation of microcracks, thus reducing the potential total amount of creep in the specimen.

Effect of mixture composition

To study the effect of mixture composition, Specimen L7 from the proprietary mixture was loaded at 11 days of age at a 4.3 MPa (0.63 ksi) tensile stress level. This specimen was cast horizontally to produce a preferential fiber orientation along the longitudinal axis of the specimen. Drying specific creep values were obtained during the 90-day period of the creep tests and compared to those from Specimens L5 and L6 of the nonproprietary mixture, which had the same casting orientation. Results from these experiments (refer to Fig. 7) show an increase of specific creep for the proprietary mixture of 33% over the nonproprietary mixture at approximately the same stress level, and just 12% less specific creep than Specimen L5, which was loaded at a higher stress level of 4.9 MPa (0.71 ksi). Results by Garas Yanni[2] in untreated square section specimens, made of a proprietary mixture and tested at a stress level of 40% of tensile strength, show specific tensile creep of approximately five times greater than those shown in Table A.1 for the nonproprietary mixture tested at 7 days of age. A probable reason for this behavior resides in the finer raw materials and microstructure that is typically obtained from the silica fume-ground quartz mixtures that in turn produce an increase in both shrinkage and creep (refer to Fig. 4 and 7).

Creep of cracked specimens

Specimens L1, from the nonproprietary material, and L7, from the proprietary mixture, cracked during load transfer. However, results from this research suggest that there is no change in behavior for the uncracked portion of the material, as shown by a comparison of Specimens L1 (cracked) and L2 (uncracked), shown in Fig. 5(a) and (b). The position of the cracks was such that it permitted to record deformations with the linear potentiometers during the 90-day period of the creep tests (refer to Fig. 8). Results from these measurements indicate that right after cracking, the material starts experiencing fiber slip events in conjunction with drying creep. The fiber slip measured in the specimen made with the nonproprietary mixture (L1) was larger at transfer but experienced only one additional fiber slip event during the whole test period. Specimen L7, made with the proprietary mixture, experienced several fiber-slip events during the 90-day period of the test. These findings suggest that cracked UHPC elements in tension, under sustained loads, will experience a significant amount of fiber slip.

CONCLUSIONS

From the results of the tests in this investigation, the following conclusions can be drawn:

1. After 94 days of testing, the drying shrinkage of the silica fume-ground quartz (proprietary) mixture is 53%

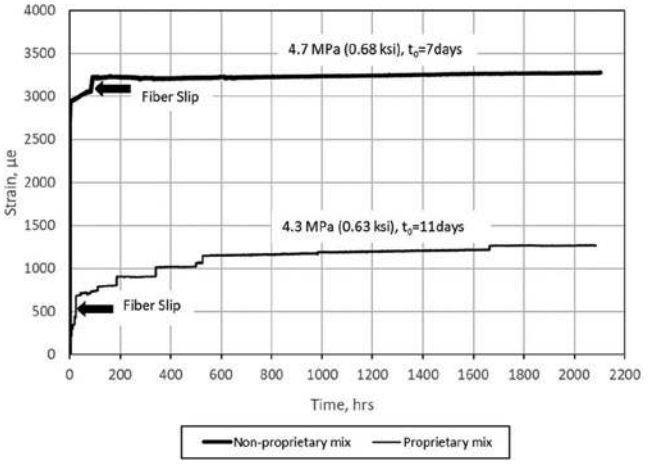

Fig. 8—Drying creep of cracked specimens.

greater than that of the metakaolin-limestone powder (nonproprietary) mixture.

2. The age at loading greatly affects primary creep but not secondary creep. After some progress in the hydration process, it seems that there are no significant changes in the viscoelastic properties of specimens loaded at 7 or 11 days of age at the same stress level.

3. Specific drying creep of the proprietary mixture is approximately 33% greater than that of the nonproprietary mixture at approximately a 4.1 MPa (0.6 ksi) stress level at 90 days.

4. Specific creep of 90-degree cast nonproprietary ultra-high-performance concrete (UHPC) is greater than the specific creep of 0-degree cast UHPC, even at a smaller stress level.

5. Recorded creep deformations of cracked specimens show a substantial amount of fiber slip at constant stress levels.

AUTHOR BIOS

ACI member **Rodolfo Bonetti** *received his PhD in civil engineering from the University of Texas at Austin, Austin, TX, in 2022. He received his BS from Pontificia Universidad Católica Madre y Maestra, Santiago, Dominican Republic; and his MS from Virginia Tech, Blacksburg, VA. His research interests include the characterization of cementitious composites and the behavior of concrete structures.*

Oguzhan Bayrak *is the Phil M. Ferguson Professor in civil engineering at the University of Texas at Austin. His research interests include the behavior, analysis, and design of reinforced and prestressed concrete structures; bridge engineering; evaluation of structures in distress; structural repair; fiber-reinforced polymers; and earthquake engineering.*

Kevin Folliard *is the Warren S. Bellows Centennial Professor in civil engineering at the University of Texas at Austin. His research interests include portland cement concrete, concrete durability, high-performance concrete, and controlled low-strength materials.*

Thanos Drimalas *is a Research Associate in the Department of Civil, Architectural and Environmental Engineering at the University of Texas at Austin, where he received his PhD in civil and environmental engineering in 2007. He is a member of ACI Committees 201, Durability of Concrete; 301, Specifications for Concrete Construction; 321, Concrete Durability Code; and 350C, Environmental Engineering Concrete Structure Code. His research interests include concrete durability and the use of supplementary cementitious materials (SCMs) in concrete.*

ACKNOWLEDGMENTS

The authors are appreciative of Burgess, Huber Engineered Materials, Composites One LLC, Bekaert, and Sika USA for providing materials for this research.

NOTATION

t_0 = time at start of test (in days)
t_n = time at end of test (in days)
ε_o = initial elastic strain

REFERENCES

1. Bažant, Z. P., and Xi, Y., "Drying Creep of Concrete: Constitutive Model and New Experiments Separating Its Mechanisms," *Materials and Structures*, V. 27, No. 1, Jan. 1994, pp. 3-14. doi: 10.1007/BF02472815

2. Garas Yanni, V. Y., "Multi-Scale Investigation of Tensile Creep of Ultra-High Performance Concrete for Bridge Applications," PhD dissertation, Georgia Institute of Technology, Atlanta, GA, 2009, 291 pp.

3. Switek, A. E., "Time-Dependent Response of Ultra-High Performance Fibre Reinforced Concrete (UHPFRC) under Low to High Tensile Stresses," PhD thesis, École Polytechnique Fédérale de Lausanne, Lausanne, Switzerland, 2011, 223 pp. doi: 10.5075/epfl-thesis-4899

4. Bissonnette, B., and Pigeon, M., "Tensile Creep at Early Ages of Ordinary, Silica Fume and Fiber Reinforced Concretes," *Cement and Concrete Research*, V. 25, No. 5, July 1995, pp. 1075-1085.

5. Graybeal, B. A., "Material Property Characterization of Ultra-High Performance Concrete," Report No. FHWA-HRT-06-103, Federal Highway Administration, Turner-Fairbank Highway Research Center, McLean, VA, 2006, 188 pp.

6. Bonetti, R.; Bayrak, O.; Folliard, K.; and Drimalas, T., "A Framework for Determining the Direct Tensile Properties of Ultra-High-Performance Concrete," *ACI Materials Journal*, V. 120, No. 2, Mar. 2023, pp. 87-96. doi: 10.14359/51738374

7. Bissonnette, B.; Pigeon, M.; and Vaysburd, A. M., "Tensile Creep of Concrete: Study of Its Sensitivity to Basic Parameters," *ACI Materials Journal*, V. 104, No. 4, July-Aug. 2007, pp. 360-368.

8. Neville, A. M.; Dilger, W. H.; and Brooks, J. J., *Creep of Plain and Structural Concrete*, Construction Press, London, UK, 1983, 361 pp.

APPENDIX A

Table A1—Summary of deformations in tensile creep specimens

Tensile creep specimens deformations summary				
Specimen name	Initial deformation ε_0, με	Final deformation Initial + Creep ε_{90}, με	Specific creep at 90 days SC_{90}, με/MPa (με/ksi)	Creep coefficient at 90 days Cr_{90}
L1	111	264	32.5 (225)	2.38
L2	111	266	33.0 (228)	2.40
L5	128	206	15.9 (110)	1.61
L6	106	149	10.6 (73)	1.41
L7	70	131	14.1 (97)	1.87
L9	91	141	13.6 (94)	1.55
L10	94	137	11.7 (81)	1.46

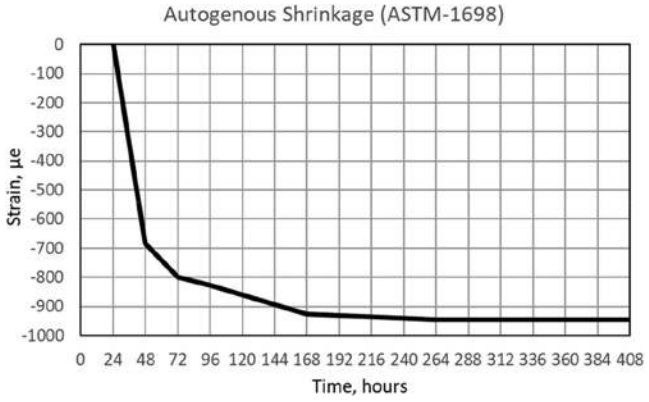

Fig. A1—Autogenous shrinkage of nonproprietary UHPC. (Note: Results shown are average of three samples.)

We're Building the Future

Mission: We make strategic investments in ideas, research, and people to create the future of the concrete industry

Through its councils and programs, the ACI Foundation helps to keep the concrete industry at the forefront of advances in material composition, design, and construction. Our focus:

Our Concrete Innovation Council identifies technologies and innovation that are aligned with ACI and industry strategies and helps facilitate their use when appropriate

Our Concrete Research Council advances the knowledge and sustainable aspects of concrete materials, construction, and structures by soliciting, selecting, financing, and publishing research

Our Scholarship Council supports our future concrete innovators and leaders by administering fellowships and scholarships to help bridge the financial gap for students

Our Veterans Rebate for ACI Certification program helps honorably discharged veterans and increases skills in the industry's workforce. ACICertification.org/veteranrebate

aci Foundation
Building the Future

ACI MATERIALS JOURNAL TECHNICAL PAPER

Title No. 120-M30

Predicting Fracture from Thermodynamic Modeling of Cementitious Systems

by Y. Wang, K. Bharadwaj, H. S. Esmaeeli, P. Zavattieri, O. B. Isgor, and W. J. Weiss

This paper describes an approach to predict the mechanical and fracture behavior of cement-based systems by combining thermodynamic and finite element analysis models. First, the reaction products in a hydrated cementitious paste are predicted using a thermodynamic model. Second, a pore partitioning model is used to segment the total porosity into porosity associated with gel pores and capillary pores. A property-porosity relationship is used to predict the elastic modulus, tensile strength, and fracture energy of the hardened cement paste. The paste's modulus, fracture energy, and tensile strength, along with information on the aggregate properties and interfacial transition zone properties, are used as inputs to a finite element analysis model to predict the flexural strength and fracture response of mortars.

Keywords: elastic modulus; finite element analysis (FEA); fracture; mechanics; porosity; tensile strength; thermodynamic modeling.

INTRODUCTION

The concrete industry is actively working on reducing the CO_2 emissions associated with conventional concrete manufacture through several approaches.[1,2] First, the clinker content of concrete can be reduced by substituting a portion of the ordinary portland cement (OPC) with supplementary cementitious materials (SCM) or filler powders.[3-7] Second, the paste content in the concrete can be reduced through appropriate mixture design.[8-11] Third, the service life of the concrete can be improved, thereby reducing the annual carbon content.

This paper discusses an approach to lower the cement content used in concrete through improved mixture design by providing a tool to predict the mechanical behavior of concrete more accurately. Conventional mixture design approaches often rely on the use of empirical/experimental predictions of the performance of concrete,[12] especially when nonconventional cements and SCMs like fly ash, slag, silica fume, and so on, are used.[13] This often does not take full advantage of the benefits of the SCM being added to the system, such as improvements to the compressive strength of concrete made with the SCM.[14-17] Sometimes, empirical modifications are made to predict the compressive strength of systems containing SCMs like fly ash[18]; however, these calibrations are typically SCM-specific. Many historical SCM sources are changing or becoming less available,[3,5,19] and as a result, there has been a desire to identify alternative SCMs (for example, municipal waste incineration ash, bottom ash, boiler slag, natural pozzolans, and agricultural waste ash),[20-29] and to develop approaches to use off-spec materials.[20] Testing each SCM individually to predict the performance of concrete made with the SCM is time-consuming and expensive. There exists a need for robust tools to predict the performance of concrete using these SCMs (for example, strength, diffusivity, time to corrosion, shrinkage, and freezing-and-thawing performance).

There is a growing body of research that uses thermodynamic models to predict the reaction products for cementitious materials.[30-37] While powerful, these techniques do not describe the spatial distribution of these reaction products. For example, they can predict the total pore volume but not the size and distribution of the pores. To overcome this limitation, the authors have developed an approach, the pore partitioning model (PPM), to interpret the results of the thermodynamic calculations to predict the pore structure.[38,39] Computational tools have also been developed that can link thermodynamics, kinetics, pore structure information, and predicted performance.[17,40,41] This tool requires several inputs, including the chemistry of the binder used (OPC and SCM chemistries and contents, and the SCM reactivity, which can be measured using a pozzolanic reactivity test[42-44]), the physical properties of the concrete constituents (specific gravity and fineness of the OPC and SCMs, aggregate properties, and so on), and the mixture proportions of the concrete (amounts of air, paste, and aggregate). The tool can then be used for any cementitious material combination, in any proportion, to predict key properties of the hydrated system, including strength, porosity, electrical resistivity, formation factor, and ionic diffusion coefficients.[8,16,17,40,41] These predicted properties have been used to develop performance-based mixture proportioning methods[8,20] and service life prediction models.[45]

Despite these recent developments, there are opportunities to improve the models. For example, in the performance-based mixture design tool noted earlier,[8,20] the compressive strength was predicted using the empirical gel-space ratio from Powers and Brownyard,[46] which was developed for OPC systems. The flexural strength was then calculated using the empirical relation to compressive strength from ACI 318-19. Several researchers have been examining ways to improve the strength predictions for OPC + SCM systems,

ACI Materials Journal, V. 120, No. 2, March 2023.

MS No. M-2022-201.R1, doi: 10.14359/51738493, received November 17, 2022, and reviewed under Institute publication policies.

such as coupling micromechanical models with thermodynamic modeling[15,47-51] or by using computer simulations such as CEMHYD3D.[52] Approaches using fractal scaling have also been proposed to predict the mechanical response of cementitious composites.[53] While these approaches are promising, there is a potential to predict mechanical behavior using fracture mechanics.[54-58] Fracture mechanics can natively predict flexural strength,[54,55,58] which can be used as a target criterion in the performance-based mixture design approach.

This paper proposes a framework that enables the mechanical and fracture behavior of a heterogenous concrete to be predicted using the chemical composition and reactivity of the cementitious materials used and the mixture proportions of the concrete. This is achieved through a four-step approach that predicts the reaction products of the paste and uses these products to determine the pore structure and mechanical properties. The framework is compared with experimental data on pastes and mortars. This framework is designed to be a generic tool that can be used to predict the fracture behavior of concrete using a wide variety of cement and alternative cement chemistries.

RESEARCH SIGNIFICANCE

This paper demonstrates a four-step framework to predict the mechanical response of cementitious composites using the outputs of thermodynamic modeling. Thermodynamic modeling is used to predict the reaction products, and a PPM predicts the porosity and pore volumes. This is used to predict the mechanical properties of the paste using property-porosity relationships and scaled to mortar and concrete using a finite element model (FEM). This approach considers the binder chemistry and pore volumes to predict concrete's mechanical properties. The FEM approach considers the natural variability in the cementitious matrix and aggregate shape and distribution.

MODELING FRAMEWORK

The modeling framework developed to predict the mechanical and fracture characteristics of cement paste and mortar in this paper consists of four parts and is shown in Fig. 1. First, the chemical composition of the cementitious binder and mass fraction of the constituents are combined with a thermodynamic modeling framework (that includes kinetics) to predict the reaction products of OPC and OPC + SCM pastes.[32-34,59,60] Next, the PPM is used to predict the paste porosity and volumes of different sizes of pores (gel and capillary pores).[38,39] The predicted pore volumes are then used as inputs to a property-porosity model[61,62] to predict the elastic modulus (E_p) and fracture energy (G_p^c) of the paste. The E_p and G_p^c are used to calculate the tensile strength of the paste (f_{tp}') using the concepts of linear-elastic fracture mechanics (LEFM). The E_p, G_p^c, and f_{tp}' are then used as inputs to an FEM to predict the mechanical and fracture behavior of mortar.

Thermodynamic model

Thermodynamic calculations are used to predict the volumes and compositions of the reaction products that form when cement paste hydrates. In this work, the GEMS3K software[63] is used in conjunction with the default PSI/Nagra database and the CemData v18.01 database[32] to predict the reaction products that form. This approach has been extensively validated and shown to accurately predict the reaction products of OPC and OPC + SCM systems.[32-34,63-65] While all possible phases that can form in cementitious binder systems are available in this database, the formation of siliceous hydrogarnet, carbonate-ettringite, and OH-hydrotalcite are blocked from forming based on evidence from the literature that these phases are unlikely to form in significant quantities at the time frames chosen in this study.[38,40] The H/S of the C-S-H formed in the simulations was also corrected based on recent experimental evidence.[32,65]

Thermodynamic modeling allows for calculating the products of the cementitious and pozzolanic reactions at thermodynamic equilibrium (that is, at an infinite time). However,

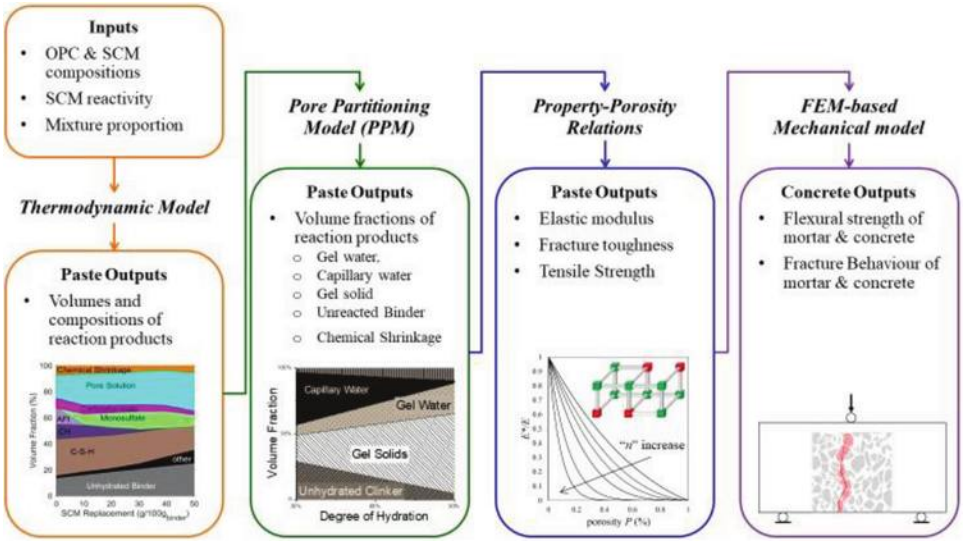

Fig. 1—Four-step modeling framework proposed consists of: (a) thermodynamic model; (b) pore partitioning model (PPM); (c) property-porosity relations; and (d) finite element model.

most cementitious systems are studied at a finite time and have not yet reached thermodynamic equilibrium. Kinetic models are often used in conjunction with thermodynamic models to predict the results of thermodynamic models at a given time. In this work, the modified Parrot-Killoh model[66] is used to calculate the degree of hydration (DOH) of the cement clinker phases (C_3S, C_2S, C_3A, and C_4AF) at a given age (denoted as DOR_{ph}), which is the mass fraction of the clinker phase available to react at a given time. The mass fraction of minor oxides in the cement (Na_2O, K_2O, MgO, and SO_3) is determined from the degree of clinker hydration following the method outlined in Taylor.[67] The DOH of the system at a given age is the mass normalized DOR_{ph} of the four clinker phases.

Pore partitioning model

Thermodynamic modeling can only provide the total amount of liquid water in the OPC paste after the hydration reaction occurs. Recent works[38-40] have shown that thermodynamic models can be synergistically combined with the concepts of the Powers-Brownyard model[68] using a PPM to calculate the volume fraction of gel solids, gel pores (pores less than 5 nm in size[40]), capillary pores (pores between 5 nm and a few μm in size[40]), and pores due to chemical shrinkage that are present in the OPC systems. The PPM has been successfully used to predict the porosity and pore volumes of OPC pastes.[38] The PPM has been extended to OPC mortar and concrete materials to predict the total porosity and several porosity-related performance properties using a pore partitioning model for concrete (PPMC).[17,40]

The total porosity of the paste (ϕ_p in vol. %) is calculated as the sum of the volume fractions of gel water (v_{gw}), capillary water (v_{cw}), and pores due to chemical shrinkage (v_{cs}), as shown in Eq. (1)

$$\phi_p = v_{gw} + v_{cw} + v_{cs} \tag{1}$$

The porosity of the paste can be scaled up to calculate the porosity of the mortar system (ϕ_m) using the PPMC[17] using the volume fraction of paste in the mortar (V_p), the volume fraction of the air voids (V_{air}), and the volume fraction of aggregates (V_{agg}), as shown in Eq. (2)

$$\phi_m = V_p\phi_p + V_{air} + V_{agg}\phi_{agg} \tag{2}$$

where ϕ_{agg} is the porosity of the aggregate (in vol. % of the aggregate).

Property-porosity relations

The third step of the framework uses property-porosity relations to predict the mechanical properties of the paste—that is, E_p, $G_p{}^c$, and f_{tp}'. The pore volumes and distribution of hydration products are parameters that affect the mechanical and fracture properties.[69] A higher porosity in OPC systems typically means a lower load-carrying capacity due to the lower volume of hydrates. Pores can also act as stress concentration sites in the hydrated OPC paste and promote failure under loading by introducing microcracks. Hence, increasing the porosity of the paste reduces the material's elastic modulus, strength, and fracture energy.[70]

A model proposed by Jelitto and Schneider[61,62] that incorporates the porosity and the distribution of solids is used to predict the mechanical properties of the paste assuming an open porous microstructure (when all the pores are connected and some of the solid hydration products [the load-carrying phases] are connected, with some disconnections; refer to Fig. 3 in Jelitto and Schneider[61] for a schematic of the model).

The E_p and $G_p{}^c$ is calculated using Eq. (3) and (4), respectively

$$\frac{E_p}{E_p^{\phi=0}} = \left(\frac{1-d}{d^2} + \frac{1}{3d-2d^2}\right)^{-1}\left(1-\phi_p\right)^n \tag{3}$$

$$\frac{G_p^c}{G_p^{\phi=0}} = d^2\left(1-\phi_p\right)^n \tag{4}$$

where ϕ_p is the paste porosity (calculated using Eq. (1)); $E_p{}^{\phi=0}$ and $G_p{}^{\phi=0}$ are the elastic modulus and fracture energy of the paste at a hypothetical state of zero porosity; and d is a geometric parameter of the paste microstructure calculated using Eq. (5)

$$d = \cos\left(\frac{2\pi - \cos\left(2\phi_p - 1\right)^{-1}}{3}\right) + \frac{1}{2} \tag{5}$$

The values of $E_p{}^{\phi=0}$ are calculated using the rule of mixtures (using the series model to obtain the lower bound) and is calculated as shown in Eq. (6)

$$E_p^{\phi=0} = \frac{E_{gel}E_{ub}}{v'_{gel}E_{ub} + v'_{ub}E_{gel}} \tag{6}$$

where E_{gel} is the elastic modulus of the hydrated gel phase (considered to be 29.25 GPa[47]); E_{ub} is the elastic modulus of the unhydrated clinker grains (considered to be 139.90 GPa[47]); v_{ub}' is the volume of unhydrated clinker in the hypothetical zero-porosity system; and v_{gel}' is the volume of the gel phase in the hypothetical zero-porosity system. The values of v_{ub}' and v_{gel}' are calculated using Eq. (7) and (8), respectively

$$v'_{ub} = \frac{v_{ub}}{v_{ub} + v_{gw} + v_{gs}} \tag{7}$$

$$v'_{gel} = \frac{v_{gw} + v_{gs}}{v_{ub} + v_{gw} + v_{gs}} \tag{8}$$

The f_{tp}' can be computed assuming cement paste is an ideal brittle material with a single crack using Eq. (9).

$$f'_{tp} = \left(\frac{E_p \cdot G_p^c}{\pi a}\right)^{0.5} \tag{9}$$

where f_{tp}' is the strength of the paste; and a is half the internal crack length.

In general, LEFM can be considered as a good approximation for cementitious pastes when the crack size is larger than 1 mm.[71] However, for smaller-length scales, the Griffith equation tends to overestimate the flexural strength of ordinary cement paste.[71] As the crack length and representative volume decreases, the characteristic fracture length scale becomes relevant, and other considerations should be considered.[54] While in this work the initial crack size was calculated to be 0.3 mm from the ball-on-three-balls (B3B) experiments, a statistical approach is also used that takes into account the variability in the defect size and distribution of defects using a Weibull distribution of tensile strength and fracture energy in the finite element analysis (FEA) model.

FEA-based mechanical model for heterogenous materials

In the fourth step, two-dimensional FEA models[54] are created to study the tensile strength development of mortar composites (refer to Fig. 1, block 4) using mechanical properties for the paste matrix determined from the previous step, along with the morphological and mechanical characteristics of the aggregate and interfacial transition zone (ITZ). This model integrates a continuum-based finite element approach and a bilinear cohesive zone model to predict the resulting tensile strength of mortar beams. The cohesive zone model introduces the nonlinear fracture mechanics concepts to the simulation to predict the fracture behavior of quasi-brittle materials,[72-74] representing a progressive damage zone behind the crack tip. The interface elements are inserted between the bulk elements to transfer the normal and tangential forces until debonding. For instance, a two-dimensional boundary value problem of the mortar representative volume element is shown in Fig. 2(a). Schematics of three sets of interface elements inserted within fine aggregate particles, the cement paste matrix, and their interface are shown in Fig. 2(b). The cohesive interface law describes the evolution of tensile and shear tractions in terms of both normal and tangential displacement jumps within interface elements.

The normal tensile and shear traction at the interface is determined from the cohesive interface law. The nodal forces in the plane of the element are computed from the known interface traction as $T' = \int_S N_S^T t dS$, where T' is the force vector (T_n and T_t); t is the computed interface traction vector (t_n and t_t); and N_s is the shape function vector; all quantities are defined in the local coordinates of the element. The cohesive law for interface elements is formulated in terms of normal and shear components of stresses $\sigma = (T_n, T_t)$ on the interface element and corresponding relative displacements $u = (u_n, u_t)$, shown in Fig. 2(c) and (d). A bilinear cohesive law in opening and shear modes is implemented using the finite element package Abaqus.[75] Readers are referred to Esmaeeli et al.[54] for further detailed information on the multiscale cohesive law development for cementitious systems. A Weibull strength distribution is used to account for: 1) the presence of preexisting defects in the material; and 2) the fact that these defects are smaller than 1 mm, and this is discussed in detail in the "Results and Discussion" section.

MODEL VALIDATION

This study uses the modeling framework of experiments to calibrate and validate the E_p, G_p^c, and f_{tp}' calculated using Eq. (3), (4), and (9), and the tensile strength of mortar (f_{tm}') predicted by the FEM. The E_p, f_{tp}', and f_{tm}' were measured experimentally for OPC pastes and mortars across a wide range of porosities. Experimental data from the literature was also used to validate the model predictions for E_p and G_p^c. Five paste and one mortar samples are prepared for each target porosity. Table 1 depicts the mixture proportions for paste and mortar samples for each target paste porosity. Note that the water-binder ratio (w/b) and curing durations for the mixtures were selected using the outputs of the PPM to achieve a target porosity. A Type I/II cement was used (53% C_3S, 17% C_2S, 7% C_3A, 9% C_4AF, 0.62% Na_2O_{eq}, 3.8% MgO, 3% $CaCO_3$, and 2.8% SO_3).

Preparing paste cylinders

Five cylinders of 50 mm diameter and 100 mm length were cast to measure the E_p using ultrasonic pulse velocity (UPV) and f_{tp}' using the B3B test. The pastes were cast following a modified version of ASTM C305-20,[76] outlined in Bharadwaj et al.[40] and Fu and Weiss.[77] The cement was added to the mixing bowl and thoroughly dispersed by dry mixing in a vacuum mixer (203 mbar = 80% vacuum) at 300 rotations per minute (rpm) for 90 seconds. Next, water was added and the cement and water were mixed for 90 seconds at 300 rpm. The mixer was then stopped for a 15-second rest period, during which the material collected on the sides of the mixing bowl and paddle were scraped back into the bulk of the mixing bowl. After the rest period, the wet paste was then mixed for another 90 seconds at 400 rpm. After the mixing, the fresh paste was cast into polyurethane molds, vibrated to remove the air (care was taken to prevent excessive bleeding), and sealed using plastic film and duct tape to prevent the loss of moisture. The molds containing the fresh paste were rotated for 24 hours after casting to minimize bleeding. After 24 hours, the samples were double-bagged to prevent moisture loss and sealed-cured at 23 ± 2°C until the testing age.

Preparing mortar cylinders and prisms

The mortar was mixed following the procedure outlined in ASTM C305-20.[76] Natural river sand with a maximum size of 4.75 mm (passing No. 4 sieve) was used in this work. The sand had a specific gravity of 2.65 and an absorption capacity of 2.7%. More details about the sand can be found in Bharadwaj et al.[16] The sand was used in its saturated surface-dry state to not change the w/b of the mixture. The fresh mortar was placed in prism molds which were pre-coated with a release agent. For this study, prisms of 125 x 25 x 25 mm were cast. The mortar-filled molds were vibrated to minimize entrapped air within the sample, and care was taken to prevent excessive segregation. The molds were covered with plastic wrap to minimize evaporation and allowed to harden for 24 hours. After 24 hours, the prisms were demolded and cured in saturated lime solution until the testing age.

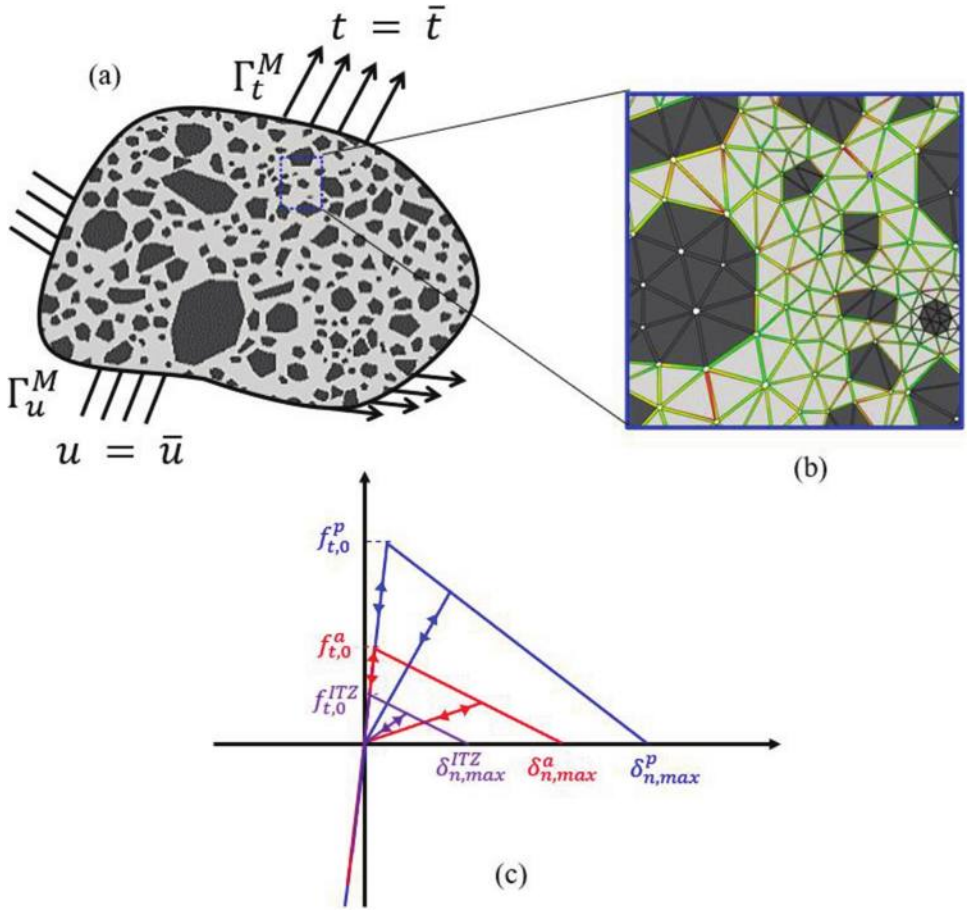

Fig. 2—Schematic representation of two-dimensional mesostructure of heterogeneous cementitious material: (a) under mixed-mode loading. This heterogeneous structure is composed of: (b) continuum bulk elements for paste and aggregate, and interface elements for paste, aggregate, and ITZ, with cohesive law defined in: (c) cohesive opening model.

Table 1—Mixture proportions of paste and mortar mixtures

Name	*w/b*	Target ϕ_p*	Curing time, days	Cement, kg/m^3	Water, kg/m^3	Sand, kg/m^3
Paste						
P-30	0.35	30%	56	1498	524	—
P-35	0.40	35%	56	1394	558	—
P-40	0.50	40%	56	1223	612	—
P-45	0.50	45%	10	1223	612	—
P-50	0.60	50%	10	1090	654	—
P-60	0.65	60%	3	1034	672	—
Mortar†						
M-45	0.50	45%	10	612	306	1361

*ϕ_p are rounded to nearest 5%.

†Mortar samples are 50% paste by volume.

Measurement of elastic modulus using UPV test

At the testing age, the cylinders were demolded and their ends were cut to ensure a flat surface to maximize contact with the UPV equipment. A UPV test kit was used to calculate the time it takes for an ultrasonic pulse to travel across the sample. The length of the sample was measured using vernier calipers, and the velocity of the sound wave through the sample (v_{pulse}) was determined by dividing the measured sample length with the measured pulse time. The elastic modulus of the material (E) was calculated using Eq. (10)[9]

$$E = v_{pulse}^2 \cdot \rho \left(\frac{(1+\upsilon)\cdot(1-2\upsilon)}{1-\upsilon} \right) \quad (10)$$

where ρ is the density of the material (calculated based on the mixture proportions); and υ is the Poisson's ratio of

the material (considered to be 0.29 for pastes and 0.20 for mortars from the literature[77,78]).

Measurement of strength using B3B test

The f_{tp}' was measured using the B3B test using 2.54 mm slices cut from the cylinders using a precision saw. The B3B test is an experimental approach for estimating the tensile strength of a thin disk-shaped sample loaded with the fourth ball from the top opposite the three balls.[77,79-82] Börger et al.[79] stated that this test is free of alignment errors with less than 2% characteristic error. It should be noted that the strength obtained by this is higher than that of beam tests, but this is likely due to size effects. Fu and Weiss[77] suggested that samples tested with an effective volume lower than 100 mm^3 for paste samples are unlikely to exhibit a size effect.

The tensile strength of paste material is determined by calculation of maximum principal stress at the center of the disk using Eq. (11)[77]

$$f_{tp}' = \frac{P_{max}}{t^2} \cdot \left[c_0 + \frac{c_1 + c_2 \frac{t}{R} + c_3 \left(\frac{t}{R}\right)^2 + c_4 \left(\frac{t}{R}\right)^3}{1 + c_5 \left(\frac{t}{R}\right)} \times \left(1 + c_6 \left(\frac{R_a}{R}\right)\right) \right] \tag{11}$$

where R is the radius of the disk (mm); R_a is the radial distance from the center of the disk to the center of the support balls (mm); and c_0 to c_6 are dimensionless constants which are functions of Poisson's ratio and Weibull modulus listed as follows: $c_0 = -16.35$, $c_1 = 20.78$, $c_2 = 622.62$, $c_3 = -76.88$, $c_4 = 50.38$, $c_5 = 33.74$, and $c_6 = 0.06$.

Measurement of strength using three-point bending test

The tensile strength of the mortar prisms (f_{tm}') is measured using the three-point bending (3PB) test following the procedure in ASTM C78/C78M-21.[83] In this study, the tensile strength of one mortar mixture with a w/b of 0.50 cured for 10 days (target paste porosity of 45%) was measured experimentally. A beam of 25.4 mm depth x 25.4 mm width x 125 mm length was tested. The tensile strength of the sample is calculated based on the recorded peak load (P_{peak}), loading span (L), width (B), and thickness (D) of samples using Eq. (12)

$$f_{tm}' = \frac{3P_{peak} \cdot L}{2B \cdot D^2} \tag{12}$$

RESULTS AND DISCUSSION

Thermodynamic modeling and pore partitioning model

The first two steps of the framework proposed in this paper are the thermodynamic model and PPM, respectively. Figure 3(a) shows the output of the thermodynamic model (that is, volume fractions of reaction products) at the target porosity values. In general, an increase in the porosity is achieved by either an increase in the w/b or a decrease in the curing age (which translates to a lower overall DOH of the system). Therefore, systems with a higher porosity have a higher volume of pore solution in the system. The volume fraction of the reaction products is also lower in systems with a higher target porosity. The volume of unhydrated cement decreases as the water-cement ratio (w/c) increases at a given age due to an increase in the DOH at a given age (refer to porosity values of 30 to 40% and 45 to 50%). A decrease in the curing time at a given w/b results in the volume fraction of unhydrated cement increasing due to a lower DOH in systems cured for shorter durations (porosity values of 40 to 45% and 50 to 60%).

Figure 3(b) shows the Powers-Brownyard phases of the systems as a function of their target porosity. As the target porosity increases, the volume of capillary water increases as the increase in target porosity is achieved by increasing the w/b and/or reducing curing time. For the same reason, the volume of hydration products, gel solids, and gel pores decrease with increased target porosity.

Property-porosity relations

It is well-established that the pore network of cementitious materials is connected with disconnections existing between some portion of the pores[84] and some portion of the gel solids.[85,86] In the property-porosity relations used (refer to Eq. (3) and (4)), the parameter n is related to the disconnections in the gel solids phase and is estimated by fitting the equation to the experimental measurements of elastic modulus. The E_p obtained from the UPV test is the dynamic modulus, and the static modulus is obtained by scaling down the measured value of E_p by 0.75 based on experimental observations in Trifone[87]; however, it should be noted that the mechanical properties used in this paper are a normalized value (that is, $E_p/E_p^{\phi=0}$), so this scaling is only performed for the experimentally obtained E_p in Fig. 4. Figure 4(a) shows a plot of the model predicted (lines) and experimentally measured (markers) $E_p/E_p^{\phi=0}$ as a function of the paste porosity. From the model predictions, it is seen that an increase in porosity decreases the E_p as there is a higher volume of voids and a lower volume fraction of load-carrying gel solids. At a given porosity, an increase in the parameter n leads to a lower E_p as n indicates the disconnections in the load-bearing phase. In general, the experimental measurements follow the trend of the model predictions, and all but one data point lie within $n = 0.5 \pm 0.15$. The value of $n = 0.5$ is chosen for this work as it fits the experimental data to within 7%.

Figure 4(b) plots $G_p^c/G_p^{c\phi=0}$ as a function of porosity. An increase in porosity leads to a lower G_p^c due to a lower amount of solid material, and an increase in n leads to a lower G_p^c at a given porosity due to an increase in the disconnectivity in the solid phase. The predictions of G_p^c for the limited experimental data from the literature[88,89] is within 3% for $n = 0.5$, supporting the chosen value of n.

Figure 4(c) shows the model predicted f_{tp}' and the experimentally measured f_{tp}'. An increase in the porosity decreases the f_{tp}' as the voids in the paste increase. An increase in n decreases the f_{tp}' as the number of disconnections in the load-bearing hydrate phases increases. The predicted f_{tp}' is within

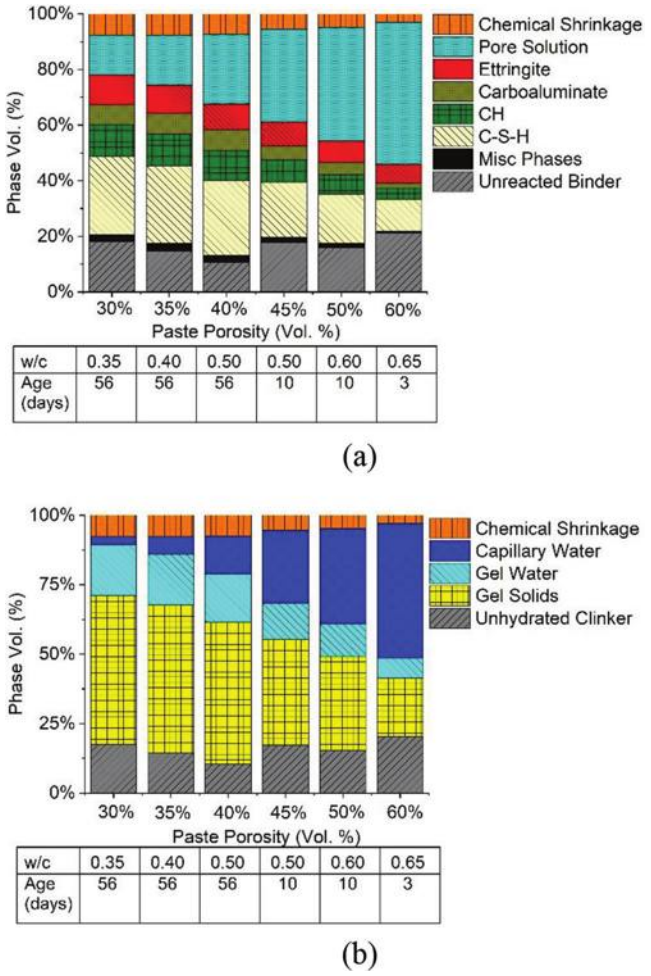

Fig. 3—Plots of: (a) reaction products; and (b) Powers-Brownyard phases as function of total porosity of paste. (Note: These plots are function of porosity as experiments were designed to capture behavior of property-porosity relations at wide range of porosities.)

2% for $n = 0.5$, supporting the chosen value of n. The deviation of the data point at $\phi_p = 60\%$ from the trend line is likely due to the high w/b and low curing age chosen, resulting in a larger disconnectivity in the load-bearing phases, resulting in a lower E_p and f_{tp}'.

Numerical predictions of mortar

Finite element model—The flexural strength of mortar (f_{tm}') is predicted using a finite element approach. A computational model of the 3PB test is created to predict the f_{tm}'. The boundary conditions are simulated as rigid rollers with frictionless contact between the rollers and the mortar beam (Fig. 5(a)). A plain strain condition is chosen for the model, and the load is applied directly by the top roller, which is subjected to a prescribed displacement (δ). It is considered that the fracture process takes place inside a representative volume element (RVE),[90] which contains the geometry and spatial distribution of different phases. In this study, the RVE contains three phases: cement paste, aggregate, and their ITZ. The mesostructure of the RVE is generated by scanning an optical image of a mortar sample and then importing it as a finite element mesh for the numerical analysis (refer to Fig. 5(b)). After generating the RVE, the cohesive interface elements are inserted into the model[54] (refer to Fig. 5(c) and (d)). To improve the computational efficiency, the RVE with cohesive interfacial elements is only embedded into the midspan of the mortar beam where the fracture process takes place. It is assumed that the region outside the RVE is free of inelastic deformation, damage, or cracks and is modelled as a continuum material representing the mortar with homogenized properties. To determine the size of the RVE and avoid boundary effects, an RVE size analysis is performed (refer to Appendix A* for details).

A Weibull distribution is employed in the FEM to account for the effect of preexisting cracks on the resulting f_{tm}' prediction. It is considered that the preexisting cracks only occur in cement paste and the ITZ and assumed that the aggregate is free of preexisting cracks (that is, f_{tp}', G_p^c, f_{tITZ}', and G_{ITZ}^c have variability in the model). The Weibull distribution for the f_{tp}' is given by Eq. (13),[91] and the form of the Weibull distribution for the other parameters is similar.

$$p\left(f_{tp}'\right) = \frac{m}{f_{tp}'}\left(\frac{f_{tp}}{f_{tp}'}\right)^{m-1} \exp\left[-\left(\frac{f_{tp}}{f_{tp}'}\right)^{m}\right] \tag{13}$$

where f_{tp}' is the nominal strength; and m is the Weibull modulus, which controls the shape of the distribution around f_{tp}'. The value of m for brittle materials, such as mortar and cement paste, can generally take a value between three and 10.[92,93] Figure 6(a) shows an example statistical histogram for the Weibull distribution of f_{tp}' with $m = 5$. Figure 6(b) shows an example where each cohesive element contains a different value of f_{tp} (represented by color map).

Determination of E, f_t', *and* G_c—As shown in Fig. 5(a), the region of the mortar prism outside the RVE is modeled as a continuum material. As such, the E, f_t', and G_c of the components of mortar (that is, the cement paste, aggregate, and the ITZ) need to be determined. For the cement paste, aggregate, and ITZ, the E for continuum elements, and the f_t' and G_c for cohesive elements need to be determined. The E_p, G_p^c, and f_{tp}' are calculated from the porosity-properties relations using the values of $n = 0.5$ and $n = 1$. The mechanical properties of the ITZ are difficult to characterize as they are affected by the aggregate surface roughness, aggregate types, and sample curing conditions.[94,95] Experimental results show that the ITZ is typically weaker than the cement paste.[96-100] As such, the f_{tITZ}' and G_{ITZ}^c are a fraction of the f_{tp}' and G_p^c. Following the literature,[96,97] the f_{tITZ}' is 25% of the f_{tp}', and the G_{ITZ}^c is 25% of the G_p^c. The E_{agg}, G_{agg}^c, and f_{tagg}' are obtained from Weiss et al.[98] Table 2 shows an example of the values of the mechanical properties that are used as inputs for the model for one system ($\phi_p = 30\%$). For the systems with other ϕ_p, the properties are obtained in a similar manner.

Influence of Weibull distribution on f_{tm}' *prediction*—After the mechanical properties of the cement paste are

*The Appendix is available at **www.concrete.org/publications** in PDF format, appended to the online version of the published paper. It is also available in hard copy from ACI headquarters for a fee equal to the cost of reproduction plus handling at the time of the request.

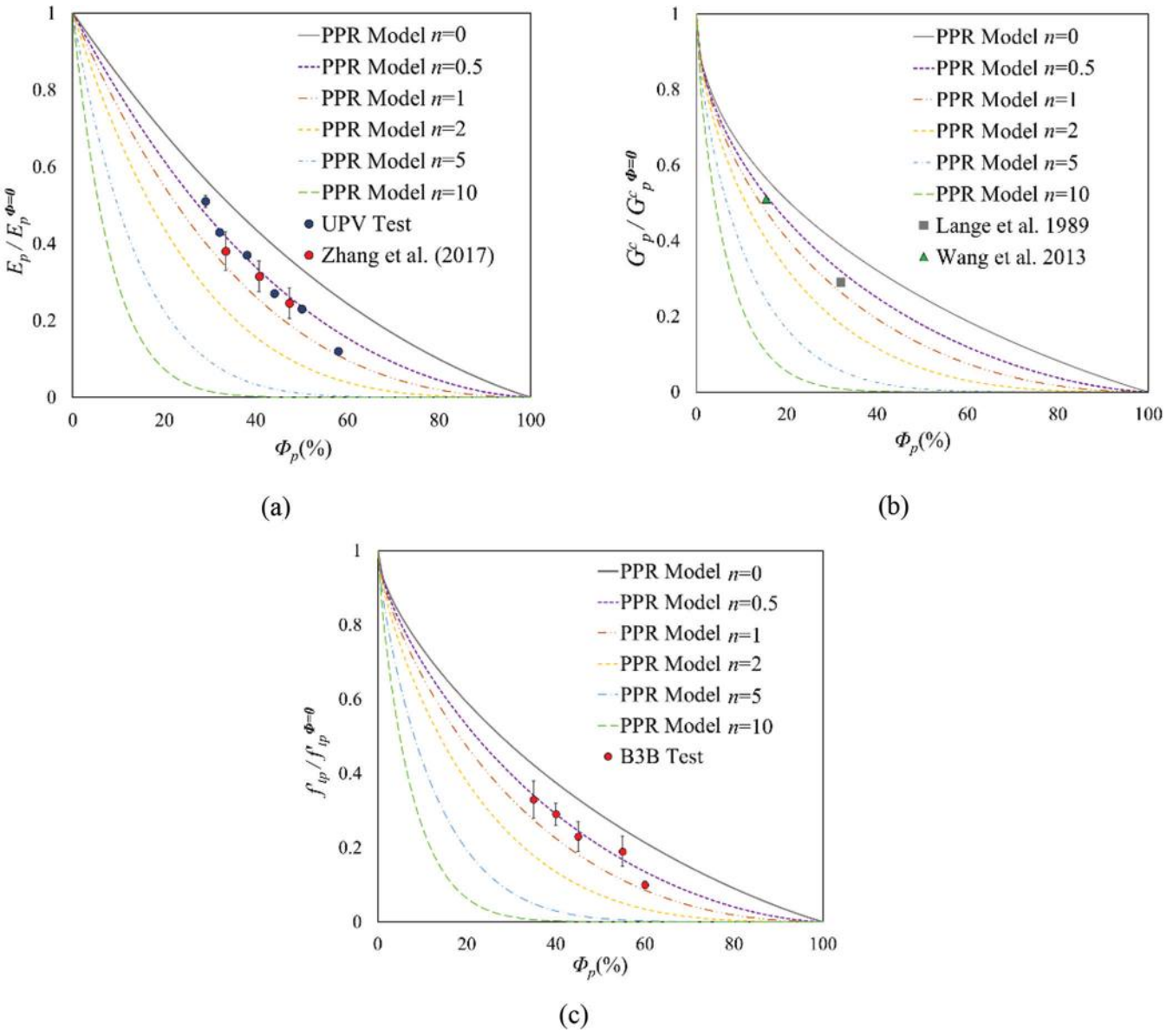

Fig. 4—(a) Elastic modulus; (b) fracture energy; and (c) tensile strength of paste as function of paste porosity.

determined, a Weibull distribution is applied to the cement paste and ITZ strength and fracture energy to represent mortar samples with the same material properties but with random distributions of preexisting cracks. Four models for beams (with dimensions of 25 x 25 x 125 mm^3) under a 3PB loading condition are developed with the same RVE, material properties (cement paste with ϕ_p = 30% and n = 1), and Weibull modulus m. The value of m is assumed to be the same for the paste and ITZ and is considered as 5 following Esmaeeli et al.[54] The only difference between these models is the distribution of preexisting cracks in the RVE obtained from Weibull distributions. Figure 7(a) presents the simulation results of flexural stress-deformation curves for these four models. Up to a displacement value of 0.057 mm, all the models overlap; however, the samples failed at different stresses due to the random distribution of preexisting cracks. The model predicts a f_{tm}' of 12.84 ± 0.50 MPa. From the 3PB experiment described in the previous section, the standard deviation in the measured flexural stress is 0.53 MPa, which is consistent with the numerical prediction. Only the standard deviation of the experimental results and model predictions are compared to validate the variation in the flexural strength prediction caused by the Weibull distribution; the average flexural strength will be discussed in a later section. From Figure 7(b), two crack patterns from the simulations are observed. Similar to the observations on the crack path in the experiment, the cracks propagate in different paths due to the random distribution of preexisting cracks. These consistencies between experiments and simulations support the validity of the model and indicate that m = 5 is appropriate for the f_{tm}' prediction.

Influence of aggregate shape and distribution on f_{tm}' *prediction*—Three beam models (with dimensions of 25 x 25 x 125 mm^3) are studied under 3PB loading conditions to study the influence of aggregate shape and distribution. Studying the influence of aggregate size and minerology on the fracture behavior is outside this paper's scope and can be found in Esmaeeli et al.[106] and Santos et al.[107] Studying the

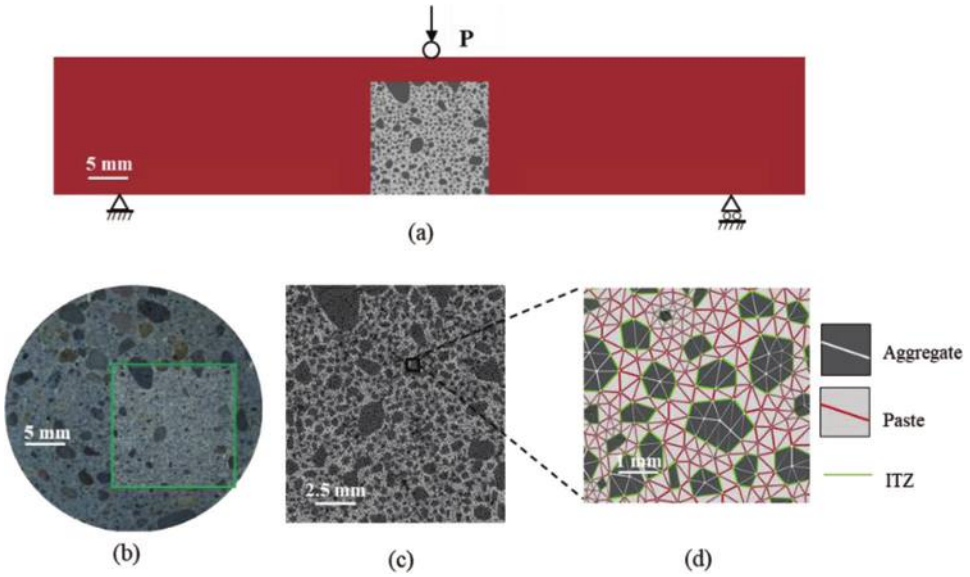

Fig. 5—(a) Schematic of FEM showing loading conditions for 3PB test; (b) optical image of mortar sample and digitized meso-structure of RVE (inset green box; length of white line indicates 5 mm); (c) RVE and FEM mesh; and (d) details of FEM mesh includes aggregates, paste, and ITZ between them. (Full-color PDF can be accessed at www.concrete.org.)

Table 2—Material properties of cement paste, ITZ, and aggregate

Properties	f_t', MPa	G_c, N/mm	E, GPa
Paste, ϕ_p = 30%, n = 0.5	29.4	0.051	26.9
Paste, ϕ_p = 30%, n = 1	24.6	0.045	23.9
ITZ, n = 0.5	7.3	0.013	—
ITZ, n = 1	6.1	0.011	—
Aggregate	9.8	0.120	65.2

applicability of the model with different aggregate mineralogies is scope for future work. The material properties (cement paste with ϕ_p = 30%, n = 1, and m = 5), RVE size (Appendix A), and aggregate volume fraction (Appendix B) are identical for the three beams. Four simulations for each RVE are performed with the same Weibull parameters to account for the random preexisting cracks (indicated by the standard deviation in the f_{tm}' predictions). Figure 8 shows the f_{tm}' predictions, RVEs, and crack patterns in the RVEs. The f_{tm}' predicted for RVE (No. 1), (No. 2), and (No. 3) (which represent three different aggregate shapes and distributions generated) are 12.84 ± 0.50 MPa, 13.49 ± 0.49 MPa, and 12.64 ± 0.64 MPa, respectively. The average f_{tm}' prediction for the three RVEs is 12.99 ± 0.44 MPa. The standard deviation of the experimentally measured f_{tm}' is 0.53 MPa, which is consistent with the numerical prediction. The comparison of the variability indicates that the variation of f_{tm}' prediction due to the different aggregates shape and spatial distribution is reasonable, and the f_{tm}' predictions remain within the margin of experimental accuracy.

f_{tm}' *prediction for mortar with different* ϕ_p—After determining material properties and validating the FEA model framework, the influences of porosity (ϕ_p) on the f_{tm}' predictions are studied. As mentioned in the previous section, 3PB experiments for mortar beams (25 x 25 x 125 mm^3 and ϕ_p = 45%) were conducted. A model for the same beam is

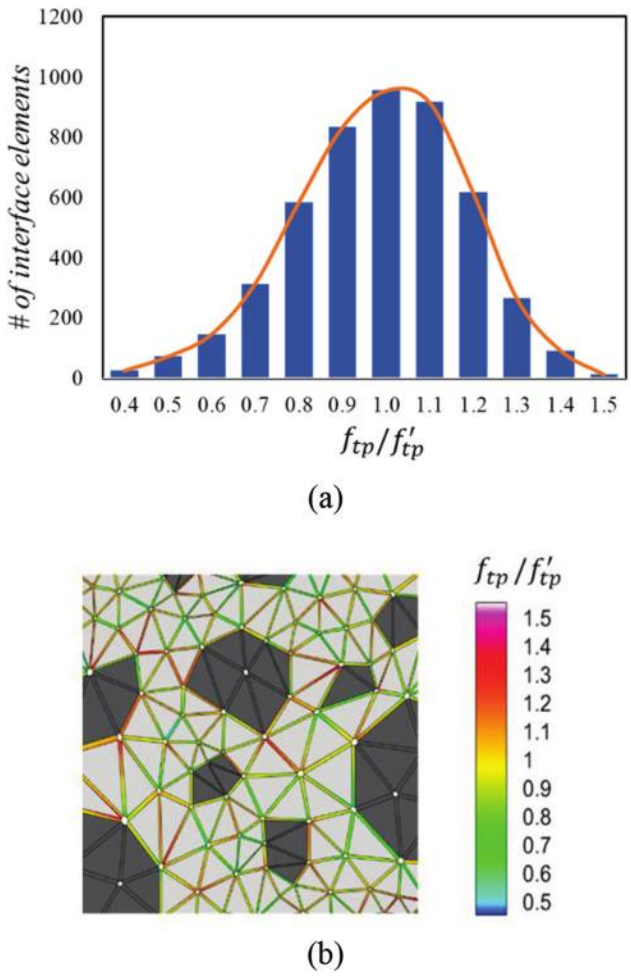

Fig. 6—(a) Histogram for Weibull distribution of f_{tp}' *(orange curve represents Eq. (13)); and (b) example of cohesive element strength distribution (triangular continuum elements were shrunk for illustration purposes). Color map represents* f_{tp}/f_{tp}' *values. (Full-color pdf can be accessed at www.concrete.org.)*

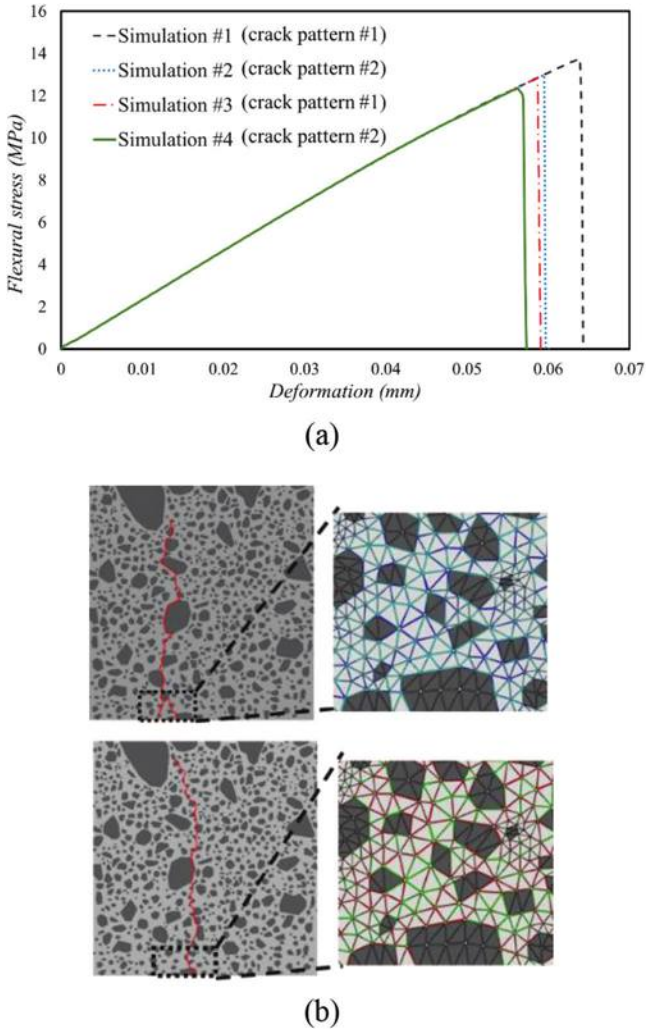

Fig. 7—(a) Simulation results of flexural stress versus deformation curves for samples with same material parameters but random distribution of preexisting cracks; and (b) two crack patterns due to random distribution of preexisting cracks. Color maps represent random distribution of preexisting cracks (crack pattern No. 1 on top; crack pattern No. 2 on bottom). (Full-color PDF can be accessed at www.concrete.org.)

developed to validate the f_{tm}' prediction. In addition, simulations for mortar beams with ϕ_p of 30, 39, and 55% are also performed to investigate the influence of ϕ_p on f_{tm}'. The model is run for two values of the disconnection parameter n ($n = 0.50$ and $n = 1$) to simulate the typically observed range of n in OPC pastes.

Figure 9 presents the f_{tm}' predictions and the experiment results for mortar beams with different ϕ_p. The measured f_{tm}' at $\phi_p = 45\%$ is 8.44 ± 0.53 MPa and the f_{tm}' predicted by the model is 9.69 ± 0.21 MPa (for $n = 0.5$). The range of experimental f_{tm}' (7.72 to 9.43 MPa) lies within the experimental margin of error (±1.5 MPa) to the model predicted f_{tm}' (9.33 to 9.87 MPa). Two data points from the literature[101,102] are also plotted. The data point at $\phi_p = 52\% \pm 2\%$ is closer to the $n = 1$ model curve, likely due to the early age of testing (3 days), resulting in a higher n. From the f_{tm}' predictions results, it can be observed that as the ϕ_p of the

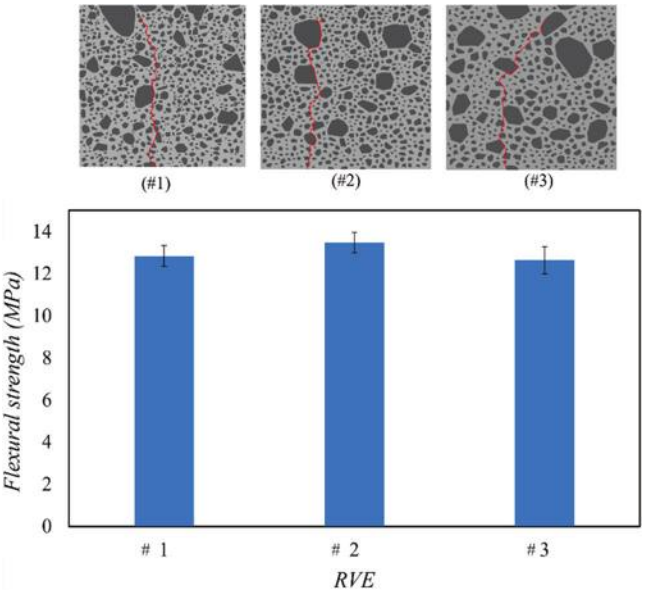

Fig. 8—Flexural strength predictions and crack patterns from three RVEs with different aggregate shape and distribution.

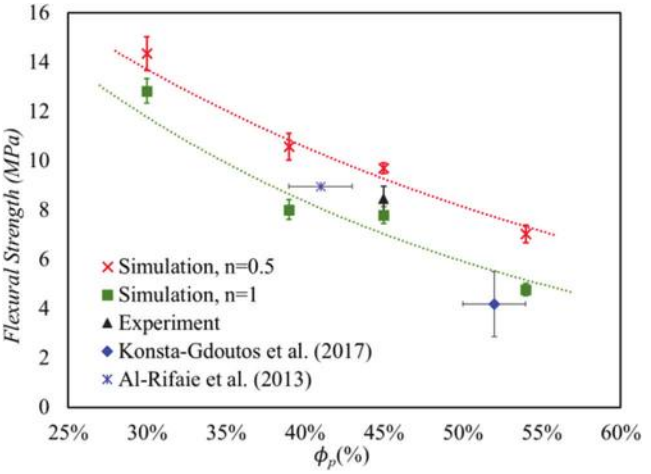

Fig. 9—Experiment and simulation results for mortar beams with different ϕ_p; red and greed dashed lines are trend lines of simulation predictions with two values of disconnection parameter n *(*n *= 0.50 and* n *= 1). (Note: Trend lines are intended to be visual guides; full-color PDF can be accessed at www.concrete.org.)*

mortar increases, the f_{tm}' of the mortar decreases, which is consistent with results from the literature.[99,103] The results suggest that the modeling can capture the influence of paste porosity (predicted from thermodynamic modeling) on the f_{tm}' development. The data to support each step of the model is in the typical range of ϕ_p seen in concrete (30 to 55%) and obtaining data beyond this range is scope for future work.

CONCLUSIONS

This paper described a four-step approach to predict the mechanical response of ordinary portland cement (OPC) systems. The first step in this process is the use of a thermodynamic model to predict the reaction products of the hydration reaction. The second step is using the results of

thermodynamic modeling as inputs to using a pore partitioning model (PPM) to predict the porosity and pore volumes (volumes of gel pores, capillary pores, and pores due to chemical shrinkage) in the hydrated paste. The third step calculates property-porosity relations to predict the mechanical properties of the paste—that is, the E_p, G_p^c, and f_{tp}' as a function of the porosity. The disconnections in the hydrated gel solids (that is, the n value) is calibrated using experimental data, and using the value of n, the G_p^c and f_{tp}' are predicted. The fourth step in this paper is the use of finite element models (FEMs) to predict the mechanical behavior of mortars made with the OPC using the mechanical properties of the paste (from step 3) as the inputs. The model is run for two values of the disconnection parameter n (n = 0.50 and n = 1) to simulate the typically observed range of n in OPC pastes; the model predictions (7.54 ± 0.35 MPa to 9.69 ± 0.21 MPa) are similar to the experimental measurements (8.44 ± 0.53 MPa) for the mortar beam with ϕ_p = 45%, within the margin of experimental error. This four-step approach natively considers the binder chemistry to predict the mechanical response of cementitious pastes and concrete. It can be coupled with a performance-based mixture design framework[8] to natively predict the concrete's flexural strength. Overall, this work is a step toward self-sufficient models that predict concrete performance,[45] which can be used as tools to better design low-carbon concrete.

AUTHOR BIOS

ACI member **Yu Wang** *is a PhD Student in the Lyles School of Civil Engineering at Purdue University, West Lafayette, IN. He received his BS in hydraulic and hydropower engineering from Northwest A&F University, Xianyang, Shaanxi, China, and his MS in civil engineering from Northwestern University, Evanston, IL. His research interests include multi-scale concrete numerical simulations, fiber-reinforced cementitious composite, and architected cement-based material for three-dimensional (3-D) printing.*

ACI member **Keshav Bharadwaj** *is a Postdoctoral Scholar at Oregon State University, Corvallis, OR, where he also received his PhD in civil engineering. His research interests include thermodynamic modeling, reactivity, transport in cementitious systems, and linking the microstructure of concrete to the engineering performance of concrete.*

Hadi S. Esmaeeli *performed this work as a Postdoctoral Researcher at Purdue University, where he also received his PhD. His research interests include bio-inspired design and development of architected materials using novel additive manufacturing processes, and automated robotic technologies for applications in civil infrastructures.*

Pablo D. Zavattieri *is the Jerry M. and Lynda T. Engelhardt Professor in Civil Engineering at Purdue University, where he also received his PhD. His research interests include the interface between solid mechanics and materials engineering, and bio-inspired and architected materials.*

O. Burkan Isgor, *FACI, is a Professor in the School of Civil and Construction Engineering at Oregon State University. He is Chair of ACI Committee 222, Corrosion of Metals in Concrete, and a member of ACI Committees 236, Material Science of Concrete; and 365, Service Life Prediction. His research interests include corrosion of steel in concrete, service-life modeling, and nondestructive testing.*

W. Jason Weiss, *FACI, is the Edwards Distinguished Professor of Engineering in the School of Civil and Construction Engineering at Oregon State University. He is Editor in Chief of the* ACI Materials Journal *and a Member of the ACI Board of Direction.*

ACKNOWLEDGMENTS

The authors gratefully acknowledge the financial support provided by ARPA-E (Advanced Research Projects Agency-Energy), the Federal Highway Administration (FHWA), and the National Science Foundation (Grant No. NSF CMMI 1728358). The authors gratefully acknowledge support from the Edwards Distinguished Chair at Oregon State University. The authors also acknowledge fruitful discussions with Dr. J. King of the Advanced Research Projects Agency, Department of Energy, USA.

REFERENCES

1. UN Environment, Scrivener, K. L.; John, V. M.; and Gartner, E. M., "Eco-Efficient Cements: Potential Economically Viable Solutions for a Low-CO_2 Cement-Based Materials Industry," *Cement and Concrete Research*, V. 114, 2018, pp. 2-26. doi: 10.1016/j.cemconres.2018.03.015

2. Miller, S. A.; John, V. M.; Pacca, S. A.; and Horvath, A., "Carbon Dioxide Reduction Potential in the Global Cement Industry By 2050," *Cement and Concrete Research*, V. 114, 2018, pp. 115-124. doi: 10.1016/j.cemconres.2017.08.026

3. Juenger, M.; Provis, J. L.; Elsen, J.; Matthes, W.; Hooton, R. D.; Duchesne, J.; Courard, L.; He, H.; Michel, F.; Snellings, R.; and De Belie, N., "Supplementary Cementitious Materials for Concrete: Characterization Needs," *MRS Online Proceedings Library*, V. 1488, 2012, pp. 8-22.

4. Juenger, M. C. G.; Winnefeld, F.; Provis, J. L.; and Ideker, J. H., "Advances in Alternative Cementitious Binders," *Cement and Concrete Research*, V. 41, No. 12, 2011, pp. 1232-1243. doi: 10.1016/j.cemconres.2010.11.012

5. Juenger, M. C. G.; Snellings, R.; and Bernal, S. A., "Supplementary Cementitious Materials: New Sources, Characterization, and Performance Insights," *Cement and Concrete Research*, V. 122, 2019, pp. 257-273. doi: 10.1016/j.cemconres.2019.05.008

6. Lothenbach, B.; Scrivener, K.; and Hooton, R. D., "Supplementary Cementitious Materials," *Cement and Concrete Research*, V. 41, No. 12, 2011, pp. 1244-1256. doi: 10.1016/j.cemconres.2010.12.001

7. Tennis, P. D.; Thomas, M. D. A.; and Weiss, W. J., "State-of-the-Art Report on Use of Limestone in Cements at Levels of Up to 15%," PCA R&D SN3148, Portland Cement Association, Skokie, IL, 2011, 78 pp.

8. Bharadwaj, K.; Isgor, O. B.; Weiss, J. W.; Chopperla, K. S. T.; Choudhary, A.; Vasudevan, G. D.; Glosser, D.; Ideker, J. H.; and Trejo, D., "A New Mixture Proportioning Method for Performance-Based Concrete," *ACI Materials Journal*, V. 119, No. 2, Mar. 2022, pp. 207-220.

9. Mehta, P. K., and Monteiro, P. J. M., *Concrete: Microstructure, Properties, and Materials*, McGraw Hill, New York, 2006, 684 pp.

10. Mindess, S.; Young, J. F.; and Darwin, D., *Concrete*, second edition, Pearson Education, Inc., Hoboken, NJ, 2003, 657 pp.

11. de Larrard, F., *Concrete Mixture Proportioning: A Scientific Approach*, CRC Press, New York, 1999, 448 pp.

12. ACI Committee 211, "Standard Practice for Selecting Proportions for Normal, Heavyweight, and Mass Concrete (ACI 211.1-91) (Reapproved 2009)," American Concrete Institute, Farmington Hills, MI, 1991, 38 pp.

13. Thomas, M., "Optimizing the Use of Fly Ash in Concrete," Publication IS548, Portland Cement Association, Skokie, IL, 2007, 24 pp.

14. Thomas M., *Supplementary Cementing Materials in Concrete*, CRC Press, Boca Raton, FL, 2013, 210 pp.

15. Zajac, M.; Skocek, J.; Adu-Amankwah, S.; Black, L.; and Haha, M. B., "Impact of Microstructure on the Performance of Composite Cements: Why Higher Total Porosity Can Result in Higher Strength," *Cement and Concrete Composites*, V. 90, 2018, pp. 178-192. doi: 10.1016/j.cemconcomp.2018.03.023

16. Bharadwaj, K.; Chopperla, K. S. T.; Choudhary, A.; Glosser, D.; Ghantous, R. M.; Vasudevan, G. D.; Ideker, J. H.; Isgor, O. B.; Trejo, D.; and Weiss, W. J., "CALTRANS: Impact of the Use of Portland-Limestone Cement on Concrete Performance as Plain or Reinforced Material - Final Report," Oregon State University, Corvallis, OR, 2021, 320 pp., https://ir.library.oregonstate.edu/concern/articles/7h149x67f. (last accessed Feb. 16, 2023)

17. Bharadwaj, K.; Glosser, D.; Moradllo, M. K.; Isgor, O. B.; and Weiss, W. J., "Toward the Prediction of Pore Volumes and Freeze-Thaw Performance of Concrete Using Thermodynamic Modelling," *Cement and Concrete Research*, V. 124, 2019, Article No. 105820. doi: 10.1016/j.cemconres.2019.105820

18. Lam, L.; Wong, Y.; and Poon, C. S., "Degree of Hydration and Gel/Space Ratio of High-Volume Fly Ash/Cement Systems," *Cement and Concrete Research*, V. 30, No. 5, 2000, pp. 747-756. doi: 10.1016/S0008-8846(00)00213-1

19. American Coal Ash Association, "Ash at Work: Applications, Science, and Sustainability of Coal Ash," Farmington Hills, MI, 2020, 199 pp.

20. Isgor, O. B.; Ideker, J.; Trejo, D.; Weiss, J. W.; Bharadwaj, K.; Choudhary, A.; Teja, C. K. S.; Glosser, D.; and Vasudevan, G., "Development of a Performance-Based Mixture Proportioning Procedure for Concrete

Incorporating Off-Spec Fly Ash," Report No. 000000003002018795, Energy Power Research Institute (EPRI), Palo Alto, CA, 2020, 78 pp.

21. Bahurudeen, A.; Kanraj, D.; Dev, V. G.; and Santhanam, M., "Performance Evaluation of Sugarcane Bagasse Ash Blended Cement in Concrete," *Cement and Concrete Composites*, V. 59, 2015, pp. 77-88. doi: 10.1016/j.cemconcomp.2015.03.004

22. Bahurudeen, A.; Marckson, A. V.; Kishore, A.; and Santhanam, M., "Development of Sugarcane Bagasse Ash Based Portland Pozzolana Cement and Evaluation of Compatibility With Superplasticizers," *Construction and Building Materials*, V. 68, 2014, pp. 465-475. doi: 10.1016/j.conbuildmat.2014.07.013

23. Bahurudeen, A., and Santhanam, M., "Influence of Different Processing Methods on the Pozzolanic Performance of Sugarcane Bagasse Ash," *Cement and Concrete Composites*, V. 56, 2015, pp. 32-45. doi: 10.1016/j.cemconcomp.2014.11.002

24. Clavier, K. A.; Paris, J. M.; Ferraro, C. C.; and Townsend, T. G., "Opportunities and Challenges Associated With Using Municipal Waste Incineration Ash as a Raw Ingredient in Cement Production–A Review," *Resources, Conservation and Recycling*, V. 160, 2020, Article No. 104888. doi: 10.1016/j.resconrec.2020.104888

25. Hogan, F. J., and Meusel, J. W., "Evaluation for Durability and Strength Development of a Ground Granulated Blast Furnace Slag," *Cement, Concrete and Aggregates*, V. 3, No. 1, 1981, pp. 40-52. doi: 10.1520/CCA10201J

26. Seraj, S.; Cano, R.; Ferron, R. D.; and Juenger, M. C. G., "The Role of Particle Size on the Performance of Pumice as a Supplementary Cementitious Material," *Cement and Concrete Composites*, V. 80, 2017, pp. 135-142. doi: 10.1016/j.cemconcomp.2017.03.009

27. Diaz-Loya, I.; Juenger, M.; Seraj, S.; and Minkara, R., "Extending Supplementary Cementitious Material Resources: Reclaimed and Remediated Fly Ash and Natural Pozzolans," *Cement and Concrete Composites*, V. 101, 2019, pp. 44-51. doi: 10.1016/j.cemconcomp.2017.06.011

28. Kalina, R. D.; Al-Shmaisani, S.; Ferron, R. D.; and Juenger, M. C. G., "False Positives in ASTM C618 Specifications for Natural Pozzolans," *ACI Materials Journal*, V. 116, No. 1, Jan. 2019, pp. 165-172. doi: 10.14359/51712243

29. Seraj, S., "Evaluating Natural Pozzolans for Use as Alternative Supplementary Cementitious Materials in Concrete," PhD thesis, The University of Texas at Austin, Austin, TX, 2014, 176 pp.

30. Kulik, D. A.; Miron, G. D.; and Lothenbach, B., "A Structurally-Consistent CASH+ Sublattice Solid Solution Model For Fully Hydrated C-S-H Phases: Thermodynamic Basis, Methods, and Ca-Si-H_2O Core Sub-Model," *Cement and Concrete Research*, V. 151, 2022, Article No. 106585. doi: 10.1016/j.cemconres.2021.106585

31. Lothenbach, B., and Gruskovnjak, A., "Hydration of Alkali-Activated Slag: Thermodynamic Modelling," *Advances in Cement Research*, V. 19, No. 2, 2007, pp. 81-92. doi: 10.1680/adcr.2007.19.2.81

32. Lothenbach, B.; Kulik, D. A.; Matschei, T.; Balonis, M.; Baquerizo, L.; Dilnesa, B.; Miron, G. D.; and Myers, R. J., "Cemdata18: A Chemical Thermodynamic Database for Hydrated Portland Cements and Alkali-Activated Materials," *Cement and Concrete Research*, V. 115, 2019, pp. 472-506. doi: 10.1016/j.cemconres.2018.04.018

33. Lothenbach, B.; Matschei, T.; Möschner, G.; and Glasser, F. P., "Thermodynamic Modelling of the Effect of Temperature on the Hydration and Porosity of Portland Cement," *Cement and Concrete Research*, V. 38, No. 1, 2008, pp. 1-18. doi: 10.1016/j.cemconres.2007.08.017

34. Lothenbach, B., and Winnefeld, F., "Thermodynamic Modelling of the Hydration of Portland Cement," *Cement and Concrete Research*, V. 36, No. 2, 2006, pp. 209-226. doi: 10.1016/j.cemconres.2005.03.001

35. Lothenbach, B., and Zajac, M., "Application of Thermodynamic Modelling to Hydrated Cements," *Cement and Concrete Research*, V. 123, 2019, Article No. 105779.

36. Myers, R. J.; Bernal, S. A.; and Provis, J. L., "A Thermodynamic Model for C-(N-)A-S-H Gel: CNASH_ss. Derivation and Validation," *Cement and Concrete Research*, V. 66, 2014, pp. 27-47. doi: 10.1016/j.cemconres.2014.07.005

37. Myers, R. J.; Lothenbach, B.; Bernal, S. A.; and Provis, J. L., "Thermodynamic Modelling of Alkali-Activated Slag Cements," *Applied Geochemistry*, V. 61, 2015, pp. 233-247. doi: 10.1016/j.apgeochem.2015.06.006

38. Azad, V. J.; Suraneni, P.; Isgor, O.; and Weiss, W. J., "Interpreting the Pore Structure of Hydrating Cement Phases Through a Synergistic Use of the Powers-Brownyard Model, Hydration Kinetics, and Thermodynamic Calculations," *Advances in Civil Engineering Materials*, V. 6, No. 1, 2017, pp. 1-16.

39. Glosser, D.; Azad, V. J.; Suraneni, P.; Isgor, O. B.; and Weiss, W. J., "An Extension of the Powers-Brownyard Model to Pastes Containing Supplementary Cementitious Materials," *ACI Materials Journal*, V. 116, No. 5, Sept. 2019, pp. 205-216. doi: 10.14359/51714466

40. Bharadwaj, K.; Ghantous, R. M.; Sahan, F.; Isgor, O. B.; and Weiss, W. J., "Predicting Pore Volume, Compressive Strength, Pore Connectivity, and Formation Factor in Cementitious Pastes Containing Fly Ash," *Cement and Concrete Composites*, V. 122, 2021, Article No. 104113. doi: 10.1016/j.cemconcomp.2021.104113

41. Bharadwaj, K.; Ghantous, R. M.; Sahan, F. N.; Isgor, O. B.; and Weiss, W. J., "Toward the Prediction of Pore Volumes and Compressive Strength of Concrete Using Thermodynamic Modelling," 6th International Conference on Construction Materials, Fukuoka, Japan, 2020.

42. Bharadwaj, K.; Isgor, O. B.; and Weiss, W. J., "Interpretation of the Results of the Pozzolanic Reactivity Test for Supplementary Cementitious Materials: Insights From Thermodynamic Modeling," *Cement and Concrete Composites*, 2022. (in review)

43. Bharadwaj, K.; Isgor, O. B.; and Weiss, W. J., "A Simplified Approach to Determine the Pozzolanic Reactivity of Commercial Supplementary Cementitious Materials," *Concrete International*, V. 44, No. 1, Jan. 2022, pp. 27-32.

44. Suraneni, P., and Weiss, J., "Examining the Pozzolanicity of Supplementary Cementitious Materials Using Isothermal Calorimetry and Thermogravimetric Analysis," *Cement and Concrete Composites*, V. 83, 2017, pp. 273-278. doi: 10.1016/j.cemconcomp.2017.07.009

45. Isgor, O. B., and Weiss, W. J., "A Nearly Self-Sufficient Framework for Modelling Reactive-Transport Processes in Concrete," *Materials and Structures*, V. 52, No. 6, 2019, Article No. 130. doi: 10.1617/s11527-019-1422-1

46. Powers, T. C., "Structure and Physical Properties of Hardened Portland Cement Paste," *Journal of the American Ceramic Society*, V. 41, No. 1, 1958, pp. 1-6. doi: 10.1111/j.1151-2916.1958.tb13494.x

47. Pichler, B., and Hellmich, C., "Upscaling Quasi-Brittle Strength of Cement Paste and Mortar: A Multi-Scale Engineering Mechanics Model," *Cement and Concrete Research*, V. 41, No. 5, 2011, pp. 467-476. doi: 10.1016/j.cemconres.2011.01.010

48. Pichler, B.; Hellmich, C.; and Eberhardsteiner, J., "Spherical and Acicular Representation of Hydrates in a Micromechanical Model for Cement Paste: Prediction of Early-Age Elasticity and Strength," *Acta Mechanica*, V. 203, No. 3-4, 2009, pp. 137-162. doi: 10.1007/s00707-008-0007-9

49. Pichler, B.; Hellmich, C.; Eberhardsteiner, J.; Wasserbauer, J.; Termkhajornkit, P.; Barbarulo, R.; and Chanvillard, G., "The Counteracting Effects of Capillary Porosity and of Unhydrated Clinker Grains on the Macroscopic Strength of Hydrating Cement Paste–A Multiscale Model," *Mechanics and Physics of Creep, Shrinkage, and Durability of Concrete: A Tribute to Zdeněk P. Bažant*, U. Franz-Josef, J. M. Hamlin, and R. J.-M. Pellenq, eds., 2013, pp. 40-47.

50. Pichler, B.; Hellmich, C.; Eberhardsteiner, J.; Wasserbauer, J.; Termkhajornkit, P.; Barbarulo, R.; and Chanvillard, G., "Effect of Gel-Space Ratio and Microstructure on Strength of Hydrating Cementitious Materials: An Engineering Micromechanics Approach," *Cement and Concrete Research*, V. 45, 2013, pp. 55-68. doi: 10.1016/j.cemconres.2012.10.019

51. Termkhajornkit, P.; Vu, Q. H.; Barbarulo, R.; Daronnat, S.; and Chanvillard, G., "Dependence of Compressive Strength on Phase Assemblage in Cement Pastes: Beyond Gel–Space Ratio—Experimental Evidence and Micromechanical Modeling," *Cement and Concrete Research*, V. 56, 2014, pp. 1-11. doi: 10.1016/j.cemconres.2013.10.007

52. Principigallo, A.; Lura, P.; van Breugel, K.; and Levita, G., "Early Development of Properties in a Cement Paste: A Numerical and Experimental Study," *Cement and Concrete Research*, V. 33, No. 7, 2003, pp. 1013-1020. doi: 10.1016/S0008-8846(03)00002-4

53. Carpinteri, A., and Accornero, F., "Rotation Versus Curvature Fractal Scaling in Bending Failure," *Physical Mesomechanics*, V. 22, No. 1, 2019, pp. 46-51.

54. Esmaeeli, H. S.; Shishehbor, M.; Weiss, W. J.; and Zavattieri, P. D., "A Two-Step Multiscale Model to Predict Early Age Strength Development of Cementitious Composites Considering Competing Fracture Mechanisms," *Construction and Building Materials*, V. 208, 2019, pp. 577-600.

55. Bažant, Z. P., and Planas, J., *Fracture and Size Effect in Concrete and Other Quasibrittle Materials*, Taylor & Francis, New York, 2019, 640 pp.

56. Lilliu, G., and van Mier, J. G. M., "3D Lattice Type Fracture Model for Concrete," *Engineering Fracture Mechanics*, V. 70, No. 7-8, 2003, pp. 927-941. doi: 10.1016/S0013-7944(02)00158-3

57. Shah, S. P.; Swartz, S. E.; and Ouyang, C., *Fracture Mechanics of Concrete: Applications of Fracture Mechanics to Concrete, Rock and Other Quasi-Brittle Materials*, John Wiley & Sons, Inc., New York, 1995, 588 pp.

58. Wriggers, P., and Moftah, S. O., "Mesoscale Models for Concrete: Homogenisation and Damage Behaviour," *Finite Elements in Analysis and Design*, V. 42, No. 7, 2006, pp. 623-636. doi: 10.1016/j.finel.2005.11.008

59. Lothenbach, B.; Le Saout, G.; Gallucci, E.; and Scrivener, K., "Influence of Limestone on the Hydration of Portland Cements," *Cement and Concrete Research*, V. 38, No. 6, 2008, pp. 848-860. doi: 10.1016/j.cemconres.2008.01.002

60. Lothenbach, B.; Winnefeld, F.; Alder, C.; Wieland, E.; and Lunk, P., "Effect of Temperature on the Pore Solution, Microstructure and Hydration Products of Portland Cement Pastes," *Cement and Concrete Research*, V. 37, No. 4, 2007, pp. 483-491. doi: 10.1016/j.cemconres.2006.11.016

61. Jelitto, H., and Schneider, G. A., "A Geometric Model for the Fracture Toughness of Porous Materials," *Acta Materialia*, V. 151, 2018, pp. 443-453. doi: 10.1016/j.actamat.2018.03.018

62. Jelitto, H., and Schneider, G. A., "Fracture Toughness of Porous Materials–Experimental Methods and Data," *Data in Brief*, V. 23, 2019, Article No. 103709. doi: 10.1016/j.dib.2019.103709

63. Kulik, D. A.; Wagner, T.; Dmytrieva, S. V.; Kosakowski, G.; Hingerl, F. F.; Chudnenko, K. V.; and Berner, U. R., "GEM-Selektor Geochemical Modeling Package: Revised Algorithm and GEMS3K Numerical Kernel for Coupled Simulation Codes," *Computational Geosciences*, V. 17, No. 1, 2013, pp. 1-24.

64. Deschner, F.; Lothenbach, B.; Winnefeld, F.; and Neubauer, J., "Effect of Temperature on the Hydration of Portland Cement Blended With Siliceous Fly Ash," *Cement and Concrete Research*, V. 52, 2013, pp. 169-181. doi: 10.1016/j.cemconres.2013.07.006

65. Kulik, D. A., "Improving the Structural Consistency of C-S-H Solid Solution Thermodynamic Models," *Cement and Concrete Research*, V. 41, No. 5, 2011, pp. 477-495. doi: 10.1016/j.cemconres.2011.01.012

66. Glosser, D.; Suraneni, P.; Isgor, O. B.; and Weiss, W. J., "Estimating Reaction Kinetics of Cementitious Pastes Containing Fly Ash," *Cement and Concrete Composites*, V. 112, 2020, Article No. 103655. doi: 10.1016/j.cemconcomp.2020.103655

67. Taylor, H. F. W., *Cement Chemistry*, Thomas Telford, London, UK, 1997, 459 pp.

68. Powers, T. C., and Brownyard, T. L., "Studies of the Physical Properties of Hardened Portland Cement Paste," *ACI Journal Proceedings*, V. 43, No. 9, Nov. 1946, pp. 249-336.

69. Chandler, H. W.; Merchant, I. J.; Henderson, R. J.; and Macphee, D. E., "Enhanced Crack-Bridging by Unbonded Inclusions in a Brittle Matrix," *Journal of the European Ceramic Society*, V. 22, No. 1, 2002, pp. 129-134. doi: 10.1016/S0955-2219(01)00242-4

70. Liu, D.; Šavija, B.; Smith, G. E.; Flewitt, P. E. J.; Lowe, T.; and Schlangen, E., "Towards Understanding the Influence of Porosity on Mechanical and Fracture Behaviour of Quasi-Brittle Materials: Experiments and Modelling," *International Journal of Fracture*, V. 205, No. 1, 2017, pp. 57-72. doi: 10.1007/s10704-017-0181-7

71. Birchall, J. D.; Howard, A. J.; and Kendall, K., "Flexural Strength and Porosity Of Cements," *Nature*, V. 289, No. 5796, 1981, pp. 388-390. doi: 10.1038/289388a0

72. Dugdale, D. S., "Yielding of Steel Sheets Containing Slits," *Journal of the Mechanics and Physics of Solids*, V. 8, No. 2, 1960, pp. 100-104. doi: 10.1016/0022-5096(60)90013-2

73. Barenblatt, G. I., "The Mathematical Theory of Equilibrium Cracks in Brittle Fracture," *Advances in Applied Mechanics*, V. 7, 1962, pp. 55-129. doi: 10.1016/S0065-2156(08)70121-2

74. Hillerborg, A.; Modéer, M.; and Petersson, P.-E., "Analysis of Crack Formation and Crack Growth in Concrete by Means of Fracture Mechanics and Finite Elements," *Cement and Concrete Research*, V. 6, No. 6, 1976, pp. 773-781. doi: 10.1016/0008-8846(76)90007-7

75. Hibbit, H. D.; Karlsson, B.; and Sorensen, E., "Abaqus Analysis User's Manual," Version 6.12, Simulia, Providence, RI, 2012.

76. ASTM C305-20, "Standard Practice for Mechanical Mixing of Hydraulic Cement Pastes and Mortars of Plastic Consistency," ASTM International, West Conshohocken, PA, 2020, 3 pp.

77. Fu, T., and Weiss, W. J., "The Ball-On-Three-Ball (B3B) Test–Application to Cement Paste and Mortar," *Advances in Civil Engineering Materials*, V. 9, No. 1, 2020, pp. 128-142. doi: 10.1520/ACEM20180070

78. Swamy, R. N., "Dynamic Poisson's Ratio of Portland Cement Paste, Mortar and Concrete," *Cement and Concrete Research*, V. 1, No. 5, 1971, pp. 559-583. doi: 10.1016/0008-8846(71)90060-3

79. Börger, A.; Supancic, P.; and Danzer, R., "The Ball on Three Balls Test for Strength Testing of Brittle Discs: Stress Distribution in the Disc," *Journal of the European Ceramic Society*, V. 22, No. 9-10, 2002, pp. 1425-1436. doi: 10.1016/S0955-2219(01)00458-7

80. Erbektas, A. R.; Isgor, O. B.; and Weiss, J. W., "Comparison of Chemical and Biogenic Acid Attack on Concrete," *ACI Materials Journal*, V. 117, No. 1, Jan. 2020, pp. 255-264. doi: 10.14359/51720293

81. Fu, T.; Montes, F.; Suraneni, P.; Youngblood, J.; and Weiss, J., "The Influence of Cellulose Nanocrystals on the Hydration and Flexural Strength of Portland Cement Pastes," *Polymers*, V. 9, No. 9, 2017, Article No. 424. doi: 10.3390/polym9090424

82. Qiao, C.; Suraneni, P.; and Weiss, J., "Flexural Strength Reduction of Cement Pastes Exposed to $CaCl_2$ Solutions," *Cement and Concrete Composites*, V. 86, 2018, pp. 297-305. doi: 10.1016/j.cemconcomp.2017.11.021

83. ASTM C78/C78M-21, "Standard Test Method for Flexural Strength of Concrete (Using Simple Beam With Third-Point Loading)," ASTM International, West Conshohocken, PA, 2021, 5 pp.

84. Sant, G.; Bentz, D.; and Weiss, J., "Capillary Porosity Depercolation in Cement-Based Materials: Measurement Techniques and Factors Which Influence Their Interpretation," *Cement and Concrete Research*, V. 41, No. 8, 2011, pp. 854-864. doi: 10.1016/j.cemconres.2011.04.006

85. Bentz, D. P., and Garboczi, E. J., "A Digitized Simulation Model for Microstructural Development," *Ceramic Transactions*, V. 16, 1990, pp. 211-226.

86. Bentz, D. P., and Garboczi, E. J., "Percolation of Phases in a Three-Dimensional Cement Paste Microstructural Model," *Cement and Concrete Research*, V. 21, No. 2-3, 1991, pp. 325-344. doi: 10.1016/0008-8846(91)90014-9

87. Trifone, L., "A Study of the Correlation Between Static and Dynamic Modulus of Elasticity on Different Concrete Mixes," MS thesis, West Virginia University, Morgantown, WV, 2017, 105 pp.

88. Wang, B.; Han, Y.; and Liu, S., "Effect of Highly Dispersed Carbon Nanotubes on the Flexural Toughness of Cement-Based Composites," *Construction and Building Materials*, V. 46, 2013, pp. 8-12. doi: 10.1016/j.conbuildmat.2013.04.014

89. Lange, D. A.; Jennings, H. M.; and Shah, S. P., "The Influence of Pore Structure on the Properties of Cement Paste: Initial Observations about Research-In-Progress," *MRS Online Proceedings Library*, V. 137, 1988, pp. 47-54.

90. Nguyen, V. P.; Stroeven, M.; and Sluys, L. J., "Multiscale Continuous and Discontinuous Modeling of Heterogeneous Materials: A Review on Recent Developments," *Journal of Multiscale Modelling*, V. 03, No. 04, 2011, pp. 229-270. doi: 10.1142/S1756973711000509

91. Rim, J. E.; Zavattieri, P.; Juster, A.; and Espinosa, H. D., "Dimensional Analysis and Parametric Studies For Designing Artificial Nacre," *Journal of the Mechanical Behavior of Biomedical Materials*, V. 4, No. 2, 2011, pp. 190-211. doi: 10.1016/j.jmbbm.2010.11.006

92. Espinosa, H. D., and Zavattieri, P. D., "A Grain Level Model for the Study of Failure Initiation and Evolution in Polycrystalline Brittle Materials. Part I: Theory and Numerical Implementation," *Mechanics of Materials*, V. 35, No. 3-6, 2003, pp. 333-364. doi: 10.1016/S0167-6636(02)00285-5

93. Espinosa, H. D., and Zavattieri, P. D., "A Grain Level Model for the Study of Failure Initiation and Evolution in Polycrystalline Brittle Materials. Part II: Numerical Examples," *Mechanics of Materials*, V. 35, No. 3-6, 2003, pp. 365-394. doi: 10.1016/S0167-6636(02)00287-9

94. Qudoos, A.; Atta-ur-Rehman; Kim, H. G.; and Ryou, J.-S., "Influence of the Surface Roughness of Crushed Natural Aggregates on the Microhardness of the Interfacial Transition Zone of Concrete With Mineral Admixtures and Polymer Latex," *Construction and Building Materials*, V. 168, 2018, pp. 946-957. doi: 10.1016/j.conbuildmat.2018.02.205

95. Xiao, J.; Li, W.; Sun, Z.; Lange, D. A.; and Shah, S. P., "Properties of Interfacial Transition Zones in Recycled Aggregate Concrete Tested by Nanoindentation," *Cement and Concrete Composites*, V. 37, 2013, pp. 276-292. doi: 10.1016/j.cemconcomp.2013.01.006

96. Zimbelmann, R., "A Contribution to the Problem of Cement-Aggregate Bond," *Cement and Concrete Research*, V. 15, No. 5, 1985, pp. 801-808. doi: 10.1016/0008-8846(85)90146-2

97. Husem, M., "The Effects of Bond Strengths between Lightweight and Ordinary Aggregate-Mortar, Aggregate-Cement Paste on the Mechanical Properties of Concrete," *Materials Science and Engineering: A*, V. 363, No. 1-2, 2003, pp. 152-158. doi: 10.1016/S0921-5093(03)00595-1

98. Weiss, J.; Couch, J.; Pease, B.; Laugesen, P.; and Geiker, M., "Influence of Mechanically Induced Cracking on Chloride Ingress in Concrete," *Journal of Materials in Civil Engineering*, ASCE, V. 29, No. 9, 2017, p. 04017128. doi: 10.1061/(ASCE)MT.1943-5533.0001922

99. Chen, X.; Wu, S.; and Zhou, J., "Influence of Porosity on Compressive and Tensile Strength of Cement Mortar," *Construction and Building Materials*, V. 40, 2013, pp. 869-874. doi: 10.1016/j.conbuildmat.2012.11.072

100. Zhang, H.; Gan, Y.; Xu, Y.; Zhang, S.; Schlangen, E.; and Šavija, B., "Experimentally Informed Fracture Modelling of Interfacial Transition Zone at Micro-Scale," *Cement and Concrete Composites*, V. 104, 2019, Article No. 103383. doi: 10.1016/j.cemconcomp.2019.103383

101. Konsta-Gdoutos, M. S.; Batis, G.; Danoglidis, P. A.; Zacharopoulou, A. K.; Zacharopoulou, E. K.; Falara, M. G.; and Shah, S. P., "Effect of CNT and CNF Loading and Count on the Corrosion Resistance, Conductivity and Mechanical Properties of Nanomodified OPC Mortars," *Construction and Building Materials*, V. 147, 2017, pp. 48-57. doi: 10.1016/j.conbuildmat.2017.04.112

102. Al-Rifaie, W. N.; Mahdi, O. M.; and Ahmed, W. K., "Development of Nanocement Mortar as a Construction Material," *Advanced Materials Research*, V. 795, 2013, pp. 684-691. doi: 10.4028/www.scientific.net/AMR.795.684

103. Kumar, R., and Bhattacharjee, B., "Porosity, Pore Size Distribution and In Situ Strength of Concrete," *Cement and Concrete Research*, V. 33, No. 1, 2003, pp. 155-164. doi: 10.1016/S0008-8846(02)00942-0

104. Mondal, P.; Shah, S. P; and Marks, L. D., "Nanomechanical Properties of Interfacial Transition Zone in Concrete," *Nanotechnology in Construction 3: Proceedings of the NICOM3*, Z. Bittnar, P. J. M. Bartos, J. Němeček, V. Šmilauer, and J. Zeman, eds., Springer, Berlin, Germany, 2009, pp. 315-320. doi: 10.1007/978-3-642-00980-8_42

105. Jebli, M.; Jamin, F.; Malachanne, E.; Garcia-Diaz, E.; and El Youssoufi, M. S., "Experimental Characterization of Mechanical Properties of the Cement-Aggregate Interface in Concrete," *Construction and Building Materials*, V. 161, 2018, pp. 16-25. doi: 10.1016/j.conbuildmat.2017.11.100

106. Esmaeeli, H. S.; Shishehbor, M.; Weiss, W. J.; and Zavattieri, P. D., "A Two-Step Multiscale Model to Predict Early Age Strength Development of Cementitious Composites Considering Competing Fracture Mechanisms," *Construction and Building Materials*, V. 208, 2019, pp. 577-600. doi: 10.1016/j.conbuildmat.2019.02.134

107. Santos, A. R.; do Rosário Veiga, M.; Silva, A. S.; and de Brito, J., "Microstructure as a Critical Factor of Cement Mortars' Behaviour: The Effect of Aggregates' Properties," *Cement and Concrete Composites*, V. 111, 2020, Article No. 103628. doi: 10.1016/j.cemconcomp.2020.103628

REVIEWERS IN 2022

In 2022, the individuals listed on these pages served as technical reviewers of papers offered for publication in ACI periodicals. A special "thank you" to them for their voluntary assistance in helping ACI maintain the high quality of its publication program.

A, Selva Ganesa Moorthi
IIT Madras
Chennai, Tamil Nadu, India

A, Suresh Kumar
Kalasalingam Academy of Research and Education
Krishnan Kovil, Tamil Nadu, India

Abavisani, Iman
Semnan University
Sabzevar, Razavi Khorasan, Islamic Republic of Iran

Abbas, Aamer
Al-Mustansiriya University
Baghdad, Baghdad, Iraq

Abbas, Abdelgadir
Carleton University
Ottawa, ON, Canada

Abbas, Waleed A.
University of Technology
Baghdad, Baghdad, Iraq

Abbas, Zainab
Babylon, Iraq

Abbasnejadfard, Mostafa
International Institute of Earthquake Engineering and Seismology
Tehran, Islamic Republic of Iran

Abdalla, Hany
College of Technological Studies
Shuwaikh, Kuwait

Abdallah, Amr
University of Manitoba
Winnipeg, MB, Canada

AbdelAleem, Basem
St. John's, NL, Canada

Abd-Elfatah, Sahar
Higher Institute for Engineering and Technology
Alexandria, Egypt

Abdelgader, Hakim
Universityof Tripoli
Tripoli, State of Libya

AbdElLatef, Mohammed
Iowa State University
Ames, IA, United States

Abdellatef, Mohammed
University of New Mexico
Albuquerque, NM, United States

Abdel-Wahab, Noran
Houston, TX, United States

Abdullah, Ahmad
Aswan University
Sahary City, Aswan, Egypt

Abdullah, Saman
University of California, Los Angeles
Los Angeles, CA, United States

Abdul-Razzaq, Khattab
University of Diyala
Diyala, Iraq

Abed, Ziyad
University of Technology
Baghdad, Baghdad, Iraq

Abellan-García, Joaquin
Universidad del Norte
Barranquilla, Colombia

Abera, Yonatan
Dilla University
Dilla, Ethiopia

Abouhussien, Ahmed
GE-Hitachi Nuclear Energy International, LLC
Markham, ON, Canada

Abraham, Sarah Mariam
Birla Institute of Technology and Science Pilani
Pilani, Rajasthan, India

Abu Obeidah, Adi
Rutgers, The State University of New Jersey
Piscataway, NJ, United States

Abu Taqa, Ala
Qatar University
Doha, Qatar

Abu Yosef, Ali
Pivot Engineers
Austin, TX, United States

Abuzeid, Al-Tuhami
Badr for Consulting and Retrofitting
Nasr City, Ciro, Egypt

REVIEWERS IN 2022

Accornero, Federico
Politecnico di Torino
Torino, Italy

Acun, Bora
UBC Okanagan
Kelowna, BC, Canada

Adak, Dibyendu
National Institute of Technology Meghalaya
Shillong, Meghalaya, India

Adekunle, Saheed
King Fahd University of Petroleum and Minerals
Dhahran, Saudi Arabia

Adil, Goran
University of Missouri - Kansas City
Kansas City, MO, United States

Adinkrah-Appiah, Kwadwo
Sunyani Polytechnic
Sunyani, Ghana

Afif, Rahma
Damascus University Faculty of Civil Engineering
Damascus, Syrian Arab Republic

Aflakisamani, Mahdi
Université de Sherbrooke
Sherbrooke, QC, Canada

Agarwal, Pankaj
Indian Institute of Technology Roorkee
Roorkee, Uttarakhand, India

Aghamohammadi, Omid
Isfahan University of Technology
Isfahan, Islamic Republic of Iran

Aguayo, Federico
University of Washington Seattle Campus
Seattle, WA, United States

Ahani, Elshan
Tabriz, East Azerbaijan, Islamic Republic of Iran

Ahmad, Mohd Hilton
Universiti Tun Hussein Onn Malaysia
Batu Pahat, Johor, Malaysia

Ahmad, Subhan
Aligarh Muslim University Faculty of Engineering and Technology
Aligarh, Uttar Pradesh, India

Ahmadi, Jamal
Iran University of Science of Technology
Tehran, Tehran, Islamic Republic of Iran

Ahmed, Ehab A.
Toronto Metropolitan University
Toronto, ON, Canada

Ahmed, Mizan
University of Wollongong
Wollongong, NSW, Australia

Ahmed, Mshtaq
King Saud University
Riyadh, Riyadh, Saudi Arabia

Aire, Carlos
National Autonomous University of Mexico
Mexico City, DF, Mexico

Akakin, Tumer
Aggregate and Ready Mix Association of Minnesota
Eagan, MN, United States

Akalin, Ozlem
PLUSTECHNO Ltd.
Istanbul, Turkey

Akcay, Burcu
Kocaeli University
Kocaeli, Turkey

Akhlaghi, Alireza
Isfahan, Islamic Republic of Iran

Akkaya, Yildir
İstanbul Teknik Üniversitesi
Maslak, Sariyer, Istanbul, Turkey

Akkaya, Yilmaz
Istanbul Technical University
Maslak, Istanbul, Turkey

Al Mansouri, Omar
CSTB
Marne-la-Vallée, France

Alam, A.K.M. Jahangir
Bangladesh University of Engineering and Technology (BUET)
Dhaka, Bangladesh

Alam, Md Shah
University of Bahrain
Sakhir, Bahrain

Alapati, Prasanth
Georgia Institute of Technology College of Engineering
Atlanta, GA, United States

Al-Azzawi, Adel
Al-Nahrain University
Baghdad, Iraq

Al-Bahadli, Hussein
Najaf, Iraq

Aldemir, Alper
Hacettepe University
Ankara, Turkey

Aldwaik, Mais
Russeifa, Zarqa, Jordan

Al-Hadithi, Abdulkader
University of Anbar
Ramadi, Al-Anbar, Iraq

Al-Hamd, Rwayda Kh. S.
Baghdad, Iraq

Al-Harthy, Ali
Sultan Qaboos University
Al-Khaudh, Oman

Ali, Shehroze
University of Wollongong
Wollongong, NSW, Australia

Al-Jaberi, Zuhair
Missouri University of Science and Technology
Rolla, MO, United States

Al-Khafaji, Ali
Missouri University of Science and Technology
Rolla, MO, United States

Almasabha, Ghassan
The Hashemite University
Sahab, Amman, Jordan

Almbaidheen, khalil
Mapei SpA
Dubai, Dubai, United Arab Emirates

Almottiri, Falah
College of Technological Studies (PAAET)
Ardiya, Kuwait, Kuwait

Almuhsin, Bayrak
University of Technology
Karrada, Baghdad, Iraq

Alqam, Maha
The University of Jordan
Amman, Jordan

Al-Sadoon, Zaid
University of Sharjah College of Engineering
Sharjah, United Arab Emirates

Alseid, Bara'
The University of Jordan
Amman, Jordan

Al-Sodani, Khaled
University of Hafr Al Batin
Hafr Al Batin, Eastern Province, Saudi Arabia

Alsubari, Belal
Miami College of Henan University
Kaifeng, Henan, China

Al-Tameemi, Hussein
Adnan Menderes University
Aydin, Turkey

Al-Tarafany, Dhiaa
Al-Nahrain University
Baghdad, Baghdad, Iraq

Alyousif, Ahmed
Toronto Metropolitan University Faculty of Engineering and Architectural Science
Toronto, ON, Canada

Al-Zubaidi, Aseel
University of Technology
Baghdad, Baghdad, Iraq

Al-Zuheriy, Ahmed
University of Technology
Baghdad, Baghdad, Iraq

Andersson, Ronny
Höllviken, Sweden

Angst, Ueli
ETH Zurich
Zurich, Switzerland

Antommattei, Oscar
Austin, TX, United States

Antoni, Antoni
Petra Christian University
Surabaya, Indonesia

Antunes, Rodrigo
University of Florida
Gainesville, FL, United States

Anwari, Qareeb Ullah
NUST Institute of Civil Engineering
Islamabad, Islamabad, Pakistan

Arafa, Ahmed
Université de Sherbrooke
Sherbrooke, QC, Canada

Aras, Murat
Bilecik Şeyh Edebali University
Bilecik, Bilecik, Turkey

REVIEWERS IN 2022

Arce, Gabriel
Virginia Transportation Research Council
Charlottesville, VA, United States

Arfiadi, Yoyong
Universitas Atma Jaya Yogyakarta
Yogyakarta, DIY, Indonesia

Aristizabal-Ochoa, Jose
National University of Colombia
Medellín, Antioquia, Colombia

Arito, Philemon
University of Namibia
Ongwediva, Oshana, Namibia

Asadian, Alireza
Concordia University
Montréal, QC, Canada

Ashish, Deepankar Kumar
Yonsei University
Seodaemun-gu, Seoul, Republic of Korea

Ashrafy, Mohammad
Islamic Azad University – Arak Branch
Kermanshah, Islamic Republic of Iran

Assaad, Joseph
University of Balamand
Balamand, Lebanon

Assi, Lateef
Al-Mustaqbal University College
Hilla, Babylon, Iraq

Atea, Rafid
University of Kufa
Kufa, Najaf, Iraq

Attia Ahmed, Mohamed
Ain Shams University Faculty of Engineering
Cairo, Egypt

Attiogbe, Emmanuel
Discovery Bay, CA, United States

Attiyah, Ali
University of Kufa
Kufa, Iraq

Avci, Eyübhan
Bursa Teknik Üniversitesi
Bursa, Yıldırım, Turkey

Awida, Tarek
SQC International Consultants
Kuwait, Kuwait, Kuwait

Aydin, Ertug
Lefke Avrupa Üniversitesi
Lefke, Cyprus

Aykac, Sabahattin
Gazi University, Faculty of Engineering and Architecture
Ankara, Turkey

Azarijafari, Hessam
Massachusetts Institute of Technology
Cambridge, MA, United States

Azevedo, Antonio
Universidade do Porto Faculdade de Engenharia
Porto, Porto, Portugal

Aziminejad, Armin
Islamic Azad University Science and Research Branch
Tehran, Tehran, Islamic Republic of Iran

Aziz, Ali
Al-Mustansiriyah University-College of Engineering
Baghdad, Baghdad, Iraq

Aziz, Tariq
NED University of Engineering and Technology
Karachi, Sindh, Pakistan

B C, Gayana
National Institute of Technology Karnataka
Surathkal, Karnataka, India

B S, Shubhalakshmi
Dayananda Sagar College of Engineering
Bangalore, Karnataka, India

B S, Sindu
CSIR Structural Engineering Research Centre
Chennai, India

Bae, Baek Il
Hanyang Cyber University
Seoul, Seoul, Republic of Korea

Bahekar, Prasad
Visvesvaraya National Institute of Technology
Nagpur, Maharashtra, India

Bahij, Sifatullah
King Fahd University of Petroleum and Minerals
Dhahran, Dammam, Saudi Arabia

Bai, Shaoliang
Chongqing University
Chonqqing, China

Balouch, Sana
University of Dundee
Dundee, United Kingdom of Great Britain and Northern Ireland

Barbosa, Maria Teresa
Federal University of Juiz de Fora
Juiz de Fora, Brazil

Barboza, Aline
Universidade Federal de Alagoas
Maceió, Alagoas, Brazil

Barman, Manik
University of Minnesota Duluth
Duluth, MN, United States

Barragan, Bryan
BASF Construction Chemicals
Treviso, Treviso, Italy

Barreto, Matheus
University of the State of Minas Gerais
Divinópolis, Minas Gerais, Brazil

Bassuoni, Mohamed T.
University of Manitoba
Winnipeg, MB, Canada

Baty, James
Concrete Foundations Association
Mount Vernon, IA, United States

Bawono, Ali Aryo
TUMCREATE
Singapore, Singapore

Bayuaji, Ridho
Institut Teknologi epuluh Nopember
Surabaya, East Java, Indonesia

Bederina, Madani
Université Amar Telidji
Laghouat, Laghouat, Algeria

Beglarigale, Ahsanollah
Okan Üniversitesi
Istanbul, Turkey

Behnoud, Ali
Aurecon Australia Group Ltd. Sydney
Neutral Bay, NSW, Australia

Bektas, Fatih
Minnesota State University, Mankato
Mankato, MN, United States

Belleri, Andrea
University of Bergamo
Dalmine, Italy

Benliang, Liang
Shanghai, China

Benmokrane, Brahim
University of Sherbrooke
Sherbrooke, QC, Canada

Bernardo, Luis
University of Beira Interior
Covilhã, Portugal

Bettadapura, RaghuPrasad
Indian Institute of Science
Bangalore, Karnataka, India

Beyene, Mengesha
Turner-Fairbank Highway Research Center
McLean, VA, United States

Bharadwaj, Keshav
Oregon State University
Corvallis, OR, United States

Bhargava, Kapilesh
Bhabha Atomic Research Centre
Mumbai, Maharashtra, India

Bhattacharjee, Bishwajit
Indian Institute of Technology Delhi
New Delhi, Delhi, India

Bhogayata, Ankur
Marwadi Education Foundation's Group of Institutions
Rajkot, Gujarat, India

Bhojaraju, Chandrasekhar
St Joseph Engineering College
Mangalore, Karnataka, India

Bian, R. B.
Jiangsu Research Institute of Building Science
Nanjing, Jiangsu, China

Bilek, Vlastimil
ZPSV a.s.
Brno, Czech Republic

Bilisik, Kadir
Erciyes University
Kayseri, Central Anatolia, Turkey

Billah, Abu Hena
Lakehead University
Thunder Bay, ON, Canada

Binici, Baris
Middle East Technical University
Ankara, Turkey

Bisschop, Jan
University of Oslo
Oslo, Norway

REVIEWERS IN 2022

Blikharskyy, Yaroslav
Lviv Polytechnic National University
Lviv, Ukraine

Borzovič, Viktor
Slovak University of Technology in Bratislava, Faculty of Civil Engineering
Bratislava, Slovakia

Bouzid, Haytham
Université Ibn Khaldoun Tiaret
Tiaret, Algeria

Braestrup, Mikael
Ramboll Group A/S
Kobenhavn, Denmark

Brahma, Abdelmalek
Université Saad Dahlab Blida
Blida, Algeria

Brena, Sergio
University of Massachusetts Amherst
Amherst, MA, United States

Bujnak, Jan
Peikko Group Corporation
Kráľová nad Váhom, Slovakia

Bulavytskyi, Maksym
State Enterprise "State Research Institute of Building Structures"
Kyiv, Ukraine

Burgoyne, C
University of Cambridge
Cambridge, United Kingdom of Great Britain and Northern Ireland

Burris, Lisa
The University of Texas at Austin
Austin, TX, United States

Buttignol, Thomaz Eduardo
Universidade Estadual de Campinas - Campus Cidade Universitaria Zeferino Vaz
Campinas, SP, Brazil

Büyükkaragöz, Alper
Faculty of Technology
Ankara, Turkey

C, Akin
KCG College of Technology
Chennai, India

C, Vijayaprabha
Karaikudi, Tamil Nadu, India

Caldarone, Michael
Des Plaines, IL, United States

Campos, Claudia
Universidade Federal Fluminense
Rio de Janeiro, Rio de Janeiro, Brazil

Canbay, Erdem
Middle East Technical University
Ankara, Turkey

Cannella, Francesco
Università degli Studi di Palermo
Palermo, Sicilia, Italy

Cao, Zhi
University of Antwerp
Antwerp, Belgium

Capozucca, Roberto
Faculty of Engineering
Ancona, Italy

Carino, Nicholas
Chagrin Falls, OH, United States

Carloni, Christian
Case Western Reserve University
Cleveland, OH, United States

Carpio, Víctor
Escuela Politécnica Nacional
Quito, Pichincha, Ecuador

Carrette, Jordan
Crosier Kilgour & Partners Ltd.
Winnipeg, MB, Canada

Cavunt, Yavuz
Istanbul Technical University
Istanbul, Turkey

Ceresa, Paola
Istituto Universitario di Studi Superiori di Pavia (IUSS)
Pavia, Italy

Chakkamalayath, Jayasree
Kuwait Institute for Scientific Research
Safat, Kuwait

Chakraborty, Arun
Indian Institute of Engineering Science and Technology, Shibpur
Howrah, West Bengal, India

Chang, Wei
Harbin, China

Chao, Shih-ho
The University of Texas at Arlington
Arlington, TX, United States

Chapirom, Aphai
Suranaree University of Technology Institute of Science
Nakhon Ratchasima, Nakhon Ratchasima, Thailand

Charalambidi, Barbara
Technical University of Crete
Chania, Greece

Chellappan, C. Selin Ravikumar
Malla Reddy Engineering College
Secunderabad, Telangana, India

Chen, Kang
Chongqing, China

Chen, Tao
China Academy of Building Research
Beijing, China

Chen, Xin
Shenyang, Liaoning, China

Chen, Xu
University of Colorado Boulder
Boulder, CO, United States

Cheng, Hu
Jiangnan University
Wuxi, Jiangsu, China

Cheng, Min-Yuan
National Taiwan University of Science and Technology
Taipei, Taiwan, China

Chidambaram, R. Siva
CSIR-Central Building Research Institute
Roorkee, Uttarakhand, India

Chijiwa, Nobuhiro
Tokyo Institute of Technology
Tokyo, Japan

Cho, Soon-Ho
Gwangju University
Gwangju, Republic of Korea

Choi, Oan
Soongsil University
Seoul, Republic of Korea

Choi, Yoon Suk
Korea Conformity Laboratories
Seoul, Republic of Korea

Chowdhury, Sharmin
Boğaziçi University
Istanbul, Turkey

Chu, S. H.
University of Hong Kong
Hong Kong, Hong Kong, China

Chung, Lan
Dankook University
Seoul, Republic of Korea

Cintra, Danielli
Vitória, Espírito Santo, Brazil

Cladera, Antoni
University of the Balearic Islands
Palma, Balearic Islands, Spain

Clementino, Fabio
IFPI
Teresina, Piauí, Brazil

Çolak, Andaç Batur
Niğde, Turkey

Costa, Ricardo
University of Coimbra
Coimbra, Portugal

Dang, Yudong
Tongji University
Shanghai, China

Daugevičius, Mykolas
Vilnius Gediminas Technical University
Vilnius, Lithuania

Dave, Shemal
Marwadi Education Foundation's Group of Institutions
Jamnagar, Gujarat, India

Dave, Urmil
Nirma University of Science and Technology
Ahmedabad, Gujarat, India

DC, Mitra
College of Engineering Trivandrum
Thiruvananthapuram, Kerala, India

De Brito, Jorge
IST / TUL
Lisbon, Portugal

de Oliveira, Gabriel
UNICAMP
Campinas, São Paulo, Brazil

De Rooij, Mario
TNO
Delft, the Netherlands

REVIEWERS IN 2022

Debbarma, Solomon
Indian Institute of Technology Bombay
Mumbai, Maharashtra, India

DeFord, Harvey
Florida Department of Transportation
Gainesville, FL, United States

Degtyarev, Vitaliy
Lexington, SC, United States

Demis, Sotiris
University of Patras
Patras, Greece

Den Uijl, Joop
Delft University of Technology
Delft, the Netherlands

Desai, Vijay
Central Water and Power Research Station
Pune, Maharashtra, India

Dhole, Rajaram
Katy, TX, United States

Dhonde, Hemant
University of Houston
Houston, TX, United States

Doh, Jeung-Hwan
Griffith University
Gold Coast, QLD, Australia

Domaneschi, Marco
Politecnico di Torino
Torino, Piedmont, Italy

Domingo, Alberto
Universitat Politècnica de València
Valencia, Spain

Dong, Jiangfeng
Sichuan University
Chengdu, China

Dong, Wei
Kunming, Yunnan, China

Dong, Yu-li
Huaqiao University
Quanzhou, Fujian, China

Dongell, Jonathan
Pebble Technology International
Scottsdale, AZ, United States

Dontchev, Dimitar
University of Chemical Technology and Metallurgy
Sofia, Bulgaria

Du, Lianxiang
The University of Alabama at Birmingham
Birmingham, AL, United States

Du, Yingang
Anglia Ruskin University
Chelmsford, United Kingdom of Great Britain and Northern Ireland

Dugvekar, Mitali
MANIT
Bhopal, Madhya Pradesh, India

Dundar, Cengiz
Çukurova University
Adana, Turkey

Dutta, Anjan
Indian Institute of Technology Guwahati
Guwahati, Assam, India

Dutta, Debabrata
Camellia Group Education
Kolkata, West Bengal, India

Duvallet, Tristana
University of Kentucky
Lexington, KY, United States

Dymond, Ben
Northern Arizona University
Flagstaff, AZ, United States

Einpaul, Jürgen
EPFL
Lausanne, Switzerland

El Maghraby, Yosra
The British University in Egypt
Cairo, Egypt

El Meski, Fatima
American University of Beirut
Beirut, Lebanon

El Refai, Ahmed
Québec, QC, Canada

El Semelawy, Mohamed
The University of Western Ontario
London, ON, Canada

EL Shafey, Asmaa
King Khalid University - Sarat Ebida campus
Sarat Ebida, Abha, Saudi Arabia

El-Ariss, Bilal
United Arab Emirates University
Al Ain, Abu Dhabi, United Arab Emirates

Eldarwish, Aly
Alexandria, Egypt

El-Dash, Karim
College of Technological Studies
Kuwait, Kuwait

El-Gendy, Mohammed
Tetra Tech Canada
Winnipeg, MB, Canada

El-Hawary, Moetaz
Kuwait University
Kuwait, Kuwait

El-Maaddawy, Tamer
United Arab Emirates University
Al Ain, Abu Dhabi, United Arab Emirates

Elmenshawi, Abdelsamie
University of Calgary
Calgary, AB, Canada

El-Refaie, Sameh
El-Gama City, Mataria, Cairo, Egypt

El-Salakawy, Ehab
University of Manitoba
Winnipeg, MB, Canada

Elsayed, Tarek
Cairo, Egypt

Eltahawy, Reham
Ain Shams University
Cairo, Egypt

Eskandari, Rasoul
Kashmar, Razavi Khorasan, Islamic Republic of Iran

Etman, Emad
El-Mahalla El-Kobra, Egypt

Ezeldin, Samer
The American University in Cairo
Cairo, Egypt

Faleschini, Flora
University of Padova
Padova, Italy

Fanella, David
Concrete Reinforcing Steel Institute
Schaumburg, IL, United States

Fantilli, Alessandro Pasquale
Politecnico di Torino
Torino, Italy

Faraone, Gloria
San Diego State University
San Diego, CA, United States

Fargier, Luis
Kiewit Infrastructure Engineers
Englewood, CO, United States

Faria, Duarte
Faculdade de Ciências e Tecnologia
Caparica-Lisbon, Portugal

Farrow, William
Lebanon, NJ, United States

Farshadfar, Omid
Thornton Tomasetti
Lawrence, KS, United States

Farzam, Masood
Structural Engineering
Tabriz, Islamic Republic of Iran

Farzampour, Alireza
Virginia Tech
Rockville, MD, United States

Fatemi, Hassan
Montréal, QC, Canada

Feng, De-Cheng
Southeast University
Nanjing, China

Feng, Muzai
Walter P Moore
Dallas, TX, United States

Fernandez Montes, David
Madrid, Madrid, Spain

Fikry, Ahmed
Cairo, Egypt

Fiset, Mathieu
Université du Québec à Chicoutimi
Chicoutimi, QC, Canada

Fitik, Birol
Hochschule für Technik Stuttgart
Stuttgart, Germany

Foraboschi, Paolo
Università Iuav di Venezia - Dipartimento di Architettura
Venice, VE, Italy

G D R N, Ransinchung
Roorkee, Uttarakhand, India

REVIEWERS IN 2022

G., Dhinakaran
SASTRA University
Thanjavur, India

G. S., Rampradheep
Kongu Engineering College
Erode, Tamil Nadu, India

Gabrijel, Ivan
University of Zagreb, Faculty of Civil Engineering
Zagreb, Croatia

Gan, Dan
Chongqing, China

Ganesan, N.
National Institute of Technology Calicut
Calicut, India

Gao, Peng
Hefei University of Technology
Hefei, China

Garcia Troncoso, Natividad Leonor
ESPOL
Guayaquil, Ecuador

Gayed, Ramez
University of Calgary
Calgary, AB, Canada

Geng, Yan
MCC Central Research Institute of Building and Construction Co. Ltd.
Beijing, Beijing, China

Ghahremannejad, Masoud
The University of Texas at Arlington
Arlington, TX, United States

Ghaly, Ashraf M
Union College
Schenectady, NY, United States

Ghannoum, Wassim
The University of Texas at Austin
Austin, TX, United States

Gheni, Ahmed
Komar University of Science and Technology
Sulaymaniyah, Iraq

Ghiami Azad, Amir Reza
University of Tehran
Tehran, Islamic Republic of Iran

Ghimire, Krishna
Kansas State University
Manhattan, KS, United States

Ghoddousi, Parviz
Iran University of Science and Technology
Tehran, Tehran, Islamic Republic of Iran

Gholamhoseini, Ali
Auckland, Auckland, New Zealand

Ghugal, Yuwaraj
Government College of Engineering, Karad
Karad, Maharashtra, India

Gong, Bill
Markham, ON, Canada

Gong, Wei
Jiangsu University of Science and Technology
Zhenjiang, China

Gongxun, Wang
Hunan University of Science and Technology
Xiangtan, China

González, Javier
University of the Basque Country
Bilbao, Basque Country, Spain

Govan, G. Elangovan
Civil Engineer
Chennai, Tamil Nadu, India

Grandić, Davor
University of Rijeka
Rijeka, Croatia

Guades, Ernesto
Technical University of Denmark
Lyngby, Denmark

Guan, Bowen
Xi'an, China

Guan, Junfeng
North China University of Water Resources and Electric Power
Zhengzhou, Henan, China

Gunasekara, Chamila
RMIT University Melbourne City Campus
Melbourne, VIC, Australia

Guner, Serhan
University of Toledo
Toledo, OH, United States

Guo, Honglei
Wuhan Polytechnic University
Wuhan, Hubei, China

Guzmán, Andrés
Universidad del Norte
Barranquilla, Atlántico, Colombia

Gyawali, Tek
Pokhara University
Lekhnath, Nepal

Habbaba, Ahmad
Technische Universität München
Garching, Germany

Habulat, Afifudin
Universiti Teknologi MARA
Permatang Pauh, Penang, Malaysia

Haddad Kolour, Hosain
University of Maine
Orono, ME, United States

Hadi, Muhammad
University of Wollongong
Wollongong, NSW, Australia

Hadje-Ghaffari, Hossain
John A. Martin & Associates, Inc.
Los Angeles, CA, United States

Hafezolghorani, Milad
Universiti Putra Malaysia
Serdang, Selangor, Malaysia

Haggag, Hesham
Haggag Consultancy for Construction
Cairo, Cairo, Egypt

Haj Seiyed Taghia, Seiyed Ali
Qazvin, Islamic Republic of Iran

Han, Baoguo
Dalian University of Technology
Dalian, China

Han, TianCheng
Southeast University
Nanjing, Jiangsu, China

Haneefa Kolakkadan, Mohammed
SSN College of Engineering
Kalavakkam, Tamil Nadu, India

Hanif, Asad
Hong Kong University of Science and Technology
Kowloon, Hong Kong, China

Hao, Qingduo
Harbin, China

Harith, Iman
Babylon, Iraq

Harris, G.
Cambridge, MA, United States

Hassan, Assem
Toronto, ON, Canada

Hassan, Mohamed
University of Sherbrooke
Sherbrooke, QC, Canada

Hassani, Arash
University of Arizona
Tucson, AZ, United States

Hassanpour, Sina
Sharif University of Technology
Tehran, Tehran, Islamic Republic of Iran

Hawileh, Rami
American University of Sharjah
Sharjah, United Arab Emirates

Helmy, Huda
Applied Science international
Durham, NC, United States

Hendi, Ali
Islamic Azad University, Khomeini Shahr Branch
Khomeyni Shahr, Islamic Republic of Iran

Henigal, Ashraf
Suez University
Suez, Egypt

Hernández-Montes, Enrique
University of Granada
Granada, Granada, Spain

Ho, Johnny
The University of Hong Kong
Hong Kong, Hong Kong, China

Holly, Ivan
Slovak University of Technology in Bratislava Faculty of Civil Engineering
Bratislava, Slovakia

Hong, Sung-Gul
Seoul National University
Seoul, Republic of Korea

Hooton, Doug
University of Toronto
Toronto, ON, Canada

Horowitz, Bernardo
Recife, PE, Brazil

Hossain, Khandaker
Toronto Metropolitan University
Toronto, ON, Canada

REVIEWERS IN 2022

Hosseini, Seyed Mohammad
University of Sherbrooke
Sherbrooke, QC, Canada

Hosseinpoor, Masoud
Universite de Sherbrooke Faculté de Génie
Sherbrooke, QC, Canada

Huang, Chung-Ho
National Taipei University of Technology
Taipei, Taiwan, China

Huang, Jianwei
Southern Illinois University Edwardsville
Edwardsville, IL, United States

Huang, Jong-Shin
National Cheng Kung University
Tainan, Taiwan, China

Huang, Le
Wuhan University
Wuhan, Hubei, China

Huang, Xiaobao
GM-WFG/GM-N American Project Center
Warren, MI, United States

Huang, Yuan
Hunan University
Changsha, Hunan, China

HUSEM, Metin
Civil Engineering Department, Karadeniz Technical University
Trabzon, Turkey

Hussain, Raja
King Saud University
Riyadh, Saudi Arabia

Huts, Andriy
Politechnika Rzeszowska im. Ignacego Łukasiewicza
Rzeszów, Poland

Hwang, Hyeon Jong
Seoul National University
Seoul, Republic of Korea

Hwang, Shyh-Jiann
National Taiwan University
Taipei, Taiwan, China

Ibrahim, Ayoob
University of Wollongong
Wollongong, NSW, Australia

Ibrahim, Tamer
Menofia, Egypt

Idrees, Maria
University of Engineering and Technology Lahore
Lahore, Punjab, Pakistan

Irassar, Edgardo
Departamento Ingeniería Civil - UNCPBA
Olavarría, Buenos Aires, Argentina

Iskander, George
University of Calgary Schulich School of Engineering
Calgary, AB, Canada

Islam, Mohammad Momeen Ul
The University of Adelaide
Adelaide, SA, Australia

Ismail, Kamaran
The University of Sheffield
Sheffield, United Kingdom of Great Britain and Northern Ireland

Ismail, Mohamed
Memorial University of Newfoundland
St. John's, NL, Canada

Izzet, Amer
University of Baghdad
Baghdad, Baghdad, Iraq

J S, Alein
SRM Institute of Science and Technology
Kattankulathur, India

Jafari, Khashayar
Tehran, Islamic Republic of Iran

Jagad, Gaurav
Sardar Vallabhbhai National Institute of Technology
Surat, Gujarat, India

Jahami, Ali
Beirut Arab University
Beirut, Lebanon

Jang, Seung Yup
Korea National University of Transportation
Uiwang, Gyeonggi-do, Republic of Korea

Jansen, Daniel
California Polytechnic State University
San Luis Obispo, CA, United States

Januzzi, Rafael
Universidade Federal de Ouro Preto
Ouro Preto, Minas Gerais, Brazil

Jazaei, Robabeh
Slippery Rock University of Pennsylvania
Slippery Rock, PA, United States

Jeng, Chyuan-Hwan
National Chi Nan University-Taiwan
Puli/Nantou, Taiwan, China

Jensen, James
San Mateo, CA, United States

Jian, Xiangru
Tongji University
Shanghai, China

Jiang, Hua
McDermott International, Inc.
Plainfield, IL, United States

Jiang, Liying
Jensen Hughes, Inc.
Lexington, MA, United States

Jing, Denghu
Southeast University
Nanjing, Jiangsu, China

Jing, Gouqing
Beijing Jiaotong University
Beijing, China

John V., Thomas
CUSAT
Kochi, Kerala, India

Jozić, Dražan
Faculty of Chemical Technology
Split, Croatia

Juvandes, Luis
Faculdade de Engenharia da Universidade do Porto - FEUP
Porto, Portugal

K, Sargunan
Malla Reddy Engineering College
Secunderabad, India

K., Balaji Rao
CSIR-Structural Engineering Research Centre
Chennai, India

Kabir, Mohammad Z.
Amirkabir University of Technology
Tehran, Tehran, Islamic Republic of Iran

Kaklauskas, Gintaris
Vilnius Gediminas Technical University
Vilnius, Lithuania

Kaliyavaradhan, Senthil
Hunan University
Changsha, Hunan, China

Kalkan, Ilker
Kırıkkale University
Kırıkkale, Turkey

Kamath, Muralidhar
Manipal Academy of Higher Education
Dakshina Kannada, Karnataka, India

Kamde, Deepak
Indian Institute of Technology Madras
Chennai, TN, India

Kan, Yu-Cheng
Chaoyang University of Technology
Taichung County, Taiwan, China

Kanagaraj, Ramadevi
Kumaraguru College of Technology
Coimbatore, Tamil Nadu, India

Kandasami, Siva
Bristol, United Kingdom of Great Britain and Northern Ireland

Kang, Shao-Bo
Chongqing University
Chongqing, Chongqing, China

Kankam, Charles
Kwame Nkrumah University of Science & Technology
Kumasi, Ghana

Kanta Rao, Velidandi
Central Road Research Institute
New Delhi, Delhi, India

Kanukollu, Venkata Madhav
D M S S V H College of Engineering
Machilipatnam, Andhra Pradesh, India

Kar, Arkamitra
Birla Institute of Technology and Science Pilani
Hyderabad, Telangana, India

Karayannis, Christos
Democritus University of Thrace
Xanthi, Greece

Karimi, Hossein
Eindhoven University of Technology
Eindhoven, the Netherlands

Kasap Keskin, Özlem
Muğla Sıtkı Koçman Üniversitesi
Muğla, Turkey

Ke, Guo-ju
Research Institute of Highway, Ministry of Transport
Beijing, China

REVIEWERS IN 2022

Kellouche, Yasmina
Université Hassiba Benbouali de Chlef
Chlef, Algeria

Keskin, Süleyman
Muğla Sıtkı Koçman Üniversitesi
Muğla, Turkey

Khabaz, Amjad
Hasan Kalyoncu University
Gaziantep, Turkey

Khaliq, Wasim
National University of Sciences and Technology
Islamabad, ICT, Pakistan

Khan, Sadaqat Ullah
NED University of Engineering and Technology
Karachi, Sindh, Pakistan

Khanzadeh Moradllo, Mehdi
Temple University
Philadelphia, PA, United States

Khatib, Jamal
University of Wolverhampton
Wolverhampton, United Kingdom of Great Britain and Northern Ireland

Khennane, Amar
UNSW Canberra at ADFA
Canberra, ACT, Australia

Kim, Jinyoung
Ajou University
Suwon, Gyeonggi-do, Republic of Korea

Kim, Sang-Woo
Kongju National University
Cheonan, Chungnam, Republic of Korea

Kim, Taehwan
University of New South Wales
Sydney, NSW, Australia

Kirgiz, Mehmet
İstanbul Üniversitesi - Cerrahpaşa
Istanbul, Turkey

Kisicek, Tomislav
Civil Engineering Faculty
Zagreb, Croatia

Kitayama, Kazuhiro
Tokyo Metropolitan University
Tokyo, Japan

Klemczak, Barbara
Silesian University of Technology
Gliwice, Poland

Köksal, Fuat
Yozgat Bozok University
Yozgat, Turkey

Koting, Suhana
University of Malaya
Kuala Lumpur, Federal Territory of Kuala Lumpur, Malaysia

Kramer, Kimberly
Kansas State University
Manhattan, KS, United States

Kreiger, Eric
U.S. Army Corps of Engineers Construction Engineering Research Laboratory
Champaign, IL, United States

Krstulovic-Opara, Neven
ExxonMobil Production Co
Houston, TX, United States

Kumar, Rakesh
Central Road Research Institute
Delhi, India

Kumar, Sundar
CSIR Structural Engineering Research Centre
Chennai, Tamil Nadu, India

Laco, Jan
D-Phase a.s.
Bratislava, Slovakia

Lai, James
Sacramento, CA, United States

Lakhani, Hitesh
Institute of Construction Materials
Stuttgart, Germany

Lakshmi, R
Kamaraj College of Engineering and Technology
Virudhunagar, Tamil Nadu, India

Lapi, Massimo
Università degli Studi di Firenze
Firenze, Italy

Lawler, John
Wiss, Janney, Elstner Associates, Inc.
Northbrook, IL, United States

Lederle, Rita
University of St. Thomas
Saint Paul, MN, United States

Lee, Chadon
Chung-Ang University
Anseong, Gyeonggi-do, Republic of Korea

Lee, Chang Hoon
Cornell University
Ithaca, NY, United States

Lee, Daniel
The Royal Danish Academy of Fine Arts, School of Architecture
Copenhagen, Denmark

Lee, Deuckhang
Chungbuk National University
Cheongju, Republic of Korea

Lee, Hung-Jen
National Yunlin University of Science and Technology
Douliou, Taiwan, China

Lee, Ju Dong
Texas A&M Transportation Institute
Bryan, TX, United States

Li, Fumin
China University of Mining and Technology
Xuzhou, Jiangsu, China

Li, Genfeng
Chongqing University of Arts and Sciences
Chongqing, China

Li, Shuguang
China Institute of Water Resources and Hydropower Research
Beijing, China

Li, Zhengqi
Houston, TX, United States

Libre, Nicolas Ali
Missouri University of Science and Technology
Rolla, MO, United States

Liepins, Atis
Simpson Gumpertz & Heger Inc.
Waltham, MA, United States

Lignola, Gian Piero
Università degli Studi di Napoli Federico II Scuola Politecnica e delle Scienze di Base
Napoli, Italy

Lin, Wei-Ting
Department of Civil Engineering
Ilan, Taiwan, China

Liu, Chengqing
Southwest Jiaotong University
Chengdu, Sichuan, China

Liu, Jing
Railway Engineering Research Institute
Beijng, China

Liu, Kai-Wei (Victor)
Texas A&M Transportation Institute
College Station, TX, United States

Liu, Peng
Changsha, China

Liu, Qingzhi
Minneapolis, MN, United States

Liu, Xuejian
The University of Texas at Arlington
Arlington, TX, United States

Liu, Yanbo
Florida Atlantic University
Dania Beach, FL, United States

Liu, Yanhua
Yangtze University
Jingzhou, China

Liu, Zanqun
School of Civil Engineering
Changsha, China

Liu, Zhao
Southeast University
Nanjing, Jiangsu, China

Liu, Zhengyu
Iowa State University of Science and Technology
Ames, IA, United States

Lizarazo Marriaga, Juan
Universidad Nacional de Colombia - Sede Bogotá
Bogotà, Colombia

Lolli, Francesca
Georgia Institute of Technology
Atlanta, GA, United States

Looi, Daniel
Swinburne University of Technology - Sarawak Campus
Kuching, Malaysia

López-Almansa, Francisco
Technical University of Catalonia
Barcelona, Spain

Lotfy, Abdurrahmaan
Lafarge Canada Inc.
Toronto, ON, Canada

Lu, Tingting
Xi'an, Shaanxi, China

Lu, Yang
Boise State University
Boise, ID, United States

REVIEWERS IN 2022

Luke, Allyn
New Jersey Institute of Technology
Englewood, NJ, United States

Luo, Baifu
Harbin, China

Lushnikova, Nataliya
National University of Water Management and Nature Resources Use
Rivne, Ukraine

Maage, Magne
Skanska Norge AS
Trondheim, Norway

Mabsout, Mounir
American University of Beirut
Beirut, Lebanon

Macht, Jürgen
Kirchdorf, Austria

Madani, Hesam
Graduate University of Advanced Technology
Kerman, Islamic Republic of Iran

Mahadik, Vinay
University of Stuttgart
Stuttgart, Germany

Mahdavi, Maziar
The University of Texas at Arlington
Arlington, TX, United States

Mahdy, Mohamed
Faculty of Engineering, Mansoura University
Mansoura, Dakhlia, Egypt

Maheswaran, Chellapandian
Mepco Schlenk Engineering College
Sivakasi, Tamil Nadu, India

Mahfouz, Ibrahim
Cairo, Egypt

Mahfouz, Sameh
Arab Academy for Science, Technology and Maritime Transport
Cairo, Cairo, Egypt

Mahinroosta, Mostafa
Tehran, Tehran, Islamic Republic of Iran

Mander, John
Texas A&M University
College Station, TX, United States

Mardi, Sahand
QIAU
Qazvin, Islamic Republic of Iran

Mari, Antonio
Universitat Politécnica de Catalunya
Barcelona, Barcelona, Spain

Martinez Andino, Marcos
DeSimone Consulting Engineers
Atlanta, GA, United States

Mata-Falcón, Jaime
ETH Zurich, Institute of Structural Engineering
Zurich, Zurich, Switzerland

Matta, Fabio
University of South Carolina
Columbia, SC, United States

Mazzotti, Claudio
University of Bologna
Bologna, Bologna, Italy

Mbessa, Michel
University of Yaoundé I - ENSP
Yaoundé, Cameroon

Meddah, Mohammed Seddik
Kingston University London
Kingston, Surrey, United Kingdom of Great Britain and Northern Ireland

Medeiros-Junior, Ronaldo
Universidade Federal do Paraná
Curitiba, Paraná, Brazil

Megid, Wael
TISEC Inc.
Morin-Heights, QC, Canada

Mehany, Shehab
University of Sherbrooke
Sherbrooke, QC, Canada

Menkulasi, Fatmir
Wayne State University
Detroit, MI, United States

Menu, Bruce
Université Laval Faculté des Sciences et de Génie
Québec, QC, Canada

Milestone, Neil
Callaghan Innovation
Lower Hutt, New Zealand

Mirrashid, Masoomeh
Semnan University
Semnan, Islamic Republic of Iran

Mirza, Faiz
Umm Al-Qura University
Makkah, Saudi Arabia

Mirzaee, Alireza
Shiraz, Islamic Republic of Iran

Mishra, Dhanada
KMBB College of Engineering and Technology
Khordha, Odisha, India

Mishra, Laxmi
MNNIT
Allahabad, UP, India

Mogili, Srinivas
National Taiwan University
Taipei, Taiwan, China

Mohamed, Ashraf
Alexandria University
Alexandria, Egypt

Mohamed, Nayera
Assiut University
Assiut, Egypt

Mohammed, Tarek
Islamic University of Technology
Gazipur, Dhaka, Bangladesh

Mohee, Fai
TMBN Extrados Inc.
Toronto, ON, Canada

Moini, Reza
Purdue University
West Lafayette, IN, United States

Mondal, Bipul
Chittagong University of Engineering & Technology
Chittagong, Bangladesh

Monkman, Sean
CarbonCure Technologies
Halifax, NS, Canada

Montoya Coronado, Luis Alberto
Palma, Spain

Moradi, Hiresh
Amirkabir University of Technology
Tehran, Islamic Republic of Iran

Moretti, Marina
National Technical University of Athens
Athens, Greece

Moser, Robert
U.S. Army Engineer Research and Development Center
Vicksburg, MS, United States

Mostafa, Mostafa M. A.
Al-Azhar University - Assiut Branch
Qena, Egypt

Mostofinejad, Davood
Isfahan University of Technology
Isfahan, Islamic Republic of Iran

Motaref, Sarira
University of Connecticut
Storrs, CT, United States

Mukai, David
University of Wyoming
Laramie, WY, United States

Mullins, Gray
University of South Florida
Tampa, FL, United States

Munir, Muhammad Junaid
RMIT University
Melbourne, VIC, Australia

Munjal, Pankaj
Birla Institute of Technology and Science Pilani
Pilani, Rajasthan, India

Munoz, Jose
Federal Highway Administration
McLean, VA, United States

Naaman, Antoine
University of Michigan
Ann Arbor, MI, United States

Nabavi, Seyed Esrafil
Rezvanshahr, Islamic Republic of Iran

Nafie, Amr
Cairo, Egypt

Naganathan, Sivakumar
Universiti Tenaga Nasional
Kajang, Selangor, Malaysia

Nair, Sooraj
United States Gypsum Corp
Libertyville, IL, United States

Najimi, Meysam
Iowa State University
Ames, IA, United States

Nakamura, Hikaru
Nagoya University
Nagoya, Aichi, Japan

REVIEWERS IN 2022

Nalon, Gustavo
Universidade Federal de Viçosa
Viçosa, Minas Gerais, Brazil

Narayanan, Subramanian
Gaithersburg, MD, United States

Naser, M. Z.
Clemson University
Clemson, SC, United States

Nazarimofrad, Ebrahim
Bu-Ali Sina University
Hamedan, Islamic Republic of Iran

Negrutiu, Camelia
Technical University of Cluj-Napoca
Cluj-Napoca, Cluj, Romania

Nguyen, Tan
Ton Duc Thang University
Ho Chi Minh City, Vietnam

Nguyen, Thi Thu Dung
Shimizu Corporation
Chuo-ku, Tokyo, Japan

Noshiravani, Talayeh
EPFL
Lausanne, Switzerland

Nowak-Michta, Aneta
Cracow University of Technology
Cracow, Poland

Obla, Karthik
National Ready Mixed Concrete Association (NRMCA)
Silver Spring, MD, United States

Omar, Mohamed
Dubai, United Arab Emirates

Omer, Alkailani
Dalhousie University
Halifax, NS, Canada

Orta, Luis
ITESM
Zapopan, Jalisco, Mexico

Ortiz-Lozano, Jose
Autonomous University of Aguascalientes
Aguascalientes, Aguascalientes, Mexico

Othman, Nor Hazurina
Universiti Tun Hussein Onn Malaysia
Batu Pahat, Johor, Malaysia

Oukaili, Nazar
University of Baghdad
Baghdad, Iraq

Oundhakar, Abhijeet
Invictus Consultancy Services
Navi Mumbai, Maharashtra, India

Oyguc, Resat
İstanbul Teknik Üniversitesi
Istanbul, Turkey

P., Mary
Indian Institute of Technology Madras
Chennai, Tamil Nadu, India

Pacheco, Alexandre
Universidade Federal do Rio Grande do Sul (UFRGS)
Porto Alegre, RS, Brazil

Pacheco, Jose
MJ2 Consulting, PLLC
Chicago, IL, United States

Paiva, Maria
UFRJ
Rio de Janeiro, RJ, Brazil

Pakala, Purushotham
Arup
Concord, CA, United States

Palieraki, Vasiliki
National Technical University of Athens
Zografou, Athens, Greece

Panda, Sushree
Kalinga Institute of Industrial Technology
Bhubaneswar, India

Pandit, Poornachandra
Manipal Institute of Technology
Manipal, India

Pantazopoulou, Stavroula
York University
Toronto, ON, Canada

Parastesh, Hossein
University of Science and Culture
Tehran, Tehran, Islamic Republic of Iran

Parsekian, Guilherme
UFSCar
São Carlos, Brazil

Parthasarathy, Pavithra
Hong Kong University of Science and Technology
Kowloon, Hong Kong, China

Patil, Sagar
Tatyasaheb Kore Institute of Engineering and Technology
Warananagar, Maharashtra, India

Pauletta, Margherita
University of Udine
Tavagnacco, Udine, Italy

Peng, Fei
Hunan University
Changsha, China

Perez Caldentey, Alejandro
Universidad Politécnica de Madrid
Madrid, Madrid, Spain

Perez Ruiz, Diego
Pontificia Universidad Javeriana Sede Cali
Cali, Valle del Cauca, Colombia

Persson, Bertil
Bara, Sweden

Phillippi, Donald
Kansas State University
Manhattan, KS, United States

Piccinin, Roberto
Hilti, Inc.
Tulsa, OK, United States

Pierott, Rodrigo
Universidade Estadual do Norte Fluminense Darcy Ribeiro
Campos Dos Goytacazes, RJ, Brazil

Pinho, Jose
Tribunal de Contas do Estado do Pará
Belém, Pará, Brazil

Pisani, Marco
Politecnico di Milano
Milan, Italy

Pocesta, Ylli
Debar, North Macedonia

Pol, Chandrakant
Walchand College of Engineering
Sangli, Maharashtra, India

Polavaram, Krishna Chaitanya
Indian Institute of Technology Madras
Chennai, Tamil Nadu, India

Pourbaba, Masoud
Islamic Azad University, Maragheh
Maragheh, East Azarbaijan, Islamic Republic of Iran

Pugliaro, Andrea
Senior Materials and Laboratory Engineer (Civil and Geotechnical)
Savona, Italy

Putra Jaya, Ramadhansyah
Universiti Teknologi Malaysia
Gambang, Pahang, Malaysia

Pv, Premalatha
CARE School of Engineering
Tiruchirappalli, India

Qasrawi, Hisham
The Hashemite University
Zarqa, Jordan

Qi, Chengqing
CEMEX
Riverview, FL, United States

Qian, Ye
University of Hong Kong
Hong Kong, China

Qiao, Chunyu
Wiss, Janney, Elstner Associates, Inc.
Austin, TX, United States

Quintana Gallo, Patricio
Czech Technical University in Prague
Praha, Czech Republic

Rafi, Muhammad
NED University of Engineering and Technology
Karachi, Sindh, Pakistan

Raghavendra, T.
R.V. College of Engineering, Visvesvaraya Technological University
Bangalore, Karnataka, India

Ragheb, Wael
Alexandria University
Alexandria, Egypt

Raj, Bharati
NSS College of Engineering, Palakkad
Palakkad, India

Rajbanshi, Soumi
Indian Institute of Technology Guwahati
Guwahati, Assam, India

Ram, V.
BITS Pilani, Hyderabad Campus
Hyderabad, Andhra Pradesh, India

REVIEWERS IN 2022

Ramanathan, Sivakumar
Oregon State University
Corvallis, OR, United States

Ramaswamy, Ananth
Indian Institute of Science
Bangalore, Karnataka, India

Ramirez-Garcia, Alberto
University of Arkansas
Fayetteville, AR, United States

Ramos, António
Faculdade de Ciências e Tecnologia
Monte de Caparica, Portugal

Ramyar, Kambiz
Ege University
Izmir, Turkey

Rangelov, Milena
Federal Highway Administration
Washington, DC, United States

Rao, Sarella
National Institute of Technology Warangal
Warangal, Andhra Pradesh, India

Rashad, Alaa
Housing and Building National Research Center
Giza, Egypt

Rashed, Youssef F.
Faculty of Engineering
Giza, Giza, Egypt

Rasheed, Abdur
Shaqra University
Shaqra, Saudi Arabia

Rasul, Mehboob
Sumitomo Mitsui Construction Co., Ltd.
Chuo, Japan

Rasulo, Alessandro
University of Cassino and Southern Lazio
Cassino, Italy

Razaqpur, A. Ghani
McMaster University
Hamilton, ON, Canada

Ridha, Maha (Lianne)
Melbourne, VIC, Australia

Rizwan, Syed Ali
Superior University Lahore
Lahore, Pakistan

Robberts, John
Robberts & Marshall Structural Engineers (Pty) Ltd
Pretoria, South Africa

Rodhia, Rohit
Varanasi, Uttar Pradesh, India

Rojas Aguero, Rosangel
Universidade Federal do Rio Grande
Rio Grande, Rio Grande do Sul, Brazil

Rombach, Guenter
Hamburg University of Technology
Hamburg, Germany

Ross, Brandon
Clemson University
Clemson, SC, United States

Rupnow, Tyson
Louisiana Transportation Research Center
Baton Rouge, LA, United States

S, Kumaravel
Annamalai University
Cuddalore, Tamil Nadu, India

Sabouni, Faisal
Architectural Consulting Group
Abu Dhabi, United Arab Emirates

Sadowska-Buraczewska, Barbara
Bialystok University of Technology
Białystok, Poland

Saedi, Houman
Tarbiat Modares University & University of Tabriz and TSML CO.
Tehran, Islamic Republic of Iran

Saeki, Tatsuhiko
Niigata University
Niiagta, Japan

Safiuddin, Md.
George Brown College
Toronto, ON, Canada

Sagadevan, Radha
Indian Institute of Technology Madras
Chennai, Tamil Nadu, India

Said, Shwan
Erbil, Iraq

Sakban, Haider
Piscataway, NJ, United States

Saleh Ahari, Reza
Ege University
Izmir, Turkey

Salib, Sameh
Markham, ON, Canada

Sancak, Emre
Suleyman Demirel University
Isparta, Turkey

Sancharoen, Pakawat
Thammasat University
Klong Luang, Pathumthani, Thailand

Santa Maria, Hernan
Pontificia Universidad Católica de Chile
Santiago, RM, Chile

Santos, Jose
University of Madeira
Funchal, Portugal

Santos, Sérgio
SBS Engineering Consultancy
Goiânia, Goiás, Brazil

Sargam, Yogiraj
CarbonCure Technologies
Dartmouth, NS, Canada

Sartaji, Parisa
Ardabil, Islamic Republic of Iran

Sato, Yuichi
Kyoto University
Kyoto, Kyoto, Japan

Sayed Ahmed, Mahmoud
Toronto Metropolitan University
Toronto, ON, Canada

Sayyar Roudsari, Sajjad
North Carolina Agricultural and Technical State University
Greensboro, NC, United States

Schackow, Adilson
Santa Catarina State University
Joinville, Santa Catarina, Brazil

Schlicke, Dirk
Graz University of Technology
Graz, Austria

Seco, Laura
Coimbra, Portugal

Sener, Erkan
TES-İŞ Mühendislik Ltd.
Tuzla, Istanbul, Turkey

Sengupta, Piyali
National University of Singapore
Singapore, Singapore

Seręga, Szymon
Cracow University of Technology
Kraków, Poland

Serry, Mohamed
Arab Contractors
Cairo, Egypt

Shabana, Islam
University of Sherbrooke
Sherbrooke, QC, Canada

Shafigh, Payam
Kuala Lumpur, Malaysia

Shafiq, Nasir
Universiti Teknologi Petronas
Tronoh, Perak, Malaysia

Shagerdi Esmaeeli, Hadi
Purdue University
West Lafayette, IN, United States

Shah, Aanal
CEPT University
Ahmedabad, Gujarat, India

Shaheen, Ehab
University of Calgary
Calgary, AB, Canada

Shahmansouri, Amir Ali
University of Mazandaran
Babolsar, Islamic Republic of Iran

Shaikh, Fawad
Stanford, CA, United States

Sharma, Akanshu
Institute of Construction Materials
Stuttgart, Germany

Shayan, Ahmad
ARRB Group
Vermont South, VIC, Australia

Shehata, Medhat
Toronto Metropolitan University
Toronto, ON, Canada

Shen, Yin
Tongji University
Shanghai, China

Sherif, Mohtady
Toronto Metropolitan University Faculty of Engineering and Architectural Science
Toronto, ON, Canada

REVIEWERS IN 2022

Sherman, Matthew
Simpson Gumpertz & Heger, Inc.
Melrose, MA, United States

Shetty, Kiran
Manipal Institute of Technology
Manipal, Karnataka, India

Shi, Caijun
Hunan University
Changsha, Hunan, China

Shi, Tao
Zhejiang University of Technology
Hangzhou, Zhejiang, China

Shim, Hyunbo
Korea Concrete Institute
Seoul, Republic of Korea

Shin, Hyeongyeop
Seoul National University
Gwanak-gu, Seoul, Republic of Korea

Shivali, Ram
Central Soil and Materials Research Station
New Delhi, India

Shrive, Nigel
University of Calgary
Calgary, AB, Canada

Shukla, Abhilash
Jaypee University of Information Technology
Waknaghat, Himachal Pradesh, India

Siad, Hocine
Toronto Metropolitan University
Toronto, ON, Canada

Siddique, Mohammad
Bangladesh University of Engineering and Technology
Dhaka, Bangladesh

Silfwerbrand, Johan
KTH Royal Institute of Technology
Stockholm, Sweden

Silva, Marcos
Campinas, Brazil

Singh, Abhishek
National Council for Cement and Building Materials
Ballabgarh, Haryana, India

Singh, Brijesh
Faridabad, Haryana, India

Singh, Harvinder
Guru Nanak Dev Engineering College
Ludhiana, Punjab, India

Singh, Navdeep
Jalandhar, Punjab, India

Sirivivatnanon, Vute
University of Technology Sydney
Broadway, NSW, Australia

Sivey, Paul
Sivey Enterprises
Hilliard, OH, United States

Smadi, Mohammad
Jordan University of Science and Technology
Irbid, Jordan

Soares, Renan Gustavo Pacheco
Universidade Federal de Pernambuco
Recife, Pernambuco, Brazil

Sobhani, Jafar
Building and Housing Research Center
Tehran, Tehran, Islamic Republic of Iran

Solnosky, Ryan
Penn State University Park
University Park, PA, United States

Soltani, Masoud
Tarbiat Modares University
Tehran, Tehran, Islamic Republic of Iran

Sonyal, Muhammad
University of Engineering and Technology Lahore
Lahore, Punjab, Pakistan

Sotiriadis, Konstantinos
Ústav Teoretické a Aplikované Mechaniky Akademie věd České Republiky
Praha, Czech Republic

Souza, Rafael
Universidade Estadual de Maringá
Maringá, Paraná, Brazil

Spinella, Nino
University of Catania Faculty of Engineering
Catania, Italy

Spyridis, Panagiotis
Institute for Structural Engineering
Vienna, Austria

Sreekala, R.
Structural Engineering Research Centre
Chennai, Tamil Nadu, India

Sreenivasappa, Nandeesh
Ramaiah Institute of Technology
Bangalore, Karnataka, India

Stojadinovic, Bozidar
Swiss Federal Institute of Technology
Zurich, Switzerland

St-Pierre, Daniel
Intertek Testing Services NA Ltd.
Coquitlam, BC, Canada

Stucchi, Fernando
University of São Paulo Polytechnic School
Adamantina, SP, Brazil

Su, Junsheng
Tianjin University
Tianjin, China

Su, Yu-Min
National Kaohsiung University of Science and Technology
Kaohsiung, Taiwan, China

Suda, Vijaya
CMR Technical Campus
Secunderabad, India

Sultan, Mohamed
Al-Azhar University
Cairo, Egypt

Sun, Jing
Beijing, China

Sun, Tao
Wuhan, China

Suryawanshi, Yogesh
JSPM's Imperial College of Engineering and Research Wagholi
Pune, Maharashtra, India

T., Hemalatha
CSIR-Structural Engineering Research Centre
Chennai, Tamil Nadu, India

Tabsh, Sami
American University of Sharjah
Sharjah, United Arab Emirates

Tadros, Maher
e.Construct, USA, LLC
Omaha, NE, United States

Tahmasebinia, Faham
University of Wollongong
Wollongong, NSW, Australia

Tajaddini, Abbas
University of Bath Faculty of Engineering and Design
Bath, United Kingdom of Great Britain and Northern Ireland

Tan, Kiang Hwee
National University of Singapore
Singapore, Singapore

Tanacan, Leyla
Istanbul Technical University
Istanbul, Turkey

Tang, Fujian
Dalian University of Technology
Dalian, Liaoning, China

Tankut, Tugrul
Middle East Technical University
Ankara, Turkey

Tanner, Jennifer
University of Wyoming
Laramie, WY, United States

Tao, Lei
Shell Oil Company
Houston, TX, United States

Tarafder, Nilanjan
Siliguri, West Bengal, India

Tariq, Samia
University of Engineering and Technology, Lahore
Lahore, Punjab, Pakistan

Tatiraju, Ramanjaneyulu
North Dakota State University
Fargo, ND, United States

Tekin, Ilker
Bayburt University
Bayburt, Turkey

Thokchom, Suresh
Manipur Institute of Technology
Imphal, Manipur, India

Tixier, Raphael
Western Technologies Inc.
Phoenix, AZ, United States

Tiznobaik, Mohammad
The University of British Columbia | Okanagan Campus
Kelowna, BC, Canada

Tognonvi, Tohoue Monique
Université de Sherbrooke
Sherbrooke, QC, Canada

REVIEWERS IN 2022

Tomas, Antonio
Technical University of Cartagena (UPCT)
Cartagena, Spain

Tripura, Deb
NIT Agartala
Agartala, India

Tsubaki, Tatsuya
Yokohama National University
Yokohama, Japan

Ueda, Naoshi
Kansai University
Suita, Osaka, Japan

Umipig, Jorge
Vista Land & Lifescapes, Inc.
Mandaluyong City, Metro Manila, Philippines

Ungermann, Jan
RWTH Aachen University
Aachen, Germany

Uzel, Almıla
Yeditepe University
Istanbul, Turkey

Vakilly, Sedigheh
Isfahan, Islamic Republic of Iran

Vancura, Mary
Saint Paul, MN, United States

Vasovic, Dejan
University of Belgrade, Faculty of Architecture
Belgrade, Serbia

Velázquez Rodríguez, Sergio
Universidad Panamericana
Zapopan, Jalisco, Mexico

Villacis, Eugenia de las
Escuela Politécnica Nacional
Quito, Pichincha, Ecuador

Vintzileou, Elizabeth
National Technical University of Athens
Athens, Greece

Vosahlik, Jan
ICON
Austin, TX, United States

Vu, Ngoc Son
Hanoi University of Civil Engineering
Hanoi, Vietnam

Wally, Gustavo
Universidade Federal do Rio Grande do Sul
Porto Alegre, Brazil

Wang, Dun
Research Institute of Structural Engineering and Disaster Reduction, Tongji University
Shanghai, China

Wang, Huanzi
San Jose, CA, United States

Wang, Penggang
Qingdao University of Technology
Qingdao, China

Wang, Xiao-Yong
Kangwon National University
Chuncheon, Republic of Korea

Wardhono, Arie
State University of Surabaya
Surabaya, Jawa Timur, Indonesia

Wegner, Leon
University of Saskatchewan College of Engineering
Saskatoon, SK, Canada

Wei-Jian, Yi
Changsha, China

Werner, Anne
SIUE
Edwardsville, IL, United States

Wierciszewski, Mark
Port Authority of New York and New Jersey
Jersey City, NJ, United States

Wilde, W James
Texas State University
San Marcos, TX, United States

Won, Moon
Texas Tech University
Lubbock, TX, United States

Wong, Sook Fun
Nanyang Technological University
Singapore, Singapore

Worley II, Robert
University of Vermont
Burlington, VT, United States

Woyciechowski, Piotr
Warsaw University of technology
Warsaw, Poland

Wu, Chenglin
Missouri University of Science and Technology
Rolla, MO, United States

Wu, Hao
Tongji University
Shanghai, China

Wu, Kai
Nanjing, Jiangsu, China

Wu, Yu-You
Foshan University
Foshan, Guangdong, China

Wu, Zhimin
Dalian University of Technology
Dalian, Liaoning, China

Xie, Guoshuai
Wuhan University
Wuhan, Hubei, China

Xie, Jun
Zhangjiakou, China

Xie, Tianyu
RMIT University
Melbourne, VIC, Australia

Xu, Aimin
ARRB Group
Melbourne, VIC, Australia

Yan, Jie
Zhangjiakou, China

Yan, Peiyu
Tsinghua University
Beijing, China

Yang, Junlong
Dalian University of Technology
Dalian, China

Yang, Shuyan
Yinchuan City, China

Yang, Sung Chul
Hongik University
Mapo-gu, Republic of Korea

Yankelevsky, David
National Building Research Institute
Haifa, Israel

Yapa, Hiran
University of Peradeniya Faculty of Engineering
Peradeniya, Sri Lanka

Yasso, Samir
University of Mosul
Mosul-Bartella, Nineveh, Iraq

Yazbeck, Fouad
360 TANGENT Engineering Consultancy
Abu Dhabi, United Arab Emirates

Yekrangnia, Mohammad
Shahid Rajaee Teacher Training University
Tehran, Islamic Republic of Iran

Yepez, Fabricio
Universidad San Francisco de Quito
Quito, Pichincha, Ecuador

Yildirim, Hakki
Istanbul, Turkey

Yildirim, Salih
Columbia University
New York, NY, United States

Yin, Shiping
China University of Mining and Technology
Xuzhou, China

Yindeesuk, Sukit
University of Illinois at Urbana-Champaign
Urbana, IL, United States

Yingjie, SHAN
Central South University
Changsha, Hunan, China

YK, Guru
Indian Institute of Science
Bangalore, India

Yost, Joseph
Villanova University
Villanova, PA, United States

Yousefpour, Hossein
The University of Texas at Austin
Austin, TX, United States

Youssef, AHmed
Giza, Giza, Egypt

Yuniarsyah, Eko
Institut Teknologi Bandung
Bandung, Indonesia

Zad, Nader
Kansas State University
Manhattan, KS, United States

REVIEWERS IN 2022

Zaidi, S. Kaleem
Aligarh Muslim University
Aligarh, UP, India

Zanuy, Carlos
Universidad Politécnica de Madrid
Madrid, Madrid, Spain

Zapata, Luis
Universidad Industrial de Santander
Bucaramanga, Santander, Colombia

Zeidan, Mohamed
Southeastern Louisiana University College of Science and Technology
Hammond, LA, United States

Zhang, Feng
Nanjing Hydraulic Research Institute
Nanjing, China

Zhang, Jiaolong
Tongji University
Shanghai, China

Zhang, Qian
Nanjing, China

Zhang, Wei
Tsukuba Daigaku
Tsukuba, Japan

Zhao, Xingzhuang
University of Maryland at College Park
College Park, MD, United States

Zhao, Xin-Yu
South China University of Technology
Guangzhou, China

Zheng, Jianjun
Zhejiang University of Technology
Hangzhou, China

Zheng, Yu
Dongguan University of Technology
Dongguan, Guangdong, China

Zheng, Yulong
Jiangsu University
Zhenjiang, China

Zhenhong, Wang
China Institute of Water Resources and Hydropower Research
Beijing, China

Zhong, Rui
Southeast University
Nanjing, China

Zhou, Shengjun
MacGregor, QLD, Australia

Zhu, Wenjun
L'Institut National des Sciences Appliquées de Toulouse
Toulouse, Toulouse, France

Zhu, Yanping
Missouri University of Science and Technology
Rolla, MO, United States

Zimmer, Alec
Simpson Gumpertz & Heger Inc.
Waltham, MA, United States

Zornoza, Emilio
University of Alicante
Alicante, Alicante, Spain

Zych, Mariusz
Politechnika Krakowska im. Tadeusza Kościuszki
Kraków, Poland

ACI MATERIALS JOURNAL

The American Concrete Institute (ACI) is a leading authority and resource worldwide for the development and distribution of consensus-based standards and technical resources, educational programs, and certifications for individuals and organizations involved in concrete design, construction, and materials, who share a commitment to pursuing the best use of concrete.

Individuals interested in the activities of ACI are encouraged to explore the ACI website for membership opportunities, committee activities, and a wide variety of concrete resources. As a volunteer member-driven organization, ACI invites partnerships and welcomes all concrete professionals who wish to be part of a respected, connected, social group that provides an opportunity for professional growth, networking, and enjoyment.

American Concrete Institute